Spectrin-lipid interactions and their effect on the membrane mechanical properties

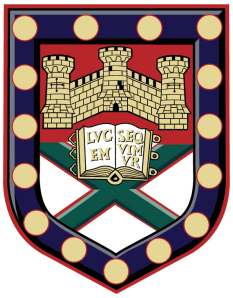

Barbara Claire Mireille Annick Sarri

School of Physics

University of Exeter

A thesis submitted for the degree of

Doctor of Philosophy in Physics

June 2014

Spectrin-lipid interactions and their effect on the membrane mechanical properties

Submitted by Barbara Claire Mireille Annick Sarri to the University of Exeter
as a thesis for the degree of Doctor of Philosophy in Physics
2014

I certify that all material in this thesis which is not my own work has been identified and that no material has previously been submitted and approved for the award of a degree by this or any other University.

Barbara Claire Mireille Annick Sarri
June 2014

To my dad, who never got the chance to go to University...

Acknowledgements

There are many people whose support and encouragement helped me through the PhD and without whom I would have given up the project, left that rainy country and gone home.

Firstly, I would like to thank my supervisor Peter Petrov for his availability and good guidance all along the PhD while allowing me great freedom for the direction of research I wanted to take and thank you for reminding me from time to time, that the project was quite difficult and that a lack of results was not necessarily due to a lack of good research skills.

Secondly, I would like to thank my second supervisor Julian Moger, who encouraged me to develop techniques in the CARS lab. Without him I don't think I would have ever dared to try to implement the micropipette aspiration in the CARS lab but his enthusiam for nonlinear optics is contagious. Thanks also for the good times in conferences and the journal club Tuesday meeting which helped to develop (hopefully) communicating skills in a convivial way.

Thirdly, I would like to thank Peter Winlove who is the head of the Biomedical Physics group. Thank you for taking care that "everybody is happy with the world" in the group, thank you for giving me extra supervision at the end of the PhD, and for having been so efficient with dealing with finances people on my behalf so many times.

I also have to thank Professor Peter Vukusic for his precious advice and excellent efficient mentoring.

In the UK, most help to PhD students comes from post-docs and I have been super lucky to be surrounded with amazing post-docs who need to be thanked. First, David Woods and Debra Shaw who shared this project. Debs taught me everything I know about protein biology from the basis and has become a really good friend. David was available at all times. For absolutely anything you would ask him (work or non-work related), he would come with a smart funny idea. I would never be thankful enough for keeping me smiling through the hard times: his sense of humour made it ok to do spectrin extraction everyday for months.

Second, Natalie Garrett and Jessica Mansfield who have been my mentors in the CARS lab. Jess has been amazing to teaching me how to switch the Mira laser into picosecond mode and was always available and happy to help when I needed to be rescued in the lab. Nat hmm, I would probably need to write another thesis to make the list of all the help you gave me during my PhD, not only for teaching me all the laser basics and more complicated techniques with such patience. Without your help I would have quit my PhD a thousand times. Thanks for believing in me when I stopped believing in myself and for being such a good friend.

Then I would like to thank inspirational hard late workers James Bell, Pete Hale and Rhys Goodhead who helped me in the CARS lab at the beginning of my PhD when Nat, Jess and Julian where away or busy.

Dave Colridge and Ellen Green are probably the best lab technicians in the world. You have made my life so much easier knowing everyone and pointing me in the right direction; knowing where everything is. Dave is magical with computers : he installed everysingle thing I needed in no-time on my laptop - like the VPN so that I would feel like I am still in the lab while writing up back in France - and fixed it when it had some smashed troubles. Like for Natalie it would be too long to list all the help you provided me: from all my heart thank you for being in Exeter!

I also need to thank: Sharon Jewell for teaching me how to grow vesicles and for explaining the micropipette aspiration experiment Petre Gologan for teaching me how to use the confocal microscope, Paul Eggleton for guidance and help for the different chromatograph columns and open up access to St Luke campus, Sharon Kelly and Professor Allan Cooper for letting us use their ITC set-up and for their help with the experiments, Miranda Smallwood for helping me with the FITC-tagged process when Debra had left, Helen Dawe for providing me with fibroblast (both actin-tagged and normal) cells, Ellen Green (again) for letting me use some of her precious α- elastin stock and Nina Meinzer for her help with the SEM.

We are also very lucky to have at our disposal an amazing team in the workshop who built amazing pieces of equipment, improving set-ups in such ways you would have never thought! Thank you all, my micropipette set-ups are all shiny and working thank to you! Like Dave and Ellen, you have made my life easier!

Thanks also to the electromag group (PhD students and post docs). They all became good friends over the years and welcome me within their group when everybody was abandoning our biophysics lab. Thanks for all thel tea time breaks, the laughs and funny scientific(ish) discussions. Tim, Al, and Chester it has been great to be in the same year as you. Celia thanks for the inspirational talk in my first week (it echoed

all the way through my PhD). Thanks Alfie and Chris for the crosswords at tea time and for making me feel like home in the UK. Thanks Tom for teaching me how to solve Rubik's cubes and being such a good friend to me and thanks Pete for teaching me how to knit. Also thanks for the moral support, Tim and Al: it really helped knowing you were suffering the writing up at the same time. Special thanks also to Helen, Tom, Caz and Leigh for the short-notice-efficient-proof-reading of my Chapters at the very end and to Tom (again) and Sam for their help for using LaTeX.

Beside of work, thank you all (both bio and electromag groups) for all the great memories: for all the Friday pub nights at the Ram or (and?) Impy, for the firehouse pizza nights, for the crazy parties at 10 Cavendish, for the pink tie pub crawl, New Year eve events, Christmas dinners and parties, Physics summer ball and other beer festivals. One of my favourite memories is the "French Day" you organized once when I was homesick.. Thanks also to Colin, Ben and Patricia for the good memories back in Heavitree making of our home the most international house of Exeter perhaps. Thank you Jo to have welcomed me in your house in the last year, at Team 17. Lizzy and Sabby it's been so great living with you (I keep amazing memories of your gardening times, evening cupcakes-making and New girl evenings). Thanks Jo boy, Katy, and Rosy (and in the very hand Graeme and Becca), I enjoyed sharing this house with you.

Finally thanks to the new enthusiastic crew in bio who resuscitated the PhD student office, especially Kelly, Martha, Lauren, Louise and Sahand and later on the new post-docs Kuprakar, Inge, Ben, Jennifer and Yusuki and the other whose name I am not familiar with yet.. It is great to know that our office is noisy with laughter and good scientific (or not) discussions again.

I have aimed to leave for a long time, but now that the drilling has stopped, now that the 2012-8-month-rain trauma has gone, I find Exeter really difficult to leave. With all the new amazing people in bio from all over the world, and the new super resolution labs, Exeter Biophysics just seems to be the perfect place to work.

Switch to French: Would have not been possible without all the support from over Sea from:

Ces remerciements sont déjà bien assez longs, rapidement quand même merci aussi à Frantz Brücker, Jean-Claude Vial and Julien Douady pour m'avoir donné le gout et l'envie de faire une thèse.

Merci à ma cobureau Laureline pour être devenue une bonne amie, pour avoir supporté mes plaintes tous ces jours de pluie, et pour tous ces week-end aux quatre coins de l'Angleterre! Merci à Aurélie et Anne pour être les meilleures amies du monde, pour être là quoiqu'il arrive, pour me redonner le moral quand rien ne va plus, et pour partager les bons moments (road trip en Italie, Apéro Skype et autres). Merci à Kévin et Isa pour leur soutient quotidien. Merci à Armand pour ces épiques mails du lundi et pour m'avoir aidé à organiser ce tour de capitales d'Europes tout durant la thèse. Merci à Kévin (encore), Clément, Cécile et Romain Gaior pour avoir toujours, toujours fait l'effort de libérer votre calendrier quand je rentrais sur Paris. Merci à Pierre, Delphine et Geoffroy d'être toujour là: ces quelques mois de rédaction à Paris ont prouvé que rien n'avait changé depuis la sortie d'école à Grenoble. Merci Corentin, Adrien, Kévin MPPC, Claire pour leur randoms email de soutient réguliers. Et merci à Prisca pour ce coup de fil qui m'a sauvé en pleine crise de rédaction. Merci aussi aux Nanotechs, pensée toute spéciale pour Louis qui fait sa thèse à l'étranger: courage pour la rédaction et merci pour tous ces Skype meetings entre expats. Ds le même esprit, merci à Nico et Joël pour avoir été d'abords de chouette compagnons de voyage lors de notre Thailand-back-pack-tour puis, plus tard, pour tous les encouragements et Skype meetings. Merci aussi à tous ces gens rencontrés au détour d'un auberge de jeunesse, d'une conférence, d'un week end capitale d'Europe ou d'un heureux hasard: Stephan, Nico, Marielle, Erik, Laurianne, Orry et plus récemment Marie-Pierre, Christelle, Farah. Vous avez participé à faire de cette aventure "thèse-vie à l'étranger" une expérience inoubliable. Un énorme merci aussi à Salimata et Rémi pour m'avoir acceuilli à Londres à chacun de mes passages, vous avez ma reconnaissance à jamais!

Merci à ces amis de toujours Léa, Fanny, Gaspard et Olivia pour leur support régulier. Les années passent, les villes (voir pays) changent et vous êtes toujours là: MERCI. Et surtout Merci à ma famille sans qui rien n'aurait été possible! Merci à mes parents: maman merci pour avoir été aux petits soins (encore plus qu'à l'habitude) quand je suis revenue rédiger à la maison. Marie et Clara merci pour m'avoir soutenu comme vous avez pu, pour m'avoir fait rigoler, pour avoir montré un enthousiasme incomparable pour mes ennuyeux schémas de lipide et pour cette complicité retrouvée! Julia passer te faire des coucou à Londres sur le chemin d'Exeter pendant la rédaction a bien aidé!

Enfin merci à toi, Christophe pour partager ma vie depuis bientôt deux ans, pour me supporter et me soutenir du mieux que tu peux!

Abstract

This thesis presents the experimental work performed on the spectrin protein. The aim of the work was to study the direct interactions of spectrin, the cytoskeleton of RBCs, with membrane lipid to determine its effects on the mechanical properties of the lipid bilayer. Motivation for this work came from a lack of unanimity in the field of spectrin, and the hypothesized potential of the protein to perforate giant unilamellar vesicles. The work aimed to investigate and determine how spectrin-lipid interactions influence membrane mesoscopic morphology and biophysics in ways that could ultimately be important to cellular function. For this purpose, a protocol was implemented to take into account the different aspects of the binding. Direct visualisation of the spectrin-lipid interaction and distribution was achieved using confocal fluorescence microscopy. Changes in the mechanical properties of the membrane were investigated using the micropipette aspiration technique. Finally the thermodynamics of the interaction were considered with isothermal titration calorimetry experiments. This allowed evaluation of the protein-lipid interaction in a complete and coherent manner. Experiments were also performed on another elastic protein, α-elastin, for comparison. In addition to its similarities with spectrin (both possess hydrophobic domains and entropy elasticity), elastin is auto-fluorescent which makes it an attractive model protein. Elastin was also used as a sample model to implement new techniques using nonlinear optics microscopy.

List of abbreviations

acq.t - acquisition time
ADE - Area Difference Elasticity
AFM - Atomic Force Microscopy
CARS - Anti-Stokes Raman Scattering
Chol - Cholesterol
CD - Circular Dichroism
DEAE - diethylaminoethyl
CFS - Correlation Fluorescence Spectroscopy
DM - Dichroic Mirror
DOPC - 1,2-dioleoyl-sn-glycero-3-phosphocholine
DOPS - 1,2-dioleoyl-sn-glycero-3-phospho-L-serine (sodium salt)
DPPCd62 - deuterated 1,2-dipalmitoyl-sn-glycero-3-phosphocholine
DS - Delay Stage
EDTA - Ethylenediaminetetraacetic acid
ELISA - enzyme linked immunosorbent
FC - Flow Cytometry
FITC - Fuorescein isothiocyanate
FP - First Peak
FPLC - Fast Protein Liquid Chromatography
FRAP - Fluorescence Recovery After Photobleaching
FRET - Fluorescence Resonance Energy Transfer
FWHL - Full Width Half Maximum
GFP - Green Fluorescent Protein
GPLs - Glycerophospholipids
GUVs - Giant Unilamellar Vesicles
ITC - Isothermal Titration Calorimetry
ITO - Indium tin Oxide
LIA - Lock-In Amplifier
LPC - LisophosphatidylCholine
LUT - Look Up Table
LUVs - Large Unilamellar Vesicles
MLVs - MultiLamellar Vesicles
MPA - MicroPipette Aspiration
MPE - Multi-Photon Excitation
MPM - Multi-Photon Microscopy
NBD - nitrobenzoxadiazole

NLO - Non-Linear Optics
OPO Optical Parametric Oscillator
PBS - Phosphate Buffer Saline
PC - Phosphatidylcholine
PCA - Principal Component Analysis
PE - Phosphatidylethanolamine
PI - Phosphatidylinositol
PMT - PhotoMultiplier Tube
POPC - 1-palmitoyl-2-oleoyl-sn-glycero-3-phosphocholine
POPS - 1-palmitoyl-2-oleoyl-sn-glycero-3-phospho-L-serine
PS - Phosphatidylserine
PSF - Point Spread Function
RBCs - Red Blood Cells
RT - Room Temperature
SDS-PAGE - sodium dedocyl sulfate polyacrylamide gel electrophoris
SEM - Scanning Electron Microscope
SHG - Second Harmonic Generation
SGLs - sphingolipids
SM - sphingomyelin
SNR - Signal to Noise Ratio
SOPC - 1-stearoyl-2-oleoyl-sn-glycero-3-phosphocholine
SOPS - 1-stearoyl-2-oleoyl-sn-glycero-3-phospho-L-serine (sodium salt)
SRG - Stimulated Raman Gain
SRL - Stimulated Raman Loss
SRS - Stimulated Raman Scattering
STED - Stimulated Emission Depletion
SUVs - Small Unilamellar Vesicles
THG - Third Harmonic Generation
TPF - Two-Photon Fluorescence
Ves - Vesicle
WB - Western Blot

Contents

List of Figures

Introduction

Cells are the basic blocks of life and all living organisms are made of cells. There exists a wide range of different cells in the human body whose exact size, composition and structure varies greatly depending on the cell function. Figure 1 represents a schematic of a typical eucaryote cell. As one can see, cells are delimited from the outer medium by a biological membrane. Nowadays the preferred model for cell membrane is the **fluid mosaic model** [1] which states that the membrane is a liquid-like membrane in which proteins and condensed lipid domains float and evolve, every element (lipids, proteins, ions) being in constant motion.

The biological membrane plays an important role in the cell life: not only does it protect the cell from the potentially hostile environment outside, it also maintains the cell internal content (say, ion concentrations) thanks to its semi-permeability. The cell membrane is also involved in many **cell signaling processes** which allow communication between cells via chemical or electrical signals. As one can see from figure 1 cell composition differs with respect to the cell family; nonetheless they are all composed of **lipids**, **sugars** and **proteins**. A more extended description of cell membrane structure and chemical, physical and mechanical properties will be given in Chapter 1.

Most cells contain a nucleus and organelles with ions in different concentrations. Embedded within the membrane, membrane proteins regulate ion transfer between both media for signaling processes and many other functions (which is allowed thanks to ion channels). Within a cell there are a wide range of different lipids and proteins with a variety of functions. The cell membrane is modified by the **glycocalyx** layer which is external to the cell membrane, on the one hand, and by the **cytoskeleton** which is internal to the cell, on the other hand. Those two networks, composed of proteins, protect the cell and give it an optimal shape and elasticity during its lifetime. As we will see these properties are of crucial importance to its biological functions, and many diseases have been related to the lipid membrane. Figure 1 represents a schematic diagram of a cell membrane.

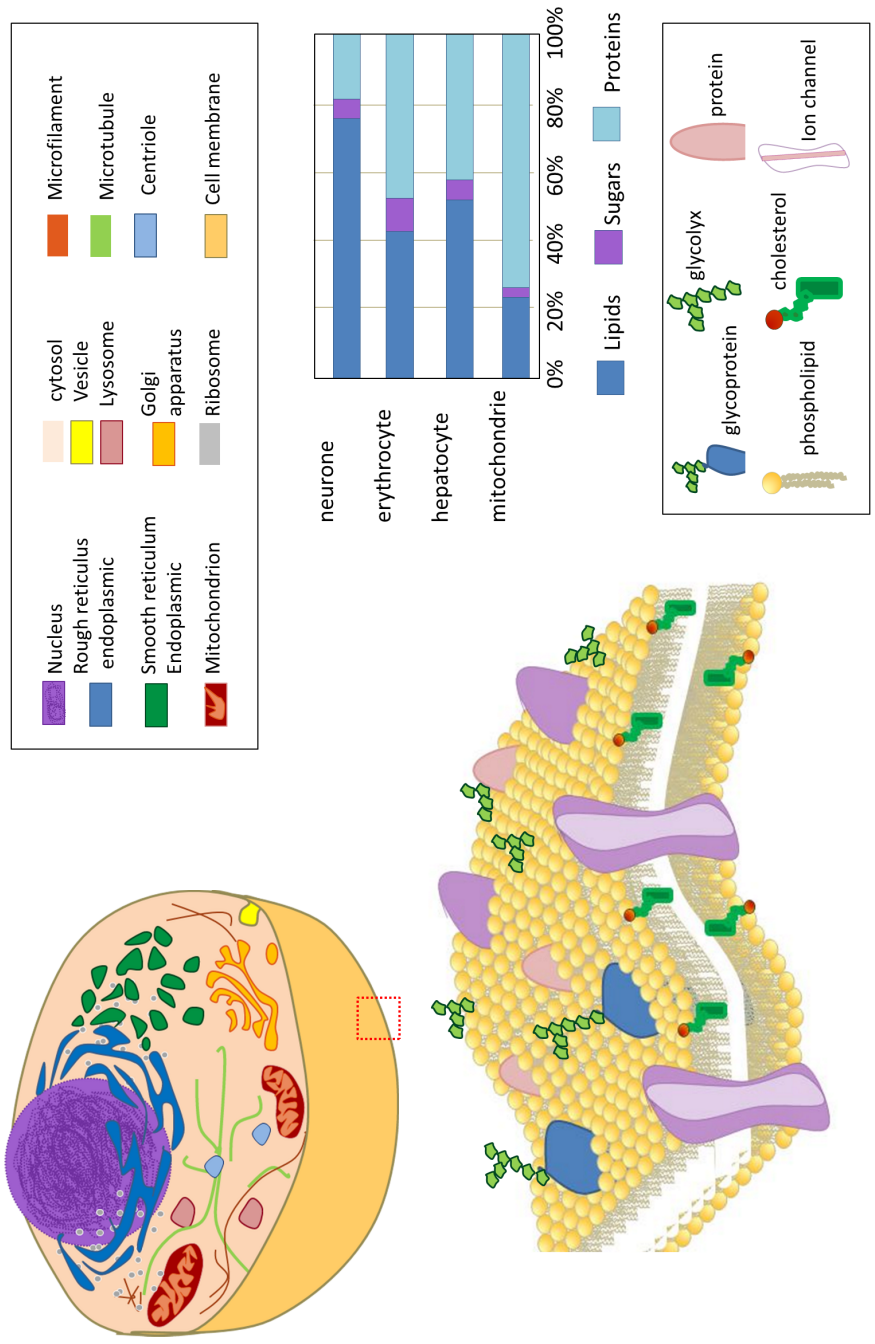

Figure 1: Schematic diagram of a eucaryote cell. The suborganisms present within a typical eucaryote cell are given on the side. The table provides the composition (in terms of lipids sugars and proteins) of different cells. The cells membrane structure is also depicted: it consists of a phospholipid bilayer which contains transmembrane and associated proteins, every element being in constant motion. Adapted from http://gardeningstudio.com/animal-cells/

The cytoskeleton of a cell is an organized mesh of biological polymers which modifies the mechanical properties of the lipid bilayer. Most of the forces exerted by the cell to move and feed itself are due to the cytoskeleton which can thus be seen as the 'cell muscle'. It is essentially composed of actin filaments (*i.e.* microfilaments), intermediate filaments and microtubules in most cells, but may also be composed of a wide range of other proteins, in different proportions, according to the cell type. The cytoskeleton is also involved in many other important functions, for example the regulation of the cell shape, the maintenance of the internal structure, the transport of proteins or mRNA to a specific place of the membrane surface as well as to help intracellular transport, to help chromosomes separate during mitosis or to participate in contraction in muscular cells. The mechanical properties of a given cell are important for the cell to play its specific role. Since different types of cells play different roles, mechanical properties of the cytoskeleton can be very different from one cell to another. Nevertheless all cells have to handle the mechanical stress they are subject to.

This thesis focuses on studying the interaction of a protein called spectrin which is the main component of the cytoskeleton of red blood cells (RBCs), and the lipid membrane, to determinate its effects on the mechanical properties of the cell membrane. This is of importance as many diseases, for example anemia, are related to the abnormal shape (textiti.e. non-donut shape) of the RBCs and the RBCs shape relies on the spectrin and its capability to maintain it through its network.

Chapter 1 and 2 are theoretical chapters giving the biological and physical background necessary to understand the work undertaken. Chapter one focuses on the physics of lipids. Particular attention is given to the mechanical properties of the lipid bilayers and techniques to study mechanical properties of cells are described.

Chapter 2 focuses on the imaging part of the work. The imaging techniques are briefly described and some elements of the theory of Non-Linear Optics (NLO) are given. Label-free techniques processes based on Raman spectroscopy are explained.

Chapter 3 is dedicated to spectrin. Full description of the dimer and tetramer form of the protein is given as well as an up-to-date knowledge about its interactions with the lipid membrane. Then full characterization of the protein is provided. Results about fluorescence experiments involving FITC-tagged spectrin with both externalized-PS red blood cells and giant unilamellar vesicles (GUVs) are presented.

In Chapter 4 the effects of elastic proteins (spectrin and elastin) on the lipid bilayer (GUVs) are investigated using the micropipette aspiration technique. α-elastin is used as a positive control.

Chapter 5 and 6 describe imaging results using NLO. Coherent-Anti Stokes Raman Scattering (CARS) and Stimulated Raman Scattering (SRS) are used and compared to label-free image the lipid bilayer whereas two-photon fluorescence (TPF) is used to image auto-fluorescent proteins. Domain separated vesicles are investigated thanks to lipid deuteration and α- elastin-lipid interactions are studied.

Chapter 6 presents a new technique combining micropipette aspiration and NLO. Hyperspectral images of vesicles are performed at the same time as micropipette aspiration using SRS, on both GUVs and fibroblast cells.

Chapter 7 focuses on the thermodynamics of the protein-lipid interactions. Isothermal Titration Calorimetry (ITC) is used to try and quantify the binding characterics of the interaction of both elastin and spectrin with the lipid bilayer. In this chapter, it is demonstrated that the purity of the spectrin preparation is of high importance.

Chapter 1

Biophysics of lipid membrane systems

In this chapter some element of the structure and nomenclature of phospholipids will be given. Model membrane systems will be described and attention will be given to the mechanical deformation they can handle. The micropipette aspiration technique will be presented as one of the main techniques used in this work. In the last part, domain formation in multi-component vesicles will be explained and the spectrin network detailed.

1.1 Biological lipids

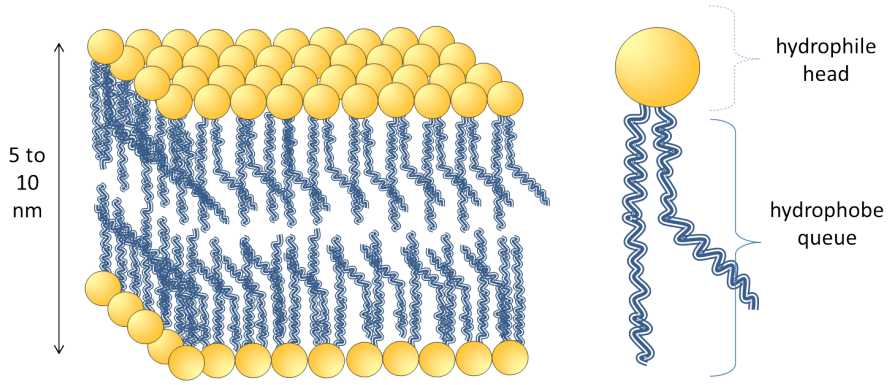

Figure 1.1: Structure of the lipid bilayer: to minimize the energy of the system, lipids in solvant adopt a bilayer structure, which protects the hydrophobic part of lipid molecules to be in contact with the solvent. Adapted from [2].

Biological membrane are mainly composed of lipids and proteins. The term lipid derives from the greek *Lipos* (fat) and designates all organic structures of small molecular

weight (typically < 5000 Da) mainly composed of hydrocarbon chains. Lipids are amphipathic molecules; they are composed of an hydrophilic head and an hydrophobic tail. This is of importance as it means that lipids in water (or other aqueous environments) can self-assemble into structures such as vesicles that will minimize the interaction of the hydrophobe part with water. Usually they assemble to form a bilayer as shown in figure 1.1; this bilayer is 5 to 9 nm thick and impermeable to water and solutes which makes it a really efficient barrier allowing the inside of the cell to be protected from the outside media (in the case of cells). To give an order of magnitude; there is around 5 million lipid molecules per micron square in the lipid membrane [2].

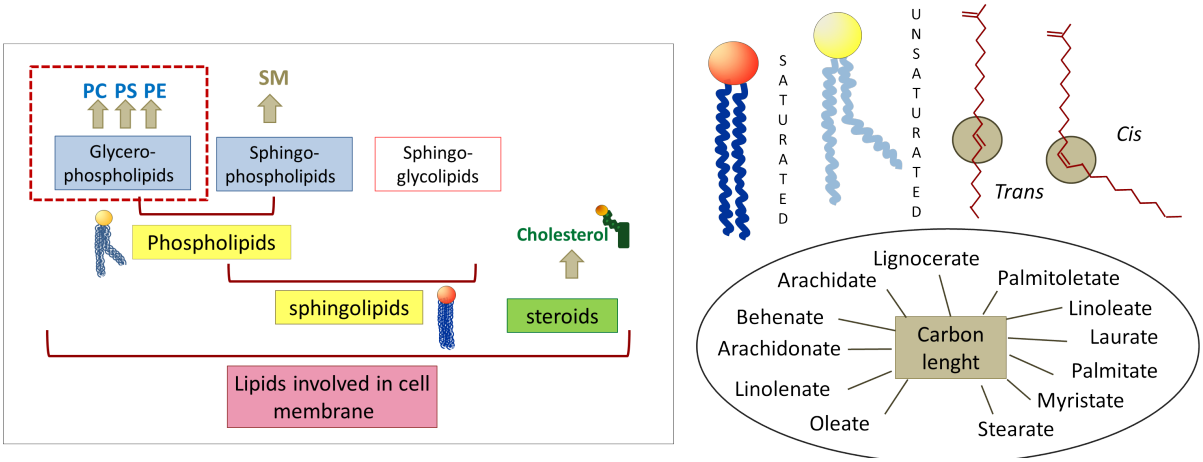

Figure 1.2: Classification of the lipids involved in the cell membrane. The sphingolipid class regroups the sphingoglycolipids and the phospholipids. Phospholipids themselves regroups the shingophospholipids (among which SM) and the glycerol phospholipids. The cholesterol on the other hand belongs to the steroids. Lipids carbon chain length can vary from 12 to 24 carbon atoms. Each lipid length has been assignated a name summarized in the insert. Lipids can be saturated or unsaturated (which involves the presence of a double bond). When unsaturated, the lipid can adopt either a *Trans* or a *Cis* configuration. This leads to a total of over 900 different lipids species.

The lipid tail is composed of one or two fatty acid chains which are referred to as the functional components of lipids. The carbon chain can be composed of twelve to twenty four carbon atoms (see Fig 1.2 which gives the names of some lipids with respect to the carbon chain length). The most common phospholipids for mammalian cells have sixteen (C16) or eighteen (C18) carbon atoms when saturated -they are respectively called **palmitic** and **oleic acids**- and eighteen (C18:1 , C18:2) or twenty (C20:4) when unsaturated [3]. For this reason these chain lengths (C16 and C18) are used preferentially in artificial membrane systems. The carbon chain can be either saturated or unsaturated (with up to 6 double bonds with either a *trans* or *cis* configuration as shown in figure 1.2 b). This produces a range of over 900 fatty acid species.

Lipids are usually classified into 7 families: **fatty acids, triglycerides, glycerophospholipids, sphingolipids, cerids, terpens** and **steroids**. Figure 1.2 summarizes the hierarchy of some lipid classes involved in the cell membrane. Triglycerides are stock lipids and are the main component of vegetable oil and human skin oil and of some animal fats whereas sphingolipids and phospholipids are involved in the cell membrane. Even though each type of cell has its own lipid composition [4], the main class of lipids found in human cells is by far the **glycerophospholipids**, (see table in figure 1.4). These are therefore the lipids we are interested in and more details about this class will be given in the following section. Another important component of the cell membrane is the cholesterol which belongs to the sterol class (a subclass of the steroids) and further description of this compound will be given later in this chapter.

1.1.1 Lipids and phospholipids

Glycerophospholipid structure

Glycerophospholipids (GPLs) are one of the main phospholipids classes as shown in Fig 1.2 a. They all have the same structure and bear the name of their **head-group**. There are 5 possible head-groups whose chemical formulae are given in figure 1.3 b : ethanolamine, choline, serine, glycerol, and inositol. Glycerophospholipid backbone is a glycerol molecule to which the head group is attached via a phosphate. Two fatty acid chains -not necessarily identical - are attached to the other side of the glycerol backbone as shown in fig 1.3-a and c . The structure of the sphingomyelin (SM), used in some vesicle mixtures for fluorescence experiments in Chapter 3, is also given (see Fig 1.3 d). The main difference between glycerophospholipids and spingolipids lies in the different backbone and the difference in chain lengths.

The table in fig 1.4-a gives the cell membrane composition for different types of cells. As one can see, the glycerophospholipid class is the most important one representing more than half of the total cell membrane mass [5]. Within this class, the most common GLP is the **phosphatidylcholine** (PC). It represents 23 %[1] of the red blood cell membrane and up to 48 % of mitochondrion. The second best represented GLP is phosphadylethanolamine (PE) which is equally involved in all the cells (around 20 %). Other negatively charged GLPs, phosphatidylserine (PS), phosphatidylglycerol (PG) and phosphatidylinositol (PI), are present to a much smaller extent, the PS representing barely 10 % of the red blood cell membrane.

[1] Proportions of lipids are given in percentage of the total mass of the cell membrane.

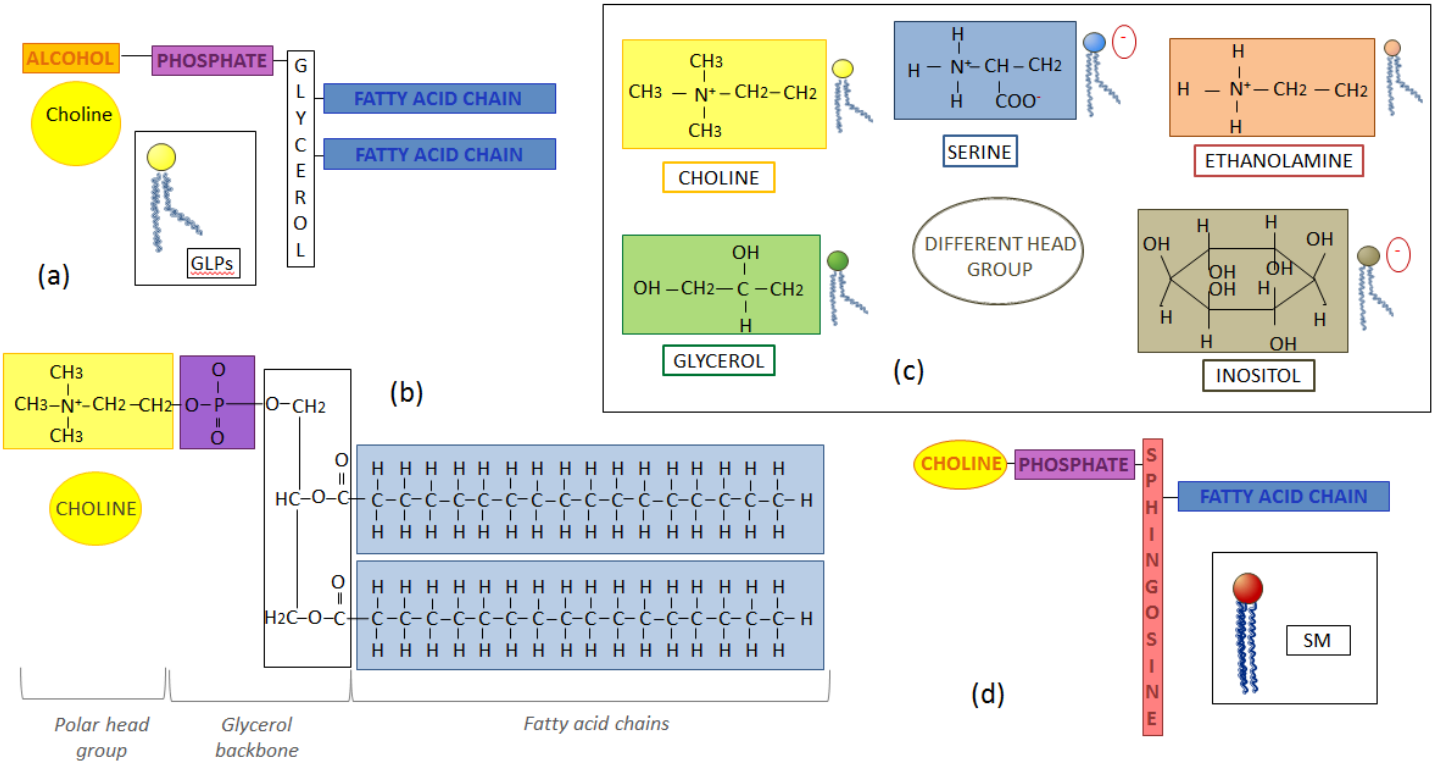

Figure 1.3: Glycerophospholipids (GPLs) structure and nomenclature: (a) gives the structure of a typical GPL. GPLs are composed of a head group attached to a glycerol backbone via a phosphate. Fatty acid chains are also linked to the backbone. (b) Gives the chemical formulae of a typical GPL. (c) summarises the different head-group (choline (yellow), serine (blue), ethanoline (pink), glycerol (green) and inositol (grey) provides their chemical formulae. (d) gives the structure of SM (to be compared with (a)).

Other lipid families important in the membrane composition are the sphingolipids and the sterols. Both form significant fractions of the red blood cell and myelin membranes whereas they are quasi-absent of both mitochondrion and microsome cell membranes. The sphingolipid family is 90 % composed of sphingomyelin (SM) and plays an important part in neuronal activity and cell transduction, it is thus present in the brain, nervous tissues and the cornea. On the other hand the sterol family mainly consists of cholesterol which plays an important role in maintaining the fluidity within the cell membrane (this element will be fully described in section 4.3 of this chapter).

Cell asymmetry

An important point that remains to be mentioned about cell membrane composition is its **asymmetry**. As illustrated in figure 1.4-b and c, PC and SM are preferentially distributed within the outer leaflet, in contrast to PE and PS, the latter one being present mainly in the inner leaflet. Glycolipids are also distributed in the outer leaflet whereas cholesterol is present in quite large proportions in both leaflets.

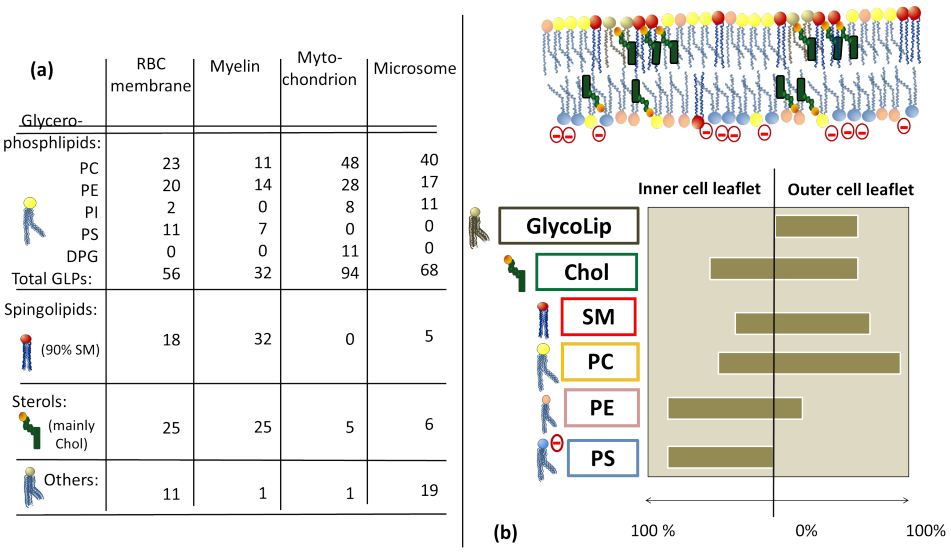

Figure 1.4: Cell membrane composition and asymmetry: (a) The table provides the distribution of lipids for different types of cells, (b) Schematic diagram illustrating the assymetric distribution of lipids within cell membrane. Adapted from [2].

This asymmetry is of importance in terms of spectrin-lipid interactions. Since the spectrin is situated in the cytosol side it can only interact with the lipids present within the inner leaflet. The lipids in model lipid systems must be chosen accordingly to correctly mimic the real biological systems. Table 1 in Appendix A sums up the lipids used in model membrane systems discussed in this thesis. Full characterization of each of them is also given in Appendix A.

1.1.2 Forces involved to maintain the lipid bilayer

The bilayer-like structure lipids adopt when in a aqueous media, results from the sum of all attractive and repulsive forces involved between lipids and with the solvent. Figure 1.5-a illustrates the interactions between two neighbouring phospholipids within the bilayer.

Like most of the components in biology[1], cohesion of lipid systems comes from *weak intermolecular interactions*. The first interaction that needs to be mentioned is the **hydrophobic force** acting on the carbon chains: because of their amphiphilic structure lipids will self-organize to minimize the exposure of the hydrophobic part to the solvent in order to minimize the energy of the system, to the benefit of the hydrophilic parts which will thus have the possibility of forming **hydrogen bonds** with the aqueous media. This way the hydrophilic heads will shield the lipid tails from being in direct

[1]Such as proteins, nucleic acids, polysaccharides

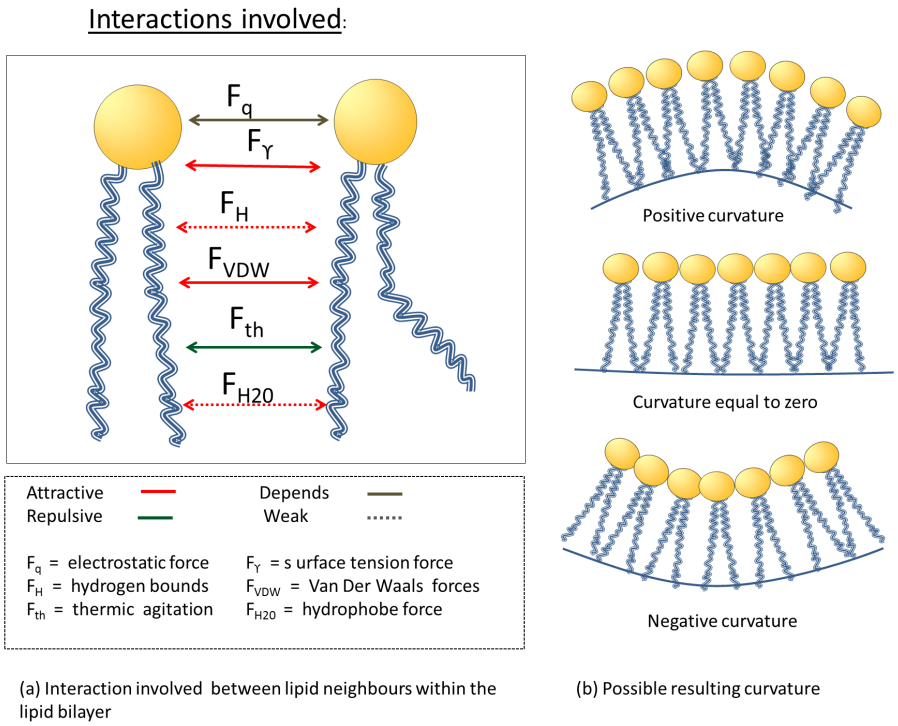

Figure 1.5: (a) Schematic diagram illustrating the intermolecular interaction forces between 2 neighbouring lipids within a lipid bilayer. (b) The resulting force can induce a curvature of the bilayer. Adapted from [6].

contact with the aqueous media. The longer the fatty acid chain the stronger the hydrophobic interactions and the stiffer the membrane.

Other interactions acting on the tails are the **Van der Waals forces**: for the distances involved within the lipid bilayer those are always attractive interactions [6], opposite to the effects resulting from the **thermal motion** which acts to increase the effective volume a hydrocarbon chain occupies. The higher the temperature the greater the thermal energy; therefore chains at higher temperatures will tend to spread from one another and occupy more space. This effect of temperature on lipid will be detailed in section 4.1 of this chapter (melting temperature section).

In addition to the head-solvent interaction (involving the interaction between the dipoles of the water molecules with the charge of the head-group and creation of H-bonds) the interactions between heads are mainly **electrostatic**. These can be either repulsive or attractive depending on the charge of the lipid head groups involved[1].

[1] As we have seen before GPLs heads can whether be neutral (PC, PE) or negatively charged (PS, PG, PI)

Finally, resulting from all the above listed forces, there exists an **interface tension** which tends to minimize the total area of the lipid-water interface.

The minimal energy state of a lipid system is not always a perfectly flat bilayer and quite a few lipid species aim for a non-lamellar structure [7]. If those lipids are present among the bilayer they tend to curve it. The final curvature can be either positive or negative as illustrated in figure 1.5-b and depends on the molecular geometry of a single lipid. This leads to different possible lipid organizations. This effect is called the polymorphism of lipid structure and will be discussed in the next section.

1.1.3 Polymorphism of lipids

The mesoscopic structures lipids can form depend on intrinsic parameters (concentration, chemical nature) and extrinsic parameters such as temperature, ionic environment[1] or pH. It has been proven that lipids can adopt two main types of structures called type I and type II when dispersed in water. Type I- structure is classically called the direct structure and has the lipids with their tails on the inside. This is the structure lipids in oil adopt when oil droplets are added to water. The opposite type II-structure, also referred as the 'inverted structure', is when lipid tails face the outside: this is the structure lipid in oil adopt around water molecules when water droplets are added to an oil solution.

Lipid organization can be explained from a geometric point of view. The shape of a single lipid molecule depends on the respective volumes of its head in comparison to that of its hydrocarbon chains. The different geometries lipids can adopt are illustrated in figure 1.6, each shape leading to a specific morphology referred to as a lipid phase [8]. A 'stack parameter', p, has been introduced [9] and allows prediction of the type of lipid phase a specific lipid will adopt from its molecular geometry. p is given by

$$p = \frac{v}{a_0 l_c} \tag{1.1}$$

where v represents the volume of the hydrophobic part, a_0 is the cross-sectional area of the polar head and l_c the length of the carbon chain.

The molecular volume of the hydrophilic part depends on the head group structure (for example the headgroup of PE is smaller than that of PC) whereas the molecular volume of the hydrophobic part depends principally on the number of unsaturated

[1] For example the presence of divalent cations

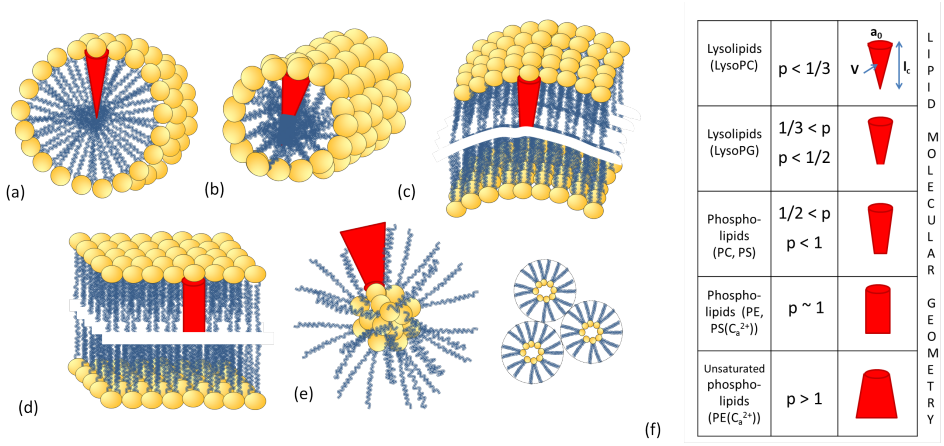

Figure 1.6: Summary of the structures lipids can adopt with respect to their molecular geometry. When the volume the head occupies is larger than the space acyl chain(s) occupy, the lipids can adopt a spheric micellar structure (a) or a cylindric micellar structure (b). When the volume of the head is similar to that of the fatty acid chains the lipids will adopt a bilayer structure (c and d). When the volume of the head is smaller compared to that of the fatty acid chains the lipids adopt an inverted micellar structure (e). (f) provides a summary table linking the stack parameter, p, to the lipid molecular geometry (red shapes). An example of lipid for each case is also provided. Adapted from [9].

cis bonds: the higher the number of unsaturated bonds the bigger the volume of the hydrocarbon chain, and hence the higher p.

Usually, phospholipids have a stack parameter around one; because they are composed of 2 fatty acid chains, single phospholipids have a cylindrical shape. This leads to a bilayer structure allowing liposomes and other bilayers with small curvature (see figure 1.6-c, d). Those are the structures we are interested in this project. Lysolipids [1],which have a single fatty acid chain usually form micellar structures (see figure 1.6-a for LPC). For certain values of p, some lipids can adopt a cylindrical micellar structure (figure 1.6- b). In general, lipids with a conical molecular shape have a positive curvature whereas the ones with a trapezoid form (like PE) have a negative curvature and form an inverted micelle structure (see figure 1.6-e). The table in figure 1.6 gives an example of lipids for each morphology. One should notice that the presence of ions can introduce a change in the lipid structure (see below).

All these mesophases appear to have physiological implications. The membrane of each organelle has an intrinsic curvature (due to its particular lipid composition) and non-lamellar structures are involved in many fundamental biological processes, for example membrane synthesis, cell division, endocytosis, cell signaling to only name a few [5].

[1] Lysosphatidylcholine (LPC) for example.

1.2 Membrane systems

As we have seen in the introduction, the cell is a complex system consisting of a large number of organelles and individual small and large molecules. This poses difficulties for the investigation of particular interactions as it is difficult to attribute the observed behaviour to the protein/ lipid/ ligand of interest.

To overcome this problem, model lipid are often used. These have become very popular over the last two decades due to their efficiency for studying a unique problem (say a cell signaling pathway, a protein-lipid interaction, ligant action), due to their ability to mimic the cell membrane and due to their relatively simple preparation. They have also allowed a better understanding of phospholipids and their physico-chemical properties. The different classes of artificial membrane system are briefly discussed below.

1.2.1 Artificial Membranes Systems and Giant Unillamellar Vesicles

There are different membrane models, referred to as vesicles. One must distinguish between multi-lamellar systems and unilamellar ones. The simplest way of preparing vesicles is to evaporate lipids in a solvent solution (*e.g.* chloroform) and then suspend them into an aqueous solution (*e.g.* glucose solution). Due to their amphiphilic properties the lipids will naturally assemble into multilamellar vesicles (MLVs) which are concentric bilayers of heterogeneous dimensions encapsulated in each other (see figure 1.7-a). The resulting vesicles are inhomogeneous in size, which can vary from 10 nm to 200 nm. This size inhomogeneity is an important drawback since it might compromise the reproducibility of an experiment. Biophysicists thus prefer unilamellar systems consisting of a single lipid bilayer, with dimensions which can be monitored. There are different categories of unilamellar vesicles, classified according to their size (see figure 1.7-b and c for illustrations):

- **Small Unilamellar vesicles (SUVs)** are liposomes consisting of a single bilayer with a diameter between 40 nm and 100 nm. They encapsulate a small volume of the solvent. These vesicles are usually obtained after treatment of MLVs (see the description in Chapter 7).
- **Large Unilamellar vesicles (LUVs)**. When the vesicle diameter is between 100 nm and 1 μm, one speak of LUVs. These can be prepared either by extrusion or by fusion of SUVs (see preparation in Material and Methods in Chapter 7).

- **Giant Unilamellar vesicles (GUVs)** are a widely used membrane system and they are the ones mostly used in our experiments. Their diameter is larger than 1 μm and can reach 100 μm. They can either be prepared by the swelling method or by electroformation [10]. The experimental protocol for both of these methods will be given in Chapter 3 section 2.2)[1]..

Different vesicle systems are useful as membrane models in different respects. The curvature in SUVs is much higher than in LUVs (and is negligible in GUVs [2]). SUVs are thus a good choice for optical spectroscopy experiments (in order to study biochemical activities for example) as they diffract the light greatly due to their size. On the other hand, SUVs and GUVs are good choices for studying protein-lipid interactions, especially trans-membrane proteins. In our study we used SUVs for the isothermal titration experiments (see Chapter 7) and mostly GUVs for all the other experiments (Chapters 3-6). GUVs appear to be the golden choice for studying membrane mechanical properties as they can be observed using optical microscopy, they can be fluorescently labelled (see section below) and exhibit large thermal fluctuations. Moreover they have dimensions comparable to cells making them more realistic - which is a requirement for a good membrane model. People thus also use them to decrypt mechanisms at the cell scale such as protein diffusion, lipid rafts etc. They are especially useful as model membranes used during this PhD for micropipette aspiration experiments to characterize the effect of (elastic) proteins on membrane mechanical properties (see Chapter 4).

It is also possible to form laterally mobile monolayer/bilayers and supported bilayers[3] (see fig 1.7-c). They are often used to study incorporation of membrane proteins, the usual imaging methods being SEM and AFM. Monolayers can also be used to study indirectly protein-lipid interactions (see literature review in Chapter 3). No further information will be given about these particular systems since they are not used in this work.

1.2.2 Morphology of giant vesicles

It has been experimentally observed that vesicles can adopt various shapes. Figure 1.8 gives an example of some non-spherical vesicles. One can see complex starfish shapes (fig 1.8-a) and some 'eight' shapes (fig 1.8-c), and some internal/external budding (1.8-g and h). Finally fig 1.8-c illustrates the shape of phase separated vesicles in mix lipid

[1] They are usually between 10-50 μm when made by electroformation/electroswelling
[2] *i.e.* at the scale of the molecule, the bilayer appears flat
[3] Those are usually made by fusion/explosion of SUVs or LUVs on a solid support

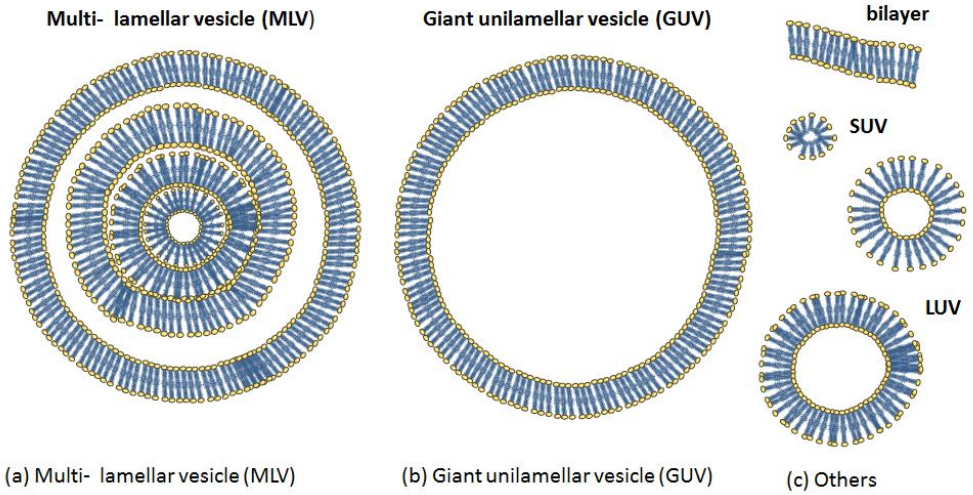

Figure 1.7: Schematic diagram illustrating different model membrane systems: (a) Giant multilamellar vesicles, (b) Giant unilamellar vesicles, (c) bilayer, large and small unilamellar vesicles. The vesicle size and membrane thickness compared to the vesicle diameter are not to scale (artist view).

vesicles which we will come back to in section 4.

There are different ways to induce shape transitions of vesicles. For example, one can change the **temperature**: a rise in temperature will induce prolate vesicles to create exterior budding [11][1]. Another way to affect the vesicle shape is to modify the solution the vesicles are grown in: changes to the osmotic concentration, pH, addition of ions, or application of an asymmetry in solutes will all cause shape changes.

Changes in **osmotic conditions** will induce changes in the volume-to-area ratio: vesicles will be deflated when the solute concentration outside the vesicle is higher than inside [12][2]. Solutes of different molecular sizes, at the same osmotic concentration, inside and outside of vesicles (for example raffinose and a glucose/raffinose mixture) will change the spontaneous curvature and cause shape change [13]. Finally, gravity might also produce a small deformation: to obtain a better contrast, in phase contrast, vesicles can be grown in a sucrose solution and diluted with a glucose solution (see chapter 4) causing the vesicles to sink to the bottom of the experiment chamber.

As said before, **multivalent ions** can induce molecular geometry of some phospholipids to change (*e.g.* calcium ions affect PS and PE head group area), due to interactions with the polar heads [14]. Ions can sometimes provoke adhesion of vesicles

[1] The effect of the temperature will be further explained in the section 4.1 of this chapter.
[2] This also allows permeation to be studied.

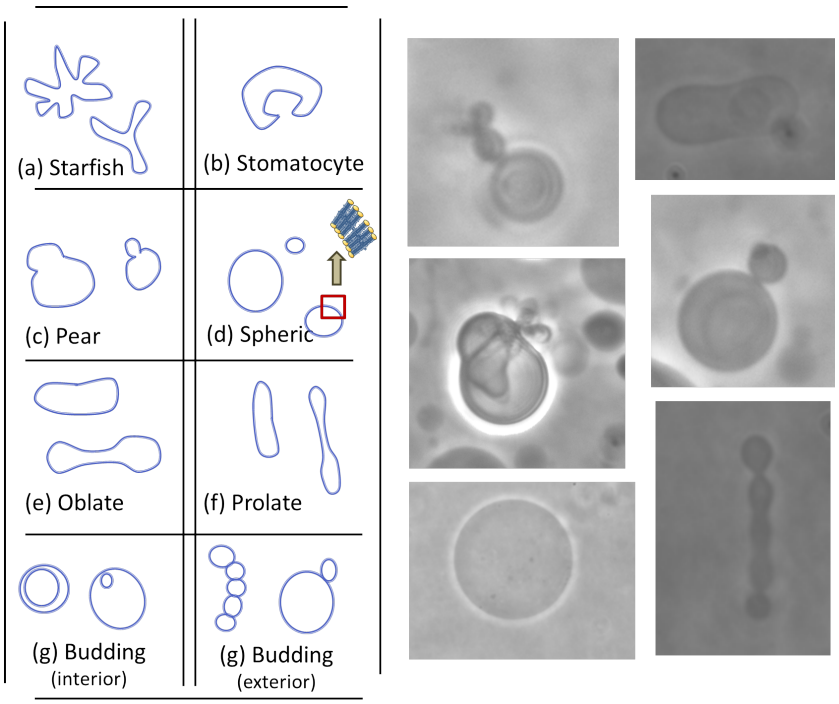

Figure 1.8: The table summarises and gives the names of the various shapes unilamellar vesicles can adopt. The montage of images illustrates some of the structures (phase contrast microscopy). The shape a GUV will adopt can be predicted using the ADE model (see Appendix A). External stimulii can also influence GUVs shapes (see text).

together [11]. In the same way, since some polar heads are charged, the **pH** can affect lipid conformations[1].

In experiments, it is important to control the osmolarity, ion concentration and temperature to ensure the stability of both the vesicles and the proteins added to the vesicle suspension.

It is worth discussing how the shape of a vesicle can be predicted from its area, reduced volume and spontaneous curvature. The general idea is to take into account the elastic contributions of both leaflets of the bilayer and their effect on the overall curvature - this is especially important if there is a significant difference between the number of lipid molecules in each leaflet (see below).

1.2.3 Microscopic versus Macroscopic scales

Depending on the length scale, the cell can be considered from a **microscopic** or a **macroscopic** point of view.

[1] As an example when the pH rises, the conformation of PC polar head with be change and 'vesiculation' will occur.

Microscopic point of view

On a microscopic scale, the membrane is seen as an assembly of individual lipids which are interacting with their neighbours. When the lipid molecules are laterally mobile, the membrane can be described as liquid (*i.e.* with zero shear elastic modulus). This is at the base of the 'mosaïc fluid model' [1] briefly described in the introduction. As one can see in figure 1.9 (A), there are three kinds of movement, lipids undergo within the bilayer: **rotational diffusion, lateral diffusion** and **transversal diffusion**.

The most important ones are the lateral diffusion (due to Brownian motion) and the rotational diffusion. These two happen at the same time but at different time scales: rotational and local motion are really quick (10^{11} movements per second) and include free rotation of lipids around their axis and/or carbon chain 'wobble' as shown on fig 1.9 (A) a. Lateral diffusion on the other hand represents the motion within the membrane plain. It is usual to quantify the distance lipids can cover by calculating the diffusion coefficient, D. Experiments performed on both cells and membrane systems using FRAP (Fluorescence recovery after photobleaching) measured this coefficient to be of the order of $10^{-12}\,\mathrm{m}^2/\mathrm{s}$ which represents a 'sweep' of $4\,\mu\mathrm{m}^2$ within 1 second for a single lipid. The diffusion coefficient differs slightly between lipid species and drastically diminishes when the membrane is in the gel state (We will see in section 4 that at lower temperature the membrane can reach a gel state) , D becoming around $10^{-15}\,\mathrm{m}^2/\mathrm{s}$ [15].

The last allowed movement is the diffusion in a direction normal to the membrane plane, also referred as *'flip-flop'* . It consists of a lipid molecule flipping from one leaflet of the membrane to the other which happens to a much smaller extent (except for cholesterol), due to the energetic barrier of moving the polar head-group through the hydrophobic region of the bilayer. For one to get some order of magnitude, it takes hours for this process to take place (D is only $\sim 10^{-8}\,\mathrm{s}^{-1}$). This process happens at a much quicker rate within cell membranes (a timescale of minutes) since it is facilitated by enzymes known as translocases and scramblases.

This fluidity is of great importance for biological processes as it ensures the lateral mobility of membrane constituents such as proteins. Proteins can be seen as 'floating in a 'lipid sea'. Nonetheless the lateral diffusion of proteins is usually greatly decreased, they are around 1000 'slower' than lipids (the larger the protein the more difficult it is for it to move around and thus big protein complexes appear to be quasi-static). The

specific membrane composition of each cell type leads to slightly different membrane fluidity.

Macroscopic point of view

On a macroscopic scale, the dimensions of the system (for example GUVs or supported bilayers) are much larger compared to the size of the lipid molecule and so one can consider the membrane as a continuous medium (see fig 1.9 B). Since the thickness is much smaller than the lateral size of the membrane one can model the membrane as a two-dimensional fluid. On this basis, the membrane mechanical properties can be described using continuous models.

1.3 Mechanical properties of membranes

In this section we will consider a membrane in a liquid state as this is the case for most lipids in the cell membrane.

Elastic properties of lipid membranes were described independently in the 1970s by Canham and Helfrich [17], [18]. Their approach is based on an analysis of the membrane elastic energy with respect to different deformation modes. This requires the membrane to be considered at a macroscopic scale (as a continuous medium) so that the continuous mechanics can be applied to the studied system. The general idea is that the membrane can be understood as a 2D fluid which can undergo 3 main types of deformation (as shown in figure 1.9 B): **area change, shear and bending**. These are described below.

1.3.1 Different modes of deformation

Area extension and compression

When the area of the membrane surface, A, is subjected to a change, ΔA, due to some stress, one speaks of extension and compression stress. Equation 1.2 gives the elastic energy density per surface area H_{ext} due to this deformation:

$$H_{\text{ext}} = \frac{1}{2} K_A \left(\frac{\Delta A}{A} \right)^2 \tag{1.2}$$

where K_A is the area expansion modulus. As one can see, it depends quadratically on the relative surface area change $\left(\frac{\Delta A}{A}\right)$. K_A is usually around 0.2 N/m for lipid

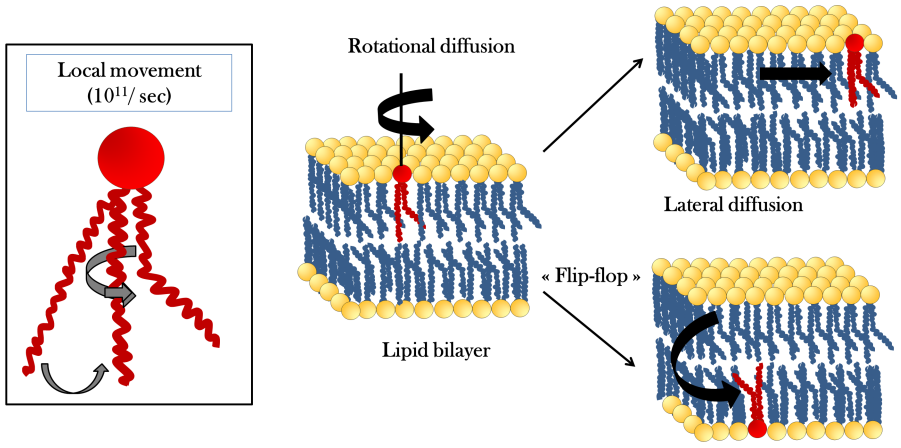

(a) Local movement of a lipid (b) Allowed movements in the lipid bilayer

(A) Microscopic scale

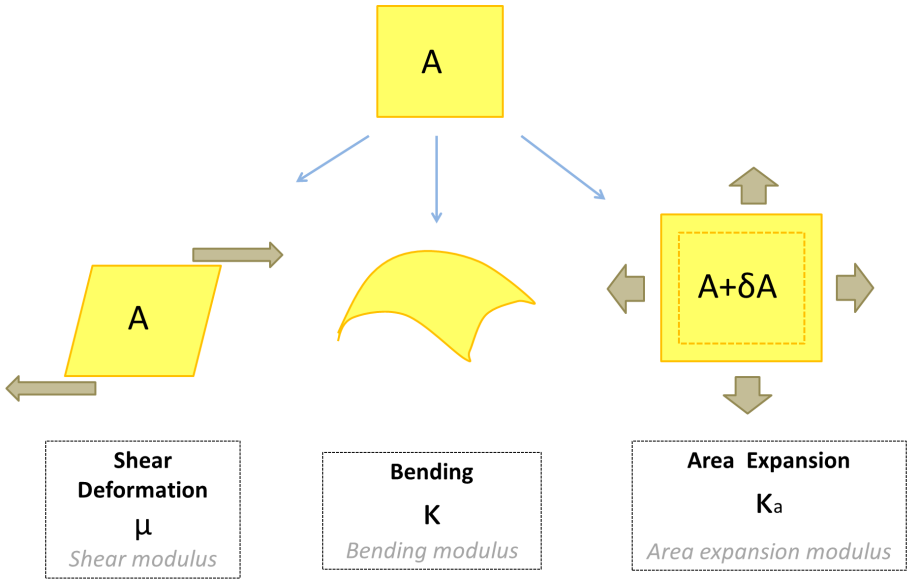

(B) Macroscopic scale

Figure 1.9: The membrane bilayer can be considered either at the microscopic scale (A) or at the macroscopic scale (B). (A) At the microscopic scale, individual lipid molecules are considered and laterally mobile within the bilayer. (a) illustrates the local movements a molecule on the spot (the lipid can rotate along its axes and tilt). (b) illustrates the movements a lipid molecule can perform within the bilayer: it can either travel with the bilayer plan (lateral diffusion) or flip from one leaflet to the other (flip-flop). Adapted from [16]. (B) At the macroscopic scale, the membrane is considered as a whole and is seen as a 2D fluid which can undergo deformations: Shear deformation (a), bending (b) and Compression/extension (area expansion) (c). Adapted from [17] and [18].

membranes [19]. Table 1.10 shows a collection of values of K_A for a few different materials.

For giant unilamellar vesicles, the maximum allowed variation in the area is quite small: only about a few percents before the membrane breaking stress is reached and the vesicle bursts. The maximum tension a vesicle can handle before bursting is called the lysis tension τ_{lysis}.

Shear

Shear is the deformation depicted in figure 1.9 B a. The membrane is deformed in two parallel but opposite directions, the surface area remaining constant. The energy density for this deformation is given by Hooke's law [20]:

$$H_{\text{shear}} = \frac{1}{2}\mu(\lambda^2 + \lambda^{-2} - 2) \tag{1.3}$$

where $\lambda = \frac{L_0+\Delta L}{L_0}$ is the lateral expansion modulus and μ is the shear elastic modulus. In the case of vesicles, the shear modulus is equal to zero as the membrane is a 2D fluid: there is a friction (hence shear **viscosity**), but no restoring force (*i.e.* $\mu = 0$). For a membrane in a gel state, the shear modulus has a non-zero value. In the case of cells, μ is not equal to zero due to the cytoskeleton (for example the actin network) and this shear deformation does need to be taken into account. For example, Sackmann demonstrated that the spectrin network (the cytoskeleton of RBCs), induces a shear elastic modulus of $\sim 10^{-6}\,\text{J/m}^2$ in red blood cells [20] (see table 1.10 for other values).

Finally, it has to be mentioned that another energy term, due to molecule *tilt* within the bilayer, H_{tilt} , does sometimes need to be taken into account [18] for lipids in gel state, however it can be neglected for liquid membranes.

Bending

Bending includes out of plane deformations and the energy associated to this deformation is given by:

$$H_{bend} = \frac{1}{2}\kappa(C_1 + C_2 - C_0)^2 + \kappa_G C_1 C_2 \tag{1.4}$$

where C_1 and C_2 are the principal curvatures of the 2D surface, C_1C_2 is the Gaussian curvature, C_0 is the spontaneous curvature of the membrane, κ is the bending modulus and κ_G the Gaussian curvature modulus (κ and κ_G both have units of energy).

Material	Shear elastic modulus μ_{cis} (J/m²)	Area expansion modulus K_A (J/m²)	Bending modulus K (J)
brass	110	100	10^{-15}
polyethylen	5	5	$5x10^{-17}$
rubber	0.05	0.06	$5x10^{-20}$
RBC	$6x\ 10^{-6}$	NA	$7x10^{-20}$
DMPC vesicle	0	0.145	$1.2x10^{-19}$

Figure 1.10: Area expansion modulus, shear elastic modulus and bending modulus for different materials [20].

The bending modulus , κ, quantifies the energy required to curve a membrane. In the case of a lipid bilayer, κ is of the order of $10k_BT$ (*i.e.* $\sim 10^{-19}$ J). This value implies that the lipid bilayer is subject to thermal fluctuations, which we will discuss in the next section. Intrinsic and extrinsic parameters (molecular geometry, ions, temperature, pH) can also influence the bending modulus.

The spontaneous curvature , C_0, has been described qualitatively previously (in section 2.2). As its name indicates, it is the curvature the lipid membrane will spontaneously adopt at equilibrium in its related state [21], [22].

The Gaussian curvature modulus term, $\kappa_G C_1 C_2$, can, in our case, be neglected as well. This comes from the *Gauss-Bonnet theorem* which states that the Gaussian curvature integrated over a closed surface (for example a topological sphere) is a *topological invariant* of space, which means that provided there is no opening (*e.g.* a hole in a vesicle membrane) the total Gaussian curvature remains unchanged whatever the deformation.

Canham-Helfrich Hamiltonian

If one integrates equation 1.4 over the surface of the membrane one finds:

$$H = \int\int_A \frac{1}{2}\left[\kappa(C_1 + C_2 - C_0)^2 + \kappa_G C_1 C_2\right] dA \tag{1.5}$$

referred to as the *Canham-Helfrich Hamiltonian*. As the energy due to the curvature is the dominant component in the case of a fluid membrane all other contributions (shear stress, tilt) can be neglected. Indeed provided you also take into account the energety

term coming from the tension σ

$$H_{\text{tens}} = \sigma \frac{\Delta A_p}{A} \tag{1.6}$$

fully described in the next section, then equation 1.5 can be rewritten as:

$$H = \int\int_A \frac{1}{2}\left[\kappa(C_1 + C_2 - C_0)^2 + \sigma\frac{\Delta A_p}{A}\right] dA \tag{1.7}$$

and gives the energy of the vesicle. A_p is the apparent area which much be distinguished from A.

One can thus pre-determine the shape of a membrane (and thus of a vesicle) by using this energetic description and the Canham-Helfrich Hamiltonian. At first approximation this is a good model; further studies [22] demonstrated later on that for a better theoretical model, one needs to also take into account the effect of both leaflets of the bilayer (especially their friction together), the inner being compressed while the outer is stretched out. This more advanced model is called the *area Difference Elasticity* (ADE) model which is a combination between the Canham-Helfrich model and the bilayer couple model. The ADE model describes both the shapes and the shape transitions the best [23]. (One can find the vesicle shape phase diagram predicted by the ADE model in Appendix A).

1.3.2 Fluctuating membrane: the effect of the tension

Enthalpic versus entropic regimes

As already mentioned, the bending modulus of lipid membrane is close in magnitude to the thermal energy ($\sim 10 k_B T$), thus the membrane will exhibit Brownian motion. Collisions with the surrounding solvent will cause thermal fluctuations of the membrane around its equilibrium position. Experimentally these fluctuations can be observed and measured. The combined effect of all collisions will induce (small) membrane deformations at different scales as shown in figure 1.11-b. The higher the temperature the bigger the thermal energy and thus the bigger the fluctuations amplitudes.

These thermal fluctuations are affected by the membrane of tension σ [24]. The tension links the free energy, F, of the membrane, with the apparent surface area of the vesicle, A_p, as $\sigma = \frac{\partial F}{\partial A_p}$. In the case of a fluid membrane one must distinguish between two regimes: the **enthalpic regime** where the membrane is really tense and

the entropic one where the membrane is fluctuating, and the tension is the result of the constant area of the membrane.

Enthalpic regime

In the enthalpic regime, the membrane is responding elastically to the applied stress. When a membrane A is stretched due to some constraint, it is said to be under tension and its area changes by ΔA. The variation of the membrane free energy due to this deformation is therefore given by $\Delta F = \sigma \Delta A$ and the surface energy density due to the tension is:

$$H_{\text{tens}} = \sigma \frac{\Delta A}{A} \tag{1.8}$$

Combining it with equation 1.2, one finds:

$$\sigma_H = \frac{\partial(H.A)}{\partial(\Delta A)} = \frac{1}{2} K_A \frac{\Delta A}{A} \tag{1.9}$$

where K_A is the area expansion modulus. As previously mentioned, this description of the tension is only valid when the area change observed is in the real area of the vesicle. Therefore the expression is no longer valid when the membrane is subject to fluctuations: in this case the membrane is said to be in the entropic regime described below.

Entropic regime

When a membrane is fluctuating, the area seen under the microscope is called the apparent area A_p which is different from the real area A_r. A_p indeed represents the projected area - which is the mean position of the membrane - and $A_p < A_r$ as shown in figure 1.11- b. When a stress is applied to the fluctuating membrane, it will first smooth the membrane. One will observe an increase in the surface area which was in fact hidden in the fluctuations, so that $\frac{A_r - A_p}{A_r} = \frac{\Delta A}{A}$. Consequently in this regime no compression/extension is involved as the stress will just reveal the membrane area stored into the fluctuations, the microscopic area remaining unchanged.

This surface 'surplus' can be calculated using the Canham-Helfrich Hamiltonian. Integrating over the whole surface gives access to the relative area expansion $\frac{\Delta A}{A}$:

$$\frac{\Delta A}{A} = \frac{k_B T}{8\pi\kappa} \ln\left(\frac{\frac{\kappa\pi}{l^2}}{\sigma}\right) \tag{1.10}$$

In this equation l is introduced as a microscopic 'cut-off'(Peliti and Leibler, 1985). Then if one defines a 'resting tension' $\sigma_0 = \frac{\kappa\pi}{l^2}$, the tension can be expressed as:

$$\sigma = \sigma_0 \exp\left(-\frac{8\pi\kappa}{k_B T}.\frac{\Delta A}{A}\right) \tag{1.11}$$

As one can see from equation 1.11, the tension depends on both the area expansion and the bending modulus κ. Experimentally, both of these regimes need to be taken into account.

When studying vesicles, the area observed under an optical microscope is A_p, and this will appear to vary as the tension on the vesicle is changed. In the entropic regime, the real area, A_r can be regarded as almost constant, and is defined by the number of molecules in the membrane [25], . This way of thinking is at the base of the micropipette aspiration experiments which will be described in the following section.

1.3.3 The micropipette aspiration technique

Micropipette aspiration is currently one of the primary methods for studying membrane mechanical properties. It was first introduced by Evans in the 70s[1] [26]. The general principle consists of applying a constraint - negative pressure - using a micropipette, to a system (GUVs or cell) and recording how it responds, *i.e.* how its surface deforms/stretches to the applied stress. These measurements give access to both the bending modulus κ and the area expansion modulus K_A (and in case of a solid membrane, *e.g.* RBC, to its shear modulus).

Figure 1.11 shows the principle of the micropipette aspiration technique and in b, the general method of a micropipette aspiration experiment. The first step consists of bringing a micropipette (typically 8-10 μm diameter) near a vesicle (typically 15-50 μm diameter) until touching it. Then a slight negative pressure is applied and a seal is formed between the pipette and the vesicle. From there, increasing the negative pressure will result in smoothing out the fluctuations (entropic regime) and then stretching the membrane elastically (enthalpic regime). A *'tongue'* whose length L can be measured (see fig. 1.11-c) will form and elongate inside the pipette until the vesicle reaches its breaking stress [28].

The applied pressure is the monitored parameter. The pressure system consists of a column of water reservoir whose height h can be adjusted (see Material and methods

[1] firstly on RBCs, then later on, on GUVs

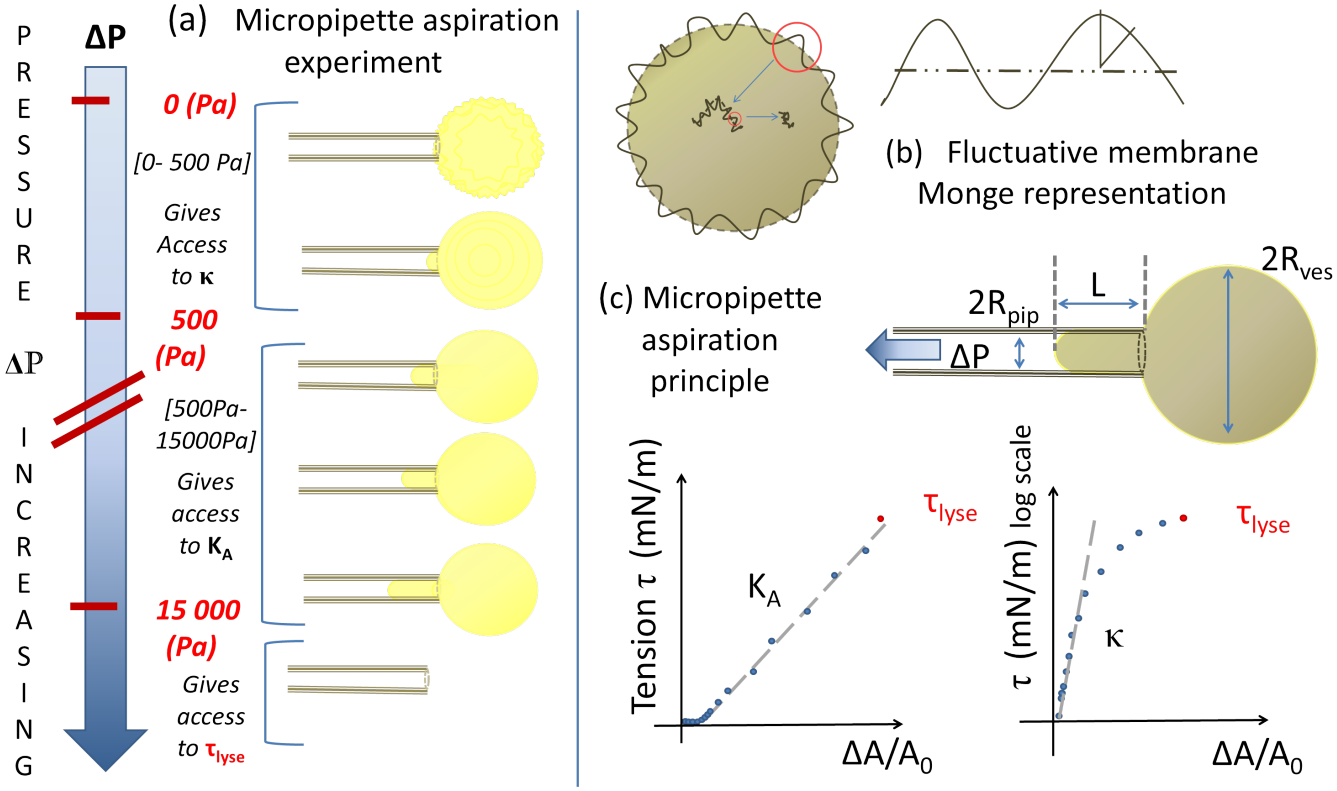

Figure 1.11: (a) Schematic diagram of a micropipette aspiration experiment. In the entropic regim (ΔP belonging to 0-500 Pa range) the vesicle fluctuations are smoothed whereas at higher pressures, (*i.e.* in the enthalpic regim (ΔP belonging to 500- 15000Pa range)) the membrane forms a tongue which elongates linearly with respect to the applied stress until the vesicle bursts when the lysis tension is reached. (b) Schematic diagram of a fluctuative membrane in the Monge representation. (c) Micropipette aspiration data analysis principle: Plotting the tension with respect to the relative area expansion gives access to both the bending modulus, κ, (log scale, right graph) and the area expansion modulus, K_A, (left graph). Adapted from [27].

Chapter 4), then from Pascal's law the applied pressure ΔP can be calculated:

$$\Delta P = \rho g \Delta h \tag{1.12}$$

where ρ is the fluid density, g the acceleration due to gravity and Δh the high difference between the sample and the water column. The pressure can then be related to the tension via Laplace's formula:

$$\sigma = \frac{R_\mathrm{l}}{2\left(1 - \frac{R_\mathrm{l}}{R_\mathrm{ves}}\right)} \Delta P \tag{1.13}$$

provided the length tongue inside the pipette is longer than twice the pipette radius. This gives an expression of the tension with respect to the pressure and both the radii

of the vesicle R_{ves} and the pipette R_{pip}:

$$\sigma = \frac{R_{\text{pip}}}{2\left(1 - \frac{R_{\text{pip}}}{R_{\text{ves}}}\right)}\Delta P \tag{1.14}$$

Then recording, the length of the tongue, the tension can be related to the relative area expansion via[1]:

$$\alpha = \frac{\Delta A}{A} = 2\pi L \frac{R_{\text{pip}}\left(1 - \frac{R_{\text{pip}}}{R_{\text{ves}}}\right)}{4\pi R_{\text{ves}}^2} \tag{1.15}$$

From the dependence between the tension and relative change in the membrane area, the bending modulus κ (in the entropic regime) and the area expansion modulus K_A (from the enthalpic regime) can be measured experimentally [2] (see fig. 1.11-c).

1.4 Mixed lipid systems: formation of domains

1.4.1 The melting temperature: T_m

Similar to other materials, lipid systems exhibit temperature dependent phase changes. The most physiologically relevant transition is the melting transition between the gel and liquid state which takes place at the **melting temperature,** T_m. Up to now we have only considered the lipid membrane as a homogeneous liquid. *In-vitro* studies [29] showed that is in not always the case. Below a certain temperature the lipid membrane becomes more solid-like: it is said to be in its gel state. The melting temperature T_m at which a lipid goes from its gel state to its liquid is intrinsic to each lipid species.

When the bilayer is in its gel state, lipid molecules are closer together and more ordered (as shown in fig. 1.12-a). To minimize its energy all the double bonds appear to be in the *trans* conformation [30] in which the Van Der Waals interactions are stronger: one talks about an *'order effect'* [31]. In this phase, the lipids thus have less freedom of movement and single lipids lose their capabilities to rotate: this phase is called the **gel phase** L_β (also called the solid ordered S_o phase). The opposite is true when in the liquid state, the probability of lipids to go from the *trans* to their *cis* conformation will increase and lipids will use more space per polar head (see fig 1.12-c). In addition, the lipids will have all the freedom of movement described in section 2.3. This phase thus appears to be more disordered and is indeed referred to as the **liquid disordered phase** L_α.

[1] To find the latter expression one need to calculate separately the volume of the vesicle in the pipette from the rest of the vesicle.

[2] The relative area expansion was calculated to be :$\Delta\alpha = \frac{k_B T}{8\pi\kappa} ln(1 + CA\sigma) + \frac{1}{K_A}\sigma$

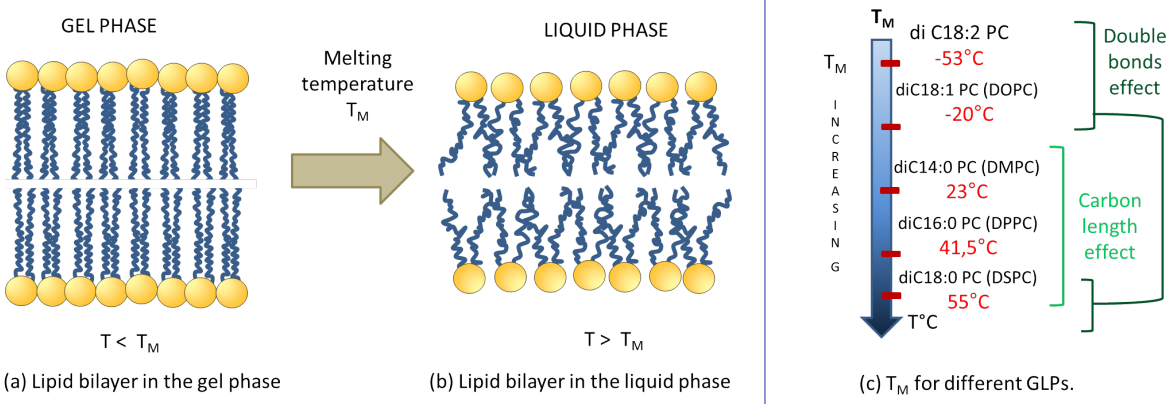

(a) Lipid bilayer in the gel phase

(b) Lipid bilayer in the liquid phase

(c) T_M for different GLPs.

Figure 1.12: Schematic diagram illustrating the effect of the temperature on lipid bilayers. There exists a temperature (the melting temperature, T_m) which drives the behavior of the lipid molecules within a bilayer and which is intrinsic to the lipid species. Below this temperature the bilayer is in a gel state (a) whereas it is in the liquid state above T_m (b). (c) Arrow scale classifying lipids with respect to their melting temperature.

T_m is dependent on two main chemical parameters: **the hydrocarbon chain length** and **the number of double bonds**. As shown in fig.1.12-c, the longer the chain the higher the melting temperature, whereas a *cis* double bond will drastically decrease T_m and the higher the number of *cis* double bonds the lower the melting temperature. These two effects can be understood from an energetic point of view: when the chains are longer the Van Deer Waals interactions between neighbouring chains are stronger and thus more energy is necessary for melting the lipid chains, hence the higher T_m. In contrast, when lipids are unsaturated especially in the *cis* conformations the chains are further away from each other and subject to weaker Van Der Walls interactions thus their chains melt at lower T_m. Finally, polar head can also have an effect on T_m but to a smaller extent[1].

The melting temperature is also sensitive to the external environment and some proteins can affect T_m. As a result studying changes in T_m might be an indirect method to study protein-lipid interactions (See beginning of Chapter 3). As a general rule, naturally occuring lipids with long chains tend to have a larger number of double bonds, and hence biological membranes exist mostly in liquid state. It is therefore sensible during *in-vitro* experiments to use membrane in liquid state. One should also be careful and stay far from the transition to avoid pre-transitional side effect [32] and in our micropipette experiments we made sure to be in the liquid phase when using

[1]There are multiple methods to measure the melting temperatures: sweep differential calorimetry calorimetry (DSP), fluorescence anisotropie, AFM, to only name a few.

mixed lipid vesicles.

1.4.2 Multi-component lipid mixtures

We now consider 2 lipid species whose melting temperatures are different (*i.e.* $T_{m1} > T_{m2}$) for example a saturated phospholipid and an unsaturated one. To reach perfect miscibility for a lipid mixture of the two lipid species (say with 1:1 molar ratio) one needs to be at a temperature higher than both T_{m1} and T_{m2}. For the same mixture, if the temperature T is now between T_{m1} and T_{m2}, a liquid phase L_α and a gel phase L_β will coexist and laterally separated (micro)domains will form. The liquid phase will be mainly composed of the lipid species whose melting temperature is the lowest (T_{m2}) whereas the gel phase will be mainly composed of the other lipid species (with melting temperature T_{m1}). In the case of microdomain segregation, the gel domains can be seen as solid little blocks floating on a lipid liquid 'sea' as shown in figure 1.13-c [33].

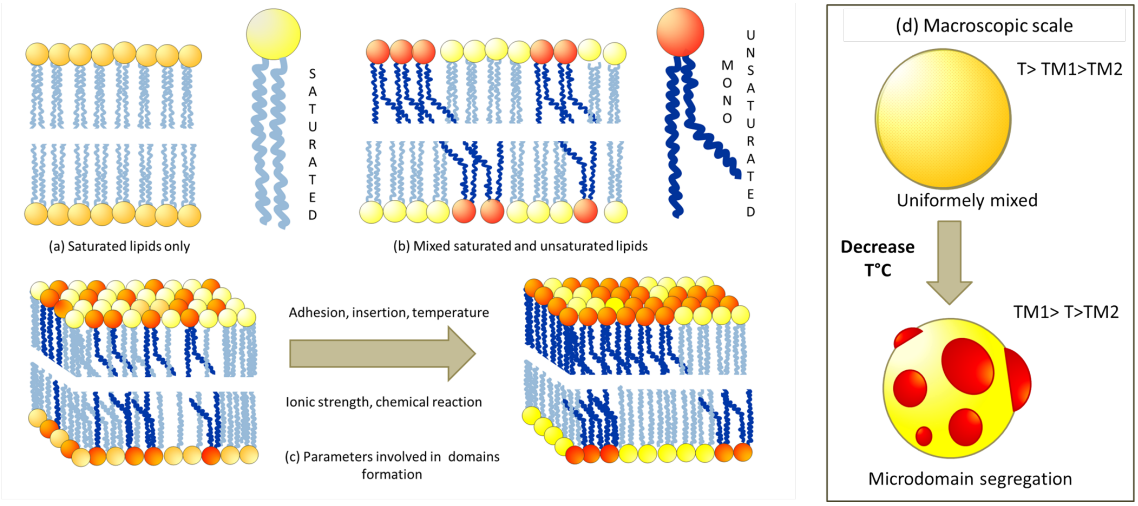

Figure 1.13: Lateral segregation in multi-component lipid bilayers: (a) Schematic diagram of a lipid bilayer composed of a single lipid species, (b) Schematic diagram depicting a bilayer membrane composed of 2 lipid species, a saturated lipid species and an unsaturated one. (c) 3D view of the lipid mixture bilayer of (b). External stimulii such as temperature, and pH can induce lateral segregation between lipid species. The insert illustrates, the effect of a decrease in temperature on a multi-component GUVs with the apparition of macrodomains at the mesoscopic/ macroscopic scale. Adapted from [16])

When different phases coexist, a line tension at the interface between the two phases appears. The system always trying to minimize its overall energy, and the line tension works to reduce the contact length between the phases[1]. These effects can lead to formation of localised domains of different curvature, which in term, could drive further the phase separation process, as different lipids (due to the shape of their molecules)

[1]The energy associated to the line tension can be calculated and is given by: $E_{LT} = 2\pi R\gamma$ where γ is the line tension and R the domain radius [24]

prefer areas of different curvature. Domain sizes and shapes will thus derive from a compromise between all the factors involved [34] [35].

Previous studies have clarified some of the parameters involved in domain segregation. It has been demonstrated that the match between GPLs acyl chain length is important, and a mismatch can induce phase separation: for example 2 PC lipids will separate into domains provided the carbon length difference is at least 4 CH_2 [36] [37][1]. On the other hand studies on GPLs with fixed carbon length but of different head group revealed that the chemical differences between the polar heads could not induce phase segregation when at the liquid state, whereas solid-liquid coexistence could happen when melting temperatures were significant different [39].

Binary mixtures involving glycerophospholipids and sphingolipids almost always separate into domains in liquid and gel state. Liquid-solid segregation also happens within the range of temperature between their respective intrinsic melting temperatures. This arises from the fundamental chemical differences between these two categories, the sphingolipids having a much higher melting temperature compared to GPLs [40].

Earlier in this thesis, it was described how the addition of ions can induce GUVs shape changes and this can now be related to domain separation. A summary of the factors able to influence/induce the formation of domains is given in figure 1.13 [16], the temperature being the predominant parameter. To summarize, the conditions for domain formation are a mixture of lipids of very different melting temperatures, a mixture of lipids of different structures (for example GPLs and sphingolipids) or the inclusion of cholesterol. The last phenomenon will be considered in the next section. Insertion of proteins can sometime induce domain formation which can thus be used as an indirect way to study protein-lipid interactions (See beginning of Chapter 3).

[1] A GPL with 2 carbon chains of different lengths can introduce domain formation as well [38].

1.4.3 Inclusion of cholesterol: The liquid ordered phase

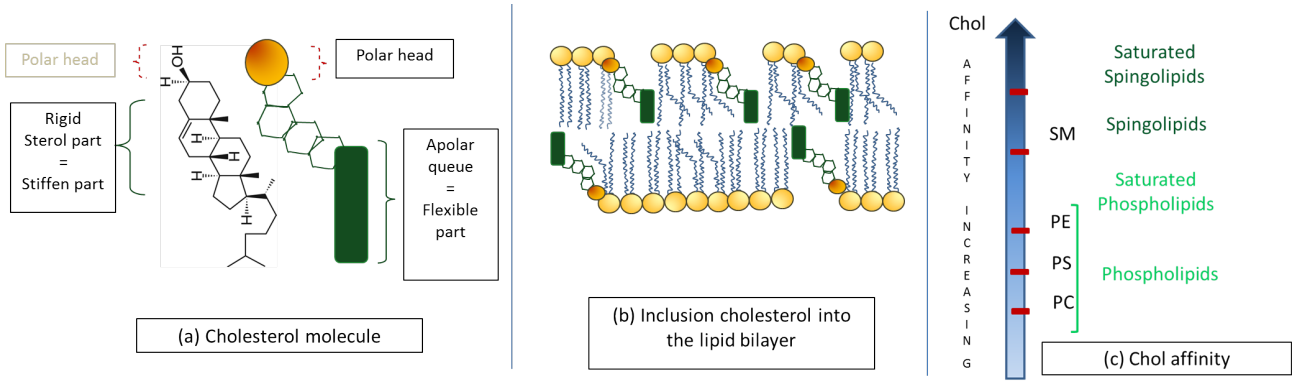

Figure 1.14: (a) shows the structure of the cholesterol molecule: it possesses a polar head, a rigid body and a flexible apolar queue. (b) Inclusion of cholesterol into the lipid bilayer: Cholesterol can insert within a phospholipid bilayer: its polar head intercalating between head groups while its acyl chain hids between phospholipids fatty acid chains. (c) Arrow scale classifying lipids with respect to their affinity with cholesterol.

Cholesterol structure

Cholesterol has already been mentioned a few times. It is an important molecule present in cell membranes. Cholesterol represents around 30 to 40 % (molar ratio) of eucaryotes' plasmid membranes [41]. As shown in figure 1.14 the cholesterol molecule is composed of a carbon backbone formed by 4 aromatic groups lying in the same plane. A small polar head comprised of only a hydroxyl group is attached to the backbone and constitutes the hydrophilic part of the molecule. Attached on the other side is a single acyl chain, composed of 8 branched out carbons [33]. One can find the cholesterol chemical formula in figure 1.14.

Inclusion of cholesterol: effect on the membrane fluidity

Cholesterol has the ability to intercalate between the lipid molecules in the membrane so that its polar head inserts between phospholipid polar heads and its acyl chain is oriented toward the hydrophobic membrane bilayer centre [42], as shown in figure 1.14-b. Cholesterol inclusion induces important changes of the lipid membrane chemical and physical properties: **it stiffens the membrane while maintaining good lateral mobility**. As it incorporates into the membrane it causes a *'condensation effect'* leading to smaller area per lipid head group. This leads to an increase in membrane rigidity. Meanwhile it also keeps good fluidity *as cholesterol postpones the liquid-gel transition*. Cholesterol is miscible in both liquid and gel phases and it actually acts as a 'buffer', loosening the gel phase while stiffening the liquid one with the creation of a new phase L_o described below [43]. It can also facilitate domain separation and

miscibility in lipid mixtures [39] [44]. It is therefore a compound of great importance in cell biology as it allows lateral mobility of lipids and proteins within the membrane bilayer and is involved in many cell processes (cell signaling and others, see 'lipid rafts' paragraph below).

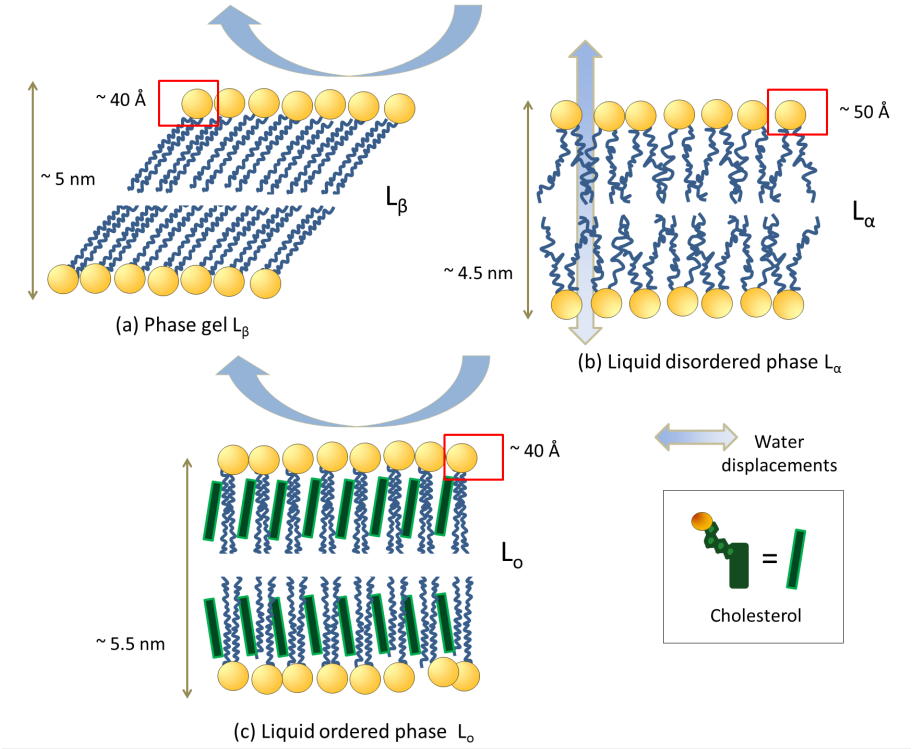

Figure 1.15: A summary of the different states a phospholipid bilayer can adopt. In the gel phase, L_β (or solid ordered, S_o) lipid are ordored (a); in the liquid phase, L_α (or liquid disordered, lil_d), lipid have more freedom motion (b). When cholesterol is inserted, a new phase appears: the liquid ordered (l_o) phase, in this phase, lipid molecules are closer together like in (a) but keep their mobility like in (b). Space the lipid head occupies (red squares) and bilayer thickness vary in the different phase. Lipid head occupies between 40 to 60 $\AA$ in the gel phase [33]. For a same lipid specie this volume rise from 5 to 10 $\AA$ in the liquid phase while the thickness diminishes of about 5 $\AA$. Insertion of cholesterol on the other hand, induces an increase of the thickness of $\sim 5-10\,\AA$. Permeability to water molecule is also reduced in the L_o phase like in L_β (Allowed water motions are depicted with blue arrows). Adapted from [45].

The liquid ordered phase

When cholesterol is mixed with saturated phospholipids, different behaviours occur depending on the concentration of cholesterol and the temperature. At low cholesterol concentration there is little change in the membrane properties. At higher concentrations - higher than 10 % molar ratio for a DPPC-chol mixture for example - a phase segregation appears between the phospholipid in its gel or liquid state (depending on the temperature compared to its T_m) and a mixture of cholesterol with that phospho-

lipid: there is **a new phase appears referred to as liquid-ordered, L_o, phase** whose properties are between the gel and the liquid phases. In the L_o phase the acyl chains are straighter, more ordered like in the gel - the cholesterol stetches them - but they have similar freedom of movement as in the liquid phase[1]. As a consequence of the condensation effect an increase in the lipid bilayer thickness is observed as shown in figure 1.15 [2]. When the cholesterol concentration increases the L_o phase proportion becomes higher until it forms the entirety of the bilayer system above 30 % cholesterol (for a DPPC-chol mixture) [48]. Finally, in the L_o phase the lipid membrane is highly impermeable to water compared to the liquid phase (see figure 1.15).

Cholesterol demonstrates a higher affinity to sphingolipids compared to GPLs. Indeed, sphingolipids can form hydrogen bonds with the cholesterol OH group which allows them to interact more readily with the cholesterol head and backbone. Preferences within GPLs also exist; figure 1.14-c summarizes the cholesterol affinity to lipids/phospholipids; cholesterol has higher affinity to saturated lipids and sensitiviy to the polar head is also present: higher affinity towards PC than PS and higher affinity towards PS than PE have been observed [49].

Ternary mixtures

The situation described above implies that mixing cholesterol with both a phospholipid and a sphingolipid could bring interesting effects and such ternary lipid mixtures have been extensively studied [50] [37]. Figure 1.16 summarizes what happens at physiological temperature: when incubated at 37°C, the three species will spontaneously separate into (micro)domains: sphingolipids in the gel state and cholesterol will preferentially interact forming a condensed L_o phase whereas GPLs in the liquid state will interact with cholesterol to a much smaller extent (as one can see on the schematic, cholesterol is not completely absent of the L_α phase). At a mesoscopic scale there is again a distribution of solid domains rich in cholesterol and sphingolipid within the liquid disordered phase composed mainly of GPLs.

This is a simple model for **lipid rafts** which are defined as microdomains within the cell membrane which are more ordered and more concentrated in cholesterol than the surrounding bilayer. The combination of lipid rafts and proteins are believed to be involved in a wide range of biological processes from signal transduction to cell

[1] Studies showed that the diffusion coefficient in the L_o phase was only reduced by a factor of 2 to 3 compared to the liquid state [46] .

[2] This has been studied by AFM on monolayers of different mixtures of POPC/ SM with and without cholesterol [47].

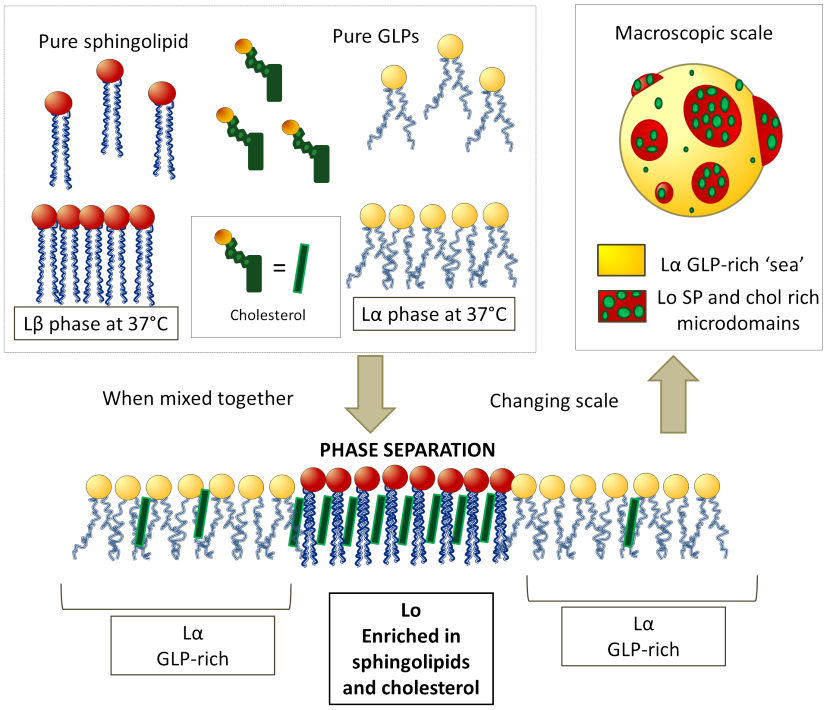

Figure 1.16: Schematic diagram of lateral segregation in ternary lipid systems. When mixing pure sphingolipid (SGL) with both cholesterol and pure glycerophospholipids, the system will spontaneously segregate at physiological temperature. Cholesterol will preferrentially interact with the sphingolipid species forming a condensed L_o phase while the GPL specie will remain in the liquid phase L_α. The insert on the right represents the lateral segregation occuring within a GUVs at the macroscopic (mesoscopic) scale. Macro and microdomains of condensed lipids, rich in SGL an cholesterol, are in the L_o phase and floating within the liquid phase composed mainly of GPLs. Adapted from the Expert Reviews in Molecular Medicine (2002)

signaling and in some infectious processes [51], [52], [53], [54]. In the 'fluid mosaic model', where everything is in perpetual motion, lipid raft life time (depending on the process involved) can be as short as a few micro-seconds. Lipid rafts can spontaneously form but can also be induced by external stimuli (see the literature). Finally, FRET[1] experiments have demonstrated that domain segregation happens at all scales, and microdomains composed of only a few molecules (nanoscale) can be found [55]. Due to the dynamics within the cells, the life-times of microdomains can be really short which makes them very difficult to study in some processes.

Studies of domains segregation in ternary mixtures have become possible thanks to **fluorescent probes**. There exists a wide range of fluorescent probes which will partition preferentially into one of the phases (for example: NBD-labelled lipids), one of the elements (for example: Annexin V) or both of them in a slightly different way (for example: Laurdan [57]); we will come back to this topic in Chapter 2. Systematic studies

[1] FRET stands for Fluorescence Resonance Energy Transfer.

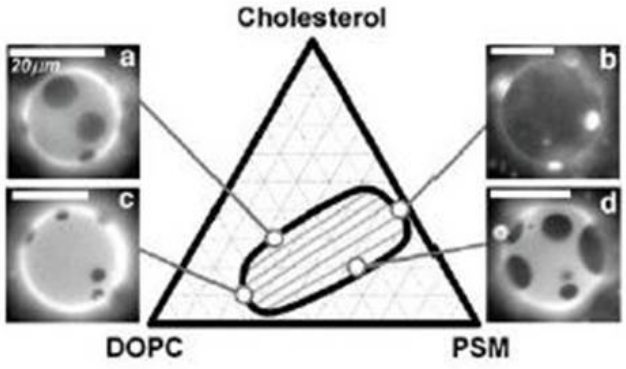

Figure 1.17: Phase diagram highlighted with fluorescence probe: Phase coexistence are studied in a ternary mixture composed of Cholesterol, DOPC and palmitoyl-SM (referred as PSM) (a) DOPC/PSM (2:1) 30 % Chol; (b) DOPC/PSM (1:19) 40 % Chol ; (c) DOPC/PSM (3:1) 10 % Chol ; (d) DOPC/PSM (1:2) 20 % Chol. From [56].

on both monolayers and GUVs using these fluorescent probes allow the construction of phase diagrams such as the example shown in figure 1.17 [56]. To obtain a target set of phases one needs to read the diagram and mix the lipids in the right proportions.

During this PhD, some ternary (DOPC:DPPC:Cholesterol) - and four-component: DOPC/DOPS/SM/Cholesterol (25/25/25/25 % molar ratio) - mixtures have been used in order to study domain and micro-domain structures and try to determinate if spectrin (and elastin) will influence this micro-domain organization (see Chapters 3 and 5).

1.5 Protein-lipid membrane interactions

1.5.1 Mechanisms to deform the membrane when protein are involved

Figure 1.18 A summarizes the different ways proteins can interact with lipid bilayers. There are two main classes of proteins: the **transmembrane proteins** and the **associated proteins**. As one can see (fig. 1.18 a, b and e) the transmembrane proteins are incorporated within the membrane. Similar to lipids they are composed of a hydrophobic part and a hydrophilic one whereas associated proteins (fig. 1.18 c, d and f) stay peripheral to the membrane sometimes only interacting with the membrane via other proteins (d). As the protein we are interested in is an associated protein we will focus on this class of proteins

Figure 1.18 B summarizes all the deformations possible due to protein-lipid membrane interactions. As one can see (in (c)) the cytoskeleton can greatly influence the

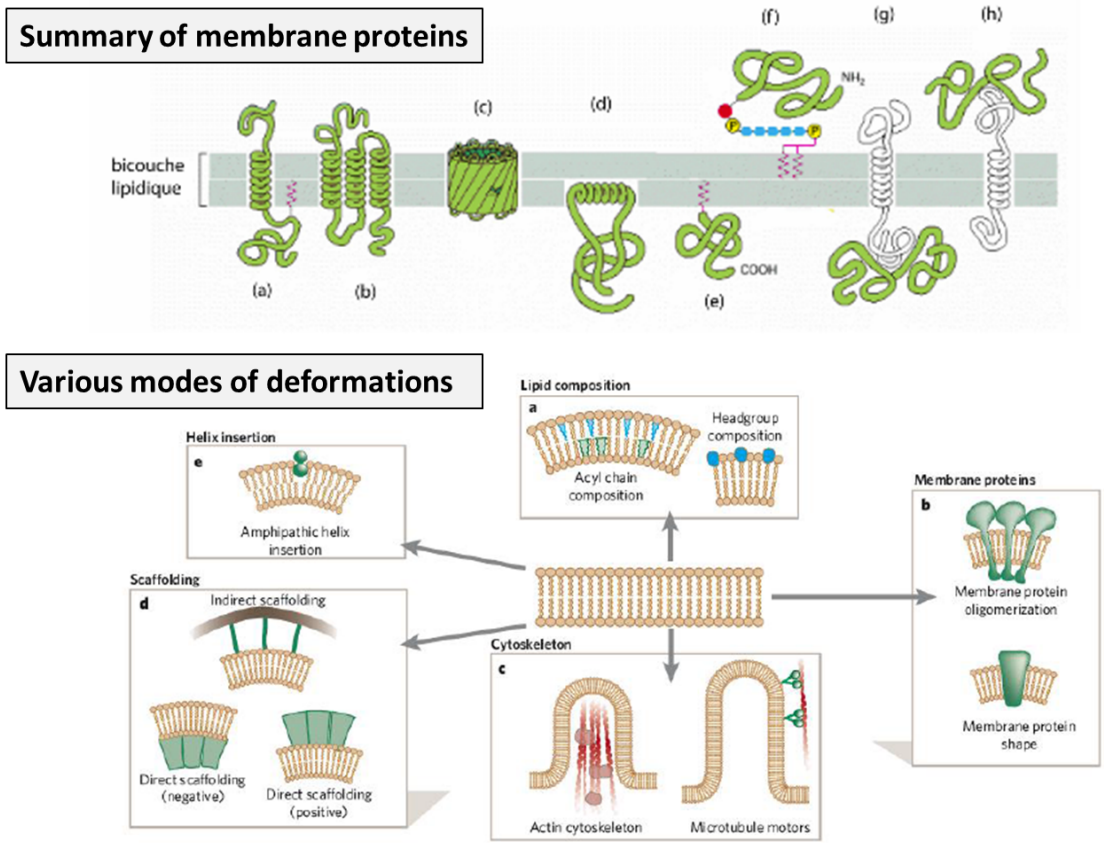

Figure 1.18: (A) Protein- lipid interactions: transmembrane versus associated protein: Schematic diagram summarizing the different classes of membrane proteins. From [58]. (B) A summary schematic of the different manners to curve a membrane. From [24]

membrane curvature.

1.5.2 The spectrin complex/network

Spectrin within red blood cells (RBCs)

Spectrin is a cytoskeletal protein and its structural organisation in red blood cells (RBCs) was first imaged using electron microscopy [59]. It was then found to be present in many epithelial cells [60] and seems to play a role in the cells of vital organs such as the heart and the brain [61]. RBCs are 8 μm diameter biconcave disk-shaped cells and represent about a quarter of all the cells in the human body. RBCs purpose is to carry and deliver oxygen (stored in the protein haemoglobin) to human tissues. To do so, they have to travel within capillaries whose diameter is sometimes smaller than the size of a RBC during all of their 100 to 120 days life, and are thus submitted to a lot of stress during this constant deformation.

RBCs are widely studied as they are one of the simplest cells (they do not contains organelles, nuclei or mitochondria, and are just filled with haemoglobin)[1]. The erythrocyte is thus a good model for studying more complicated cell membranes and the spectrin used in the experiments during this project was extracted from RBCs. Moreover it is of great importance for red blood cell to be studied as many serious hereditary illnesses such as spherocytosis, diabetes, anemia, are related to red blood cell abnormalities. Alternations in composition may affect the mechanical properties of the cell and compromise its function. The spectrin network in RBCs is detailed in the next section.

Spectrin network and the junctional complex

Spectrin is a protein of high molecular weight, composed of two polypeptide subunits (α-spectrin (also referred as band 1) and β-spectrin (also referred as band 2)) whose structures are quite similar but not-identical. The molecular weight of these subunits differs in the literature but is respectively about 240 kDa and 260 kDa and the molecules associate to form a branched helix. Spectrin is very flexible and the two subunits associate (coiled up head to head, to each other) to form a heterodimer ~ 200 nm long. Spectrin can be found in a dimeric form, composed of one of each subunit, or in a tetrameric form, composed of two dimers oriented head-to-head. The spectrin network has a well-defined meshwork consisting of a triangular lattice whose length is 70 nm (which can also be seen as an arrangement of pentagons and heptagons) as shown in figure 1.19. This network is formed by tetramers of spectrin which associate with actin filaments at each end of the tetramer.

The actin association points form the junctions of the network and also contain a protein called 4.1 and a several other components. The principal mode of attachement of the cytoskeleton to the membrane is via the protein **ankyrin** (also called 2.1). One domain of the ankyrin binds to the spectrin filament while the other domain interacts with another integral membrane protein (band 3)[2]. There are also other horizontal connections to proteins including tropomyosin, tropomodulin and adducin. Figure 1.19 contains a schematic diagram illustrating the spectrin network and the junctional complex by which it attaches to the cell membrane.

[1] As an example the lipid membrane bilayer structure was first described on RBCs (Gorder et Grendel, 1925)

[2] There is another attachment via glycophorin C.

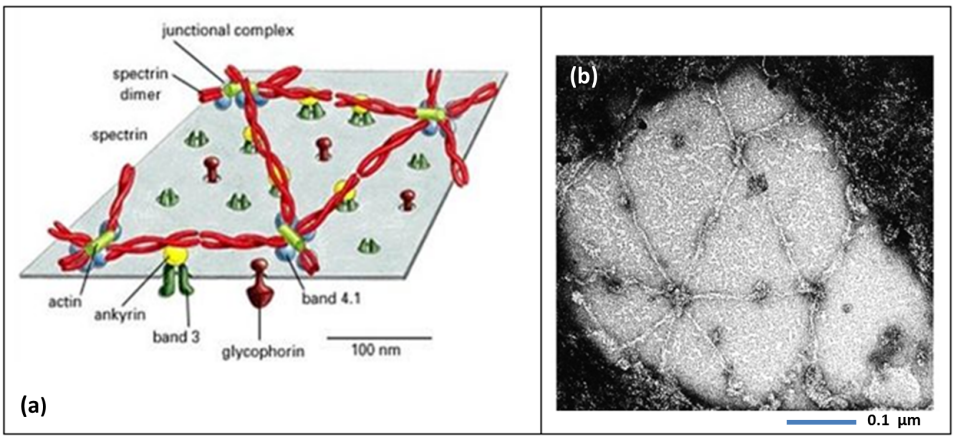

Figure 1.19: (a) Schematic of the spectrin network and junctional complex. From http://www.studyblue.com/notes/note/n/molecular-cell-chapter-17/deck/5962290. (b) Electron micrograph picture of the spectrin network. From [59].

1.5.3 Overview of the thesis

This thesis work is devoted to investigating the **direct interactions** of spectrin with lipid membranes and determine its effects on the mechanical properties of the lipid bilayer. The overall aim of this PhD project stems from earlier PhD studies [62]. **It aims to determine how interactions between spectrin and lipids influences membrane mesoscopic morphology and biophysics in ways that could ultimately be important to cellular function**.

To do so, particular attention has been paid to the preparation and purification of spectrin (see description in material and methods of Chapter 3). Once we obtained pure spectrin, the first experimental step was to tag it with a fluorophore. This was necessary in order to visualize the spectrin distribution around vesicles - for different vesicle mixtures - and confirm or deny its preferences for specific lipid species. The idea was then to determinate its effects, if any, on domain distributions in phase separated vesicles (see Chapter 3), and the membrane mechanical properties.

The second logical step was to perform micropipette aspiration measurements on uniformly mixed GUVs of different compositions with and without spectrin to investigate its effects on the area expansion modulus (see Chapter 4). Since two-photon fluorescence experiments demonstrated that the elastin appeared to bind uniformly to GUVs (see Chapter 5), this protein was investigated as well to establish the validity of the micropipette aspiration technique to study protein-lipid interaction and their effect on model membrane mechanical properties.

Another important part of the PhD work, done in parallel, was using non-linear optics microscopy techniques. These techniques were used to image protein-lipid interactions without any labeling in giant unilamellar vesicles (especially the distribution of the protein around the vesicles). Using such label-free techniques was motivated by the possibility of an interference by the fluorophore with the process of lipid-protein binding. Our aim was to analyze potential changes in the protein distribution with respect to the vesicle composition (uniformly mixed versus phase domain separated vesicles). For this part the elastin which is auto-fluorescent was used as a protein model (see Chapter 5).

At this stage the natural advancement was to develop a technique combining micropipette aspiration and Stimulated Raman Scattering to ideally be able to perform micropipette aspiration using the label free techniques to highlight the protein distribution and evolution when stress is applied. To prove both the validity and potential of this new technique, preliminary experiments on both GUVs and fibroblast cells have been performed (see Chapter 6).

Finally the last aspect of the interaction of the spectrin with lipid to be studied was its thermodynamics. This study was also carried out in parallel using the isothermal titration calorimetry technique. One more time, experiments were performed on elastin as well for a comparison (see Chapter 7). Figure 1.20 summarizes the principal objectives and techniques used during the PhD.

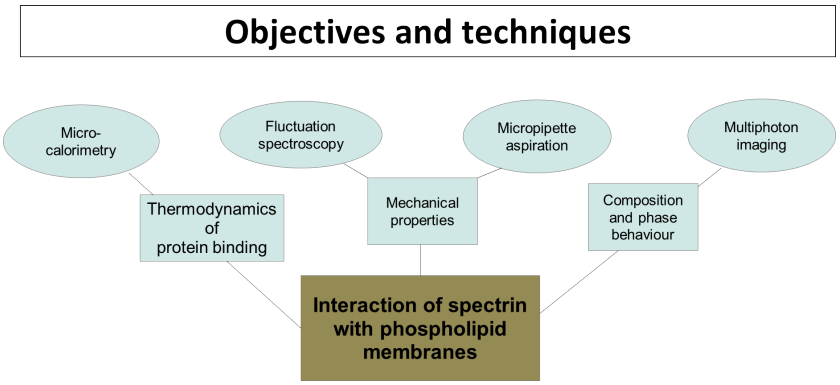

Figure 1.20: Schematic diagram summarizing the objectives of the PhD and techniques used. for investigating spectrin-lipid interactions and their effect on the membrane mechanical properties. Adapted from a diagram by David Woods.

Chapter 2

Optical Microscopy

In this chapter the different imaging techniques used during the PhD will be presented. Reminders of classical one photon fluorescence techniques will be given, before introducing multiphoton fluorescence. The Raman effect will then be explained, and label-free microscopy techniques based on the Raman effect will be explained and compared.

2.1 Fluorescence in Biology

2.1.1 Getting contrast in colourless samples

The word microscope comes from the combination of the grec *mikros* (tiny) and *skopein* (to examine). The first microscope was invented by Antonie van Leeuwenhoek in 1675 who imaged for the first time cells and bacteria[1]. Around the same period, microscope improvements were performed by Robert Hooke who built a *composed microscope* during the 17^{th} century; he published his work in *Micrographia* in 1655. Hovewer, most of the improvements have happened over the last century [63].

In 1933 the physicist Fritz Zernike demonstrated that using two complementary rings - now referred to as a *mask phase* - in the microscope light path induced slight changes in the beam phase when they passed through media of different refractive indices; the **phase contrast microscopy** (Ph2) was born. Phase changes are then converted into contrast (to which the human eye is sensitive) thanks to a grey filter ring present in the objective. By this method, features in transparent samples (*e.g.* in cells) can be distinguished and features in colourless samples, undetectable in bright field, can

[1] Some people believe that the very first microscope was 'built' in the 1590s, by two Dutch men, Zacharias Jansen and his father Hans who placed lenses in a tube.

highlighted with different intensities [64][1].

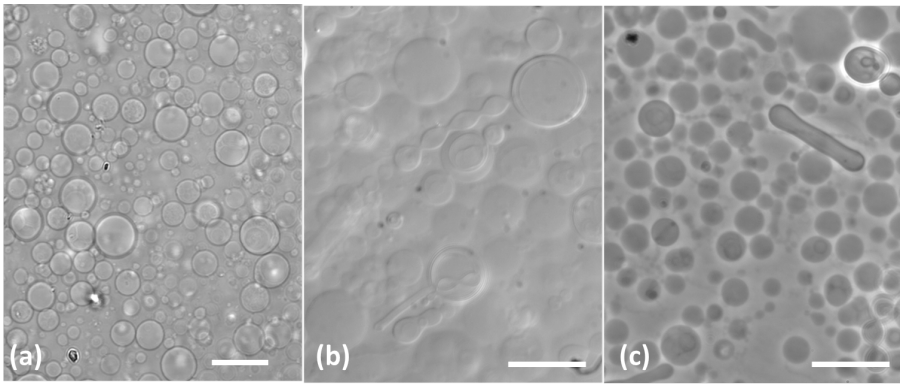

Figure 2.1: Bright field microscopy techniques. (a) Confocal microscopy, (b) Differential interferential contrast, and (c) Phase contrast. Bar scale = 20 μ.

Later on, in 1955, George Normarski invented another microscopy technique. He built a more complicated set-up using a **polarizer**, an **analyzer** and two prisms - now referred to as **Wollatson prisms**[2]. The first prism splits a polarized beam into two beams, respectively called ordinary and extraordinary beam. These interfere differently when they meet a medium boundary (for example a cell membrane)[3] before being reunified at the second prism. As a result, the eye perceives the image as if it was in 3D (better illustration of depth). Nowadays this microscope, called **differential interferential contrast** (DIC) is widely used to image cells and is usually combined with fluorescence. This is the microscopy technique preferentially used for the micropipette aspiration experiments during the PhD (For a set-up schematic see chapter 4, Material and methods).

Figure 2.1 gives an example of both of these imaging techniques. Vesicles are indistinguishable under normal bright field microscope (unshown). As one can see, a confocal microscope (this technique is described in section 1.3) allows to highlight the outline of the vesicles (2.1 a) whereas in DIC the GUVs show up in 3D (2.1 b). In Ph2 on the other hand, the GUVs appear darker than the bulk solution (2.1 c). Since Ph2 is sensitive to refractive indices, it is common to use different bounding media between the inside of vesicle and the outside (*e.g.* sucrose in the inside and a ratio of glucose/sucrose in the outside). Other techniques based on a phase gradient, such as the Hoffman technique exist, we won't extend on them since they have not been used.

[1] Fritz Zernike got the physics Nobel Prize for the discovery of the Ph2 microscopy in 1953.
[2] or Normarski prisms
[3] Homogeneous media are not affected.

The techniques described above enable to distinguish features in transparent biological sample, but it remains difficult do identify their micro organisation (*i.e.* the sub-organisms present). To overcome this problem techniques based on fluorescence have been developed. These are described in the next sections.

2.1.2 Fluorescence: Toward specificity

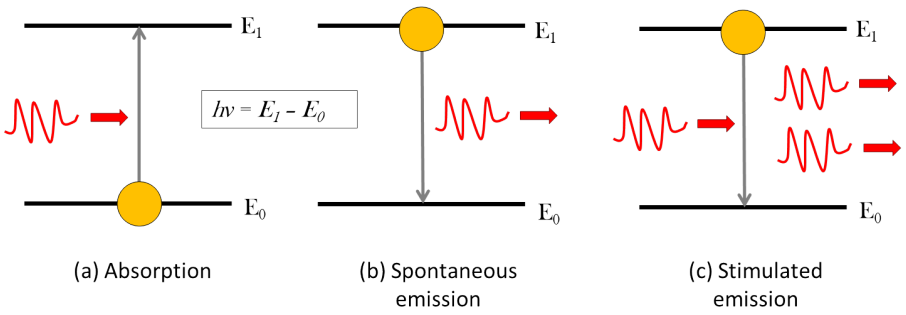

Figure 2.2: Absorption Emission and Stimulated Emission.

In 1917, Einstein demonstrated in its **light-matter interaction theory** that there are three ways light can interact with matter. These are illustrated in figure 2.2. Light can be absorbed by a system; an electron will in this case be excited (fig. 2.2 a). Light (photon) can also be emitted when an electron in an excited state spontaneously decays (*i.e.* its energy decreases from E_1 to E_0) (fig.2.2 b). In the third phonomena (2.2 c) the system (also in an excited state) is **driven to relax when excited by a photon** which results in the emission a photon having **both the same phase and energy than the exciting photon**. This process is called **stimulated emission** and is at the basis of label-free imaging techniques based on vibrational signatures (See sections 4 and 5).

Fluorescence principle

As shown in figure 2.3, the first two processes happen in a fluorescence experiment. Some light is absorbed and excites electrons (blue arrows), this process is quasi-instantaneous ($\sim 10^{-15}$ sec). The electron then undergoes both internal conversion and vibrational relaxation ($\sim 10^{-14} - 10^{-11}$ sec (yellow-wave arrows)) before the system relaxes either by emitting fluorescence at a higher wavelength ($\sim 10^{-9} - 10^{-7}$ sec (green arrows)) or by undergoing non-radiative relaxation (red-wave arrow) which might be combined with phosphorescence ($\sim 10^{-9} - 10^{-7}$ sec) (dark green arrow).

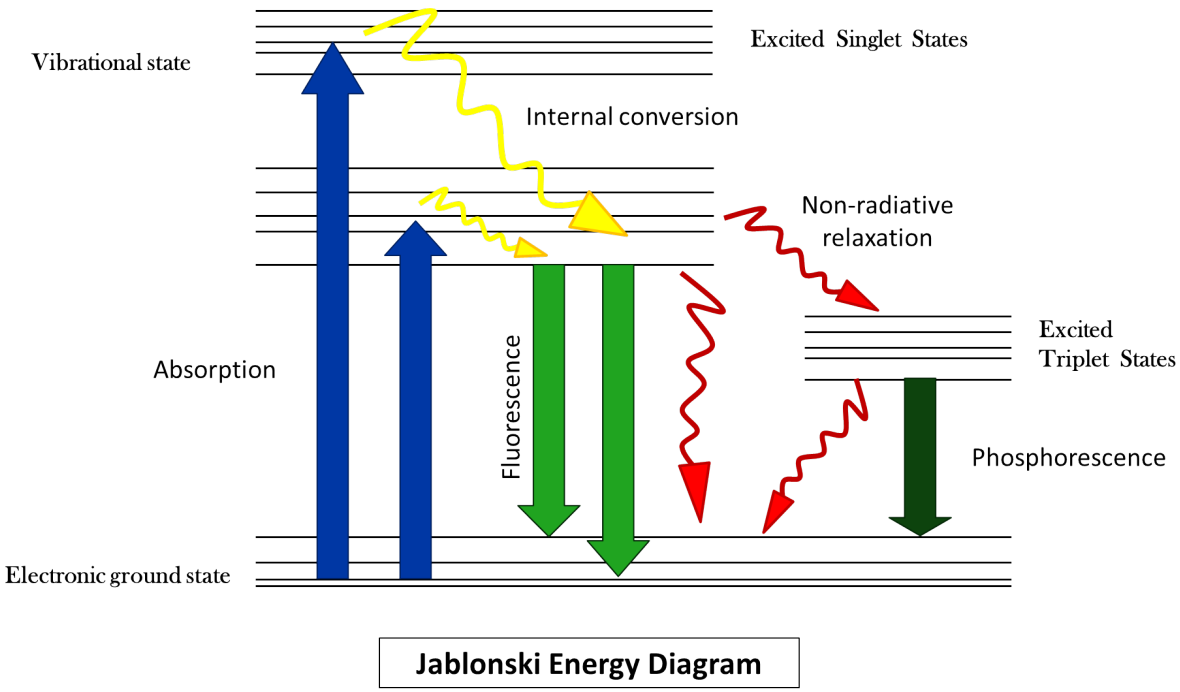

Figure 2.3: Jablonski Diagram for Fluorescence (See text).

Different fluorescence techniques

Fluorescence was discovered by Sir George Gabriel Stokes during the 19th century[1]. When speaking of fluorescence, one must distinguish between the **primary fluorescence** (also called natural fluorescence) which is the fluorescence spontaneously emitted by a system[2], from the **secondary fluorescence** which requires the addition of a fluorophore to emit light.

Fluorophores (also called fluorochromes) are composed of aromatic cycles. They are widely used in biology research and a wide range of fluorophores - emitting at various wavelengths from the UV to the IR - are available. The most common fluorophores are phycoerythrine, fluorescein isothiocyanate (FITC), Alexa Fluor and Rhodamine. These provide good contrast, but can be toxic for the sample and have the drawback of photobleaching [65]. Table 2.4 b lists popular fluorophores and gives their specificities.

Fluorophores can be combined with antibodies and antigens to target a specific element (*e.g.* a protein). One speaks of **immunofluorescence** [66]. For example, the Hoestch dye targets the A-T bases in the DNA and hence allows the highlighting of

[1] He discovered that fluorine emitted fluorescence when illuminated with UV light.
[2] One can also speak of auto-fluorescence.

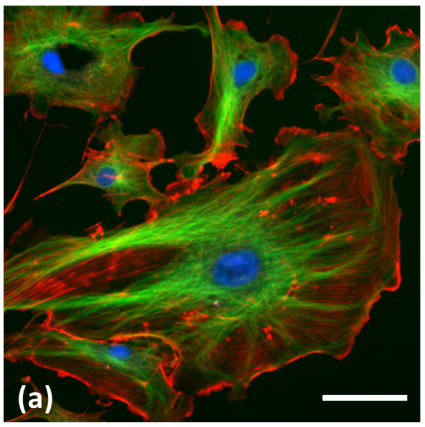

(b)

Fluorophore	Specificity/advantages
Annexin	Apoptose
Bodipy	Many λ available
DBD	Easy to use
Di-8-Anneps	Voltage sensitive dye
Fluorescein	Easy to use
Hoestch	Nucleus specific
Laurdan	TPF/VSD
Phalloidin	Actin specific
Rhodamine	Many λ available

Figure 2.4: (a) Endothelial cells under a microscope. Different elements of the cell are highlighted with different fluorophores: The nucleus is stained with DAPI (in blue), the microtubules are marked by an antibody bound to FITC (in green) and the microfilaments (*i.e.* the actin filaments) are labelled in red with phalloidin bound to TRITC. Scale bar is 10 μm. From http://upload.wikimedia.org/wikipedia/commons/0/09/FluorescentCells.jpg, (b) Table of some fluorophores.

the nucleus in cells (fig. 2.5-a). There are two types of immunofluorescence. They are distinguished by the number of antibodies intercalated between the antigen and the label. When the antibody both contains the fluorophore and targets the antigen, the immunofluorescence is direct. When 2 antibodies are required[1] the immunofluorescence is indirect. The benefit of using a secondary antibody is to enhance the fluorescence compared to the direct immunofluorescence (since there are usually multiple sites the second antibody can get attached to compared to the antigen[2]). Different fluorophores can be combined to highlight different elements within the same sample (provided the emitted wavelengths do no overlap) as illustrated in figure 2.4 a.

In 1962, Osamu Shimamura discovered and purified a protein from a jellyfish[3] which emitted green light when excited in the blue/UV. This protein now called the **green fluorescent protein (GFP)** has become ubiquitous since Douglas Praster managed to clone it *in-vitro*[4] [67]. Nowadays, it is a very efficient tool thanks to bio-engineering progresses who have made derivatives of the GFP in different wavelengths. The GFP gene can be merged with the gene of a protein of interest (gene fusion). When introduced within a cell, the fluorescent gene will be naturally synthesized (*i.e.* a protein is transcribed from the gene and translated as a string of amino acids) while the cell grows,

[1] The first antibody targets the antigen, whereas the second antibody, the one the fluorophore is attached to, targets the first antibody.

[2] One talk about monoclonal and polyclonal antibody

[3] *Aequorea victoria*

[4] They both (Osamu Shimamura and Douglas Praster) won the Chemistry Nobel prize in 2008 for the discovery of the GFP

develops and splits. As a result the element of interest can be highlighted and studied *in-vivo* with minimal artifacts. In addition, the GFP is less harmful and phototoxic compared to the fluorophores mentioned above.

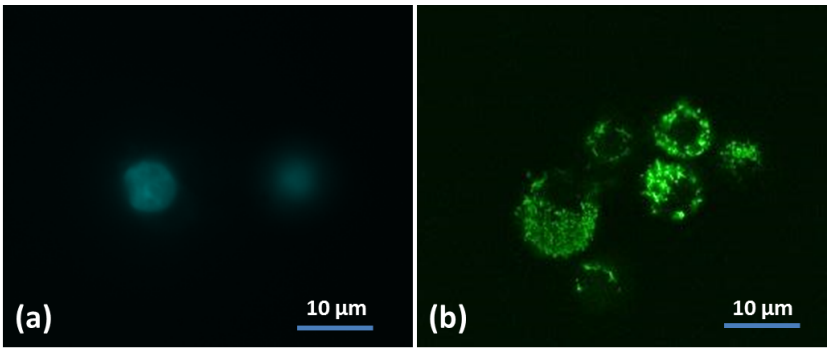

Figure 2.5: The confocal microscope allows a better resolution in the images (a) Hoechst to highlight the nucleus (DIC) (b) GFP to highlight actin filaments (confocal).

Use of fluorescence during the PhD

Highlighting Proteins

Most of these fluorescence principles have been used during the PhD:

- Primary fluorescence (auto-fluorescence) of the elastin was used to label-free image its' distribution around GUVs (see Chapter 5).
- It is also possible to attach a fluorophore to the element of interest: this is called tagging an element. We used this technique to tag the spectrin protein (See material and methods chapter 3).
- Immunofluorescence was used to ensure the purity of spectrin in indirect ELISA and Western Blot experiments (see spectrin characterization part in Material and method chapter 3).
- To ensure that non-linear optics allowed to distinguish label-free the actin-network from the cytoplasm, GFP actin-tagged fibroblasts were imaged and compared to non-labelled fibroblast cells imaged in SRS (see Chapter 6).

Highlighting lipid species in model membranes

As mentioned in Chapter 1, it is possible to use fluorescent probes to highlight domain segregation in GUVs. When making vesicles, one can incorporate lipid labelled with a fluorophore in the lipid mixture before GUVs formation (*e.g.* 2 % (molar ratio) NBD-labelled-DOPC in a DOPC: DPPC: 30 %Chol mixture). The labelled-lipid will distribute with the species in the same phase and highlight this phase. For example NBD-DOPC will be distributed with DOPC molecules and highlight the disordered phase L_d in DOPC:DOPC:30 %Chol GUVs. It is usual to highlight a phase rather than a species.

During the PhD two fluorescent probes (fluorophores) have been preferentially used: the Laurdan dye and Annexin V (see figure 2.6).

The annexin dye has the specificity to bind to charged lipids. In a two-component mixture of neutral/ charged lipids it thus allows us to discriminate between the species. The probe is added to the GUVs suspension after vesicle formation. Annexin was used to highlight the PS distribution in PC/PS and 4-components (PC/PS/SM/Chol 25 %) mixtures (see Chapter 3). In fig 2.6 (A) one can see the distribution of DOPS lipids in the 4-component mixture. Both the marcro domains (left picture) and micro domains (right picture) can be seen. These images illustrate the section 4.3 of Chapter 1 about lateral segregation of multi-component mixtures with the presence of more condensed SM:Chol domains (lipid rafts paragraph).

The Laurdan dye on the other hand interacts with both phases in different proportions (slight shift in the excitation/emission wavelengths) interacting preferentially with the gel domain phase [68]. Hence in fig 2.6 (B) the lipid species highlighted is the DPPC whose melting temperature is ∼40°C (and which is therefore in the L_o phase). As one can see in a DOPC: DPPC: 20 % Chol mixture, the GUVs incubated at 37°C separate into marcrodomains. During the PhD this probe was used as a comparative tool for demonstrating the potential of stimulated raman scattering microscopy to label-free discriminate between lipid species using deuterated lipids (see Chapter 5). This probe can also be used in two-photon excitation (Baratolli, 2008) which has not been tried during the PhD.

Other probes such as di-8-Anneps also interact with lipid membranes. They have the specificity of shifting excitation/emission spectra when a voltage is applied, and are referred to as **voltage sensitive dyes (VSD)**. These are useful to study electric potential changes in model membrane systems and excitable cell membranes (*e.g.* neurons to try and follow action potential).

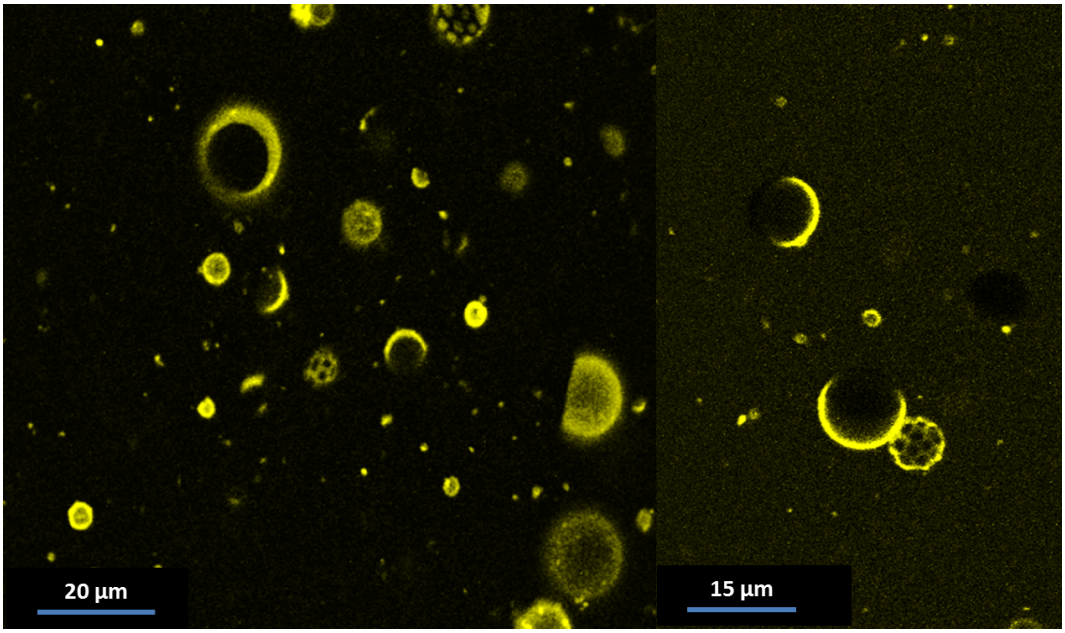

(A) Annexin probes highlighting DOPS distribution in 4 compounds GUVs.

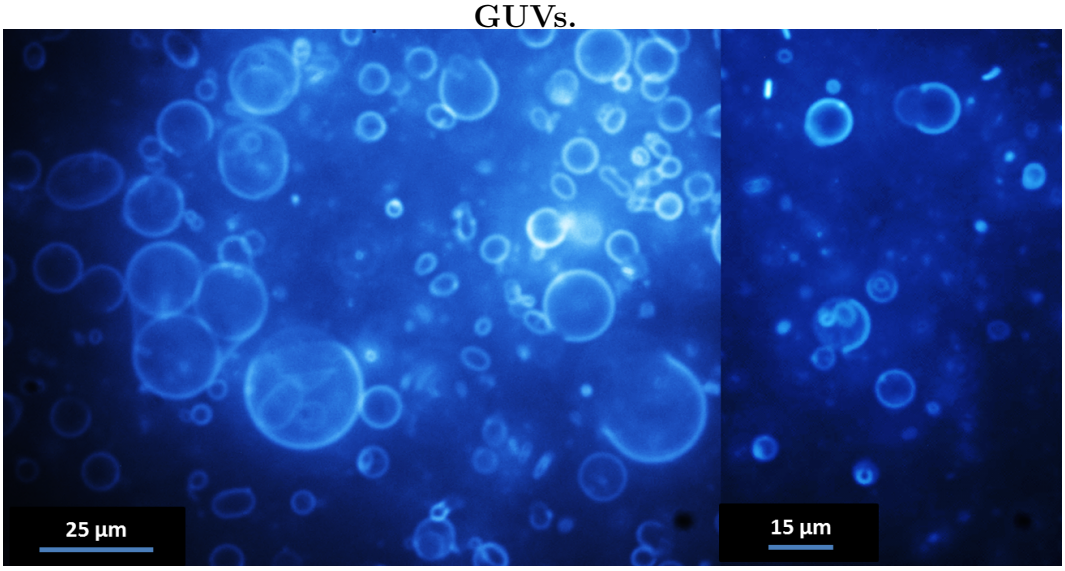

(B) Laurdan dyes highlighting the L_β phase in 3 compounds GUVs.

Figure 2.6: Different way of highlighting lipid species: (A)Four species vesicles: DOPC: DOPS: SM: Cholesterol 25/25/25/25 (molar ratio) highlighted with Annexin fluorescent dye. Annexin binds to charged lipids, hence PS in the specie highlighed in here and domains can clearly be observed. (B) Three species vesicles: DOPC:DPPC:Cholesterol (20 per cent molar ratio) highlighted using Laurdan dye, which interact preferentially with the gel phase

Time lapse-experiments

Some techniques have also been developed to study dynamic processes. They are called *time-lapse* experiments. Among them Fluorescence Recovery After Photobleaching (FRAP) and Fluorescence Correlation Spectroscopy (FCS) have become commonly used techniques. In FRAP, a laser is used to photobleach the sample fluorescence at the focal point. The area will then recover its fluorescence level as fluorescent particles in the surrounding enter the photobleached area. This method therefore allows to study the displacement of molecules and gives access to the diffusion coefficient. In FCS, intensity fluctuations of a specific area are studied. These fluctuations are due to Brownian motions of the particles entering and leaving the region of interest and this technique gives access to both the size and concentration of a studied element. Since these techniques have not been used we won't extend further on them. One can find more information in the literature (*e.g.* studies about lipid diffusion studied by FCS [69] or FRAP [46]).

2.1.3 Resolution: The diffraction limit

The Rayleigh limit

In 1873, Ernst Abbe demonstrated that when using optical microscopes one could not get a resolution better than half the wavelength of the light illuminating a sample because of all the glass optics[1]. Indeed optical microscopes do no allow to visualize the features smaller than $\lambda/2$ because the diffraction of light prevents the perfect convergence of beams, which results in a blur of the image around tiny objects.

The spatial resolution of a microscope is its capacity to distinguish between neighboring points in an image. It is quantified by to **the point spread function** (PSF)[2]. Two points closer than the Full Width at Half-Maximum (FWHM) in an picture will not be distinguishable since their images will cover one another. In the lateral direction the FWHM is given by the Rayleigh criterion :

$$R_{\text{Rayleigh}\,\Delta xy} = \frac{0.61\lambda}{NA} \tag{2.1}$$

[1] The Abbe resolution in the lateral directions is $\frac{\lambda}{2NA}$ where NA is the numerical aperture of the objective used, whereas the axial resolution according to Abbe is equal to $\frac{2\lambda}{NA^2}$.

[2] The PSF represents the 3D intensity distribution of the image of a point source.

and in the axial direction this criterion is:

$$R_{\text{Rayleigh}\,\Delta z} = \frac{2n\lambda}{(NA)^2} \tag{2.2}$$

where n is the reflective index of the media and NA the numerical aperture [70]. NA is linked to the media index n via $NA = n \sin\theta$, where θ is half-angle of the light cone formed within the objective. From equation 2.1 it can be deduced than the smaller the wavelength the higher the resolution, and the higher the numerical aperture the better the resolution. When using oil immersion objectives (which possess the higher NA, with NA ~ 1.4) and visible light (say $\lambda = 550\,\text{nm}$) the lateral resolution is typically around 200 nm, whereas the axial resolution can only reach 500 nm. This is quite problematic for biological studies as most cell components (say protein, lipids, nucleic acid) are smaller than these dimensions[1].

The confocal microscope: improving the axial resolution

Improvements in the lateral resolution were actioned when Marvin Minsk invented the confocal microscope in 1957. He discovered that placing pinholes in the light pathway could significantly improve the axial resolution. A **pinhole** placed in front of the dectector - in the plane conjugated to the focal plane - only allows fluorescence from the focus plane to be detected. Out-of-focus fluorescence (*i.e.* fluorescence from below and above planes) being blocked (rejected) by the pinhole borders (for a schematic of a confocal microscope and principle one can refer to the material and method section of Chapter 3). Nowadays the confocal microscope is commonly used in biology fluorescence studies. As one can see comparing the quality of images 2.5 a (DIC) and 2.5 b (Confocal), this process drastically improves the quality of the fluorescence images and prevents light pollution from unfocused planes (see comparison between 2.6 A (Confocal) and B (DIC)). This set-up also allows z-stacks acquisition and 3D reconstruction[2] but requires thin samples.

Super resolution techniques

Until recently it was a well-admitted fact that the diffraction limit could not be overcome. Nonetheless in 1992, Stefan Hell developed a new microscope, the 4P microscope, which allowed to improve the axial resolution from a factor 3 to 8. He added lens to concentrate the beam and create constructive/ destructive light interferences in order

[1] In addition, some biological component like DNA do not like UV.
[2] To improve the quality of images it is also possible to use deconvolution techniques.

to cut lateral light rings and then diminish the PSF [71]. Hardly anybody believed in his set-up, or in the possibility of breaking the diffraction limit. He kept working in this direction and invented two years later a new imaging technique called Stimulated Emission Depletion (STED) also based on destructive interferences of light (based on Non-linear Optics) and which paved the way to a new field of fluorescence research: **the super-resolution field**[1].

Since then, various techniques have been developed and allow to get resolution down to a few tens of nanometers [2] which makes fluorescent studies at the molecular scale possible. Since these techniques have not been used, we won't extend on them but one can find further information in the literature (*e.g.* [71]).

2.2 Two-photon fluorescence versus one photon fluorescence

2.2.1 Origins of non-linear optical effects

Non-linear optics (NLO) is a branch of optics that describes the behavior of light within media in which the dielectric polarization P is no longer proportional to the electric field E. The general expression for the non linear polarization for a material is given by :

$$\mathbf{P} = \varepsilon_0(\chi^{(1)}\mathbf{E} + \chi^{(2)}\mathbf{EE} + \chi^{(3)}\mathbf{EEE} + ...) \tag{2.3}$$

where $\chi^{(n)}$ is the n^{th} order of the nonlinear susceptibility tensor. This expression is always valid but generally, in linear optics, the first term is so much larger than the higher order terms that they are neglected and equation 2.3 becomes $P(\omega) = \varepsilon_0\chi^{(1)}(\omega)E(\omega)$. In this case $\chi(\omega)$ is the linear susceptibility of the medium. The dielectric constant is given by $\varepsilon(\omega) = 1 + \chi(\omega)$ and $n(\omega) = \sqrt{(\varepsilon(\omega))}$ is the refractive index.

However in certain media or conditions, higher order terms have to be taken into account; this is the case when the applied electric field, E, is very intense. This can be sensed having a look at the shape of the potential V(r) seen from the electron within an atom and given in figure 2.7 [3].

[1] One can an illustration of the potential of the STED microscope compared to the confocal microscopy in [71].

[2] say FRET, PALM, STORM and STIRF to name a few

[3] Since (by definition) the polarization, P, of a dielectric medium when an electromagnetic field is applied relies on the displacement of 'bound electron' within atoms

Around the minimum, r_{min}, the potential is parabolic, hence around this radius, the steadiest state is r_{min} and the electron is subject to an elastic restoring force. On the other hand, when the applied electric field is intense, the electron can explore the part of the potential behind the parabolic part; in this case, the electron is said to be subject to an **anharmonic potential**. This happens when the applied field is no longer negligible in front of the internal atomic field [72].

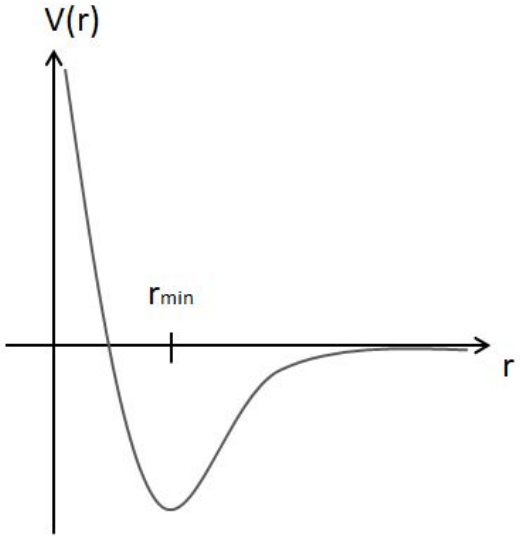

Figure 2.7: Potential from the electron point of view. Adapted from [72]

For one to get an idea of the required electric field for non-linear effects to happen, order of magnitude are given below. The atomic electric field the electron is subjected within an atom is given by $E_{\text{atom}} = \frac{e^2}{4\pi\varepsilon_0 a^2}$, where a is the radius of the atom, $a = 10^{-10}m$, *i.e.* $E_{\text{atom}} = 10^{11}V.m^{-1}$. This value is much higher than any electric field we can reach with classic laser source. However with a pulse laser, whose peak power can reach the megawatts, when applied to a 10 x 10 μm^2 spot the intensity can reach $\sim 10^{16}\ W.m^{-2}$, and since the intensity $I = \frac{\varepsilon_0 c}{2}|E_{\text{laser}}|^2$, $E_{\text{laser}} \sim 3.10^9 V.m^{-1}$, which is enough to generate non-linear responses. In fact, the domain of NLO started around the time of the first laser in the 1960s [72].

With the development of ultrafast lasers it has become possible to observe and take advantage of non-linear effects and many microscopy techniques are nowadays based on non-linear optical phenomena. $\chi^{(1)}$ provides information about the concentration

of a medium and higher terms ($\chi^{(2)}$ and $\chi^{(3)}$) can provide intrinsic information about the studied sample. For example in both Two-Photon Fluorescence (TPF) and Second Harmonic Generation (SHG), $\chi^{(2)}$ allows imaging of sample whereas in Third-Harmonic Generation (THG) and Coherent Anti-Stokes Raman Scattering (CARS) microscopy $\chi^{(3)}$ is involved in the imaging process [73]. These techniques are described in the following sections.

2.2.2 From one photon fluorescent toward two-photon fluorescence

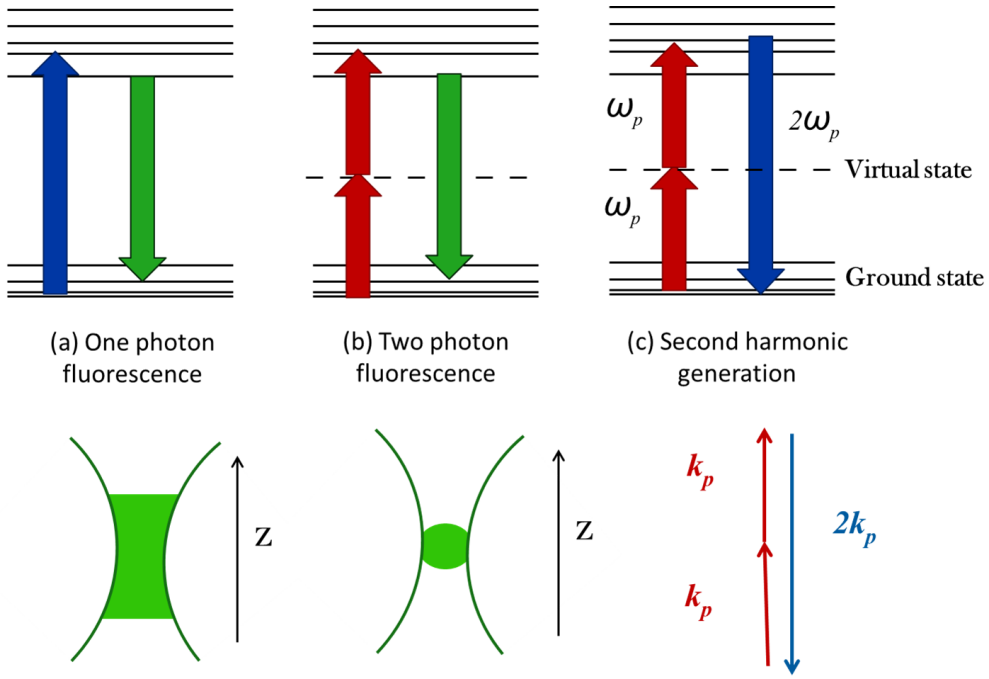

Figure 2.8: Fluorescence, Two Photons Fluorescence and Second Harmonic Generation

Multiphoton excitation (MPE) is the simplest form of **multiphoton microscopy (MPM)** and designs microscopy techniques where more than single photons are involved in electron excitation[1].

When electrons are excited by photons they can reach **quantified energy levels**. In MPE electrons absorb (quasi)-simultaneously several (*e.g.* 2 or 3) low energy photons ; the electron passing through **virtual states** before reaching a vibrational state; which is allowed by the Heinsenberg uncertainty principle: $\Delta E.\Delta t > \frac{\hbar}{2}$. These **low energy photons are usually near infrared or infrared (IR) photons** and excite the

[1] As a general rule the more photons involved in the process the weaker the observed effect

electrons to the same level as one high energy photon [74]. In the case of two-photon fluorescence (TPF), 2 photons are used to excite the electron as shown in figure 2.8 b.

Advantages of TPF

TPF light microscopy was invented by Denk and co-workers in 1990 [75] and it *'revolutionized three-dimensional in-vivo imaging of cells and tissues'*[76]. TPF (and more generally NLO techniques) are endowed with many advantages over one-photon fluorescence. First, since the photons used in MPM are near IR/ IR photons which are low-scattered compared to visible light, TPF allows **deeper penetration** of tissues. Second, since wavelength used for excitation are around half that of the emission, **the signal can be well separated from the excitation**. In addition, the use of near-IR source **diminishes both photobleaching and photodamages** in biological samples (biological sample absorb less in the near IR/ IR than at the blue / UV range). Third, since NLO requires more energy, these processes only happen at the focus point which **improves both lateral and axial resolutions** (see figure 2.8 a and b). TPF hence allows 3D sample section and reconstruction without need of pinhole as in confocal microscopy which minimizes light losses. Finally, the use of pulse lasers, necessary for TPF generation, is better withstood by biological sample since the average power will be smaller compared to continuous light sources [1] [76], [77]. TPF thus appears as a minimally invasive technique compared to one-photon fluorescence and has become an increasingly used technique to investigate living cells.

2.2.3 SHG versus TPF: Phase matching conditions

Second harmonic generation (SHG) was first demonstrated in 1961 by Franken et al., and as one can see in figure 2.8 c, the process looks similar to two-photon fluorescence. Nevertheless these two phenomena differ intrinsically: In TPF, 2 photons are used to excite an electron. The excited electron will thus 'undergo' non-radiative losses like in one-photon excitation before the relaxation. The emission of the resulting photon will happen in any direction in space and its phase will be arbitrary. In SHG on the other hand, two photons (of the same frequency) are **combined** into one photon of double frequency[2]; its phase and direction being determined. This process is a **parametric process** and thus occurs quasi-instantaneously compared to TPF ($\sim 10^{-14}$ s against $\sim 10^{-9}$ s) and non-radiative losses are not allowed [78]. To be possible, SHG needs to fulfill the **phase matching conditions**.

[1] Biological samples integrate the amount of light they receive which is quite handy when using processes based on NLO (less photodamages).

[2] SHG is sometime called frequency doubling.

There are **two conservation laws for photons in NLO**. First, the energy must be conserved, $\sum \hbar\omega_i = \hbar\omega_{signal}$, secondly the momentum must also be conserved $\sum \mathbf{k}_i = \mathbf{k}_{signal}$. 'Phase-matching' is reached when **both** of these relations are satisfied.

Combining TPF and SHG

Generally, multimodal facilities allow both TPF and SHG to be acquired simultaneously since they can be generated via the same source (infrared pulsed laser). The main differences between these techniques is that SHG requires **non-centro-symmetric** samples [1] which is not the case of TPF. Nevertheless SHG generates a higher signal at interfaces compared to TPF [79], [73]. Those techniques are thus complementary. In tissues, TPF is often used to image the elastin network while SHG is used to image the collagen distribution [80]. During the PhD, TPF was used to excite the auto-fluorescent protein, α-elastin, embedding GUVs (see Chapter 5).

Whether one considers one-photon fluorescence or MPE, adding a fluorescent marker is not always ideal. In our case we want to study the interaction between the spectrin and the lipid bilayer to investigate the effects of the protein on the membrane mechanical properties. One can feel that adding the probe might/will interfere with the interactions. Hence the need for label-free imaging techniques such as Raman based techniques which will be described in the next section.

2.3 Raman spectroscopy

2.3.1 The Raman Effect

The Raman effect was discovered by Sir C. V Raman in 1928 [81]. He brought light on the following phenomenon: when some monochromatic light arrives at a sample, a small fraction of the light is inelastically scattered and is therefore shifted in frequency. This effect can be demonstrated using both the classical or quantum descriptions.

In the classical model the light is seen as an electromagnetic wave whose oscillating electric field interacts with the molecules via its polarizability. **The polarizability of a molecule characterizes the ability of its electronic cloud to deform when an electric field is applied**. In this model molecules can be seen as masses (the atoms) linked by springs (the chemical bonds) as shown in fig 2.9 for an monoatomic

[1] Centro-symmetric sample will generate signal which will destructively interfere and annihilate itself.

chain. In the quantum model, the light is seen as a photon which hits the molecule and is inelastically scattered (see fig. 2.10 a).

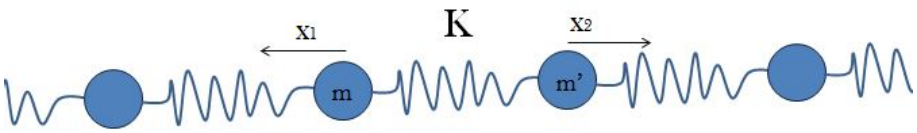

Figure 2.9: Atoms monoatomic chain.

Using the classic mechanics interpretation it is possible to establish this effect on a simplified model. If one considers a diatomic molecule (see fig. 2.9), as two masses (of respective m and m' atomic masses) linked by a spring of bending modulus K (representing the bond strenght), it is possible to calculate the total displacement of the molecule using Newton second's law [82]:

$$\mu.\frac{\mathrm{d}^2 q}{\mathrm{d}t^2} = -Kq \tag{2.4}$$

where μ is the reduced mass $\mu = \frac{mm'}{m+m'}$ and q is the total displacement $q = x_1 + x_2$. One recognizes a second order differential equation with no perturbative term which allows:

$$q = q_0 \cos(2\pi\nu_m t) \tag{2.5}$$

as a solution, where ν_m is the molecular vibrational frequency defined as:

$$\nu_m = \frac{1}{2\pi}\sqrt{\frac{K}{\mu.}} \tag{2.6}$$

As shown in equation 2.6, the molecule vibrates at a frequency depending on both the bond strength and the atom mass[1]. Each specific bond will therefore have a unique vibrational frequency referred to as its **vibrational signature**[2].

As introduced before, the polarizability, α, of a molecule is related to it displacement, q. This can be expressed as a Taylor series. In the small amplitude approximation, the

[1] This is an image, in reality as it has been mentioned earlier atoms can only get excited according to quantized vibrational states whose energy is given by $E_{vibration} = \left(j + \frac{1}{2}\right) h\nu_{vibration}$ where j is the vibrational quantum number (j= 1,2,3...) and $\nu_{vibration}$ the vibrational mode frequenty and h the Planck's constant. For simplification in our notation, $\nu_{vibration}$ is written ν_m.

[2] A same bond will be able to have more or less motion freedom due to the effect of the 2nd degree neighbouring atoms and might thus oscillates at different frequencies (*e.g.* CH_2 symmetric and assymetric vibrational modes)

first order expansion gives:

$$\alpha(t) = \alpha_0 + \frac{\partial \alpha}{\partial q} q(t) + \cdots \tag{2.7}$$

When an electromagnetic field is applied and interacts with the molecule, **it induces a dipole moment P, which will radiates at its oscillating frequency,** ν_m. The dipole moment is the product of the polarizability of the molecule with the electromagnetic field applied and can be given by:

$$P = \alpha(t) E_0 \cos(2\pi\nu_0 t) \tag{2.8}$$

Combining these two last equations gives:

$$P = \alpha_0 E_0 \cos(2\pi\nu_0 t) + q_0 \cos(2\pi\nu_m t) E_0 \cos(2\pi\nu_0 t) \frac{\partial \alpha}{\partial q} + \cdots \tag{2.9}$$

Using some trigonometric identity [1] this leads to:

$$P = \alpha_0 E_0 \cos(2\pi\nu_0 t) + q_0 E_0 [\cos(2\pi(\nu_0 - \nu_m)t) + \cos(2\pi(\nu_0 + \nu_m)t)] \frac{\partial \alpha}{\partial q} + \cdots \tag{2.10}$$

From the last equation, both elastic and inelastic interactions of the molecule with the incident light can be evidenced. The first term is the Rayleigh diffraction (elastic), this is the dominant effect where the frequency of the incident light remains unchanged. The second term on the other hand is the Raman effect and involves, as one can see on equation 2.10, both the sum and difference of the incident light frequency with the molecule vibrational frequency. The resulting light is shifted from those quantities and are called **Raman Stokes scattering** and **Raman Anti-Stokes scattering** for $(\nu_0 - \nu_m)$ and $(\nu_0 + \nu_m)$ respectively [82].

Figure 2.10 gives the Jablonski diagrams for the Raman processes compared to the Rayleigh scattering. As one can see, the Stokes energy $\hbar\omega_{\text{Stokes}}$ is smaller compared to the energy of the incident light: in this process there is creation of a phonon. The wavelength being inversely proportional to the energy, the Stokes light is red-shifted. On the opposite, the **Anti-Stokes light** $\omega_{\text{Anti-Stokes}}$ **is blue-shifted** [2] [83].

In nuclear physics, it is usual to quantify the efficiency of a process using the **cross section** σ. The cross section is defined as the probability of a light-particle interaction

[1] $\cos(a)\cos(b) = \frac{(\cos(a+b)+\cos(a-b))}{2}$

[2] In this case there is absorption of a phonon and thus the wavelength decreases as the energy becomes higher

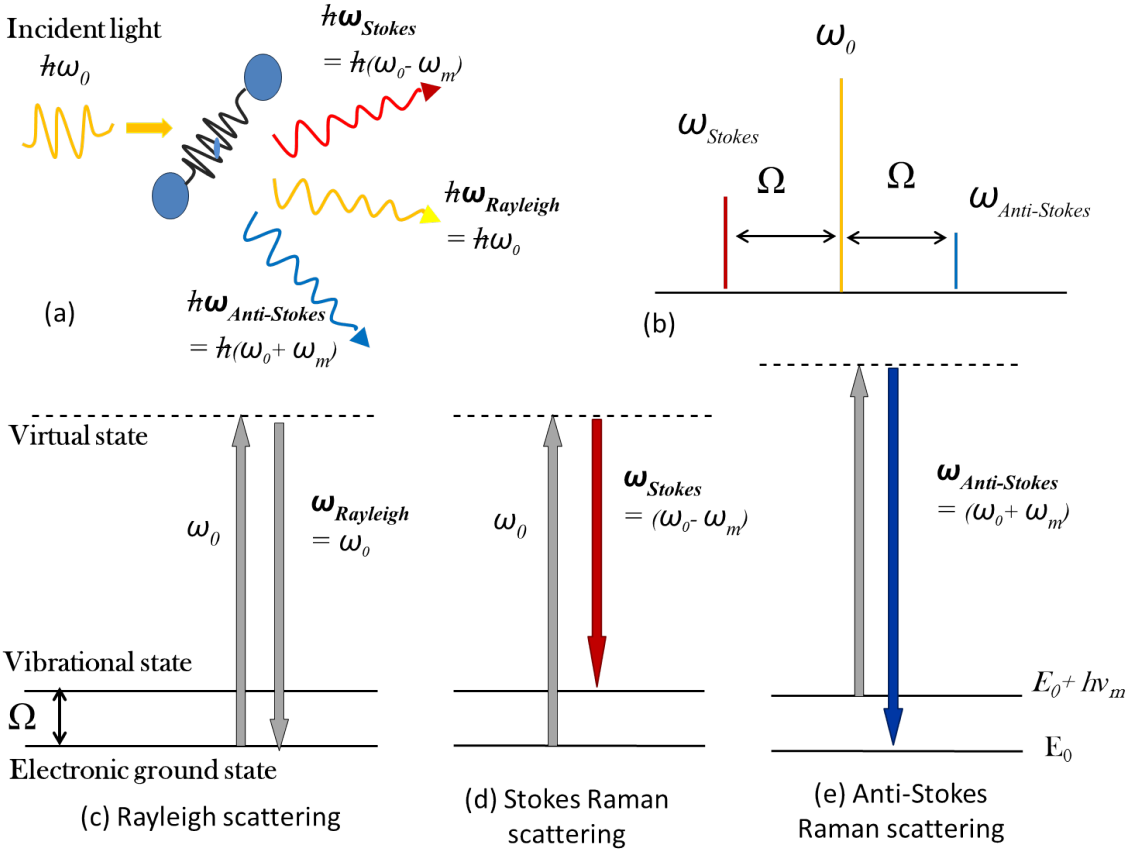

Figure 2.10: (a) Schematic diagram illustrating the Raman effect (classical and quantum models). When the incident light hits a sample, it is whether elastically scattered (*i.e.* there is no loss of energy and its wavelength remains unchanged (in yellow)) whether inelastically scattered. When the light is inelastically scattered its interacts with the sample and can whether give some energy to the system (Stokes case (in red)) whether take some energy from the system (Anti-Stokes case (in blue)).(b) Both Stokes and Anti-Stokes signatures are shifted of Ω from the incident wavelength, the Stokes process being more susceptible to happen than the Anti-Stokes one (see text), (c-e) Jablonski diagrams for: the Rayleigh scattering process (c), the Stokes Raman scattering process (d) and the Anti-Stokes Raman scattering process (e).

to occur within it surrounding particle space. Raman Stoke cross sections are typically around $10^{-33}\,\mathrm{cm}^2$ which is 10^6 to 10^8 times weaker than the Rayleigh scattering process. This means that only one photon over a million will inelastically interact with the sample. Raman thus produces a very weak signal: it is nonetheless possible to acquire data providing long acquisition times. Due to Boltzmann statistics, the Raman Stokes intensity is higher than the Anti-Stokes' one[1]and Raman spectroscopy hence focuses on the Stokes vibrational signatures.

[1]Stokes processes happen more often than Raman Anti-Stokes. Boltzmann statistics states that the population density in the vibrational levels decreases exponentially with the energy of the levels ($E = e^{-k_B T}$)

2.3.2 Raman spectroscopy

It is worth noticing that the Raman signal comes from the **molecular motion** of a chemical bond. A same chemical bond can therefore provide different Raman Shifts provided its molecular motion is different due to second order neighbouring atoms (*e.g.* C-C *Cys vs.* C-C *trans*, CH_2 or CH_3 symmetric *vs.* asymmetric CH_2 or CH_3). It is possible - using a laser, a grating and computer software - to record signature spectra. The laser is used as the monochromatic excitation source which will interact with the sample. The grating breaks the light into its spectral components. The photonic signal is then converted into an electric signal (*i.e.* photons are converted into electrons) and digitized so that the intensity data can be plotted with respect to the wavenumbers, k, since:

$$k = \frac{1}{\lambda_{\text{incident}}} - \frac{1}{\lambda_{\text{scattered}}} \text{cm}^{-1} \tag{2.11}$$

Raman spectroscopy can provide a wealth of information and it has become a standard technique to investigate biological sample compositions [84]. By collecting molecular vibrational signatures, one can determine which elements are present in living sample and tables of characteristical Raman shifts are available, both in the fingerprint (400-1200 cm^{-1}) and in the CH_2 (2800-3200 cm^{-1}) regions (see the literature).

Raman spectroscopy is especially useful in breast cancer research since such unhealty cells provide specific vibrational signatures [85]. Conformational changes of proteins (due for example to protein-lipid interactions) can also be investigated since secondary structure changes will induce modifications in the Raman profile (the peak distribution will be slightly different, the peaks intensity will vary). Finally, is also possible to follow dynamic processes (*e.g.* bio-chemical reactions) by recording Raman Shifts intensity ratios over time. One can find a typical Raman spectrum of a biological sample (lipid droplets) in the fingerprint and the CH_2 regions in chapter 5 and 6 respectively.

2.3.3 Raman Imaging

Raman spectroscopy is thus a very powerful tool since it provides chemical selectivity without the need of labeling. When combined with a 785 nm laser excitation source this techniques benefits, like TPF and SHG, of the low scattering (allowing deep penetration of tissue) and less photodamage to the sample. Nevertheless Raman spectroscopy meets the drawbacks of fluorescence interference and long integration times (due to the weakness of the signal) which make Raman mapping quasi-impossible. Another imaging techniques also based on Raman scattering (using the Anti-Stokes signature this time)

has been developed and widely used over the last decade: Coherent Anti-Stokes Raman Scattering microscopy. This technique is described in the following section.

2.4 Coherent-Anti Stokes Raman Scattering

2.4.1 CARS principle

Coherent Anti-Stokes Raman Scattering (CARS) was demonstrated by Maker and Terhune in 1965 when they worked for the Ford Motor Company (Maker and Terhune, 1965). CARS is a Four-Wave Mixing (FWM) process[1] in which three electromagnetic fields: the pump field, the Stoke field and the Probe field **interact together with the sample to produce a fourth field: the Anti-Stoke field**. The principle is described in the Jablonski diagram in figure 2.11. A pump photon of frequency ω_p excites an electron to a virtual state. A Stoke photon of frequency ω_s is stimulated emitted from this state as the same time as a probe photon of frequency ω_{pr} is absorbed to another virtual state. Then a photon of frequency $\omega_{as} = \omega_p - \omega_s + \omega_{pr}$ is emitted resulting from this interaction. This is the signal we are interested in. Maker and Terhune demonstrated that **the Anti-Stokes signal is resonantly enhanced when the beat frequency $\omega_p - \omega_s$ matches a Raman active vibrational mode** Ω. The CARS signal is improved of an order of 10^5 compared to spontaneous Raman scattering, thus because as shown in figure 2.11, all the transitions in the CARS process are driven interactions [86].

As will be further described in Chapter 5 (material and method section); to be able to get a CARS signal, pulsed lasers overlapping over space and time are required to to be able to get coherent interferences. As shown in fig. 2.11 other non-resonant four-wave mixing processes occur in the same time as the resonant CARS. These are due to electronic contributions and non-resonant-CARS provided by other molecules present in the sample. These contributions provide a non-linear background. As we will see in section 4.3, the non-linear background is the main disadvantage of CARS microscopy. Nevertheless CARS endows many advantages in addition to the one from MPE described in section 2.1: Since CARS induces signal from vibrational signal there is no photo-bleaching effect possible. There is no need for pinholes either. Finally since we record the Anti-stoke signal, the light is blue-shifted which prevents one photon fluorescence pollution. These benefits have made CARS become an increasingly used microscopy tool over the last decade [2], particularly since Zumbush *et al.* improved the

[1] Parametric non-linear-optical processes are often referred to as 'N-wave-mixing-processes' where N is the number of photons involved in the process including the emitted one.

[2] CARS microscopy was first demonstrated in 1982 by Duncan *et al.* [87]

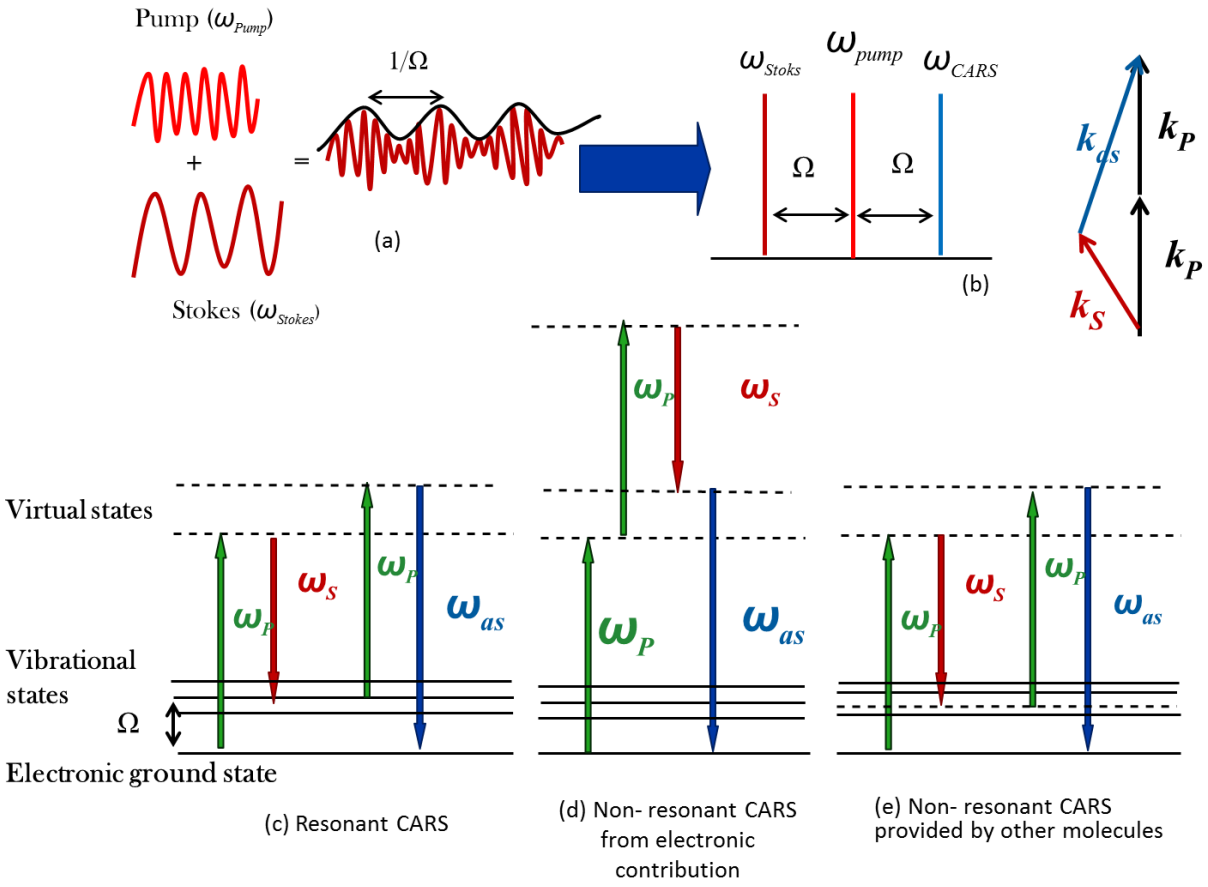

Figure 2.11: Energy diagrams for the CARS process: (a) Schematic of the pump and probe beam interacting together: the envelop of the interferences beating at the frequency $1/\Omega$, (b) Schematic of the phase matching conditions for the momentum, k_p is used for pump and probe as it is usually the same beam used for both, (c) (d) and (e) are Jablonski diagrams contributing to the CARS signal: (c) Resonant CARS, (d) and (e) non-resonant CARS due to electronic contribution and other molecule respectively.

illumination collimation with the use of infrared picosecond lasers [88].

CARS signal intensity

To be able to calculate the intensity of the signal generated by CARS, one needs to calculate the **fundamental equation of NLO**. To establish this relation one needs to use Maxwells'equations in matter reminded in equations 2.12, 2.13, 2.14 and 2.15[1]:

$$\nabla.\mathbf{D} = 0 \tag{2.12}$$

[1]The media are considered as non-magnetic with macroscopic charge and current density equal to zero (which is quasi-always the case in optics [89])

$$\nabla.\mathbf{B} = 0 \tag{2.13}$$

$$\nabla \wedge \mathbf{E} = -\frac{\partial \mathbf{B}}{\partial t} \tag{2.14}$$

$$\nabla \wedge \mathbf{B} = \frac{1}{c^2}\frac{\partial \mathbf{E}}{\partial t} + \frac{1}{\varepsilon_0 c^2}\frac{\partial \mathbf{P}}{\partial t} \tag{2.15}$$

where c is the speed of light. Applying the rotational operator to equation 2.14 and injecting it into equation 2.15 leads to:

$$\nabla \wedge \nabla \wedge \mathbf{E} = -\frac{1}{c^2}\frac{\partial^2 \mathbf{E}}{\partial^2 t} - \frac{1}{\varepsilon_0 c^2}\frac{\partial \mathbf{P}}{\partial t} \tag{2.16}$$

which simplifies using some vectorial identity [1] and the fact that $\nabla.\mathbf{E} = 0$, into:

$$\nabla^2 \mathbf{E} - \frac{1}{c^2}\frac{\partial^2 \mathbf{E}}{\partial^2 t} = \frac{1}{\varepsilon_0 c^2}\frac{\partial \mathbf{P}}{\partial t} \tag{2.17}$$

At this stage, it is usual to transpose the equation into the frequency mode using a Fourier decomposition. In the frequency mode, the polarisation can be decomposed into its linear part $P_L = \varepsilon_0 \chi^{(1)} E(\omega)$ and non-linear $P_{NL}(\omega)$ (provided the medium is isotropic and that $P_L(\omega)$ is purely real). The polarisation can thus be rewritten as:

$$P(\omega) = \varepsilon_0 \chi^{(1)} E(\omega) + P_{NL}(\omega) \tag{2.18}$$

Applying these two changes to equation 2.17, leads to the **Non-linear wave equation** [2]:

$$\nabla^2 E(\omega) + n^2(\omega)\frac{\omega^2}{c^2}E(\omega) = -\frac{\omega^2}{\varepsilon_0 c^2}P_{NL}(\omega) \tag{2.19}$$

where $n(\omega)$ is the refractive index, defined earlier, for the frequency ω. As one can see this last equation is similar to the usual equation wave for a media of index $n(\omega)$, except for the presence of a source term proportional to the polarisation of the non-linear media [89][3].

[1] $\nabla \wedge \nabla \wedge \mathbf{E} = \nabla(\nabla.\mathbf{E}) - \nabla^2\mathbf{E}$

[2] During the whole demonstration we considered $E(\omega) = E(z,t)\exp(i(kz - \omega t))$ and $P_NL(\omega) = P_NL(z,t)\exp(-(i\omega t))$

[3] In fact the product of the field amplitudes within $P_{NL}(\omega)$ transcribe the interaction between the laser beams within the non-linear media; their coupled coefficients are proportional to the non-linear susceptibilities of the media [89].

When studying a system where NLO is involved, one usually gets a **'coupled' system of equations** similar to equation 2.19. Unfortunately as new radiation fields are created, the number of unknowns is greater than the number of equations which makes the resolution of the system impossible. To solve the equation, one needs to use the **Slowly Varying Envelope Approximation** (SVEA)[1] (This approximation is valid since the impulsions propagate along the x axis (whose envelope only slowly varies over z and t)). From this, equation 2.19, can be simplified into:

$$\left(\frac{\partial}{\partial z}+\frac{n}{c}\frac{\partial}{\partial t}\right)E=\frac{i}{2\varepsilon_0}\frac{\omega}{nc}P_{NL}e^{-ikz} \tag{2.20}$$

And since in the case of CARS the third-order non-linear polarization is equal to [90], [91]:

$$\mathbf{P}^3(\omega_{as})=\varepsilon_0\chi^{(3)}(\omega_{as},\omega_p,-\omega_s)E_p^2(\omega_p)E_s^*(\omega_s) \tag{2.21}$$

when including this expression into equation 2.20, one can calculate the intensity of the CARS signal:

$$\left(\frac{\partial}{\partial z}+\frac{n}{c}\frac{\partial}{\partial t}\right)E_{as}(z,t)=\frac{i}{2\varepsilon_0}\frac{\omega_{as}}{nc}P^{(3)}e^{-ik_{as}z} \tag{2.22}$$

Decomposing the spatial and time derivatives and injecting equation 2.21 into equation 2.22 gives us:

$$\frac{\partial}{\partial z}E_{as}=i\frac{\omega_{as}}{nc}\chi^{(3)}E_p^2E_s^*e^{-i\Delta kz} \tag{2.23}$$

where $\Delta k=k_{as}-(2k_p-k_s)$ is the wavevector relation involved in the CARS process. To get the value of the signal at the distance $z=D$ in the sample, one then needs to integrate this last equation 2.23 over the optical axe, z. Using the bounding limit $E_{as}(z=0)=0$, one finds

$$E_{as}=i\frac{\omega_{as}}{nc}\chi^{(3)}E_p^2E_s^*\frac{e^{-i\Delta kz}-1}{i\Delta k} \tag{2.24}$$

and as the intensity I_{as} is proportional to the square of the Anti-Stoke field, $I_{as}\propto|E_{as}|^2$ the intensity of the CARS signal is eventually given by the expression:

$$I_{CARS}(D)\propto\left(\frac{\omega_{as}}{nc}\right)^2|\chi^{(3)}|^2D^2I_p^2I_s\,\mathrm{sinc}^2(\frac{\Delta kD}{2}) \tag{2.25}$$

[1] In this approximation one supposes that the field envelope remains the same over the wavelength scale, which makes the second derivative over space negligible over the first derivatives.

Like in SHG, to get the largest signal the phase matching condition must be fulfilled since the *sinc* function has the highest value at zero. As in SHG, within a distance, d, smaller than the exciting wavelength the signal is non-zero even if Δk differs from zero, whereas at distance, $D >> \lambda$ the signal annihilates when the phase matching conditions are not fulfilled.

It is possible to acquire CARS signal both in the Epi-direction and/or in the forward direction. It has been demonstrated that CARS signal in the Epi-direction (Epi-CARS) is higher for small features (typically $\sim$ or $< \lambda$) and interfaces whereas the CARS signal in the forward-direction (Forward-CARS) usually provides a higher signal. In Epi-CARS the non-resonant background (see section below) is also significantly reduced compared to Foward-CARS [92].

2.4.2 CARS spectra

Like for the Raman process, it is possible to record CARS spectra when tuning the beating frequency $(\omega_p - \omega_s)$ which can be performed using an optical parametric oscillator (OPO) whose function is explained in Material and method of chapter 5. To demonstrate and understand how the CARS spectra differs from the spontaneous Raman one, one needs to start from the third order polarization (and thus third order susceptibility, $\chi^{(3)}$).

In the CARS process, both pump and stoke electric field drive the molecular bonds within the molecules to **coherently oscillate** which means that all the molecular bonds oscillate in phase. The collective response produces a strong Anti-Stoke polarization field when the beating frequency matches a Raman 'band'. The radiations can hence be seen as emitted from a population of harmonic oscillator whose classic motion equation still comes from Newton 2nd law and is [82]:

$$\ddot{x} + 2\Gamma_R \dot{x} + \Omega_R x = \frac{F_{CARS}(x,t)}{m} \tag{2.26}$$

where x is the displacement from the resting position, Ω_R the resonant oscillating frequency equal to (as in the Raman process) $\Omega_R = \sqrt{(\frac{k}{m})}$, Γ_R the damping coefficient, F_{CARS} the force exerted by the incident light depending of the electric field applied E_p and E_s and m the equivalent mass.

Since the applied fields are monochromatic planes waves, they can be expressed as $E(\omega) = E(z,t)e^{i(kz-\omega t)}$ and the harmonic function

$x(t) = X(z)e^{i(kz-\omega t)} + c.c$[1] is thus solution of equation 2.26 which becomes in the frequency domain:

$$[-\omega_R^2 + i\omega 2\Gamma_R + \Omega_R^2]X(Z) = \frac{F_{CARS}(\omega)}{m} \tag{2.27}$$

and then considering that in the case of the CARS process F_{CARS} depends of both the applied electric fields E_p and E_s and the induced charge of the bound (polarizability) and is given by [78]:

$$F_{CARS}(x,\omega) = \frac{\varepsilon_0}{2}\left(\frac{\partial\alpha}{\partial x}\right)E_pE_s^* + c.c \tag{2.28}$$

then:

$$X(Z) = \frac{\varepsilon_0}{2m}\frac{(\frac{\partial\alpha}{\partial x})E_pE_s^*}{[\Omega_R^2 - \omega_R^2 + 2i\omega\Gamma_R]} \tag{2.29}$$

To now get the expression of the third order susceptibility, one needs to include into equation 2.29, the non-linear polarization induced by the Anti-Stoke field, defined in equation 2.21, $P_{NL} = \varepsilon_0\chi^{(3)}E_p^2E_s^*$ [2] which leads to:

$$P_{NL} = \varepsilon_0\chi^{(3)}E_p^2E_s^* = \frac{\varepsilon_0^2\left(\frac{\partial\alpha}{\partial x}\right)^2E_p^2E_s^*}{2m\left[\Omega_R^2 - \omega_R^2 + 2i\omega\Gamma_R\right]} \tag{2.30}$$

and the third order susceptibility is finally given by:

$$\chi^{(3)} = \frac{\varepsilon_0\left(\frac{\partial\alpha}{\partial x}\right)^2}{2m\left[\Omega_R^2 - \omega_R^2 + 2i\omega\Gamma_R\right]} \tag{2.31}$$

If we now introduce the normalized strength of the vibrational mode R, A_R, as $A_R = \frac{\varepsilon_0}{2m\Gamma_R\Omega_R}\left(\frac{\partial\alpha}{\partial x}\right)^2$ equation 2.31 becomes:

$$\chi^{(3)} = \frac{A_R\Gamma_R\Omega_R}{[\Omega_R^2 - \omega_R^2 + 2i\omega\Gamma_R]} \tag{2.32}$$

where ω is the beating frequency, $\omega = (\omega_p - \omega_s)$.

When ω happens to be close to a Raman resonant frequency Ω_R, $\Omega_R^2 - \omega_R^2 + 2i\omega\Gamma_R = (\Omega_R + \omega)(\Omega_R - \omega) + 2i\Gamma_R\omega = 2\Omega_R(\Omega_R - \Omega + i\Gamma_R)$ and the resonant third order suscep-

[1] c.c stands for complex conjugate

[2] which is also equal to $P_{NL} = N\mu_{\text{Raman induced}}$ where as seen before $\mu_{\text{Raman induced}} = \varepsilon_0\left(\frac{\partial\alpha_{ij}}{\partial x}\right)x(t)E_j$ with j the different fields components and i...

tibility near a resonant frequency becomes:

$$\chi_R^{(3)} = \frac{A_R \Gamma_R}{\Omega_R - \omega + i\Gamma_R} \tag{2.33}$$

$\Omega_R - \omega$ is referred to as the detuning and usually written Δ.

One recognizes a **Lorentzian function** where Γ_R is the half-bandwidth at the half-maximum of the Raman peak. **The third order susceptibility can thus be divided into it's resonant and non-resonant part** [91]:

$$\chi^{(3)} = \chi_R^{(3)} + \chi_{NR}^{(3)} \tag{2.34}$$

the resonant part being induced by the Raman response of the molecules present in the sample whereas the non-resonant part is independent of the excitation wavelengths. This non-resonant part is purely real and responsible for the **non-resonant background**.

It is worth noticing that $\chi^{(3)}$ is a tensor actually consisting in 81 terms, from whose only 21 are non-zero (because of symmetries) 4 of them contributing to the CARS signal, the others being electronic non-resonant contributions.

When taking a CARS spectra, one must consider both the amplitude and the phase spectra - the amplitude is the maximum displacement X_{max} and the phase is the phase difference between the applied electric fields and the response of the molecules[1].

The CARS signal being proportional to the square modulus of $\chi^{(3)}$, one finds:

$$I_{CARS} \propto |\chi^{(3)}|^2 = |\chi_R^{(3)}|^2 + |\chi_{NR}^{(3)}|^2 + 2\chi_{NR}^{(3)}\mathbf{Re}[\chi_R^{(3)}] \tag{2.35}$$

and as shown in figure 2.12, the CARS spectum is the combination of the resonant component $|\chi_R^{(3)}|^2$, the non-resonant $|\chi_{NR}^{(3)}|^2$ component and the real part of a mixing term $2\chi_{NR}^{(3)}\mathbf{Re}[\chi_R^{(3)}]$. This is the mixing term which induces some **distortion of the Raman line shape** making quantitative analysis difficult [91], [94].

2.4.3 'Improved' CARS techniques

Various techniques have been implemented to try to suppress the non-linear background (in addition of Epi-detection). These are polarisation-sensitive techniques (P-

[1] It is a good analogy to sense the phase while thinking of a pendulum as illustrated in figure 2.12-b.

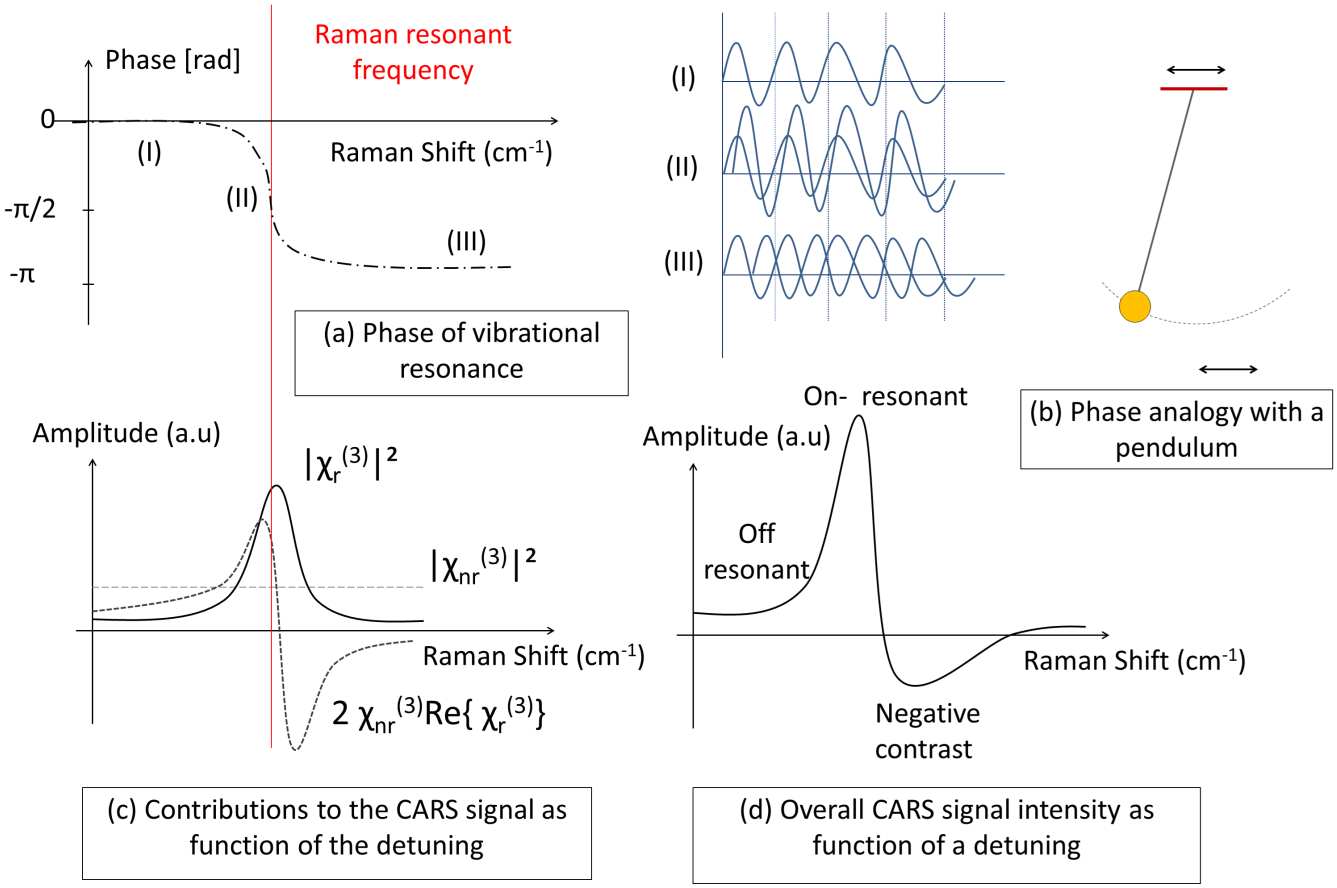

Figure 2.12: Amplitude and phase diagrams for CARS. (a) Schematic diagram giving the phase of the vibrational resonance with respect to the Raman shift. (b) The phase difference between the applied electric field and the phase of the produced CARS field can be understand via a simple analogy of an oscillating pendulum whose base (in red) is moving. When the base is moved slowly the phase is the same (textiti.e. there is no phase shift) (case (I)). When the base is moved faster a phase shift appears (case (II)). When the base is moved very quickly the pendulum phase becomes 'opposite' to the base phase (*i.e.* there π phase shift) (case (III)). Adapted from [93]. (c) Schematic diagram giving the contribution to the CARS signal of the resonant part ($|\chi_R^{(3)}|^2$), of the non-resonant part ($|\chi_{NR}^{(3)}|^2$) and of the mixing term ($2\chi_{NR}^{(3)}\mathbf{Re}[\chi_R^{(3)}]$) as a function of the detuning (d) Schematic diagram giving the overall CARS signal intensity as a function of the detuning. Adapted from [82]

.

CARS, D-CARS), time-resolved CARS (T-CARS) or phase sensitive technique (H-CARS). Since these techniques have not been used, we will only name them. One can find further informations in [95], [96] and [97] [1].

[1] There exists another techniques allowing to record CARS spectra as the same time as the imaging, using femto-pico excitation (multiplex-CARS (M-CARS)) One can find additional information in [98] and [99]

2.5 Stimulated Raman Scattering

The last imaging technique, based on NLO, used during the PhD is the Stimulated Raman Scattering (SRS) microscopy. This process was discovered in 1962 by Woodbury and Ng (Woodbury and Ng, 1962)[1]. SRS is another coherent Raman process which requires beams to be overlapped over space and time. In this process, two beams: a Pump beam and a Stoke beam interact together with the sample when the frequency difference matches a Raman resonance ($\Omega = \omega_{pump} - \omega_{Stokes}$). Contrary to the CARS process, the signal does not consist in the detection of a new wavelength (*e.g.* Anti-stoke field) but in a **small change in the intensity of one the incident beams** (pump or Stoke). When SRS is involved one can decide to do Stimulated Raman Gain (SRG) and study the intensity changes in the Stoke beam or to do Stimulated Raman Loss (SRL) and study the intensity changes in the pump beam. The spectra profile of this process are illustrated in figure 2.13 b.

For one to get a clearer idea of the process a Jablonski diagram of both CARS and SRS processes have been placed next to each other in figure 2.14. In SRS, a pump photon excites an electron to a virtual state, the pump photon of frequency ω_{pump} is thus annihilated, meanwhile a Stokes photon of frequency ω_{Stokes} is stimulated emitted by a Stoke photon belonging to an excited vibrational state (of frequency Ω); there is thus creation of a ω_{Stokes} photon. Light-matter interaction happening during the SRS process are illustrated in figure 2.14 a.

2.5.1 SRS signal

Experimentally SRS is performed using pico-second pulsed train of IR beams. One of the beam is modulated as shown in figure 2.13 a. **The signal is detected as the intensity change in the non-modulated beam**. As the generated signal is very weak compared to the excitation beams, a lock-in amplifier is necessary to detect it and allows vibrational signature imaging.

If we consider the pump and stokes beams as monochromatic plan wave (collinearly propagating along the axis z). The signal intensity of SRL can be calculated as demonstrated in [100]. The sample is an isotropic media of thickness L (with Raman-active modes). When the difference of frequency of the incident beams $\Delta\omega = \omega_p - \omega_s$, maches a Raman molecular vibration of frequency Ω. The Raman signal is amplificated due to driven characteristics of the transitions (*i.e.* stimulated excitation and emission).

[1] It was also observed in 1964 by Jones and Stoicheff.

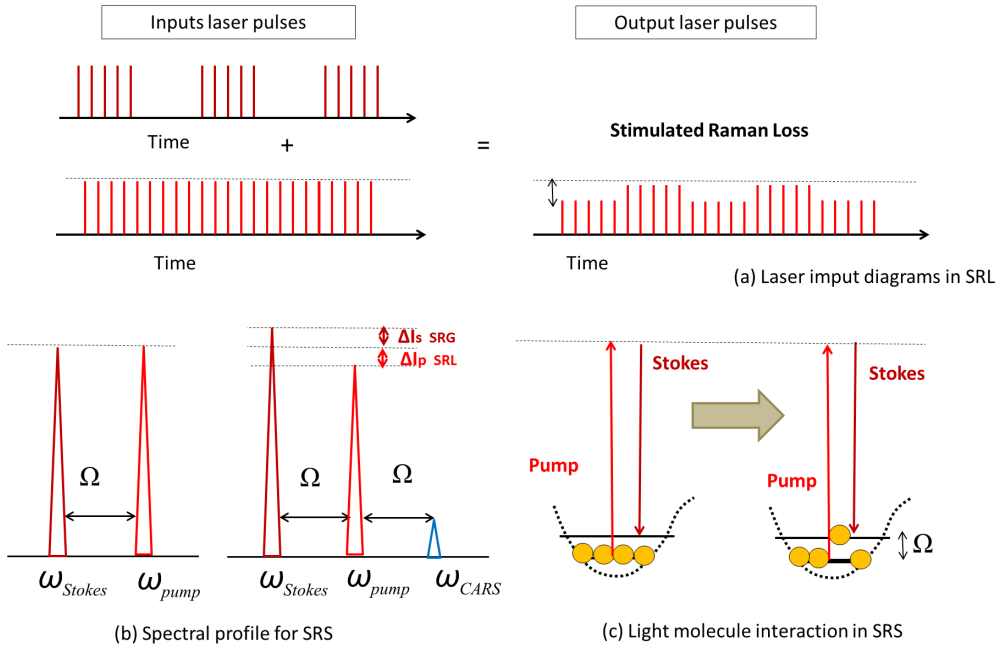

Figure 2.13: Energy diagrams for the SRS process: (a) Schematcis of the pump and probe beams interacting together. The probe beam is modulated and the SRS signal (Stimulated Raman Loss in this case) is detected in the pump beam, (b) schematic diagram giving the spectral profiles for SRG (Stimulated Raman Gain) and Stimulated Raman Loss (SRL), (c) schematic diagram illustrating the light-matter interaction happening during the SRS process. Adapted from [100].

The field generated in the sample (signal), E_{signal} is generated at the same frequency as the imput field $E_p(\omega_p, L)$. The total intensity of the signal hitting the detector, $I_p(\omega_p, L)$ is proportional to the square of the addition of the two electric field such as: $I_p(\omega_p, L) \propto |E_p(\omega_p) + E_{\text{signal}}(\omega_p, L)|^2$ [100]. As said above, the SRL signal is detected as a change in the pump beam intensity and is given by[1]:

$$\Delta I_p(\omega_p) = I_p(\omega_p L) - I_p(\omega_p 0) \tag{2.36}$$

$$\Delta I_p(\omega_p) = -\frac{3\omega_p \mu_0}{n_p n_s \epsilon_0} Im[\chi_{1111}(-\omega_p \omega_s \omega_p - \omega_s)] I_p(\omega_p 0) Is(\omega_s L) \tag{2.37}$$

where n_p is the refractive index of the medium at the pump frequency ω_p, n_s the refractive index of the medium at the stokes frequency ω_s, I_s the intensity of the Stokes beam and I_p the intensity of the pump beam.

[1] provided that $E_{\text{signal}}(\omega_p, L) << E_p(\omega_p)$

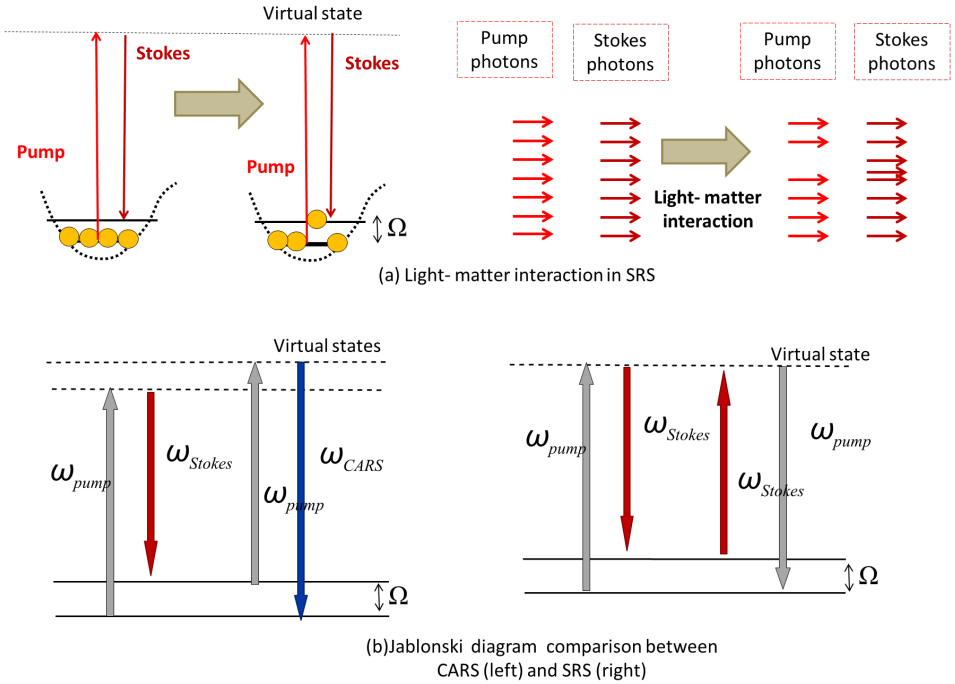

Figure 2.14: CARS process versus SRS process. (a) Schematic diagram illustrating the light matter interaction happening during the SRS process, (b) Jablonski diagrams of the CARS process (left) and of the SRS process (right). In CARS there is creation of a new electric field, the Anti-Stokes field which provides the signal, whereas in SRS no new electric field is created and the signal derives from intensity changes in one of the incident beams. Adapted from [100].

As one can see from equation 2.37 the pump intensity is attenuated (since it's imaginary part is greater (or equal to) zero) [1]. This technique is also background-free since the signal is insensitive to the real non-resonant background. In addition, the signal scales linearly with both beam power intensities and is thus directly proportional to the concentration of probed bonds.

2.5.2 SRS versus CARS

SRS versus CARS

To summarize, there are three main advantages of using SRS imaging compared to CARS. The most obvious one is the absence of background signal (background-free). Related to this lack of background is the non-distortion of the signal line (which is a problem in CARS spectra acquistion), the SRS spectrum being perfectly similar to spontaneous Raman (as they both obey the same selection rules). Eventually, the fact

[1] To obtain the expression of the signal collected in SRG one needs to subscrib p and s in equation 2.37 and add a '−' sign in the SRL imaginary component.

that SRS signal scales linearly with the bond concentration (compared to CARS which is quadratically dependent) can be taken advantage of, for quantitative measurement, or detection of low concentration elements (see Chapter 5). (Techniques can be complementary).

Use of NLO in the thesis work

During the PhD work, both techniques have been used.

- CARS was used to image lipids in MLVs and combined with TPF for imaging both protein and lipid distributions simultaneously (see Chapter 5).
- SRS proved to be more efficient than CARS to image GUVs and was used to image lipid segregation in multi-component GUVs (see Chapter 5).
- Eventually SRS was used to acquire hyperspectral images of both GUVs and cells and combined to micropipette aspiration (see Chapter 6).

The next Chapter focuses on the spectrin protein, spectrin-lipid interaction are studied using fluorescent probes.

Chapter 3

Spectrin-lipid interactions: a fluorescence study

The beginning of this chapter is dedicated to giving a background of up-to-date knowledge about the interaction of spectrin with membrane lipids. Attention will be given in the material and method section to describing the preparation of spectrin, with particular attention to the purification step. Fluorescent results obtained from experiments involving lipid of different mixtures and FITC-tagged spectrin will be presented. The effect of spectrin on uniform and domain separated vesicles will be discussed. In the last section, using externalized PS red blood cells, it will be demontrasted that spectrin interacts preferentially with PS.

3.1 Spectrin-lipid interactions: literature review, up-to-date knowledge

3.1.1 Spectrin mechanisms

The 'unusual' properties of the spectrin protein are summarized in an article by An and colleagues: *"It is difficult to envisage how relatively sparse protein filaments, coupled to the bilayer through transmembrane proteins some 70 nm apart, can impose grossly transformed mechanical properties on a membrane bilayer, which by itself possesses essentially no elasticity and is so unstable that it breaks up spontaneously into small vesicles when spectrin is dissociated"* [101].

Many articles describe the complex of proteins which binds spectrin to the membrane bilayer, but little is known about the detailed mechanical role each element plays. Experiments have been performed on the spectrin protein alone to establish its

own mechanical properties. [102] performed experiments on the protein to understand where the RBC's membrane ability to deform originates. They studied by electron micrographs and computational calculations (Fourier analysis), partially extended spectrin, where the two subunits were twisted around each other, and showed that they are coiled in a helix whose overall diameter may change. Their idea was that the $\alpha\beta$ spectrin helix would extend and go back to the initial position, thanks to **mechanical forces that each of the two helix branches exerts on each other** when subjected to mechanical stress. They found that spectrin protein size varies depending on the ionic strength of the medium and demonstrated periodic structure within the $\alpha\beta$ spectrin helix. Based on other calorimetric studies [103] they raised the idea that deformability is modified by spectrin/actin interaction: **thermal fluctuations at room temperature induce changes in spectrin length** which are reduced thanks to the attachment to actin proteins.

Pathogenic mutations in the spectrin have been investigated to see how self-association of α and β subunits are modified with mutations [104]. Using molecular modeling[1] they determinated the 3D structure of the protein. By adding mutations in the DNA sequences they investigated the changes in the 3D structure induced by those mutations. They validated their model by comparisons with drosophilia spectrin. Over the range of point mutations on the α and β subunits studied, **some induced 3D structures were close to or correlating with clinical abnormalities**. One of the conclusions they drew for explaining that some mutations are not seen in nature was that : *'the complete loss of spectrin self-association may be incompatible with life'* [104]. One can find information about illnesses linked to the other cytoskeletal membrane proteins in [61] and [105].

3.1.2 Spectrin-lipid interactions: indirect studies

Many indirect methods have demonstrated that spectrin interacts with some lipid species (PE, PS, PG, PI) and preferentially with negatively charged lipids (PS). The first methods include gel assay, pressure or phase transition changes (see below). Later fluorescence quenching was used to determine domains, especially hydrophobic domains in the spectrin protein which interact with lipids. Experiments using negatively stained spectrin have also been performed but it is electron micrograph images which gave the final quasi-direct imaging proof of such interactions (see the next session).

[1] This method seeks for minimum of energy of the protein taking into account all the chain interactions.

Early studies on spectrin revealed that this protein was able to bind to lipid membrane involving complex mechanisms. Bennett et al. (1977) used [32P] spectrin and vesicles to try to **elucidate whether spectrin without actin may interact with the membrane**. For determining if spectrin would bind to any kind of lipid or preferentially to some lipid species, they used *inside out vesicles* and *right side ones* (*i.e.* red cell ghosts). They distinguished the spectrin-lipid complexes from free lipids and free spectrin thanks to sucrose gradient sedimentation experiments. They established that spectrin only binds to inside out vesicles[1]. They then studied the effects of ionic strength (using KCl solutions in different concentrations) and pH. They found that **low ionic strength favored dissociation of spectrin-lipid complexes whereas low pH enhanced the binding** [106].

In the late 70s, Anderson and colleagues (1979) tried to elucidate whether phosphorylation of the protein was responsible for the erythrocyte shape, but were unable to find any evidence for this [107].

Studies have been carried out on lipid layers and have indirectly shown that **spectrin is likely to interact with lipids thanks to hydrophobic sites**. Mombers and colleagues (1980) studied effects of spectrin on the lateral pressure of monolayer film of phosphaticholine (PC) and phosphatidylserine (PS). They demonstrated that at lower than physiological pressure spectrin inserted into the monolayer. They recorded the rate of penetration of spectrin into lipid membrane for different lipids species and at different pH and found that **spectrin attaches preferentially to PS monolayer when pH = 5.5** which is near the isoelectric point of spectrin. They verified that raising the pH inhibits protein-lipid association and that below the isoelectric point lowering the pH did not favor spectrin penetration. This last observation raised the question of the nature of the interaction which implied that below the isoelectric point, **the interaction of the lipids with positively charged spectrin is purely electrostatic without penetration of hydrophobic residues into the interface** [108].

Changes in packing density of lipids, as well as the effect of divalent cations and spectrin denaturation have also been studied. They discovered that the results depended on the lipid species studied: spectrin protected phosphatidylglycerol (PG) vesicles to be *'attacked'* by calcium cations whereas spectrin was released from PS vesicles. Moreover PS-calcium phase was formed when calcium was added to PS vesicles solution [108].

[1] This is not that suprising since in red blood cells the spectrin network binds to the inner part of the phospholipid bilayer.

Hence the importance of studying different lipid species (saturated/unsaturated; switterionic or positively/negatively charged) to fully understand how the spectrin protein works, acts and interacts.

Maksymiw et al. (1987) studied the interaction of the spectrin dimer with model membranes of DMPS. **They elaborated a new model in which spectrin binds to negatively charged lipids thanks to Coulomb forces instead of binding to hydrophobic sites**. They collected information about interactions of spectrin with vesicles via **indirect thermodynamic methods**: densitometric evaluation of phase transitions and phase boundaries[1]. Using free energy data they investigated the shifts in the phase transition temperatures of pure lipid bilayer and, the modifications of the phase boundaries of lipid mixtures when spectrin was added (*i.e.* shifts of the liquidus and solidus lines). The phase transition perturbation was detected by plotting the change in molecular volume with respect to the temperature. As mentioned in Chapter 1, if proteins attach to vesicles they are likely to affect the chain melting transition temperature T_m. These observations were confirmed thanks to phase contrast micrographs of giant vesicles since the images of DMPS vesicles before and after addition of spectrin differ substantially. They showed that spectrin when incubated at 39°C was either able to attach to the vesicles and to **perforate the vesicles**. Spectrin would also make vesicle aggregate and induce changes in their shapes (poligonization *i.e.* cristallin state). From those experiments the conclusion that spectrin induces changes in membrane permeability could be drawn. This group also arised the idea that spectrin would act as an '*entropy spring*' [109].

Mac Donald discusses in his paper [110] the dissociation constant value of spectrin-lipid complex at different temperatures and in different media to try to quantify the strength of the interaction.

Sikorski and colleagues (1987) performed fluorescence experiments and demonstrated that **phospholipid aggregates to spectrin and stabilizes the protein**. They studied the effects of both the temperature (thermal denaturation) and the ionic strength. Their **fluorescence experiment was based on the intrinsic fluorescence of spectrin due to tryptophan residue**[2]. According to them, **the observed quenching**

[1] They also performed, in addition to densitometry experiments, film balance experiments as well as microfluorescence experiments [109].

[2] The experiment was as follow: they used sepharose column to purified spectrin and added phospholipid suspension of PE, PS and PC. They then determinate the percentage of spectrin fluorescence quenched due to addition of lipids thanks to a spectrofluorimeter.

may be due to conformational change in certain part of the protein occurring because of the binding to phospholipids [111]. Studying the effect of pH and ionic strength on the fluorescence they concluded that the interaction between spectrin and the lipid bilayer was a **'mixed' type of hydrophilic-hydrophobic interaction'**. Other studies (Isenberg et al., 1992) demonstrated that ionic strength also induces changes in the spectrin length, low ionic strength inducing expansion of the protein which might affect the number of binding sites on the molecule. Experiments varying the temperature showed that fluorescent quenching changes occur at high temperatures revealing the 'stabilizing' effect of phospholipid suspensions on the spectrin molecule. This group also point out the importance of the lipid species studied as they found results different from other groups, their own results focusing on PE and PS lipids.

A few years later other fluorescent experiments were performed using brominated fatty acid[1] and conclusions have been drawn that **spectrin may partially penetrate the lipid bilayer** [112] confirming previous experiments explained earlier [109]. They also found that **spectrin is likely to affect the membrane fluidity** as determined by changes in the spin-labelling. They confirmed these conclusions using a fluorescent probe used to assess membrane fluidity[2]. Other groups also tried to evaluate the effect of spectrin on membrane fluidity [113]. These studies used liposomes of two lipid species containing cholesterol in different amounts (since cholesterol is known to increase or decrease the membrane fluidity depending on the state the lipid layer/bilayer (see Chapter 1)). They also tested both erythrocyte and brain spectrin and evaluated their interaction with monolayer recording changes in the surface pressure. Their main result was that **the increase of the cholesterol concentration in the lipid layers made it easier for spectrin to penetrate into the membrane layers**. This group was the first to try to investigate whether spectrin was involved in lipid rafts using what they call *'raft-like monolayers'*, but they did not find any strong evidence for this.

Studies on spectrin indirectly interacting with lipid membrane were reviewed by Grzybek and colleagues [114]. They point out that, *'even though spectrin-lipid interactions clearly exist, disagreements persist regarding the nature of those interactions'*, hence the need to do further research in this area. It is important to determine whether or not spectrin is involved in lipid raft and lipid species distribution within the membrane. This is still unclear.

[1] This is usually used to reveal hydrophobic sites.
[2] Those probes are nonetheless difficult to interpret.

Cohen et al. (1986) made striking experiments using electron migrography of low angle rotary shadowed experiments concluding that **spectrin in both forms, dimer and tetramer, interact with PS vesicles**. They demonstrated that spectrin binds to vesicles at the tail end region and different sites of the protein. They did the same experiment[1] with other proteins of the complex - actin, ankyrin, albumin, protein 4.1 - but **did not find any interactions between PS liposomes and actin, ankyrin or albumin**. Their analysis showed that both dimer and tetramer were able to bind to liposomes (diameter 30 nm) in different ways: several spectrin dimer/tetramers can bind to one vesicle and one spectrin dimer/tetramer can bind to two liposomes (at both ends of the protein) suggesting the **presence of multiple binding sites to PS throughout the spectrin molecule length** [115]. With high concentrations of spectrin added to vesicles, they could also observe *'crosslinked complexes'* and sometimes the beginning of a spectrin meshwork connecting between liposomes (see fig. 3.1)

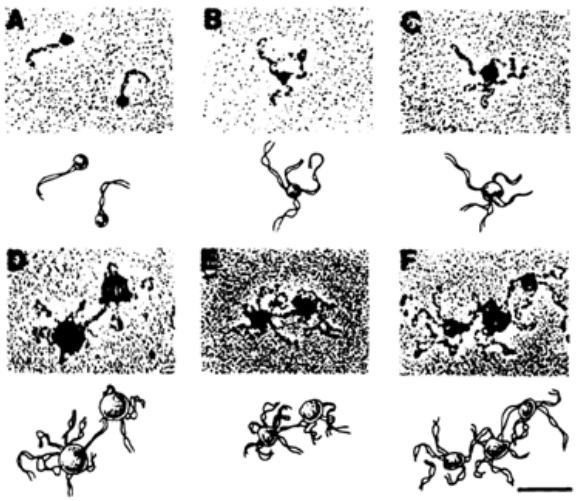

Figure 3.1: Electron micrograph of low angle rotatory shadowed platinium carbon replicas of spectrin dimer on phosphatidylserine vesicles. Spectrin dimers and tetramers interact with LUVs containing PS (A-C). Spectrin dimers/ tetramers binding to several LUVs resulting in the formation of a cross-linked network (D-E). Scale bar is 100 nm. From [115].

This experiment was the very first one giving quasi-direct image evidence about direct spectrin-membrane interactions.

3.1.3 Physico-chemical structure of the spectrin tetramer

An and colleagues (2004) managed to precisely identify which parts of the spectrin bind to negatively charged lipid membrane (PS). They hypothesize that spectrin-lipid

[1] *i.e.* same experimental conditions.

interactions play a role in the stability of the membrane and considered how it might affect their mechanical properties. They worked by 'dichotomy': first they fragmented α and β-subunits into 4 segments, segmenting the molecule thanks to what is called spectrin repeats[1]. They kept the fragments which appeared to be able to bind to PS and fragmented those pieces into narrower fragments to isolate spectrin fragments responsible for the binding[2]. To verify the specifity of binding lipids they also performed experiments with mixed PS/PC liposomes where spectrin attachement was revealed by retardation of protein migration in electrophoretic gel. Sub-fragmentation was performed until they studied single spectrin repeats.

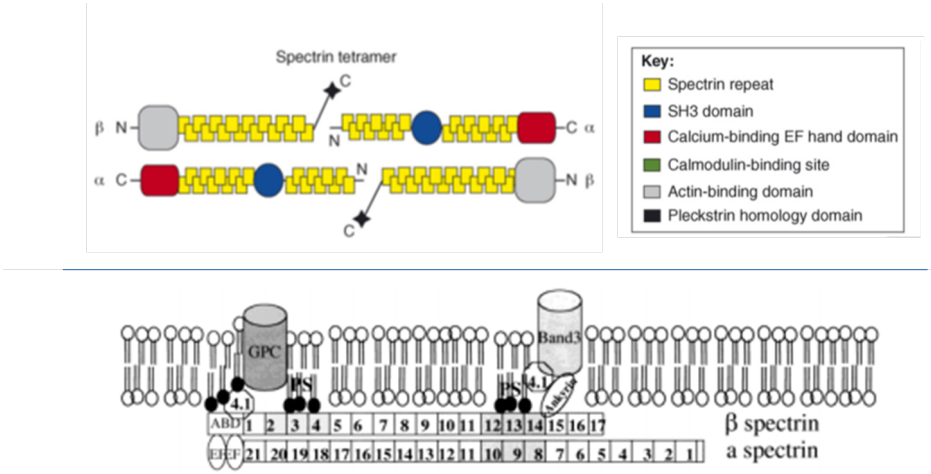

Figure 3.2: Physico-chemical structure of spectrin tetramer and identification of the binding sites. Top: Schematic diagram giving the domain structure of the spectrin tetramer. The name of the different regions are provided in the insert on the right. From [61]. Bottom: Schematic representation of the disposition of PS-binding sites in spectrin. The boxes represent the structural repeats making up most of the two spectrin domains. The repeats containing PS binding sites are shown shaded. The position of the ankyrin and 4.1R attachement sites are indicated. ABC= actin binding domain; EF= EF hand. from [101].

They found that α-8 , α-9-10 , β-2 and β-13 were the binding sites. Taking into account what is known about the junctional complex by which spectrin binds to the lipid bilayer they drew the conclusion that **PS binding sites for spectrin were very close to the sites of attachment of ankyrin**. They thus argue that direct spectrin-lipid interactions are coupled to the interaction via ankyrin. They also raise the idea that **spectrin-lipid interaction might contribute to the preservation of phospholipid asymmetry in the cell** and that those interactions stabilize the membrane [101].

[1] Triple helical repeats and using the SMART database

[2] They obtained circular dichoic spectra and thermal melting profiles of the recombinant spectrin polypeptides and identified binding of spectrin subunits to PS liposomes thanks to ultracentrifuge sedimentation assay and quantified it using SDS-PAGE gels and densitometry experiments.

Other studies led to a more specific molecular definition of the protein: there exists two different kinds of α-spectrin (α-1 and α-2) and five of the β subunit (β-1 to β-5). Basically, both α and β subunits are composed of spectrin repeats and both have N and C terminals. On α subunits, a SH3 domain is present in the middle and a calcium-binding EF hand domain is present before the C-terminal. α -2 also possesses a calmodulin-binding site. β 1 to 4 have an actin binding domain at their N-terminal. β-5 possesses much more spectrin repeats than the others and a non-extended SH3 domain. These domain binding sites are important because they promote the interactions with other proteins and are essential to spectrin function [61].

From what has been described, direct spectrin-lipid interaction seems to exist, whose functions remain unclear. Further studies are thus necessary to investigate the role (if any) of spectrin-lipid interactions (in lipid rafts, membrane stability etc) . **In this chapter we demonstrate direct visualization of spectrin-lipid interactions.** As said in Chapter 1, later on, changes in mechanical properties of GUVs when spectrin is added will be investigated (see Chapter 4).

3.2 Materials and methods

3.2.1 Confocal microscope set-up

All the fluorescence experiments were performed using a Leica SPF5 confocal microscope (Leica, Germany)(Fig.3.3). For studies involving FITC-tagged spectrin, monochromatic excitation light was provided by the 488 nm line of an Argon-ion laser. Emitted light was recorded around 530 nm ($530 +/- 15$ nm). For studies with Annexin, excitation was still at 488 nm with the combination of the 495 nm monochromatic wavelength. Emission was recorded above 550 nm ($585 +/- 21$ nm). The detector is placed in the epi-direction and consists in a photomultiplicators (PMTs). The microscope can be monitored manually or using the LA - AS software. Objectives were oil immersion objectives 20 x Leica (HC PL APO 0.70 NA) and 63 x Leica (HCX PL APO 1.4 NA).

3.2.2 Vesicle formation: swelling versus electroformation techniques

Two methods were used to obtain giant vesicles, **the swelling method** and **the electroformation method**. The electroformation method gives unilamellar vesicles. This method was developped by Angelova *et al.* and consists in applying alternating current to the sample chamber [116]. The swelling method on the other hand does not require currents: the vesicles grow naturally overnight. The main advantage of this technique is that almost any mixture of lipids can be grown. On the other hand, the

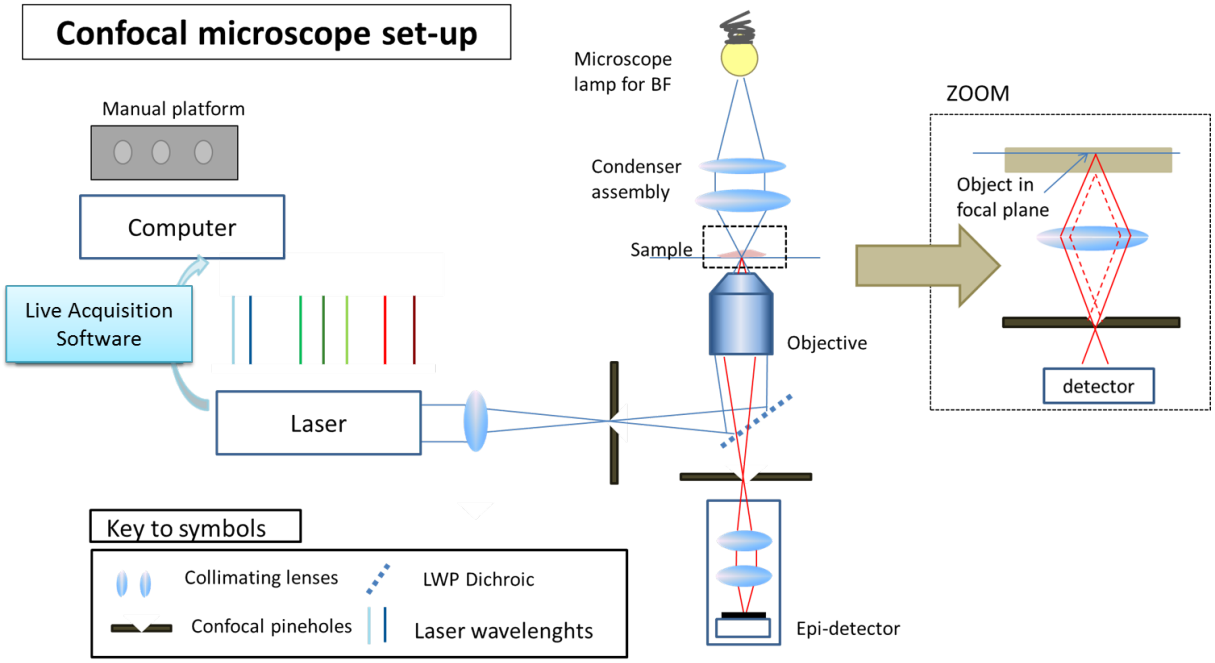

Figure 3.3: Schematic diagram of the confocal microscope set-up. The insert illustrates the principle of a confocal microscope: adding a pinehole in front of the detector selects the light from the focal plan (red line). Light beams from above and below plans are rejected (block on the side (red dotted line)).

resulting vesicle suspension consists of a mixture of GUVs and MLVs. A schematic of the two processes is shown in figure 3.4. In our experiments, the electroformation method has been used as often as possible, unfortunately it does not allow the growth of charged lipids and vesicles cannot be grown in buffer (as it interferes with the current) [117]. The swelling method was thus only used for lipid mixtures which could not be grown into vesicles with the electroformation method.

Electroformation method

Small squares of plastic covered with Indium tin oxide (ITO)[1], of the size of a microscope slide, were cut from a 50 cm by 50 cm plastic sheet (thickness 1 mm, resistivity 60Ω/m^2, Sigma Aldrich, UK). A home-made teflon ring (outer diameter 30 mm, inner diameter 25 mm and 5 mm thick) was carefully washed twice with methanol, then 2 or 3 times with chloroform. A 10, 20, 50 or 100 μl Hamilton syringe was then washed with both methanol and chloroform before being used to apply **uniformly** 10 μl of the liquid lipid solution (1 mg/ml), on the conductive face, inside a circle of the same size as the teflon ring, drawn previously on one of the ITO sheets. Both the ITO plates and the

[1] ITO has conductive properties

teflon ring were then placed in a vacuum chamber for 2 hours to allow the chloroform, in which the lipids are kept, to evaporate. Once out of the vacuum chamber, the ITO was covered with a thin uniform lipid film. In the electroformation chamber, the two ITO plates (conductive face in the inside) were separated with the teflon ring as shown in figure 3.4 and maintained together thanks to spring clips, which apply pressure so that the swelling solution cannot escape. A needle was then used to fill the chamber with the swelling solution -usually consisting of 1ml of sucrose solution (200 or 300 mM in deionized water). Alternating current was then applied following a process slightly different from the usual method by Angelova[1]. A 1.2 V peak to peak in the square wave at frequency 10 Hz was first applied for an hour before switching to a sinusoidal 1.5 V peak to peak wave at frequency 4 Hz for half an hour. The frequency was then further decreased to 2 and 1 Hz in this order for 15 min each. While the alternating current was applied the electroformation chamber was placed in the incubator at 37°C. The electroformation chamber was then taken out of the incubator and left to cool down to room temperature for 20 minutes. The vesicle solution was then transferred from the electroformation chamber to a small glass bottle. Parafilm was used to seal the screw-top and it was kept in the fridge at 4°C. The teflon ring was washed whereas the ITO plastic plates were thrown away. The vesicle suspension was kept for a week but it was usually used within a few days[2].

Swelling method

In the swelling method, a glass bottle (4 ml, Avanti) was carefully washed 5 times each in both methanol then chloroform. A 100 or 200 μl Hamilton syringe was carefully washed with both methanol and ethanol as in the electroformation method. 100 μl of lipid solution (1 mg/ml, Avanti Lipids) and 50 μl of glucose solution in methanol (4mg/ml, to get a 2:1 chloroform:methanol ratio) were added into the bottle. Nitrogen was then bubbled through the solution to quickly evaporate the solvents. For this step the bottle was rotated and kept at 45° inclination as shown in figure 3.4 so that the lipid solution was spread uniformly on the bottle bottom and sides. The bottle was then placed under a vacuum for 2 hours for further solvent evaporation. The swelling solution (like for the electroformation method, usually consisting of 1 ml of sucrose solution (200 or 300 mM)) and the closed and parafilmed bottle was then placed in the incubator at 37°C overnight. The vesicle solution was taken out of the incubator the following day and was allowed to cool down for an hour at room temperature before

[1] It her method, alternative current is applied increasing the voltage by steps, changed every ten minutes (Angelova et al., 1992).

[2] Oxydation of unsaturated lipid might occur if the vesicle suspension is kept for too long.

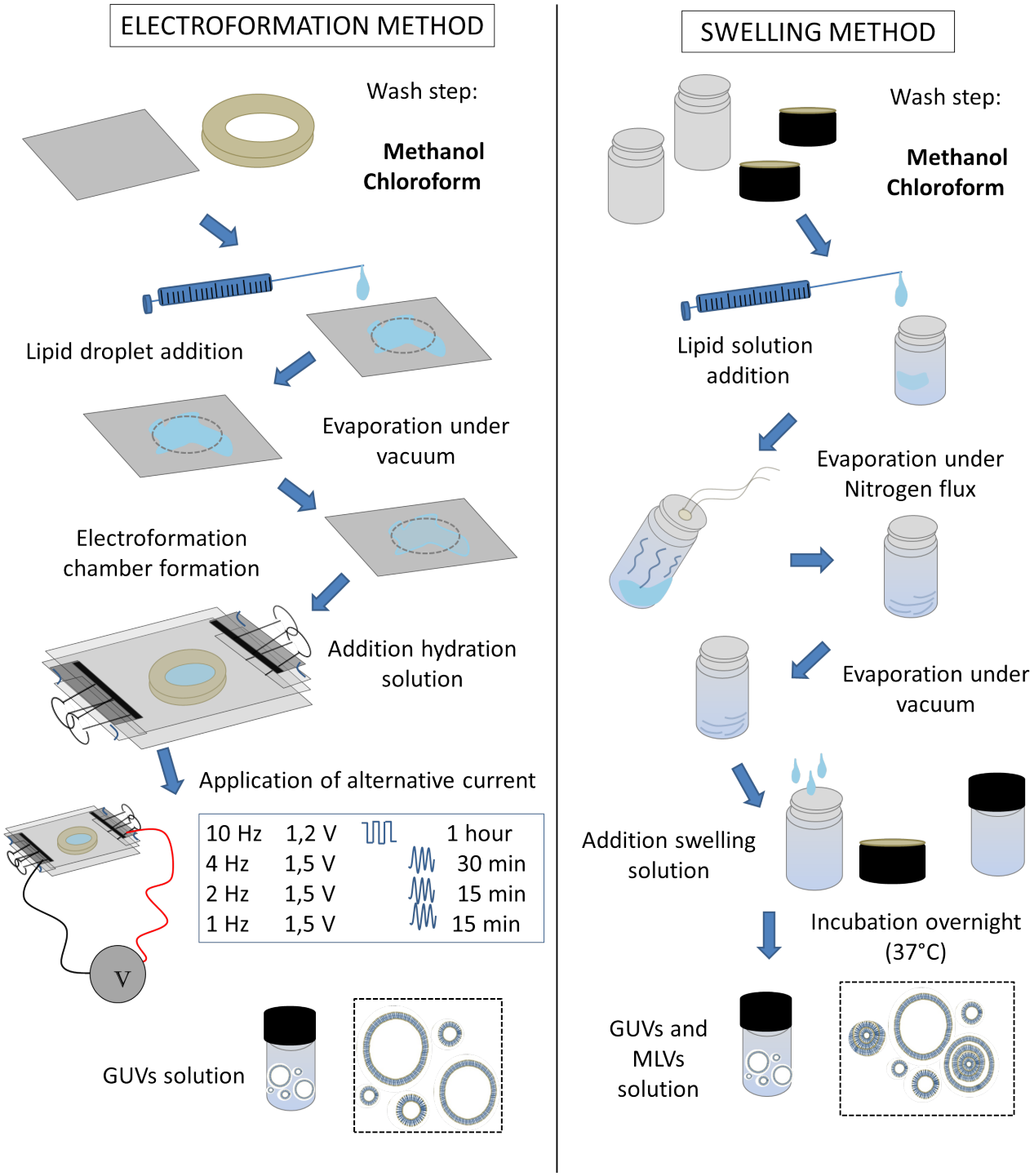

Figure 3.4: Schematic diagram comparing the electroformation method (left colone) and swelling method (right column) to grow giant vesicles (see text).

being placed in the fridge at 4°C. As in the electroformation method, the vesicles were kept for a week but were used within 2 or 3 days.

All the lipids used were obtained from Avanti lipids. All the lipids were ordered in chloroform, except for the Cholesterol and SM which arrived in powder. For the different mixtures, stock solutions were diluted to reach a final concentration of 1 mg/ml. One can find all the lipids formulae and stock numbers in the Appendix A.

3.2.3 Spectrin extraction and purification

Spectrin extraction

Spectrin was extracted from expired human red blood cells obtained from Bristol blood bank. The protocol was adapted from [118]. **The principle consists of extracting spectrin by low ionic strength buffer**. First the blood cells were washed using PBS buffer (0.15 M NaCl, 20 mM sodium phosphate, $pH = 7.6$). For this step 40 ml of blood was distributed into eight 15 ml sterile falcon tubes and were made up to 12 ml with wash buffer. The tubes were gently inverted then centrifuged at 2000 rpm for 10 minutes (acceleration 5, deceleration 1) at 4°C using a swing out rotor. The supernatant was discarded and packed cells washed once more in PBS.

A second buffer (5 mM phosphate, 0.1 mM PMSF, $pH = 8$) was then used to lyse the cells and make them release their haemoglobin. For this step, packed red blood cells were transferred to 8 x autoclaved Oak Ridge Centrifuge tubes (40 ml), each of them containing 5 ml of washed blood and filled to the top with lysis buffer. A centrifuge was used at 4°C, 48 000 g (20000 RPM) for 10 minutes between each wash to pack down the cell membranes to the bottom. The membrane formed a white pellet easily disturbed while the buffer was tainted in dark red by haemoglobin. Cells were washed 4 to 6 times using the lysis buffer to recover all the heamoglobin. Usually the older the blood the more washes they required. Washes were continued until the buffer reached a very clear slightly-peach-tainted color. Before doing the extraction step, it was necessary to add a last wash step using ice-cold autoclaved water, this is to allow the cells to seal again. At this stage it was usual to check that the pH was correct.

The pellet of ghost cells was then transferred equally into 3 or 4 15 ml falcon tubes and filled to the top with extraction buffer (0.3 mM sodium phosphate, 0.1 mM EDTA, 0.1 mM PMSF, $pH = 8$) so that the pellet/extraction buffer ratio was 1:1. The 15 ml tubes were then incubated at 37°C for 30 minutes, the tube being constantly slowly agitated. During this step the spectrin (and other proteins) detached from the cell

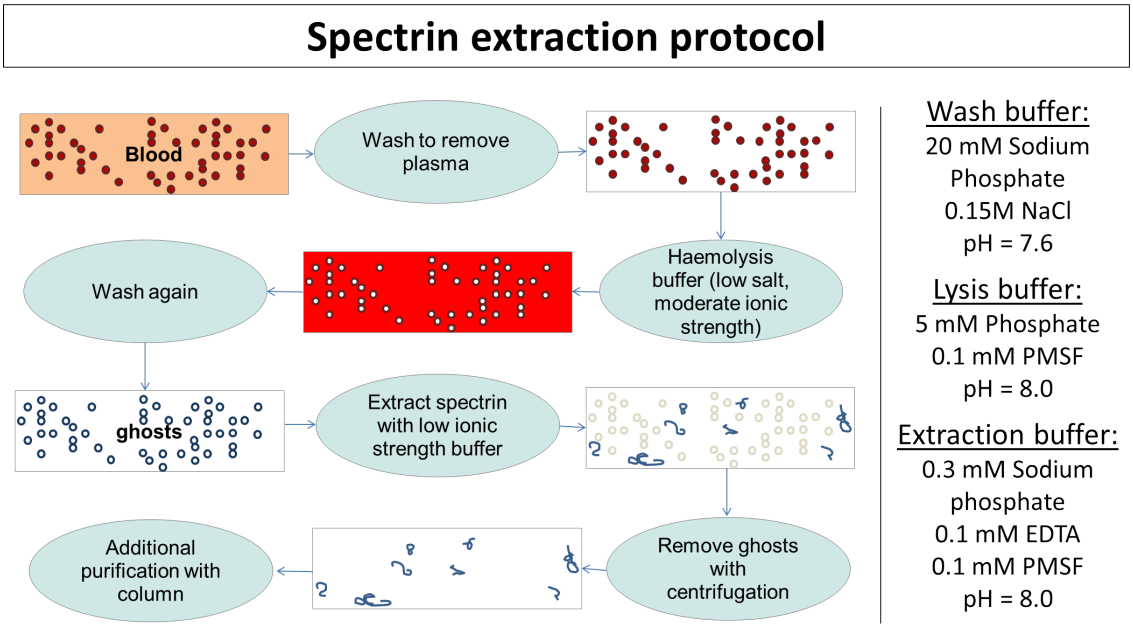

(a) Spectrin extraction protocol. Reproduced with permission from a diagram by David Woods.

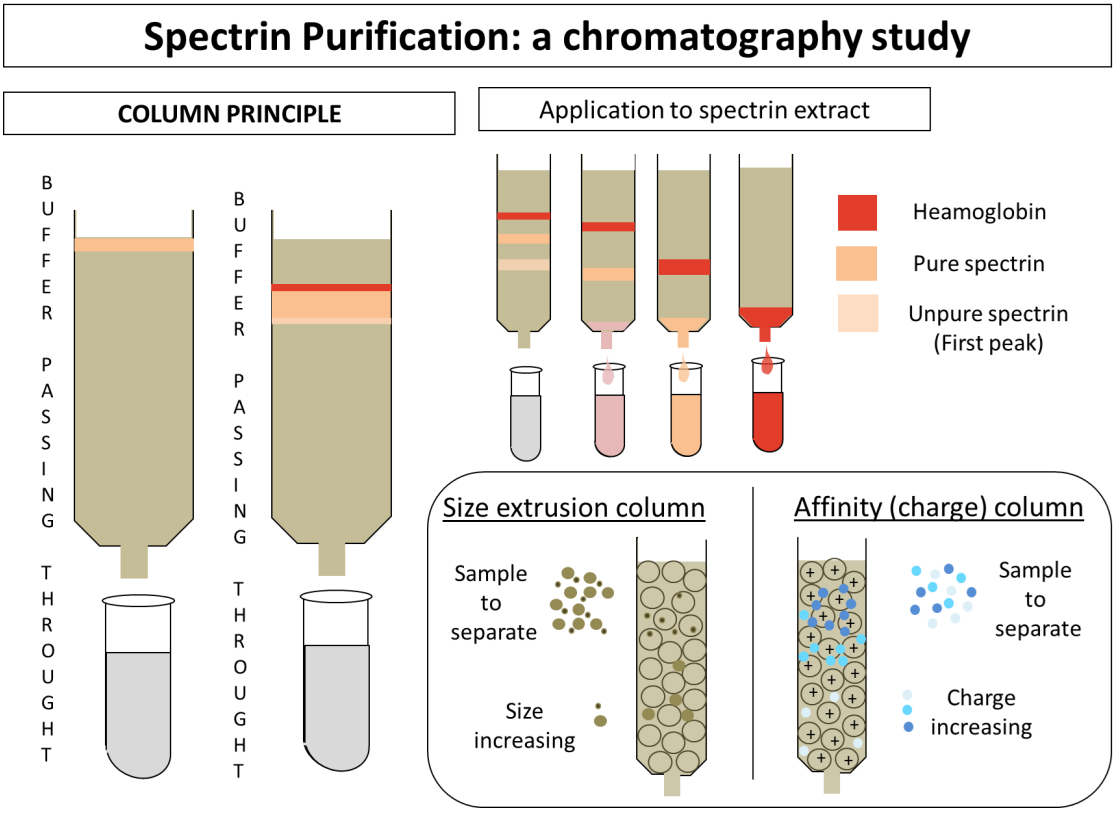

(b) Spectrin purification: different chromatography columns were tested.

Figure 3.5: Spectrin extraction and purification. (a) Schematic diagram illustrating the different steps of spectrin extraction (see text). (b) Schematic diagram comparing different types of choromatography columns for protein purification. In size extrusion columns proteins separate according to their size while in affintiy columns the proteins separate according to their charges (see insert).

membrane. To get the solution of dissociated spectrin a last centrifuge step was necessary to separate the proteins from the cell membrane at 90 000 g. The solution was then transferred into a new tube while the packed pellet was discarded. The solution was then kept at 4°C until being purified[1] to prevent protein degradation.

Spectrin purification

Purification was performed using size exclusion and affinity chromatography columns (fig 3.5 b). This work was performed with post doctoral researchers (David Woods and Debra Shaw) and under the supervisation of Dr. Paul Eggleton. A number of approaches were explored. Since most of the studies on spectrin were performed during the 80s it was fair to believe that progress had been made in chromatography columns. First, a **DEAE**[2] **column** (Hi Prop^{TM} 16/10 DEAE FF, GE Healthcare, Sweden) was tested. **A mono-Q column** (Mono Q^{TM} 5/50 GL, GE Healthcare, Sweden) was also tested. It is based on the same principle as the DEAE column but with higher salt concentration buffers which should result in better separation of proteins. Different orders and schemes have been tried with these columns. Figure 3.6 (a-c), shows the results when a sample of protein extracted from the membrane has been put through the DEAE column first and then through the Mono-Q. After passing through the DEAE column, two peaks were identified. Both of them were then run into the mono-Q column[3].

Another approach using columns size exclusion was also tested: first a **gel superdex 200** (superdex 200 10/300 GL, GE healthcare, Sweden), then a **FPLC** [4](protein A Sepharose CL-4B, GE Healthcare, Sweden). As shown in figure 3.6 d, the gel superdex column provided 2 peaks [5] which was not satisfactory whereas as one can see on (g) the FPLC column showed 3 peaks demonstrating its capability of separating pure spectrin (second peak in the middle), from impure spectrin composed of a mixture of spectrin with other proteins (first peak) and haemoglobin (third peak) (see figures 3.6 f and 3.9). In these graphs the absorbance at 280 nm is in blue and is related to the proteins'

[1] At this stage it is a good idea to quantify the spectrin concentration using a nanodrop machine.

[2] DEAE stands for diethylamninoethanol. This is a chromatography column used to purify/separate proteins, based on ions exchange. A gel matrix beds, positively charged, locks negatively charged proteins. Then the proteins are released according to their charges when the salt concentration of the solvent is increased. This usually allows good separation of proteins with respect to their 'affinity' (charge). This method requires two buffers: a neutral one A and a highly salted one B. Starting with the quasi-neutral buffer A, a ramp of a mixture of A and B (whose ratio changes over time, B proportion increasing with time) is applied to the column until being 100% of the B buffer.

[3] According to a known protein charge, the place of the peak can be pre-determined.

[4] FPLC stands for fast protein liquid chromatography.

[5] On the first try the first peak showed two peaks, but this result has never been reproduced.

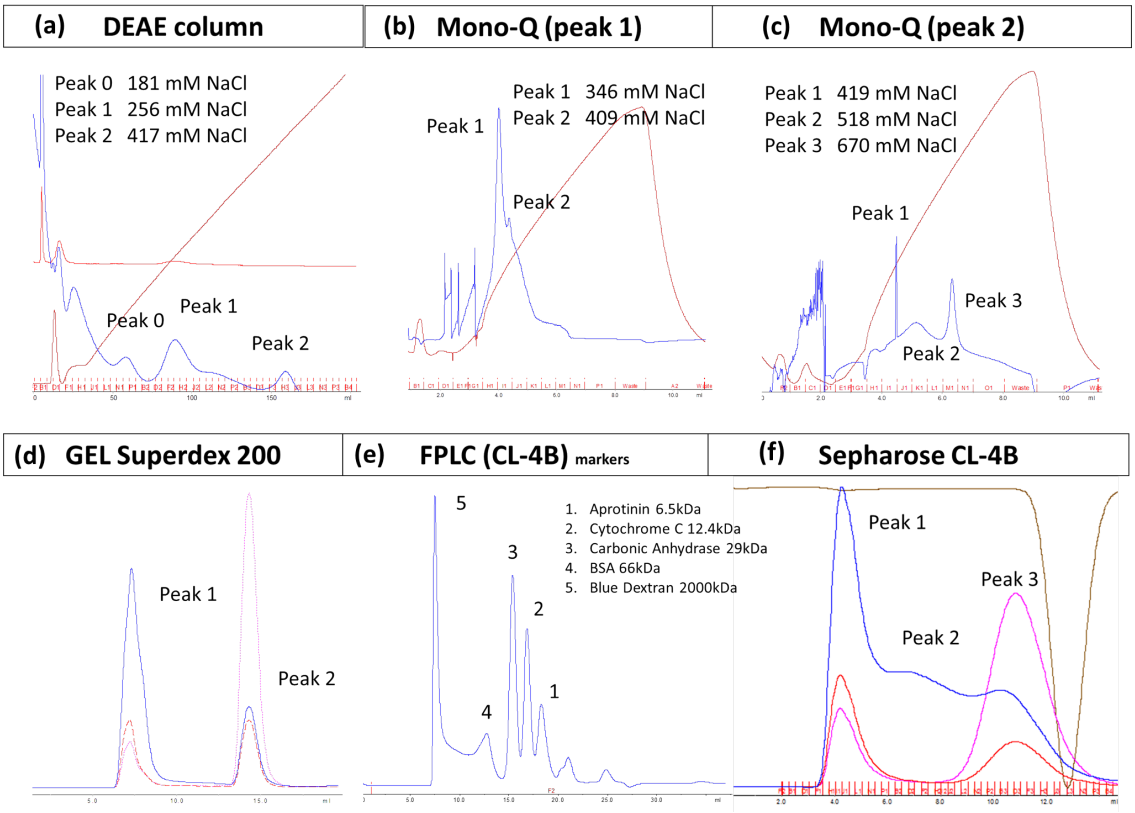

Figure 3.6: Summary table of the chromatography on the columns tested for spectrin purification. For all the spectra the x axis represents the column fractions. (a) Absorbance profiles of the DEAE column tested on membrane extract, (b) Spectra profile of the Mono-Q column tested on the first peak from the DEAE column, (c) Spectra profile of the Mono-Q column tested on the second peak from the DEAE column; (Mono-Q column was used in combination of DEAE for further purification). (d) Spectra profile of the Gel filtration superdex 200 column tested on the membrane extract. (e) Spectra profile of the CL-4B Sepharose column tested on different markers (the markers size are provide at the top). (f) Spectra profile of the FCLP CL-4B spepharose column tested on membrane extract. 3 peaks are distinquishable using the sepahrose CL-4B column contrary to the DEAE and Gel superdex 200 columns on which only 2 peaks are recorded. The sepharose CL-4B was therefore concluded to be more efficient in separating the proteins from the membrane extract (see text). Blue: absorbance at 280 nm, red: absorbance at 345 nm, pink: absorbance at 410 nm.

absorbance whereas the absorbance at 410 nm is in pink and the one at 345 nm in red. As one can see haemoglobin absorb at lot at 410 nm.

Each run into a column results in some loss of material which would get trapped by the column, hence a **compromise between the number of runs and the purity of the sample** needed to be made. To test the purity of the spectrin from each column/combination of columns, SDS-PAGE [1] gels were run. Two kinds of gel, **native gel** and **denaturant gel** were used (data not shown). Native gel were found better to distinguish between dimer and tetramer spectrin.

[1] SDS-PAGE stands for Sodium dodecyl sulfate (SDS) Polyacrylamide gel electrophoresis (PAGE).

3.2.4 Spectrin Characterization

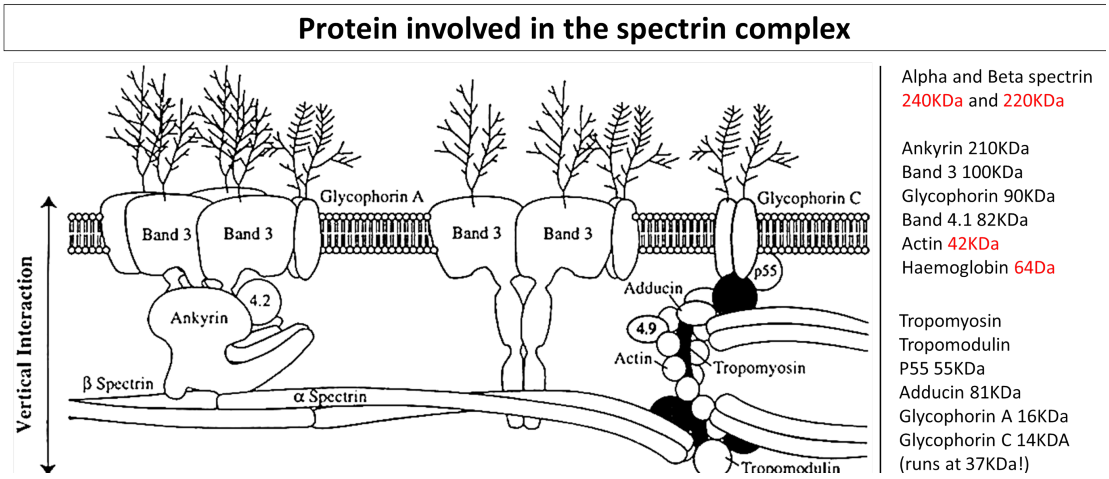

Figure 3.7: The relationship between the proteins of the junctional complex at the anchoring point of the spectrin network [119]. The list on the right provides the molecular weight of the proteins involved in the junctional complex [120].

A typical SDS-PAGE is given in figure 3.8 a. The samples tested in each column have been given a number (list on the right side). Protein are labelled, so that the purity/unpurity of each sample tested can be determined. Almost all the proteins of the complex could be identified in the various sample which was an encouraging sign. Figure 3.7 reminds us of the proteins involved in the spectrin complex. The molecular weight of each protein is given in the list on the right. Since spectrin is a big molecule - 240 KDa plus 260 KDa, for dimer; twice this weight for tetramer; spectrin dimer and tetramer are at the very top of the gel (7-15 % gel were used) whereas actin (41KDa) and hemoglobin (18KDa) are at the bottom.

Characterization of the spectrin was performed using **ELISA assay**[1] and **Western Blot**. The ELISA assay was an indirect ELISA assay. A lot of attempts were necessary to get a (weak) signal (data not shown).

As shown in figure 3.8-b, the Western Blot [2] worked really well from the first attempt with all the antibody tested (actin, mouse, rabbit), in all the concentrations of primary

[1] ELISA stands for Enzyme-linked immunosorbent assay.

[2] In a Western Blot, a SDS page is run, then the gel is transferred onto a membrane and both first and secondary antibodies (like in ELISA) are added. Then the results are developed as photographs. The western Blot is thus the best technique to validate a protein since it combines both the aspects of a gel (molecules are separated according to their sizes) and ELISA (antigen interacting specifically with the protein of interest) in a single experiment.

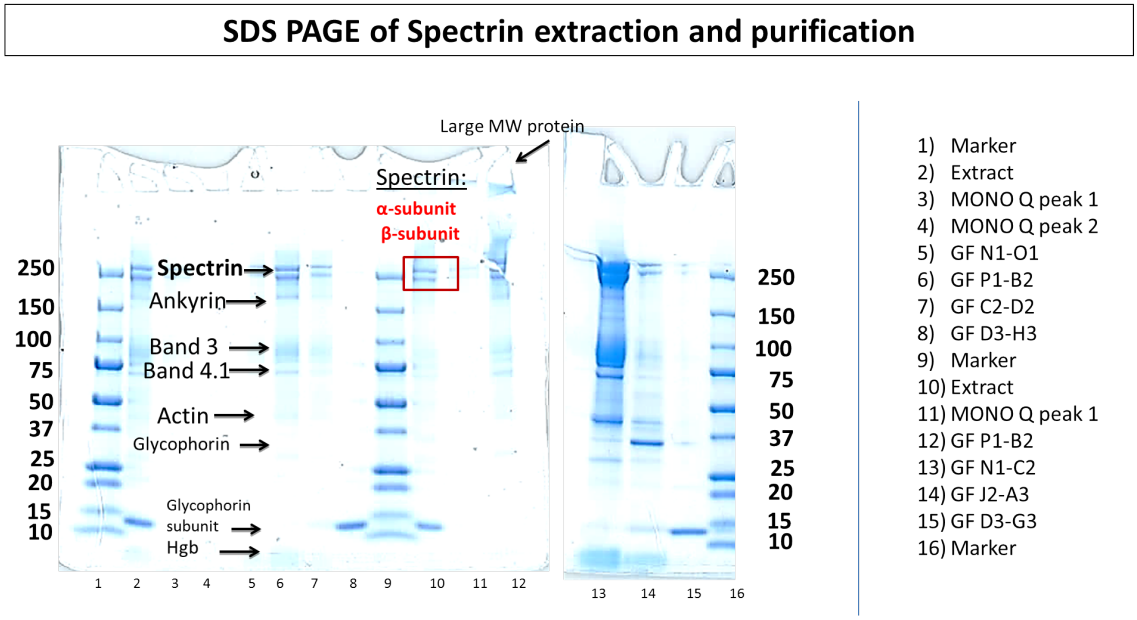

(a) SDS-PAGE gel electrophoresis for spectrin purification

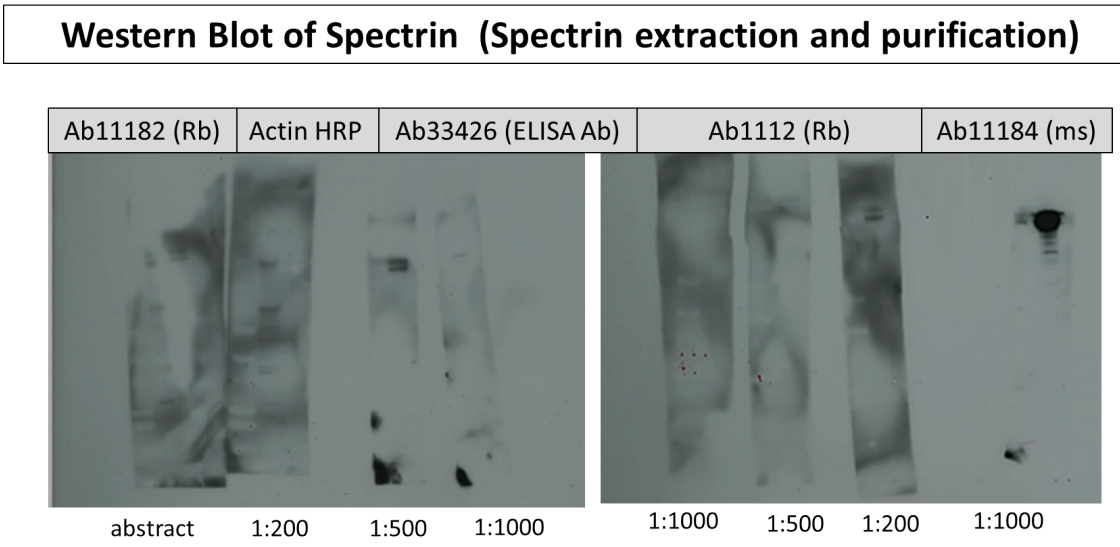

(b) Western Blot on both impure and pure spectrin samples

Figure 3.8: Spectrin Characterization. (a) Typical SDS-page Gel. The marker on the sides provides a scale for measuring the protein size. The red insert highlights the spectrin subunits. Other proteins of the complex are also identifiable. Samples (from fraction columns) tested for purity are indicated in the list on the side. (b) Summary table of the Western Blot (WB) experiments. WB were positive for all the antibodies tested (double bands at the top of the gels). Antibodies names are provided at the top. Concentration of the antibody is indicated at the bottom. Rb=rabbit antibody, ms= mouse antibody. WB was also positive for the actin (unpure spectrin).

and secondary antibodies (1:200, 1:500 and 1:1000). **This was an important result since it has not been done previously on spectrin**.

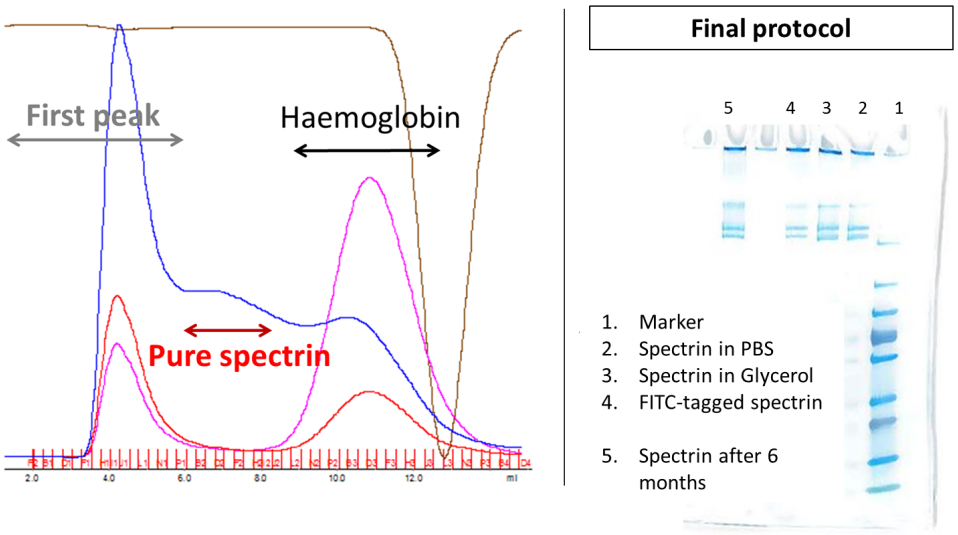

Figure 3.9: Final protocol for spectrin purification consisted in a single run through the FPLC column (Sepharose CL-4B). The CL-4B allowed separation of spectrin bound to other proteins of the complex (first peak, 'impure spectrin'), from pure spectrin (second peak) and heamoglobin (third peak). The SDS-page gel on the side demonstrates the purity of the protein (2), FITC-tagged spectrin (4) kept in PBS and the spectrin kept in glycerol (3) for months without degradation (5).

Results of this whole analysis led to the conclusion that a single run through the FPLC column was adequate to produce pure spectrin. Further runs led to loss of sample without improving the purity. Spectrin was then transfered into glycerol to be kept frozen. SDS-PAGE gel run to test the effect of the change of media on the spectrin showed that spectrin survived it and kept frozen for weeks/months without degradation (see figure 3.9, fifth column on the gel). To ensure that the concentration of the spectrin was exact, a nanodrop machine was used. To reach high concentrations of spectrin and change media, centrifugal filter units (*i.e.* concentrators) with a molecular weight cut off of 100KDa were used (Amicon Ultra 100K, Millipore, Ireland). Experiments demonstrated that spectrin could not be concentrated as much as 50 mg/ml as reported in (Gratzer et al., 1982) but usually precipitated when concentrated further than 3 mg/ml (see Chapter 7). These experiments fully validated the spectrin purity and characterization.

3.2.5 FITC-tagged spectrin

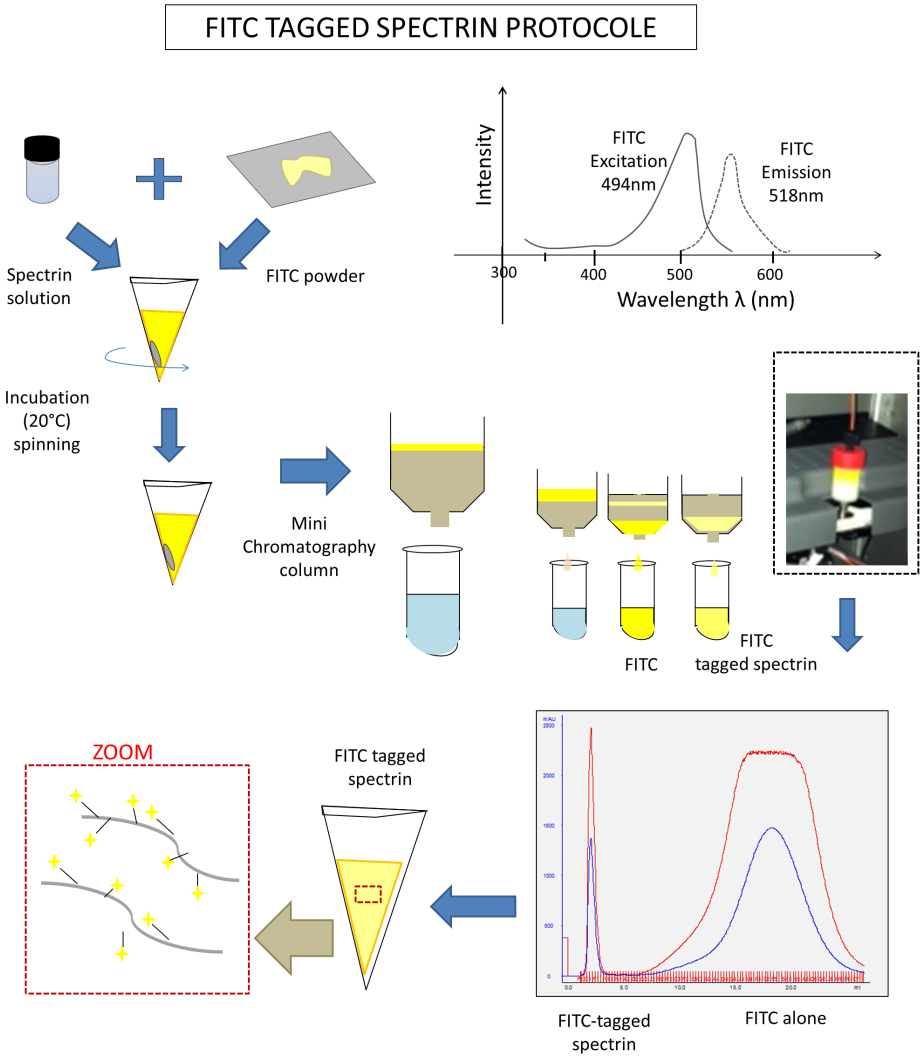

Figure 3.10: Schematic diagram illustrating the different steps to tag the spectrin protein with fluorescein (see text). The excitation and emission spectra for FITC is also provided on the top right corner. The black dotted insert provides an image of the mini column used for discriminating free FITC from FITC-tagged spectrin.

FITC tagged spectrin

Once purified, **spectrin was FITC-tagged** using a protocol adapted from [121] and illustrated in figure 3.10. FITC [1] dye (Sigma Aldrich) and spectrin (1mg/ml in PBS buffer, pH = 7.4) were mixed and incubated at room temperature for an hour while stirring to homogenize the reaction. The mixture was then cleaned by passing through a mini 5 ml column (desalting column). Fig 3.10 shows that the absorbance at 280 nm

[1] FITC stands for fluorescein isothiocyanate.

has two peaks: the first one is the spectrin tagged with FITC whereas the second one is the free FITC. Measurements of the absorbance at 345 nm allowed determination of the number of FITC molecule per spectrin. Mixing 1 mg/ml pure spectrin with FITC 1 mg/ml resulted in a ratio of 16 FITC molecules per spectrin tetramer. FITC-tagged spectrin was then frozen in the buffer media at - 20°C and wrapped in foil to prevent photobleaching of the FITC dye.

Fluorescence experiments

Preparing samples for fluorescence experiments consisted in mixing FITC-tagged spectrin and vesicle solutions, paying attention so that the buffer osmolarities matched together to avoid vesicle bursting. The mixture was embedded into aluminium to prevent from photobleaching and placed to incubate for at least one hour. Samples were then injected within a microscope slide chamber similar to the one used for micropipette aspiration (see chapter 4) and imaged using the confocal microscope described earlier.

Protocol Optimization

The first step in the fluorescent experiments was to optimize the experimental protocol. To do so, different combinations changing the vesicle/FITC-spectrin ratio, the incubation time, the temperature and the PC/PS ratio in vesicles have been tested. Those experiments were performed using small quantities of both vesicle and FITC-tagged spectrin solutions, since at this stage we could not afford to use all the FITC-spectrin for optimization and the total FITC-spectrin stock solution available was only 1 ml of 1 mg/ml. Statistics might not have been large enough (see error bars in figure 3.11) and repeating these experiments at larger scale might result in finding different optimum parameters.

As illustrated in figure 3.11 this preliminary study showed that 2 hours incubation at 37°C were necessary for FITC-tagged spectrin to generate sufficient fluorescence. A volume ratio of 1:2 (FITC-spectrin (1 mg/ml): vesicle) was found to be a good compromise. Fluorescence was higher when incubated at 37°C compared to when it was let to incubate at room temperature. This is contrary to what is expected from the literature (see section 1) but we tried to be at physiological temperature condition to mimic the body conditions. For determination of all the parameters, both the intensity (light blue in figure 3.11), and the percentage of vesicles exhibiting fluorescence needed to be taken into account. On the graphs in figure 3.11 the dark blue bars, represent

the fluorescence intensity balanced with the binding percentage; this is the parameter we tried to optimize.

3.3 Imaging spectrin distribution

3.3.1 Spectrin binds uniformly to mixed lipid vesicles

The first experiments and optimization were performed on DOPC and a mixture of DOPC and DOPS in different molar ratios[1]. As one can see in figure 3.11 FITC-tagged spectrin bound to all the PC/PS vesicles to a similar extent (graph 3). The ratio PC:PS 70:30 gave a slighly higher fluorescence signal. Morever, experiments from a previous PhD student suggested this was the optimum ratio for spectrin to bind [62]. This was thus the GUVs mixture ratio used in both fluorescence and micropipette aspiration experiments. Further fluorescent experiments on DOPC GUVs (for negative control) revealed some fluorescence signal, leading to the conclusion that spectrin would/could also bind to PC GUVs (data not shown). In the literature it can be asserted that the FITC is not interacting with the lipid and that it does not attach to the hydrophobic sites of the spectrin [121].

In later experiments, to be consistent with the micropipette aspiration experiments, SOPC and SOPC:SOPS GUVs were used instead of DOPC and DOPC:DOPS ones. SOPC and DOPC only differ in one bond (single in SOPC and double in DOPC) in one of the two carbon chains, the overall length being the same (see Appendix A for the chemical formulae of those phospholipids). GUVs mixed with FITC-spectrin showed similar fluorescence levels for SOPC:SOPS and DOPC:DOPS systems and for SOPC and DOPC (data not shown). One can see in figure 3.11 that spectrin binds uniformly to 70:30 DOPC:DOPS vesicles and in figures 3.12 and 3.13 (top right) that spectrin seems to bind uniformly to 70:30 SOPC:SOPS vesicles too.

All the following fluorescent experiments were performed in the same conditions : 2 hours incubation at 37°C, volume ratio FITC-spectrin:vesicles 1:1, no wash, use of fresh vesicles. To investigate if a correlation between the fluorescence intensity and the vesicles radii existed, fluorescence of vesicle distributions over 5 different experiments have been studied. Figure 3.12 summarizes the results: As one can see on (b) FITC-spectrin also seems to bind to SOPC vesicles. The picture at the top (a) is a typical snapshot fluorescence picture of the FITC-spectrin distribution around SOPC:SOPS (70:30) vesicles in suspension. The graph on the right gives the

[1] since they were the lipids used by previous PhD student [62]

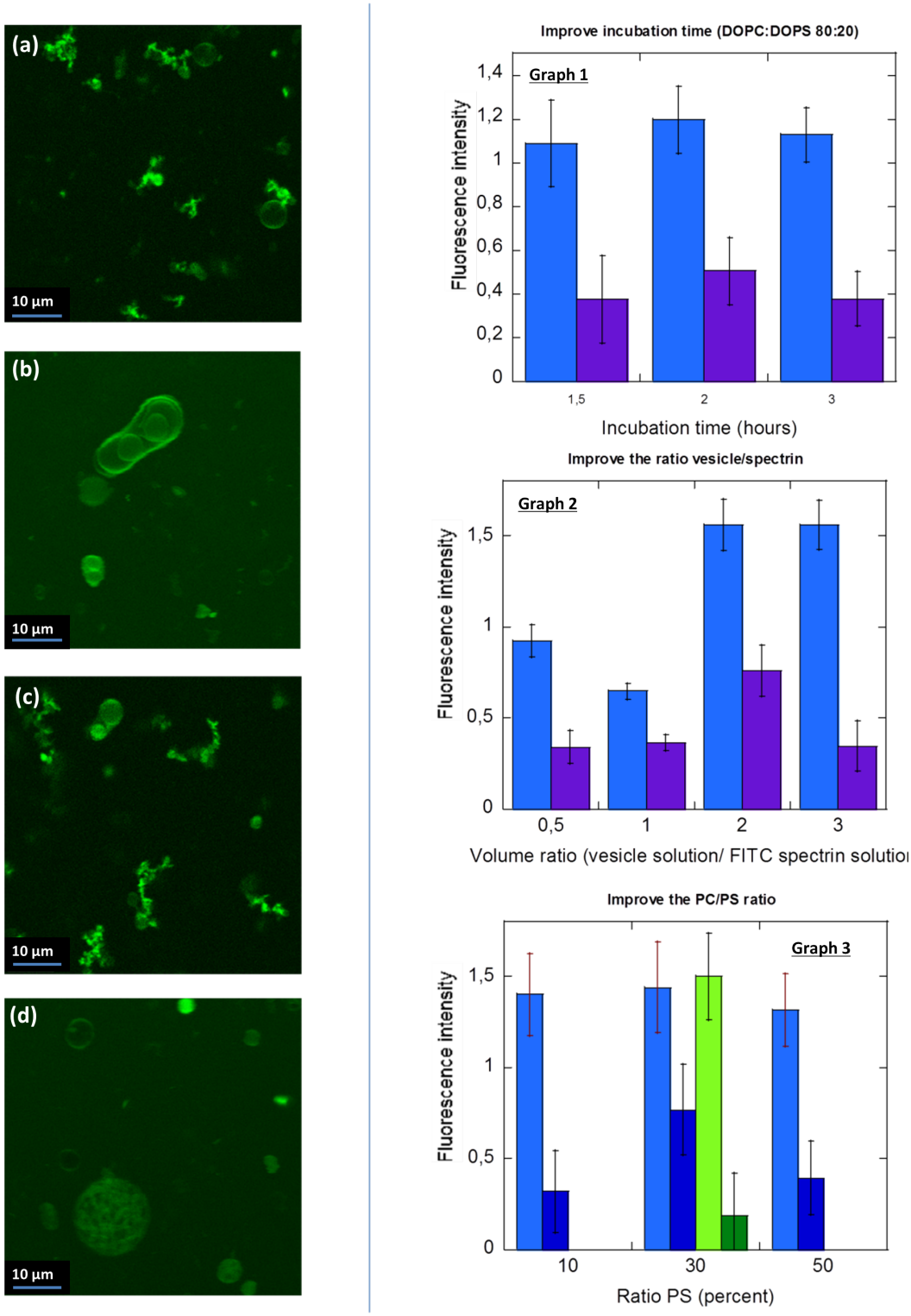

Figure 3.11: Optimizing the fluorescence of FITC-tagged spectrin. Left: Fluorescence images of FITC-spectrin distribution around DOPC/DOPS GUVs (molar ratio 70:30). The spectrin binds uniformly to the vesicles, preferring osmotically ruptured vesicles in (a) and (c). (d) The larger vesicle seems to be an invaginated GUV. Right: Graph for the optimization of different parameters: incubation time (graph 1), vesicle/FITC-spectrin volume ratio (graph 2) and PC/PS ratio (graph 3). Blue: incubation at 37 °C, Green: incubation at 21 °C. Light color: intensity, dark color: intensity balanced wit the binding percentage.

concentration of spectrin [1] in the vesicles as a function of the GUVs radii, of all 5 experiments (the total of studied SOPC/PS (70:30) vesicles was ∼140 vesicles). From this graph, no clear correlation/distribution can be deduced. Nevertheless 3 populations can be identified. Population 1 is composed of vesicles of smaller size (diameter : 5 - 15 μm) to which FITC-spectrin highly binds (the fluorescence being 2 to 3 time higher than the fluorescence of the bulk solution). Population 2 is composed of GUVs from various sizes, to which FITC-spectrin binds at a lower scale (intensity 0.5 to 1.5 time higher than the bulk solution) independly of their size. Spectrin does not bind to population 3. Like in population 2 this effect seems independant of the vesicle radii.

As one can see, some fluorescent vesicles appear as bright spheres, whereas others appears as fluorescent circles. The bright uniform vesicles could contain spectrin which has penetrated the membrane bilayer[2]. However, the vesicles could be multilamellar with interconnection between the lamellae or consist of a single heavily invaginated membrane. Such structures have been observed in vesicles prepared by swelling [ref]. Nonetheless, the fluorescence circles clearly demonstrate the ability of spectrin to uniformly surround some of the GUVs. The fluorescence level from these appeared lower than the fully fluorescent vesicles.[3] For population 1, spectrin seems to bind preferentially to smaller GUVs, with a concentration around twice as high as for population 2.

Over the 5 experiments, 4 experiments gave similar fluorescence distributions, whereas the fifth one showed that small vesicles still appeared to be the brightest whereas hardly any spectrin binded to the 10-20 μm in diameter range and spectrin seemed to bind to a smaller extent to larger GUVs. This raises the question of tiny fluctuations in compositions from one GUV to another within the same preparation: perhaps there exists some specific lipid mixture conditions for spectrin to bind to PS, emphasising that the micro lipid organization could be of greater importance than originally thought. Moreover, later on, improvement in the microscope allowed to get a higher contrast (*i.e.* better SNR), and longer acquisition time images revealed domain-like features in the PS distribution of 70:30 SOPC:SOPS vesicles which will be discussed in the next section.

[1] The fluorescence on the vesicle has been normalized against and related to the background (free FITC-spectrin in solution whose concentration is known)

[2] Some studies from [109] claimed/demonstrated that in certain conditions, spectrin could perforate the membrane bilayer (see literature review, section 1)

[3] Which might just reflect to the fact that there is less membrane. On the other hand, spectrin might prefer 'curved membrane'.

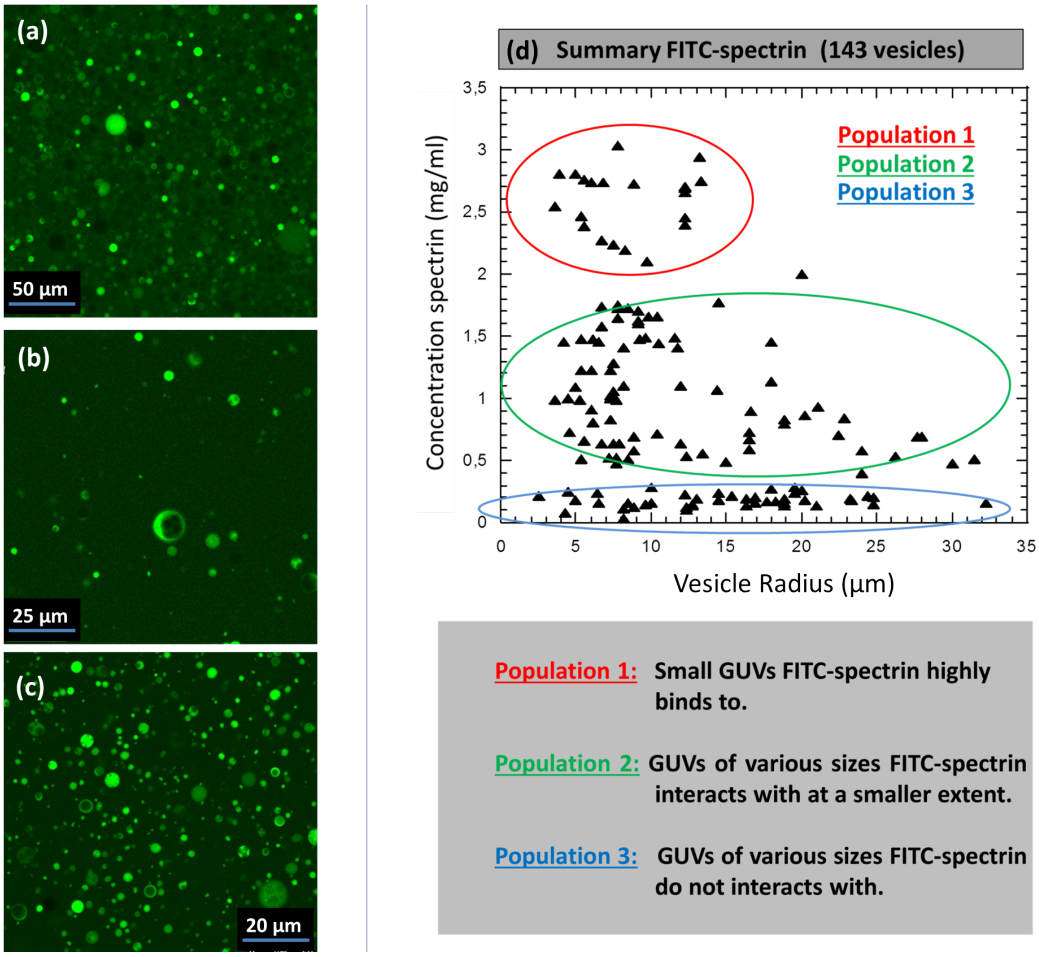

Figure 3.12: Studying the fluorescence intensity dependance of FITC-tagged spectrin on GUV diameter. (a) Fluorescence distribution of FITC-tagged spectrin around SOPC:SOPS GUVs (molar ratio 70:30), (b) Fluorescence distribution of FITC-tagged spectrin around DOPC GUVs, (c) Fluorescence distribution of FITC-tagged spectrin around SOPC:SOPS GUVs (molar ratio 70:30), with a better resolution (acquisition rate slower (10 Hz compared to 100 previsously)). (d) Graph giving the relative intensity fluorescence of a population of 143 SOPC/SOPS (molar ratio 70:30) GUVs (5 experiments) with respect to their radius. 3 populations can be identified (see the insert).

3.3.2 Spectrin domains: spectrin preferentially interacts with PS

Several papers reported that spectrin only binds to charged lipids (PS, PG, PI) (see literature review in section 1); an effort was made to verify this in our membrane system.

As introduced in Chapter 2, Annexin dye probes the negatively charged lipids, which in a SOPC:SOPS system will highlight the SOPS distribution. Annexin was incubated at room temperature for 20-30 minutes (volume ratio 5 μl of dye in 100 μl of vesicle solution). In 70:30 SOPC:SOPS vesicles domains were visible (fig 3.13) which was surprising since, as explained in Chapter 1 phospholipids whose headgroups differ do

not usually show lateral segregation[1].

Following this discovery, 70:30 SOPC:SOPS GUVs from the same preparation were incubated simultaneously on the one hand with annexin and on the other hand with FITC-tagged spectrin. Figure 3.13 summarizes the results: Annexin (highlighting the PS distribution) appears in yellow whereas the FITC (highlighting the spectrin distribution) is in green. If both Annexin and spectrin bind uniformly to some of the GUVs (fig 3.13 b and a respectively), some domains were present in the FITC and Annexin distributions around other vesicles (Image table fig 3.13-c).

As shown in figure 3.13 (c) some 'stripped' (5, 5'; 6, 6'; 8,8'; 9, 9') and round microdomain structures (1-4, 1'-4'; 7, 7'; 9,9'; 11-12, 11'-12') could be identified. Both annexin and FITC-spectrin stained the internal structure of some vesicles. At this stage it could only be speculated that, since the distribution appeared very similar, spectrin might potentially preferentially interact with SOPS compared to SOPC.

To validate this hypothesis another system composed of 4 lipid species, referred to as 4-component vesicles throughout this Chapter: DOPC, DOPS, SM and Cholesterol (molar ratio 25/25/25/25 %) which was reported to get macro and micro-domain separation [122] was used. Since all the three DOPC, SM and Cholesterol species are neutral, annexin could also be used to highlight the DOPS distribution. Fortunately, these vesicles could be formed using the electroformation method, in spite of the presence of PS, which for the most part produced unilamellar giant vesicles.

Distribution of PS using annexin in 4-component vesicles has already been illustrated previously (see section 1 of Chapter 2). As a reminder, figure 3.14 gives a z-stack of a single GUV, which possesses both micro and macro domain organisation within its bilayer. 4-component GUVs and FITC-spectrin were mixed in the same conditions as uniformly mixed vesicles and the results are presented in the next section.

FITC-tagged spectrin distribution in 4-component vesicles

Figure 3.15 illustrates a typical fluorescence result. As one can see, spectrin hardly binds to the 4-component vesicles but when it does one can distinguish round small domains. The fluorescence intensity of these domains was only just above the bulk solution fluorescence and the domains were in continuous motion which suggests that the binding might not inhibit domain migration (weak interaction). Figure 3.15 b

[1] Nevertheless, this particular 'binary lipid system' does not seem to be extensively studied.

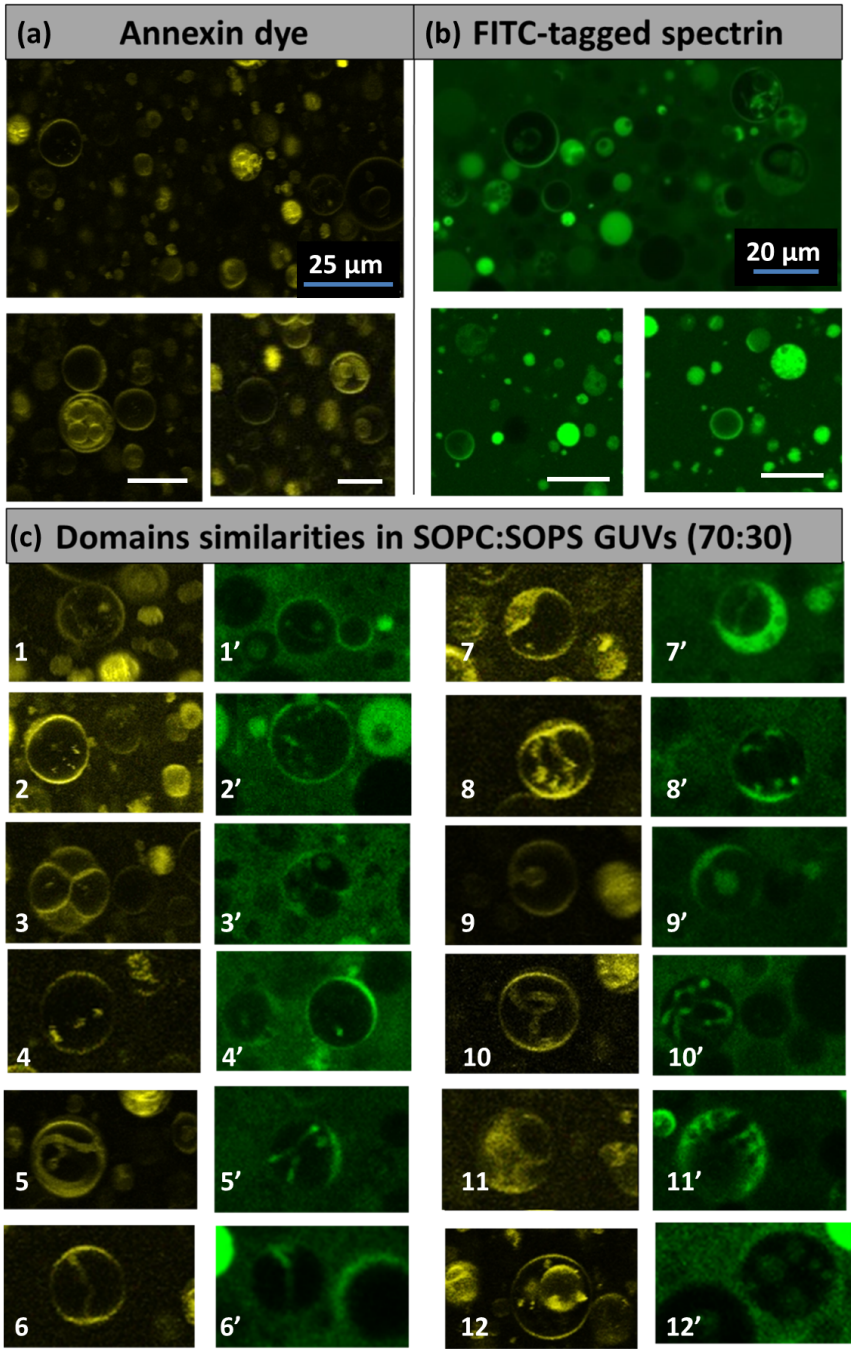

Figure 3.13: Comparing Annexin and FITC-tagged spectrin distributions around SOPC:SOPS GUVs (molar ratio 70:30). Two sets of experiments were performed. In sample 1, SOPC/ SOPS vesicles were incubated with Annexin, and in sample 2, SOPC SOPS vesicles were incubated with FITC-tagged spectrin. In both samples fluorescence images were recorded (confocal fluorescence). (a) PS distribution highlighted with Annexin, (b) Spectrin highlighted with FITC. In (a) and (b) some GUVs exhibit uniform fluorescence. Bar scales are 10 μm. (c) A comparative montage of vesicles exhibiting fluorescence. (1-12) Vesicles from the Annexin sample, (1'-12') Vesicles from the FITC-tagged spectrin sample. Both 'stripped' (5, 5'; 6, 6'; 8,8'; 9, 9') and round microdomain structures (1-4, 1'-4'; 7, 7'; 9,9'; 11-12, 11'-12') could be identified.

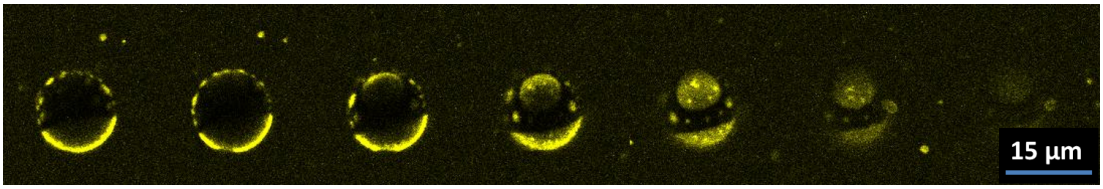

Figure 3.14: Montage of fluorescence images showing the PS distribution in a 4-component GUV (annexin staining). Both large and small domains can be identified (happy vesicle).

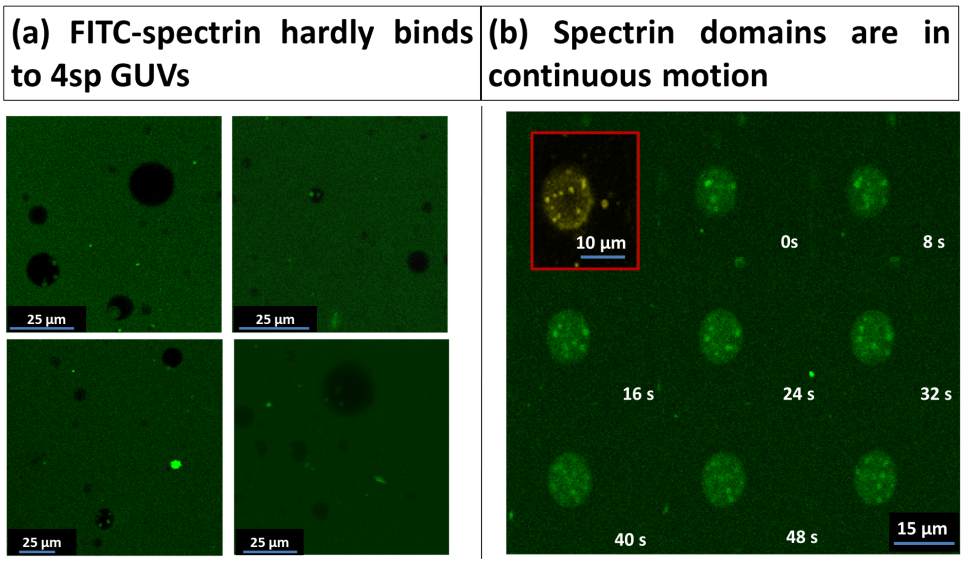

Figure 3.15: FITC-tagged spectrin binds weakly to specific sites in 4-component vesicles. (a) Montage of fluorescence images showing the weak binding of spectrin to 4-component GUVs (fluorescence level similar to that of the bulk solution) (b) Montage of fluorescence images of a time-lapse experiment. Time of each snapshot is indicated in the bottom right corner of each image. Spectrin-rich domains (higher fluorescent dots) are in motion. In addition, the spectrin distribution around the GUV looks similar to that of the Annexin around a 4-component GUV from another sed of experiments (red insert).

gives a montage of a short time lapse experiment (time is indicated in each picture of the montage). In the case of this GUV, spectrin domains appear brighter than the background, and one can follow the displacement of the microdomains from one image to another. One should also notice the similarity with the PS distribution found in some GUVs highlighted with annexin (red insert).

Similarities between FITC and Annexin distributions

In only two vesicles from two different preparations, spectrin was found to be co-distributed with PS, one is shown in Figure 3.16-b [1]. The fact that, only a couple of the GUVs exhibit FITC fluorescence whereas the others do not interact with spectrin

[1] *i.e.* Only a couple of vesicles from different experimental days (demonstrating reproducibility), showed spectrin distribution around 4-component GUVs similar to the PS distribution.

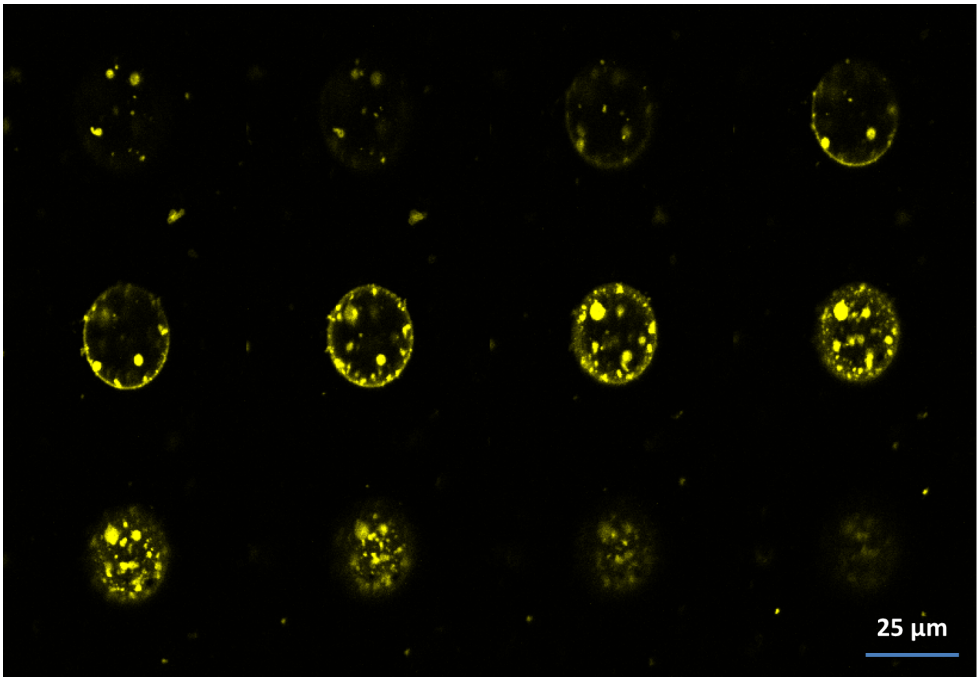

(a) Annexin fluorescence highligthing the PS distribution in a 4-component GUV (z stack)

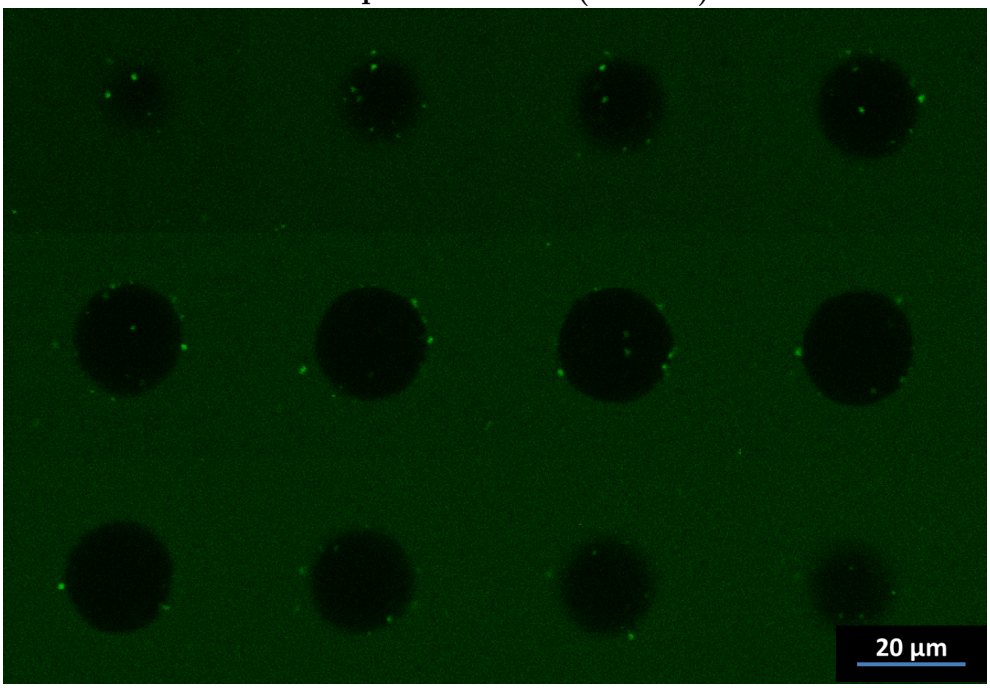

(b) FITC highligthing spectrin distribution in a 4-component GUV (z stack)

Figure 3.16: Comparative montage of Annexin/ FITC-tagged spectrin distributions around 4-component GUVs. (a) Photo-montage of a z stack showing the PS microdomain organisation of the vesicle (highlighted with Annexin, from sample 1). z difference between each image was 2.5 μm. (b) Photo-montage of a (z stack showing the spectrin domain distribution around a 4-component GUV (highlighted with FITC, from sample 2). z difference between each image was 2 μm. Annexin and FITC-tagged spectrin distributions are very similar, suggesting that spectrin might interact preferentially with PS.

illustrates the potential importance of single vesicle micro-composition. Figure 3.16 gives montages of z-stacks of annexin distribution (yellow at the top) and FITC-spectrin (green at the bottom). Acquisition of the z-stack of the sample with spectrin was hampered by microdomain motion[1]. Incubation of 4-component GUVs with both dyes (annexin then FITC-spectrin) was also tried and gave some insight that the dyes might be competing for the same sites (data not shown).

3.4 Spectrin binding to externalized PS on Red Blood Cells

3.4.1 Externalized PS RBCs: principle

To reinforce the conjecture that spectrin would bind preferentially to PS, a last experiment was performed. Collaborators use an ionophore to externalize the PS in red blood cells, for studying apoptotic red cell binding to macrophages [123], [124], [125] . This method has been used here for experiments with spectrin. The principle is as follow: When the combination of ionophore and calcium ions are mixed with RBCs, the calcium is internalized which inactivates amino phospholipid translocase. The translocase is the enzyme which together with scramblase maintains the distribution of PS on the internal side of the membrane. Once the translocase has been inactivated, the PS flips from the inner side to the outer one. With this process, cells did not appear echinocytic.

The experimental protocol was the following: 10 μl of human blood was diluted into 1 ml of PBS buffer and washed twice. The calcium was present at 1.2 mM in the PBS buffer which contained both calcium and magnesium ions (BE17, 513F500ml, from Lonza). The ionophore (A23187) was then added to aliquoted samples (typically 100 μl each) at 30 μM and incubated for 1 hour at room temperature (RT). The samples were then washed once and resuspended in calcium binding buffer before the addition of the annexin (5 μl into 100 μl of externalised PS RBCs solution, 20 minutes incubation at RT). For addition of the FITC-tagged spectrin (30 μl of 1 mg/ml FITC-spectrin within 100 μl of externalised PS RBCs solution), cells were resuspended in PBS buffer and incubated at 37°C for at least 2 hours, as in the experiments with GUVs. For experiments where both dyes were involved FITC was introduced first and incubated at 37°C for 2 hours before addition of the annexin at RT for 20 min.

[1] PS domains are likely to be in the L_d phase since its T_m is 11°C (See Appendix A).

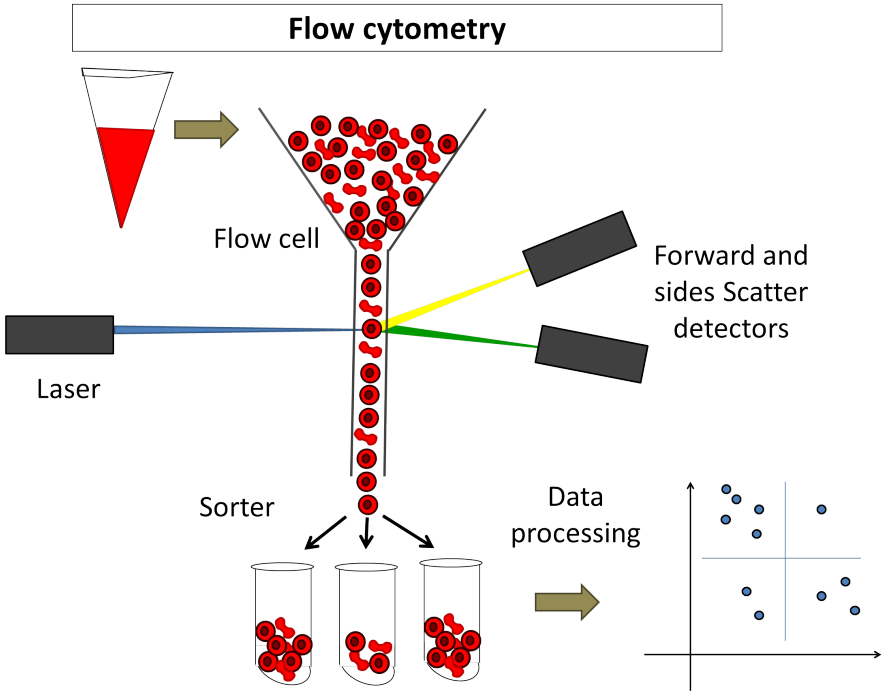

Figure 3.17: Schematic diagram illustrating a flow cytometry experiment. RBCs are loaded into a flow cells which allows only single-file movement. Cells are scanned individually by a laser and the fluorescence is recorded by forward and sides scatter detectors. Cells are then counted and sorted according to the fluorecence they emit. Data can be plotted in graphs for searching for relationships between fluorophores when cells have been tagged with different fluorophores.

Two groups of experiments have been performed using externalised PS RBCs, **flow cytometry experiments** and **fluorescence experiments** (confocal microscope). The techniques were complementary, the first one allowing good statistics, whereas the second gave access to individual cells.

3.4.2 Flow cytometry experiment

The principle of a flow cytometry experiment is depicted in figure 3.17 -b. The solution to be analyzed passes a flow cell which ends with a tube allowing cells to get through only in single file. As shown in figure 3.17 -b, individual cells are illuminated by a laser. Forward and side scatter detectors then detect the fluorescence of the cell (if any) and according to the fluorescence emitted from a cell, it is sorted and placed in the appropriate category. For each set of experiments 10 000 events (RBCs) were counted.

Four RBC samples were tested: 1 RBCs with no ionophore but with both dyes (negative control), 2 and 3 externalized PS RBCs with only annexin and only FITC-spectrin respectively and 4 externalized PS RBCs with both dyes (FITC-spectrin first

and then annexin). In all cases, fluorescence of the Annexin channel (band pass filter 585 nm +/ − 21 nm) and of the FITC-tagged spectrin (band pass filter 530 nm +/ − 15nm) were recorded and the distributions plotted. Figure 3.18 summarizes the results.

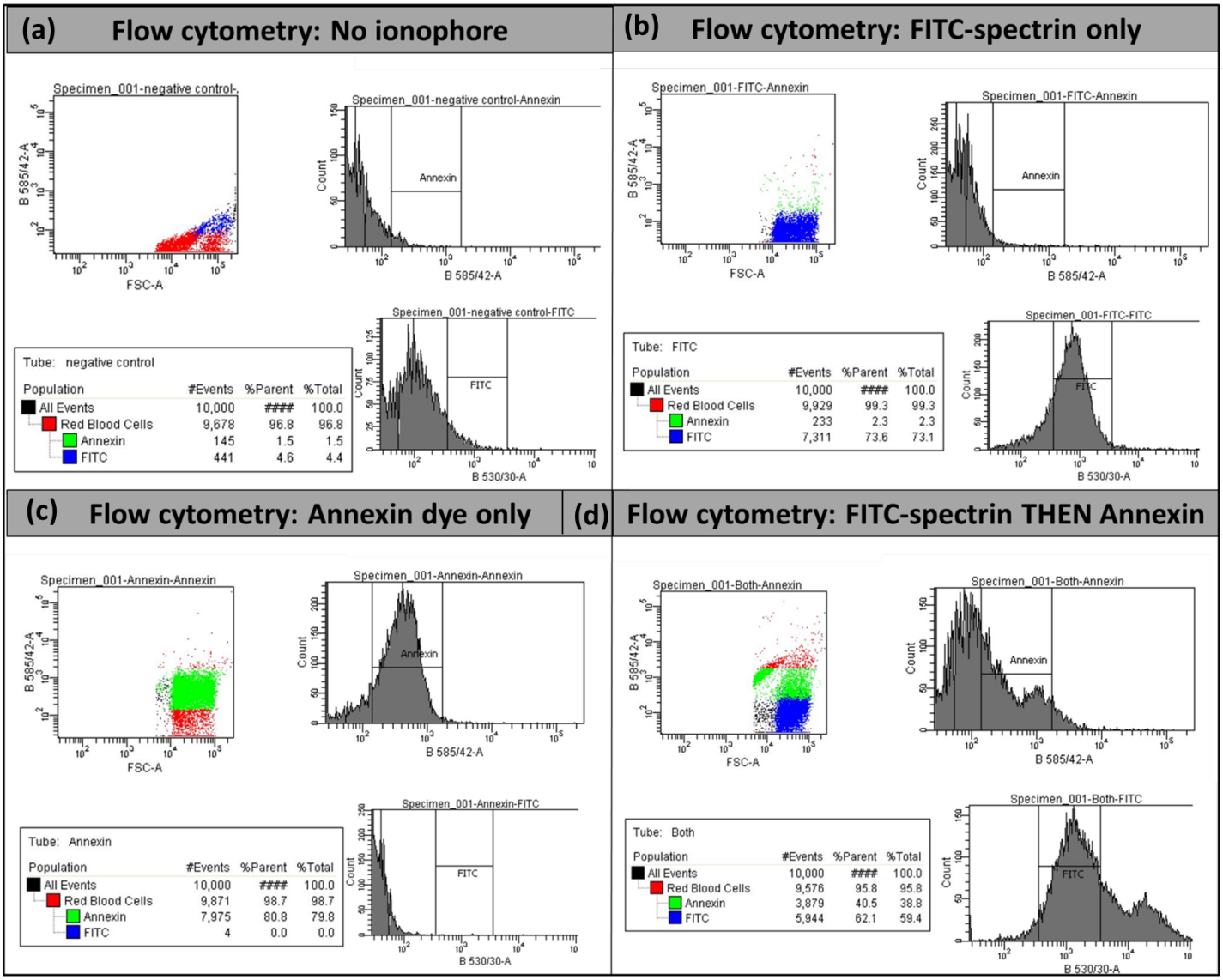

Figure 3.18: Summary table of flow cytometry (FC) measurements performed on RBCs in which PS was externalized by ionophore treatment. In (a) no ionophore was added to the RBCs (no externalization, negative control). (b) Externalized-PS RBCs were incubated with FITC-tagged spectrin (2 hours at 37°C) before FC measurements. (c) Externalized-PS RBCs were incubated for 20 min at RT before FC measurements. (d) externalized-PS RBCs were incubated with FITC-tagged spectrin (2 hours at 37°C) and then with annexin (30 min at RT). In (a) no fluorescence was recorded in any of the FITC nor Annexin channels. In (b) Fluorescence was recorded only in the FITC channel whereas in (c) fluorescence was recorded in the Annexin channel only. In (d), when both dye have been incubated, fluorescence was recorded in both channels. The number of cells exhibiting fluorescence was nonetheless significantly decreased demonstrating that the dyes are quenching each other (competition for the same sites) (see text).

As one can see, in the absence of the ionophore, hardly any cells emit fluorescence (hardly a few percent for FICT and Annexin emits fluorescence and these are probably due to a few lysed cells) whereas when only one dye was incubated, a large amount of cells exhibited fluorescence (up to 73 % in the case of 'FITC-spectrin only' compared to around 80 % for the 'Annexin only' sample) in the corresponding channel demonstrating the capability of both annexin and FITC-tagged spectrin to bind to externalized PS RBCs. A more interesting point arises from the fourth case: as one can see in figure 3.18 d when both dyes were incubated, both fluorescence levels drop quite significantly: 20 % fewer cells emit fluorescence in the FITC channel (compared to when only FITC was added) and 50 % fewer cells emit fluorescence in the annexin channel (compared to when 'only the annexin' was added). In this last experiment, the fluorescence of the annexin drops much more significantly than the FITC. This suggests that spectrin binding inhibits subsequent annexin binding.

3.4.3 Fluorescence: Spectrin and annexin, a competition for the same sites

In a complementary set of experiments, externalized PS RBCs were imaged under the confocal microscope, the fluorescence signals of FITC-tagged spectrin and of annexin were recorded in channel 1 and 2 respectively whereas channel 3 recorded a bright field image of the cells. As one can see in figure 3.19 b, FITC-spectrin did not bind to RBCs in the absence of ionophores (negative control) and in this case, in the presence of calcium, the cells look echinocytic.

On the other hand, ITC-spectrin strongly interacted with lysed cells, the fluorescence level being high and uniform around such cells (see fig. 3.19 c). This demonstrated the potential capability of pure spectrin to highly bind to the native RBCs spectrin network. Finally figure 3.19 d-e, illustrates a typical fluorescence experiment when both dyes were incubated (Annexin first, then FITC-spectrin)[1]. In this particular preliminary experiment, annexin was incubated first and then FITC-spectrin was added, and as one can see, the cells in the annexin channel exhibited more fluorescence than the FITC-channel. For the other experiments when both dyes were involved, FITC-spectrin was incubated first.

As in previous experiments, RBC samples containing no ionophore, externalized PS RBCs incubated with only FITC-spectrin on the one hand, externalized PS RBCs incubated with only annexin on the other hand and externalized PS RBCs incubated

[1] As one can see on the third channel, RBCs do look healthy (*i.e.* no echinocytic cells).

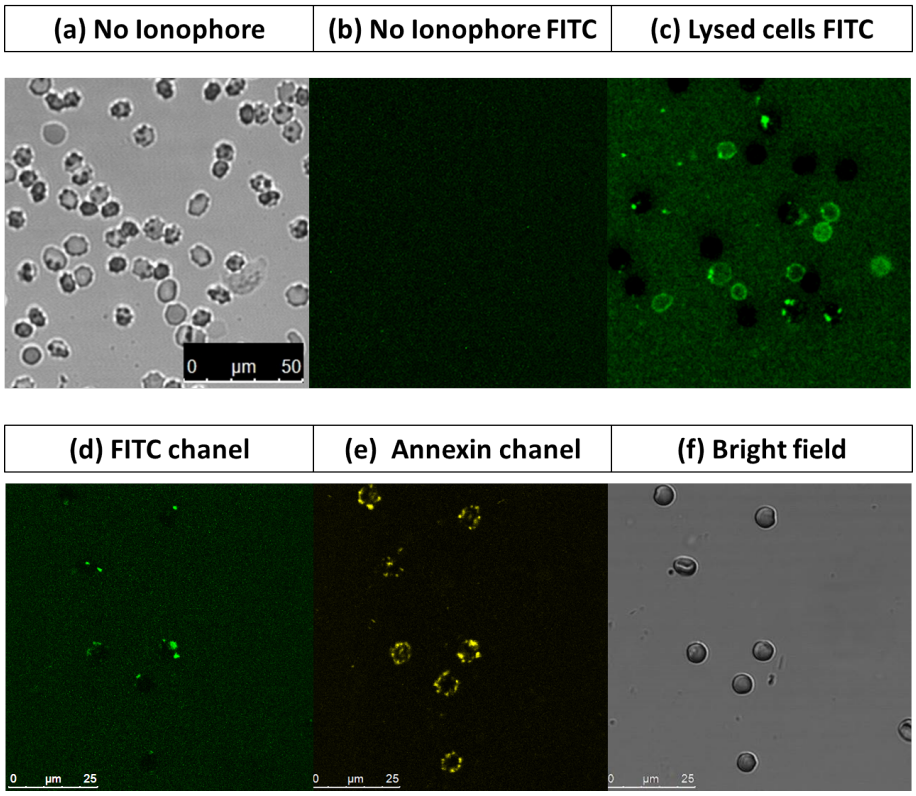

Figure 3.19: Summary table of fluorescence experiments performed on externalized PS RBCs. (a) RBCs become echinocytic in the calcium buffer when no ionophore is added, (b) FITC-spectrin does not bind to RBCs when no ionophore is added (negative control), (c) FITC-spectrin interacts preferentially with lysed RBCs. (d-e) Both Annexin and FITC were added (annexin (20 min, incubation at RT) first then FITC-tagged spectrin (1 hour, incubation at 37 °C)) to externalized-PS RBCs and imaged under the confocal microscope. (d) FITC channel showing the spectrin distribution around RBCs, (e) Annexin channel highlighting the PS domains, (f) Bright field channel: the RBCs did not look echinocytic. Spectrin and Annexin distributions look similar.

with both dyes (FITC-spectrin first, then annexin) were imaged and analyzed. Each measurement was repeated 5 times using different blood samples from healthy volunteers. The presented results are gathered from 5 images from different experiments and the number of PS/spectrin domains per cell were analysed for more than 400 RBCs in each case. Figure 3.20 summarizes the results.

As one can see on graph 1, most cells contain from 4 to 10 domains; For cells with 1 to 3 larger domains, the domains are brighter. Moreover, the longer the incubation of the annexin the higher the number of PS domains there were, until reaching in 'inverted state' where the cells would be uniformly fluorescent surrounding (PS-free) round black domains. As one can see from the bar charts in figure 3.20 (graph 2), when only FITC-spectrin was incubated, the fluorescence was not detected in about a third of the cells (compared to 10 % in the case of annexin). The number of spectrin domains/cell was lower than for annexin. In some cells 1 or 2 brighter domains were noticeable showing

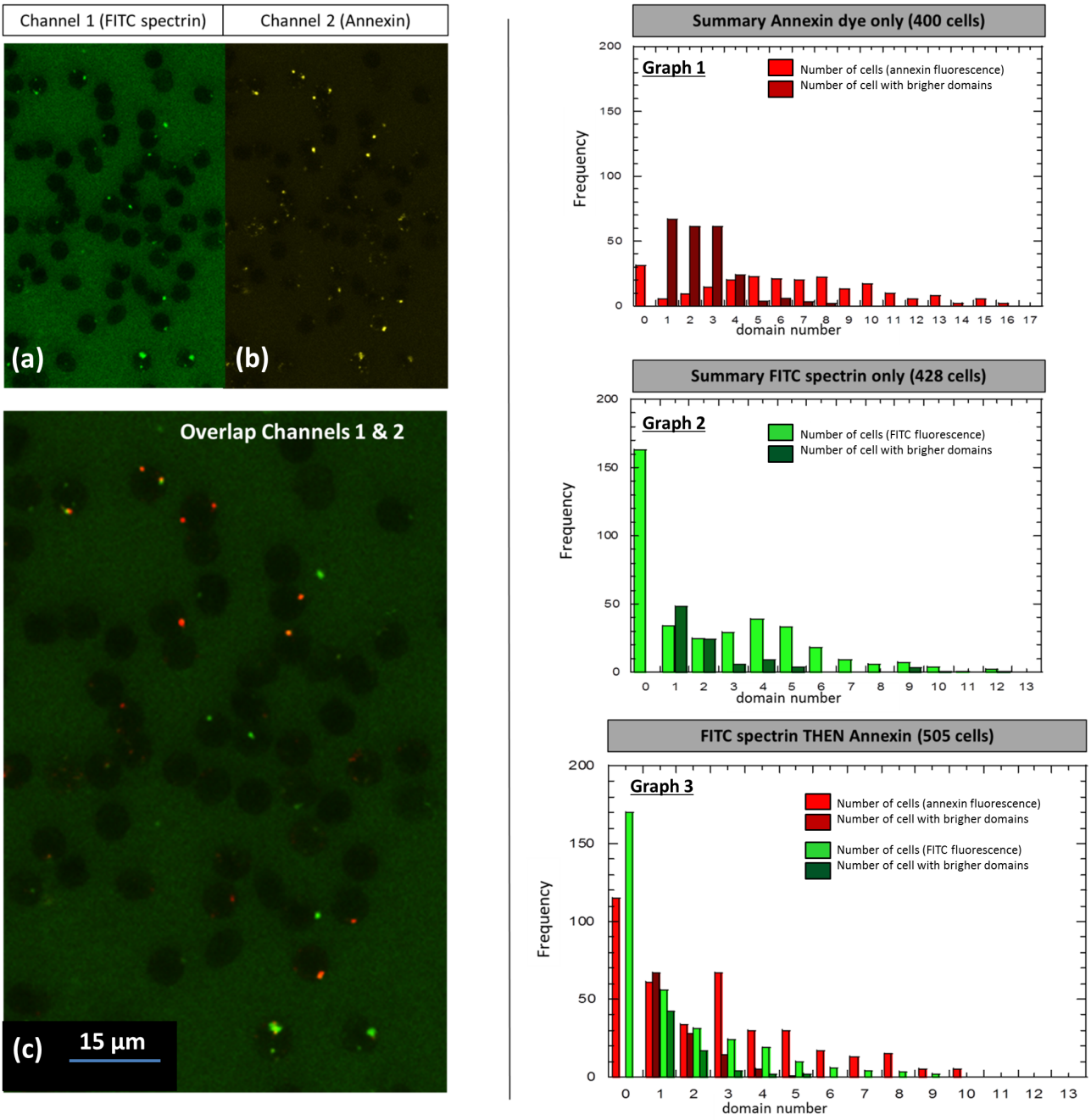

Figure 3.20: Quantitative comparison of PS and spectrin domain distribution in Externalized-PS RBCs: Left: Fluorescence experiment, externalized-PS RBCs were incubated first with FITC-tagged spectrin (1 hour at 37 °C) and then with annexin (30 min at RT). Channel 1 highlights the spectrin distribution (a), Channel 2 highlights the PS domain distribution (b). (c) is a merge picture of (a) (in green) and (b) (red) demonstrating spectrin/annexin competition for the same sites (yellow). In (c), FITC is in green, Annexin in red, overlapping appear in yellow. Right: Graph 1 gives the distribution of PS domains per cell for a population of 400 cells (highlighted with annexin), graph 2 gives the distribution of spectrin domains per cell for a population of 428 cells (highlighted with FITC). Graph 3 gives the distribution of annexin and FITC fluorescence domains per cell for a population of 505 cells (cells were incubated first with FITC (1 hour at 37 °C) and then with annexin (30 min at RT)). The number of fluorescent domains per cell diminishes for both dies suggesting a competiting for the same sites. This corroborates results from FC experiments.

similar behaviour to annexin. Finally when both dyes were incubated, some cells were co-labelled with spectrin and annexin (figure 3.20 c): the overall number of FITC-spectrin domains being similar to when only-FITC was added. However, there was a significant reduction in the number of cells showing annexin fluorescence (unlabelled fraction is now 25% compared to 10 % when only annexin was added). Both the average number of domains and the domains brighness were decreased by a factor of two.

Figure 3.20 a-c illustrates the typical domain distributions of both spectrin (a) and annexin (b) when both dyes were incubated. In figure 3.20 c both annexin and FITC-spectrin domains are in the same places on the RBCs [1], corroborating the results from the flow cytometry experiments and demonstrating that spectrin-interact preferentially with PS in the case of externalized PS RBCs.

3.5 Conclusions and future work

From the fluorescent results presented above (spectrin uniformly binding to PC and exhibiting domain features similar to the PS distribution in PC/PS mixtures) it can be concluded that spectrin interacts with both PC and PS. At this stage it can only be presumed that the mechanisms involved in PC-spectrin and PS-spectrin interactions are likely to be different; mechanisms involved in the binding in both cases remaining unclear. Some groups (see section 1) raised the idea of an electrostatic interaction between the negatively charged lipids and the positively charged part of the spectrin. The fact that spectrin distribution mimics the SOPS distribution could sustain this hypothesis (SOPS lipid is one chain saturated hence SOPC polar heads are closer from one another than DOPS ones).

Fluorescence results of 4-component vesicles demonstrated a very weak spectrin-lipid interactioin (probably with DOPS). This interaction could be an electrostatic interaction as the spectrin did not seemed to hinder domains motions. Further studies in this direction should be carried out to ensure it (FRAP, FCS measurements). It could also be an idea, to hold 4-component vesicles into a micropipette, to investigate the evolution of the microdomains the spectrin weakly binds to, when tension is applied.

Fluorescence experiments performed on GUVs showed that spectrin was likely to interact preferentially with PS. The definite proof came from the experiments on externalized PS RBCs in which annexin and FITC-tagged spectrin were definitely competing

[1] In the overlap montage (c) the annexin color has been changed on purpose from yellow to red for better clarity.

for the same sites, **hence the need for label-free imaging (see Chapter 5 and 6).**

Other groups (see section 1) demonstrated the possibility for spectrin to build beginning of network-like interactions with small vesicles, one spectrin tetramer being able to bind to several SUVs. This aggregation effect was not observed with our GUVs, which might be due to the differences in size of the membrane systems involved[1].

From the difference in fluorescence from one vesicle to another in the same GUVs preparations, the importance of 'single vesicle composition' (*i.e.* the micro-organisation of PC/PS) has been mentioned throughout the chapter and should be studied in greater detail (as it is likely to be of great importance). This could easily be performed studying monolayers whose composition can be precisely monitored. Using fluorescent spectrin and monolayer has already been performed but not in physiological conditions. Using FITC-tagged spectrin and tagging the monolayer with, for example, some NBD-PC lipid, the effect of spectin on the domain composition could be investigated, especially the potential effect of spectin on PC/PS domain boundary could be targeted.

The fact that FITC-spectrin seemed to interact greatly with lysed RBCs raise the question of the possibily for spectrin to interact with RBCs spectrin network. If the complex junction structure of the spectrin network is well-known, remaining available sites for spectrin to bind to, has not been studied in great detail. Further investigation in this area could give significant insights, potentially interesting to understanding some of the diseases in which RBCs shape are degenerated.

Finally, as developed in the introduction part of this chapter, many groups (see section 1) studied the effects of pH and temperature on spectrin-lipid interactions. We tried to be at physiological conditions in these studies (and also for the micropipette aspiration measurements) but studying the effect of differents ions (calcium and sodium for example) could give further insights to prove or deny the electrostatic hypothesis. It would also be interesting to tag the GUVs with other probes, such as voltage sensitive dyes and environmentally sensitive dyes and record the changes in intensity due to spectrin-lipid interaction. Temperature usually induces conformational changes in proteins (denaturation). Conformations of protein can also be altered due to protein-lipid interaction. Conformational changes due to spectrin-lipid interactions will be investigated in Chapter 7. In the next chapter (Chapter 4) the effect of spectrin on membrane

[1]Spectrin filaments are so small compared to GUVs radii that they do not see their curvature (*i.e.* the GUV membrane is as an infinite plane to them.

mechanical properties will be investigated.

Chapter 4

Micropipette aspiration to study protein-lipid interactions and their effects on mechanical properties

In this Chapter, the apparatus built for micropipette aspiration experiments will be described. Scanning electron microscopy charaterization of glass micropipette tips will be presented. Validation of the set-up will be demonstrated using micropipette measurements of well-known GUVs systems. In a second part the effect of an elastic protein, the α-elastin, on SOPC GUVs mechanical properties will be presented before similar measurements on spectrin. Here, the micropipette aspiration measurements were performed on both SOPC and SOPC/SOPS GUVs system with both highly purified spectrin preparation and a crude extract (first peak). Comparison of the results with other techniques will then be made. Finally in the last section results of micropipette aspiration experiments of vesicles labelled with FITC-tagged spectrin will be presented.

4.1 Material and Methods

4.1.1 Micropipette aspiration set-up

Micropipette post

For performing micropipette aspiration (MPA) measurements a micropipette aspiration apparatus was built (inspired from [27], [126] and [127]). It consists of a micro-

scope, a micro-manipulator, a micropipette holder and a hydrostatic pressure reservoir as shown in figure 4.1. It was mounted on an optical table isolator (Thorlabs) in order to minimize vibrations which would compromise the experiment. The phase contrast microscope (Olympus IX 51) was fitted with DIC attachments (Analyzer IX2-MDICT, Polarizor U-DICT, Wollaston prism U-DICT 1x2-DIC60 (Olympus, Japan)). A 60x objective 0.72 NA (LUC Plan FLN (UIS 2) Olympus) used for the imaging. The microscope stage was replaced by a home made plate supporting the micro-manipulator weight. A cut-out on the plate allowed the micropipette holder to reach the sample level (see Appendix part 6). The micromanipulator allowed movement in XYZ directions (PT3A/M, Thorlabs): Three micrometer stages were assembled to allow 2.5 cm translation freedom of motion in each spatial direction with μm precision.

A home made piece links the micro-manipulator to the 'pen-like' micropipette holder. The micropipette holder was a cylindric tube carrying the hydraulic line. 5 mm of the glass micropipette was inserted into the hydraulic line (paying attention to avoid air bubbles) and secured in the micropipette holder. The construction allowed the micropipette inclination to be very accurately monitored. As shown in figure 4.1, a PVC tubing linked the micropipette to the hydraulic reservoir. The reservoir was mounted on a graduated wood column. The hight of the reservoir was adjusted using a micrometer screw and pressures down to - 6 kPa could be applied.

Images were recorded individually using a CCD camera (uc FPGA, vision technologies) and the LA-AS software. Images were then analyzed on ImageJ as it will be described in the next session.

Vesicle chamber

A diagram of the vesicle chamber used for micropipette aspiration experiments is shown in figure 4.1 (see the insert). A microscope slide and a cover slip are held together on 3 sides by a 'U-piece' formed by melting parafilm on a hot-plate. In practice, usually 6 parafilm layers were necessary to ensure a chamber thickness of around 2 mm[1]. During the experiment, the cavity chamber needed to be refilled regularly due to evaporation.

[1] For fluorescence experiment the vesicle chamber only required a single layer of parafilm

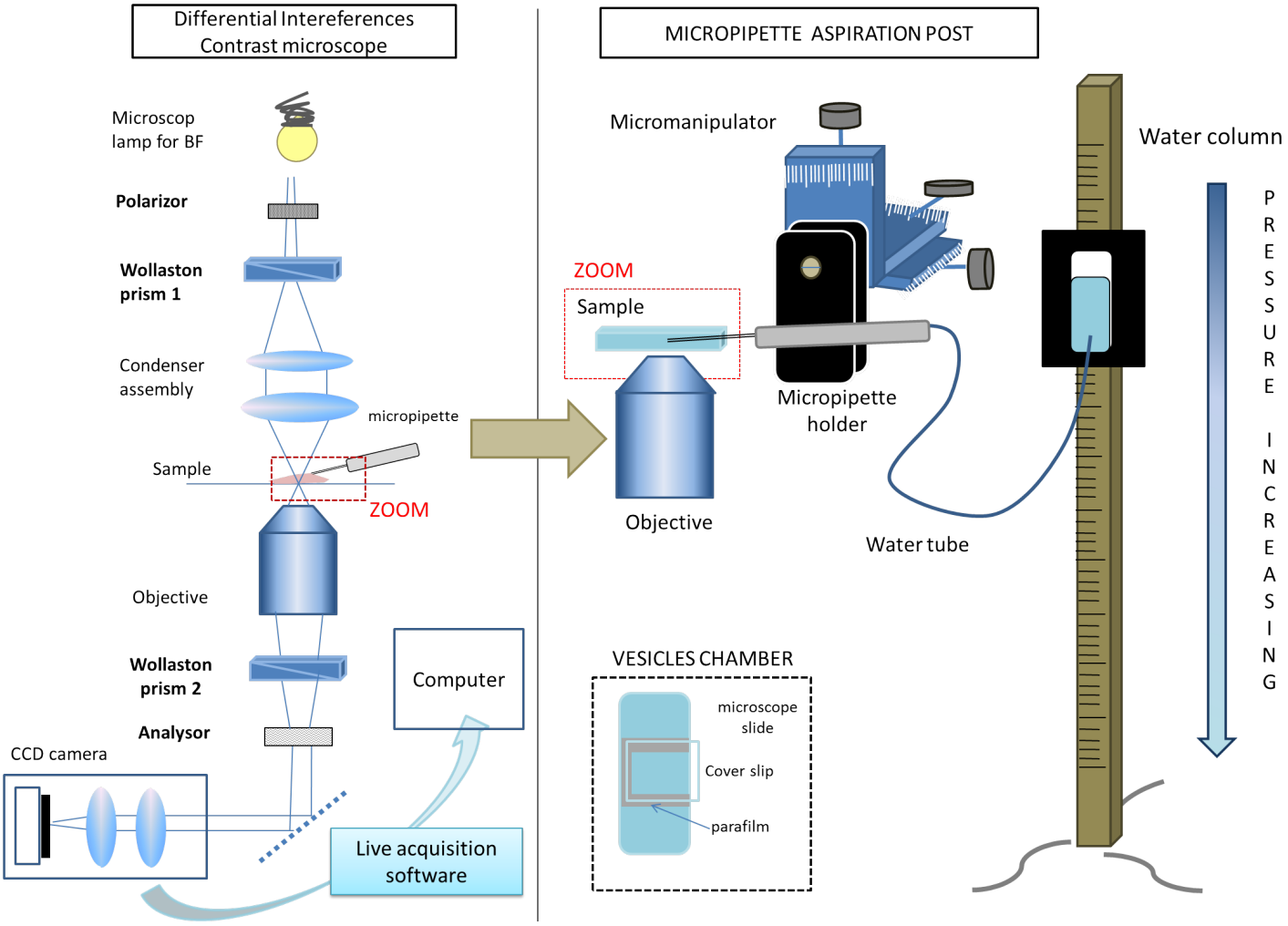

Figure 4.1: Schematic diagram of the micropipette aspiration Set-up.

Glass micropipette

Glass micropipettes were made in two steps. First, a glass capillary (borosilicate glass, outer diameter:1 mm, inside diameter: 0.75 mm diameter, world precision instrument) was pulled using a pipette puller to provide a long parallel-sided tip, approximately 3 μm in internal diameter. To ensure a tip profile which sealed against but did not penetrate the lipid membrane, the tip was then inserted into a blob of soda glass melted on a heated wire; then drawn back on the pipette whilst the bead cooled (see appendix part 4 for illustration).

4.1.2 Scanning Electron Microscopic Measurements of Pipette Tip Diameters

In micropipette aspiration experiments, it is of importance to accurately know the diameter of both the vesicle and the micropipette, the later one being more difficult to measure in bright field images. To ensure that tips diameter could be properly measured, a scanning electron microscope (SEM) has been used.

Micropipettes of different tips size were mounted in the SEM chamber (see figure 4.2 a) and imaged as show in figure 4.2 b, so that a graph linking SEM measurements to DIC images of tips of various diameters could be plotted . The relationship was linear but the slope was 0.7 (fig-4.2). This discrepancy was presumed to arise from distortion of light paths in the pipette wall. However because of the linearity of the relation it was decided not to introduce a correction into the comparative measurements presented below (as all the gradients would be affected in the same proportions).

4.1.3 Measurement protocol

The micropipette aspiration technique has been presented in Chapter 1 (see section 3). Figure 4.4 is a montage illustrating a typical micropipette aspiration experiment. The pressure applied for each measurement is annotated on the bottom right corner of each image. Between each image the reservoir was lowered by 2 cm. After each step change in aspiration pressure, the GUV membrane aspirated in the pipette stabilized within a few seconds. Images were recorded around every 30 seconds, a single experiment lasting less than 10 minutes. As one can see in figure 4.4 a membrane tongue forms and elongates linearly as the negative pressure applied increases (0-3000 Pa).

processing data

Two steps are necessary in the data processing, both of them are illustrated in figure 4.5.First, both the vesicle and micropipette diameter and tongue length were measured by plotting profiles in ImageJ (to pixel resolution) as shown in figure 4.5. The area expansion $\Delta A/A_0$ and the tension $\tau = \sigma$ were calculated using the formulae stated in figure 4.5. All the elements of interest: R_{ves}, R_{pip}, $R_{\text{ves}}/R_{\text{pip}}$, τ_{lysis}, $\Delta A_{\text{max}}/A_0$ and K_A were recorded in a table for each set of GUVs. This ensured that the ratio $R_{\text{ves}}/R_{\text{pip}}$ belonged to the right range and that the vesicle diameters for each set of experiments were well distributed (non biased measurements).

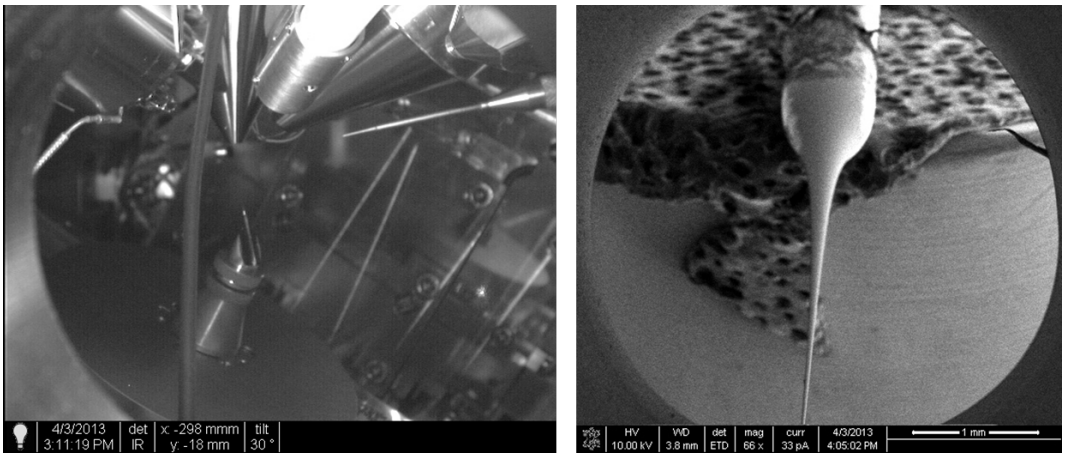

(a) SEM chamber

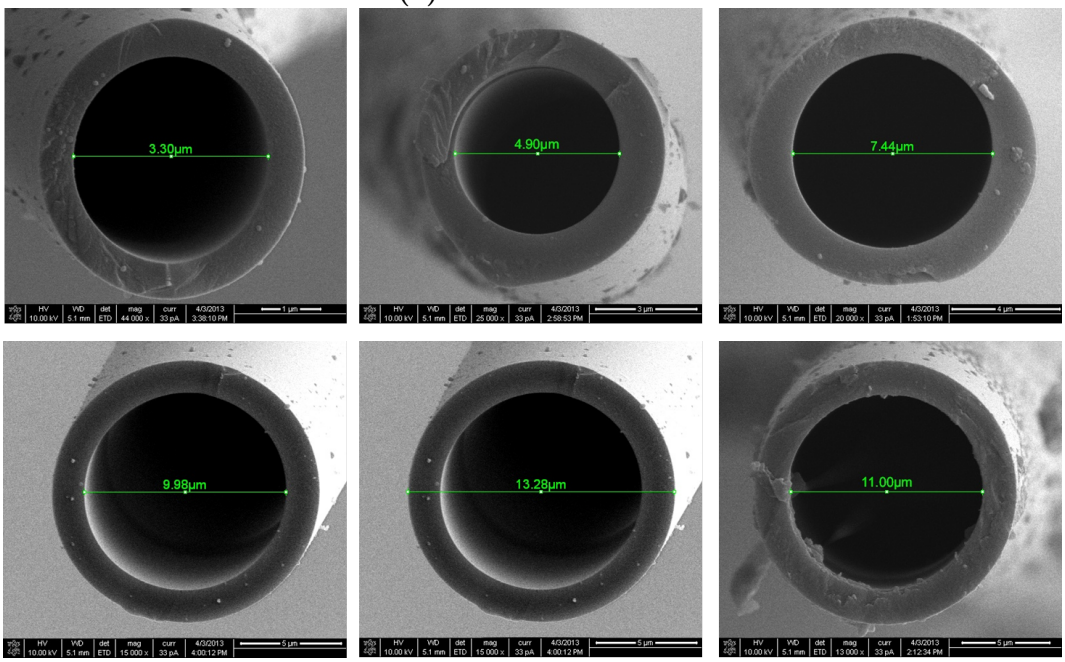

(b) Micropipettes used for characterization

Figure 4.2: Scanning electron microscopy (SEM) images of micropipettes (a) left: SEM chamber, right: a micropipette seen along its axis (b) Montage of SEM images of micropipette tips of different sizes (in front view). The micropipettes were imaged previously under DIC and a characteritic graph could be plotted (see fig. 4.3)

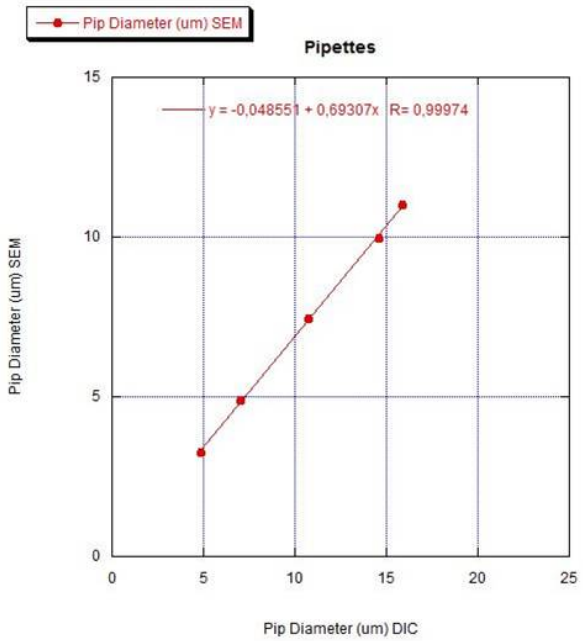

Figure 4.3: Graph linking DIC and SEM micropipette tip measurements. A correcting factor of ~ 0.7 was necessary.

While performing micropipette aspiration data analysis, attention must be paid to the unit systems [128]. A reminder of the equivalences between units (in the international system) is given in figure 4.5 (red insert) (adapted from [128]). The black dotted insert assembles the uncertainties of each parameter and hence on the measurement of K_A which is of importance when trying to evaluate the influence of the proteins on the area expansion modulus of GUVs. The calculation of the relative uncertainties of the tension, the area expansion and on the area expansion modulus are given in Appendix part 4.

4.1.4 Set-up validation: Comparing SOPC and SOPC/Chol vesicles

Once built, the micropipette aspiration apparatus was tested. To do so, SOPC GUVs, a well-known membrane system, were measured and compared to the literature. For further validation, membrane systems consisting in a mixture of SOPC and cholesterol (molar ratio 1:1) were also studied. Figure 4.6 summarizes the measurements.

Measurements on SOPC GUVs (fig 4.6 -a) were quite reproducible, K_A is around 160 mM/m (148.2 +/− 18 mN/m, $n = 7$ [1]). Vesicles 3 and 5 were excluded. They were

[1] mean +/−SD, n is the number of GUVs studied

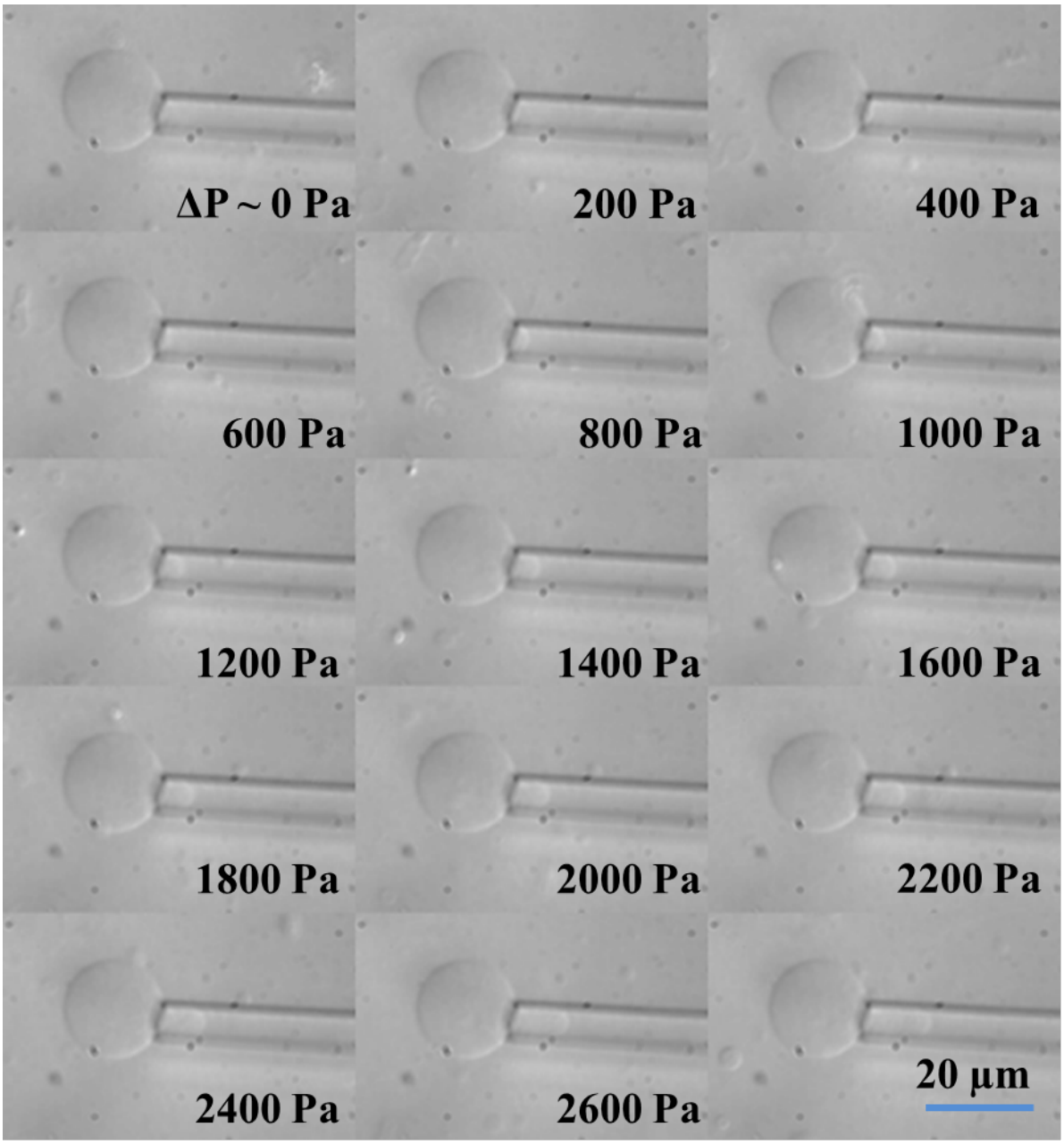

Figure 4.4: Montage of images of a GUVs aspired in a micropipette during a micropipette aspiration experiment (phase contrast microscopy). The pressure applied is provided for each image (right-bottom corner). A tongue forms and elongates linearly within the pipette while the pressure increases.

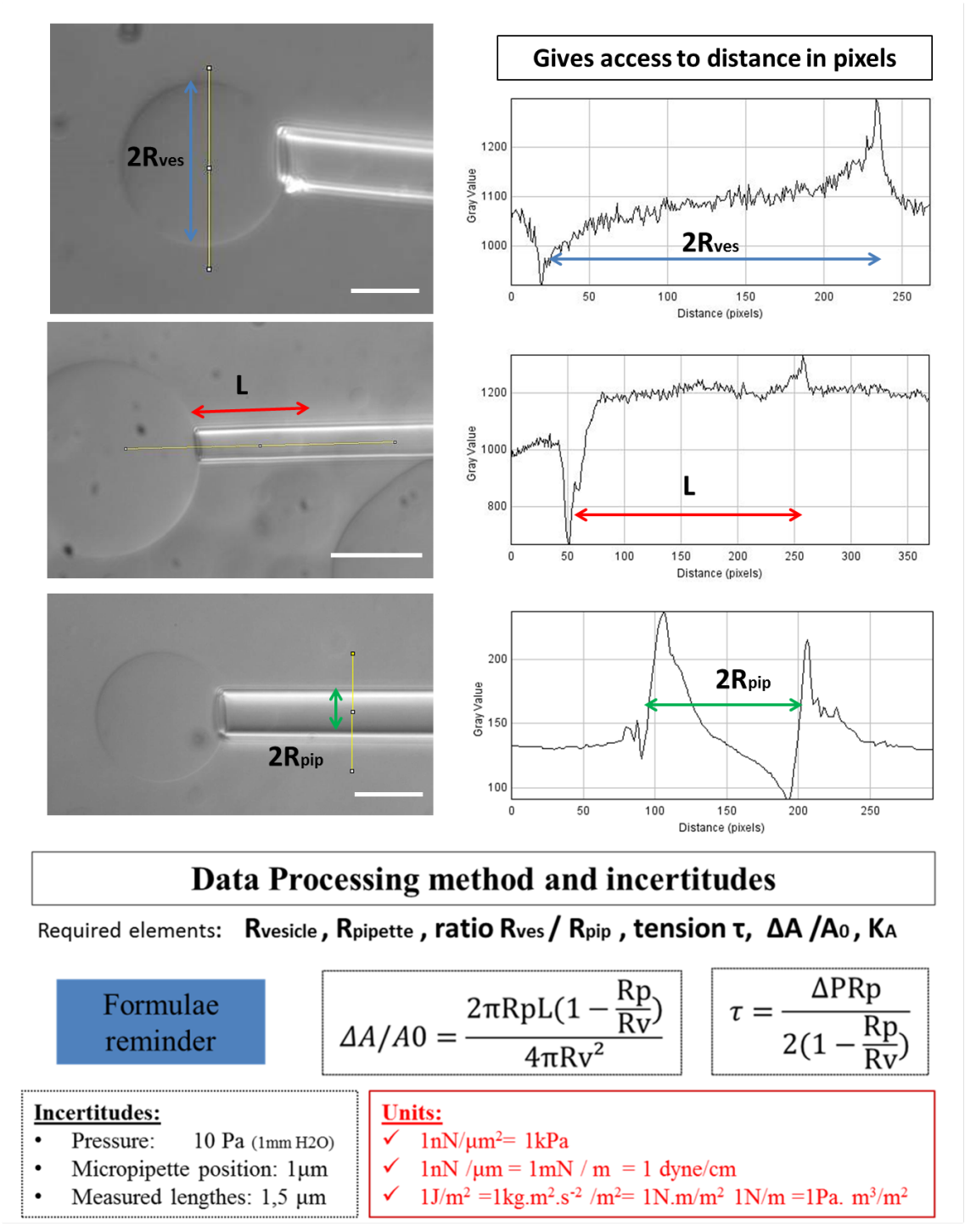

Figure 4.5: Protocol for data processing in micropipette aspiration experiments: The micropipette and vesicle radii (R_{pip} and R_{ves} respectively) and the length of the tongue inside the pipette, L, are measured plotting profile in ImageJ (pixel precision). These 3 measurements, linked to the known pressure, allows to calculate the tension, τ and the relative area expansion, $\Delta A/A_0$. Plotting τ with respect to $\Delta A/A_0$ gives access the area expansion modulus K_A. The red insert provides a list of equivalence between units necessary to calculate τ.

found to constain large quantities of membrane folded and such vesicles were always found to have lower moduli (probably because the internal membrane was continuous with the external). The table on the side in figure 4.6-a shows that the maximum relative area is around a few percents which is in agreement with the theory (see Chapter 1). The ratio R_{ves}/R_{pip} is higher than 3 which is necessary for the theory to be applicable [28] [1].

Measurements on SOPC:Chol (molar ratio 1:1) GUVs (fig 4.6-b) gave an average value for K_A around 400 mN/m (369.4 +/−110 mN/m, $n = 7$), some vesicles being able to withstand a tension up to 10 000 pN/μm. The maximum area expansion remaining similar to the SOPC GUVs. The GUVs radii fell within the same size range (15- 30 μm) in both set of experiments (so were the pipettes).

Comparison with the literature revealed that the measurements were of the expected order of magnitude for both SOPC ([129] [19];[130]; [131]; [132][2] and SOPC:Chol GUVs [133][3] and confirmed that cholesterol stiffened the membrane (see Chapter 1). According to the literature, the area expansion modulus of SOPC GUVs containing cholesterol is 2 to 3 times higher than the SOPC GUVs [133][4], and this is verified in the present work (Figure 4.7). The larger disparity in the value of K_A is believed to be due to the amount of cholesterol which differs from one GUV to another. These measurements demonstrated the functioning of the set-up.

4.2 Elastin-lipid interactions

Elastin is an elastic protein which is present in many tissues such as skin, blood vessels and lung. It is a component of the extracellular matrix which endows the tissues with the elasticity that is essential to their functions. Further description will be provided in Chapter 5. As it will also be explained later, in Chapter 5, two-photon fluorescence experiments showed that elastin uniformly binds to GUVs (see Chapter 5 section 4). Elastin is similar to spectrin in its physical properties: hydrophobic domains and entropy elasticity. It was thus a pertinent protein model to study protein-lipid interaction and ensure that the micropipette aspiration was a relevant method to investigate the effects of elastic protein on cells/membrane mechanical properties.

[1] One wants a ratio between higher than 2- 2.5 , 3.5 being ideal. This is necessary so that the vesicle can be seen as an infinite wall and the theory of micropipette aspiration could be applied.

[2] 180 mN/m [129], 190 mN/m [19]; ∼200 mN/m (Waugh et al., 1993); 235 mN/m (+/−14) [130]; from 189 to 217 mN/m [131]; 212 +/−23 mN/m [132].

[3] Our measurements for K_A may appear slightly lower values but once again this is not that much of importance as we want to investigate the effect of elastic proteins, *i.e.* the measurements were relative.

[4] ∼600 mN/m for SOPC:Chol against ∼200 mN/m for SOPC GUVs [133].

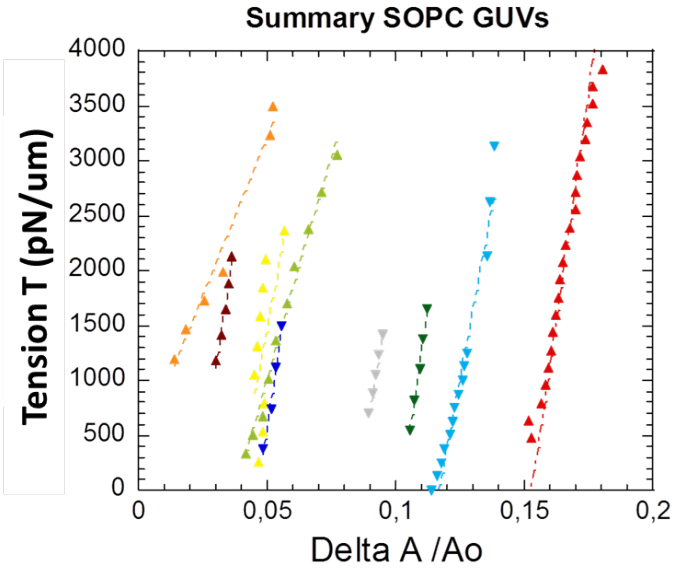

Vesicle number	Ka (mN/m)	Rves	Rves/ Rpip	τlysis (pN/ µm)	ΔA /A max
Ves 1	163.3	15.8 µm	3.47	7987	0.193
Ves 2	162.7	27.9 µm	6.91	2362	0.035
Ves 3	57.9	28.4 µm	6.35	3500	0.052
Ves 4	127.1	33.5 µm	7.35	2369	0.056
Ves 5	81.7	25.5 µm	4.75	3058	0.077
Ves 6	169.6	23.1 µm	5.20	1649	0.112
Ves 7	134.8	21.1 µm	3.99	1411	0.094
Ves 8	152.2	18.2 µm	3.45	1490	0.056
Ves 9	127.9	31.9 µm	7.37	4634	0.095

KA mean (+/- SD) : 148.2 mN/m +/- 18.0 mN/m (ves 3 & 5 discarded)

(a) Micropipette aspiration on SOPC GUVs

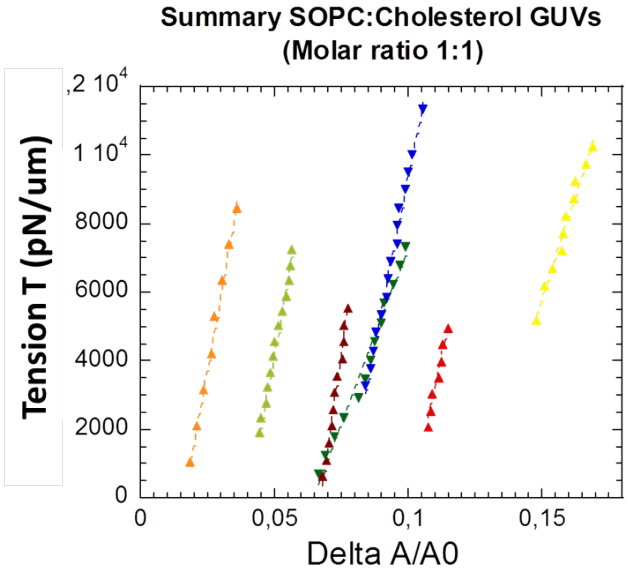

Vesicle number	Ka (mN/m)	Rves	Rves/ Rpip	τlysis (pN/ µm)	ΔA /A max
Ves 1	376.6	18.2 µm	4.77	4961	0.115
Ves 2	521.1	22.8 µm	5.63	5530	0.077
Ves 3	430.7	27.9 µm	7.66	8455	0.036
Ves 4	246.1	16.9 µm	4.34	10250	0.169
Ves 5	417.4	22.5 µm	5.21	7240	0.056
Ves 6	201.8	25.5 µm	5.60	7340	0.099
Ves 7	392.5	16.7 µm	4.20	1133	0.105

KA mean (+/- SD) : 369.4 mN/m +/- 110.3 mN/m (no ves discarded)

(b) Micropipette aspiration on SOPC:Cholesterol GUVs (molar ratio 1:1)

Figure 4.6: Summary graph of MPA measurements on (a) SOPC GUVs and (b) SOPC: Chol GUVs (molar ratio 1:1). For each set of measurement the tension τ (in mN/m) is plotted as a function of the relative area expansion $\Delta A/A_0$. A linear regression gives access to the area expansion modulus K_A. A table on the side recapitulates the measurements giving in addition of K_A the lysis tension τ_{lysis} , the radius of the vesicle R_{ves} and the ratio $R_{\text{ves}}/R_{\text{pip}}$ which needs to be higher than 2 for the theory to be applicable. The mean value and standard deviation of the element of interest, K_A, is provided in bold below the summary tables.

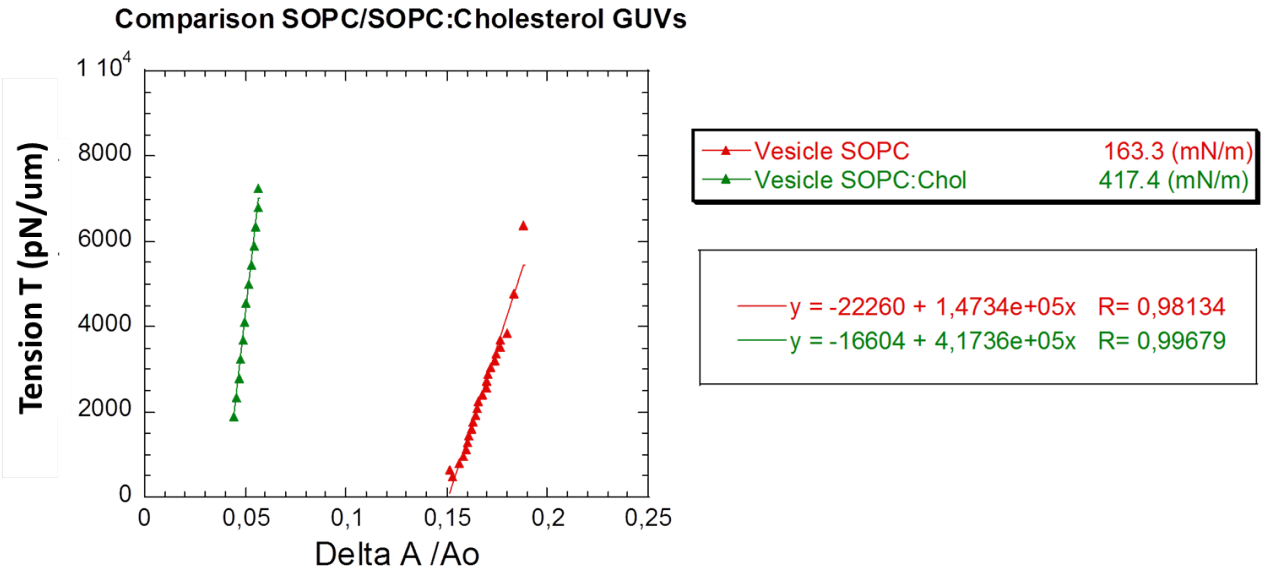

Figure 4.7: Effect of cholesterol on vesicles area expansion modulus K_A: Summary graph. The area expansion modulus of SOPC:Chol GUVs (molar ratio 1:1) is 2 to 3 times higher than the one of SOPC GUVs which is in good agreement with the literature (see text).

The elastin used was α-elastin prepared following the Partridge protocol [134]. The freeze-dried protein was diluted in various concentrations into a sucrose solution (200 mM) and incubated at 4°C overnight before use. The elastin solution was then mixed with the vesicle solution - consisting of SOPC GUV made by electroformation - at a 1:1 volume ratio of elastin/vesicle solutions. The resulting elastin-GUV solution was incubated for one hour at 37°C before the micropipette aspiration was performed.

4.2.1 Micropipette aspiration results

Since the concentration of the α-elastin solution used in the TPF experiment was 5 mg/ml, it was decided that effect of α-elastin solution containing 2, 5 and 10 mg/ml of the protein, would be studied. The 4 sets of experiments (**GUVs + α-elastin 2 mg/ml, GUVs + α-elastin 5 mg/ml, GUVs + α-elastin 10 mg/ml and GUVs without elastin (negative control)**) were performed on the same day to ensure that the protein and the SOPC GUVs would be studied in the same experimental conditions (*i.e* no oxydation of the lipid, no conformational change of the protein due to being in sucrose for too long etc).

Figure 4.8 gives summary tables for each set of experiments. The micropipette aspiration data analysis graphs are given in the Appendices. As one can see from the negative control, the area expansion modulus of SOPC GUVs is around 190 mN/m (193.2 +/−

22 mN/m, $n = 6$), most of the GUVs withstanding a tension over 6500 pN/μm before bursting. When mixed with 2 mg/ml α-elastin (*i.e.* when the elastin solution is 1 mg/ml in the GUV-α-elastin solution), the area expansion modulus increases: for all the measured GUVs, K_A is higher than 220 mN/m, with an average value of around 230 mN/m (234.3 +/− 12 mN/m, $n = 11$) and most GUVs can withstand in this case a tension over 9000 mN/m before lysing.

(a) Summary SOPC GUVs (electroformation)

Vesicle number	Ka (mN/m)	Rves	Rves/ Rpip	τlysis (pN/ µm)	ΔA /A max
Ves 1	103.2	14.1 µm	2.98	4354	0.104
Ves 2	182.0	17.9 µm	3.53	2829	0.054
Ves 3	121.0	19.0 µm	2.63	3478	0.072
Ves 4	297.0	35.0 µm	5.22	7043	0.038
Ves 5	232.5	26.5 µm	4.76	6730	0.082
Ves 6	192.2	22.9 µm	4.33	6531	0.078
Ves 7	193.3	20.3 µm	3.58	7849	0.106
Ves 8	196.0	20.7 µm	3.56	7660	0.130
Ves 9	163.7	19.6 µm	3.29	6413	0.059

KA mean (+/- SD) : 193.3 mN/m +/- 22.5 mN/m (ves 1, 3, 4 discarded)

(b) Summary SOPC + Elastin 2mg/ml

Vesicle number	Ka (mN/m)	Rves	Rves/ Rpip	τlysis (pN/ µm)	ΔA /A max
Ves 1	245.8	20.0 µm	3.75	4799	0.039
Ves 2	211.3	15.8 µm	3.47	6708	0.059
Ves 3	239.0	18.5 µm	3.65	9424	0.087
Ves 4	219.9	21.9 µm	4.45	4758	0.073
Ves 5	244.2	23.0 µm	4.89	6793	0.040
Ves 6	238.1	16.4 µm	3.67	10154	0.091
Ves 7	242.1	14.5 µm	3.08	10786	0.135
Ves 8	231.4	29.6 µm	5.92	7518	0.081
Ves 9	249.9	19.6 µm	4.24	9391	0.051
Ves 10	235.6	11.3 µm	2.54	9077	0.120
Ves 11	220.6	14.9 µm	3.38	7414	0.109

KA mean (+/- SD) : 234.4 mN/m +/- 12.2 mN/m (no ves discarded)

(c) Summary SOPC + Elastin 5mg/ml

Vesicle number	Ka (mN/m)	Rves	Rves/ Rpip	τlysis (pN/ µm)	ΔA /A max
Ves 1	160.2	26.1 µm	3.44	4798	0.077
Ves 2	188.1	23.7 µm	3.47	4319	0.096
Ves 3	153.1	23.4 µm	3.15	5434	0.070
Ves 4	200.0	21.2 µm	3.06	6668	0.091
Ves 5	224.1	22.9 µm	4.00	6110	0.060
Ves 6	169.0	23.7 µm	4.08	4993	0.082
Ves 7	176.0	17.8 µm	2.81	5391	0.109
Ves 8	186.0	20.8 µm	3.49	3333	0.108
Ves 9	200.2	18.9 µm	2.95	7725	0.121
Ves 10	207.0	13.6 µm	3.32	3085	0.071
Ves 11	190.5	12.7 µm	3.14	4736	0.096
Ves 12	192.2	15.0 µm	3.64	3962	0.117
Ves 13	152.0	18.6 µm	4.60	5935	0.083
Ves 14	174.0	10.2 µm	2.65	5206	0.142
Ves 15	151.0	13.8 µm	3.40	4290	0.096
Ves 16	173.1				

KA mean (+/- SD) : 181.0 mN/m +/- 21.3 mN/m (ves 3 & 5 discarded)

(d) Summary SOPC + Elastin 10mg/ml

Vesicle number	Ka (mN/m)	Rves	Rves/ Rpip	τlysis (pN/ µm)	ΔA /A max
Ves 1	150.7	13.7 µm	2.88	2921	0.046
Ves 2	119.0	15.9 µm	3.04	3417	0.108
Ves 3	149.0	13.0 µm	2.91	2812	0.053
Ves 4	158.4	11.4 µm	2.40	4030	0.053
Ves 5	52.1	11.6 µm	2.48	1590	0.054
Ves 6	164.4	15.1 µm	3.37	4048	0.285
Ves 7	195.3	19.9 µm	2.75	4331	0.041
Ves 8	190.5	17.0 µm	3.62	2449	0.079
Ves 9	187.7	16.0 µm	3.40	4656	0.104
Ves 10	156.4	13.4 µm	2.95	6532	0.120
Ves 11	179.2	12.9 µm	2.79	2883	0.110
Ves 12	253.8	15.8 µm	3.04	7387	0.061

KA mean (+/- SD) : 173.1 mN/m +/- 34.8 mN/m (ves 3 & 5 discarded)

Figure 4.8: Summary tables of micropipette aspiration experiments performed on SOPC GUVs mixed with elastin in different concentrations: (a) No elastin (negative control), (b) elastin 2 mg/ml, (c) Elastin 5 mg/ml and (d) 10 mg/ml. For the calculation of the mean value of the area expansion K_A vesicles whose ratios $R_{\text{ves}}/R_{\text{pip}}$ were below 2 and the ones whose K_A was very low (MLVs) have been discarded.

At an α-elastin concentration of 2.5 mg/ml (SOPC + 5 mg/ml case), 2 features were evident. The area expansion modulus of some of the vesicles - vesicles 2, 4, 8, 9, 11 and 12- seemed unaffected by the addition of elastin their K_A staying equal to when no protein is added $\sim$190 mN/m (192.7 +/− 6 mN/m, $n = 6$) whereas other vesicles became slightly softer - vesicles 1,3, 6, 7, 13-16- with a $K_A \sim 165$ mN/m (163.9 +/− 10.3 mN/m, $n = -$). At longer times, vesicles 5 and 10 showed a K_A increasing to 210 mN/m. However, almost all the vesicles burst at a tension between 4500 and 5500 pN/μm even the ones whose K_A were higher.

These two effects (lower τ_{lysis} and slightly lower K_A) are even more distinctive at a higher α-elastin concentration (SOPC + 10 mg/ml case). If the K_A of some vesicles is still around 190 mN/m -vesicles 7-9 (and 11)- most vesicles became even softer with an average area expansion modulus around 155 mN/m (155.8 +/− 6.2 mN/m, $n = 5$) and the overall average lysis tension was further decreased; down to the range 3000 - 4500 pN/μm.

As one can verify in the other columns, for 3 set of experiments the distribution of GUV size were comparable (belonging to the 15 - 25 μm range), for the 4 th one (10 mg/ml case) the distribution was very slightly smaller (11 - 20 μm) which in these proportions did not disturb the results as in all the measurements, the ratio $R_{\text{ves}}/R_{\text{pip}}$ were similar. Finally, elastin did not seem to induce any change in the maximum relative area expansion (see the $\Delta A/A_{\text{max}}$ columns).

Summary: Elastin effect on SOPC GUVs mechanical properties

Figure 4.9 summarises the effect of α-elastin on the SOPC GUVs. The first graph (fig. 4.9-a) gives the tension as a function of the relative area expansion of a typical GUV for each concentration of elastin tested whereas the second graph (fig.4.9-b) gives the evolution of both the lysis tension and the area expansion modulus as a function of the elastin concentration. From the second graph, 2 regimes could be identified. At low concentration of elastin (addition of elastin solution whose concentration belongs to 0 -2 mg/ml), the α-elastin stiffens the membrane (both K_A and τ_{lysis} increasing) whereas at higher concentrations (addition of elastin solution whose concentration was higher than 5 mg/ml), the α-elastin softens the membrane. In the latter regime, the lysis tension is greatly affected, falling to half compared to the tension of the negative control (SOPC GUV), whereas the area expansion modulus is affected to a smaller extent, its value being decreased by less than 20 % when 10 mg/ml of elastin is added compared to the negative control.

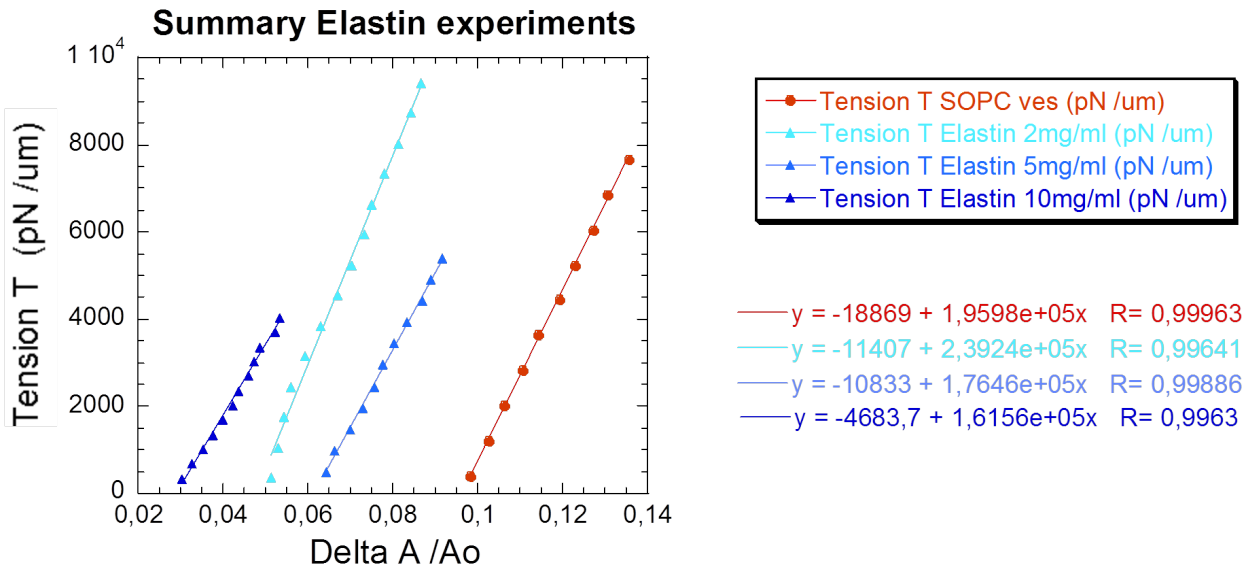

(a) Summary of Micropipette aspiration measurements on SOPC incubated with elastin.

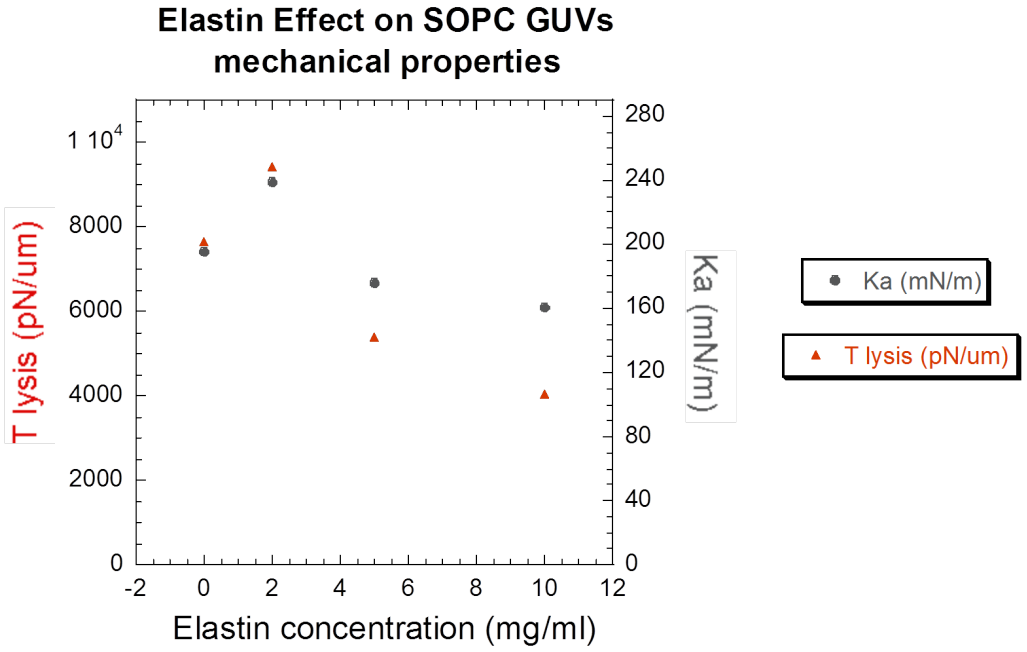

(b) Elastin effect τ_{lysis} and K_A of SOPC GUVs

Figure 4.9: Elastin effects on SOPC Giant Unilamellar Vesicle mechanical properties. (a) Summary graph providing the tension, τ, with respect to the relative area expansion, $\Delta A/A_0$, giving a MPA measurement for each set of experiments (0, 2, 5 and 10 mg/ml of elastin). Linear regressions are provided on the side. (b) Summary graph illustrating the effect of the elastin on the lysis tension τ_{lysis} and the area expansion modulus K_A. Both are plotted with respect to the concentration of the protein. At low concentrations (below 2.5 mg/ml), the elastin stiffens the membrane, whereas at higher concentration (above 2.5 mg/ml) the protein softens it.

4.2.2 Discussion

In parallel with the above studies, a post doctoral researcher (David Woods) investigated elastin-lipid interactions using fluctuation spectroscopy[1]. In this experiment, α-elastin in various concentrations was added to RBCs and their thermal fluctuations following the protein addition recorded in movies [2]. Fluctuation studies of RBCs consist in measuring shape fluctuations in the membrane, decomposing them into fundamental modes, which can then be related to the shears and bending moduli of the membranes.

Figure 4.10 gives an outline of the results, for 3 sets of concentrations for the α-elastin : 0 (negative control), 0.5 and 2 mg/ml. As one can see, at low concentration no change occured (the ninth mode remains constant at zero in both 0.5 mg/ml and 'no elastin' cases). On the other hand, at higher concentration (2 mg/ml) significant changes happened in the RBCs shapes (see evolution in the RBCs shape at the top), the amplitude of the ninth mode increasing greatly within minutes - the total duration of the experiments for each concentration studied was less than 7 minutes. At 5 mg/ml this effect on c_9 happens in a shorter time scale to a greater amplitude (data not shown).

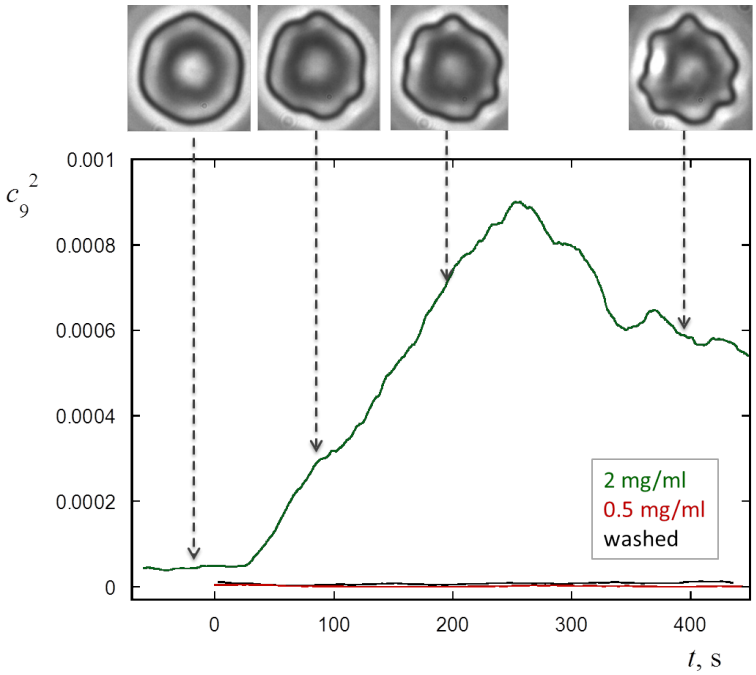

Figure 4.10: Thermal Fluctuation measurements of the ninth mode of RBCs after addition of elastin for different elastin concentrations (0, 0.5 and 2 mg/ml). Data from David Woods.

[1] For some explanation about this technique one can refer to [135].
[2] As said in Chapter 1, RBCs were reported to be fluctuating

These results are consistent with our micropipette aspiration measurements in showing 2 regimes in the elastin-lipid interactions: initially, the elastin stiffens the membrane, inducing no apparent change in shape whereas in the second regime the protein affects both its shape (becoming echinocytic) and area expansion modulus, making the membrane softer. Further interpretation of the action of elastin on the lipid membrane and its effects on mechanical properties will be provided in the discussion about elastin in Chapter 5.

4.3 Spectrin-lipid interactions

4.3.1 Micropipette aspiration results

Micropipette aspiration was performed on the two systems of GUVs previously studied in fluorescence experiments: SOPC and a mixture of SOPC and SOPS (molar ratio 70:30), both grown with the swelling method. The pure preparation of spectrin kept in glycerol was first tranferred into PBS buffer (osmolarity 200 mOsm to match the osmolarity of the sucrose solution of GUVs) using concentrators. Immediately after the change of media spectrin was mixed with the GUVs solution (volume ratio 1:1) and incubated for 2 hours at 37°C, to reproduce the conditions of the fluorescence experiments (see Chapter 3). To obtain contrast under the DIC microscope glucose solution was added to the spectrin/GUVs solution before filling the micropipette aspiration chamber. The concentration of spectrin after change of media was calculated using the nanodrop machine.

Figure 4.11 summarises all the measurements undertaken. The micropipette aspiration data analysis graphs are given in the Appendices. Only one concentration of spectrin (1 mg/ml) was tested for SOPC vesicles whereas several concentrations (0.3 mg/ml, 0.8 mg/ml and 1 mg/ml) were tried for SOPC/SOPS vesicles. The focus on this later system derives from conclusions from Chapter 3, in which spectrin is believed to be interacting preferentially with PS.

In the cases of negative controls, the distribution of the area expansion modulus was wider than before, giving an average value slightly higher for SOPC/SOPS (216.4.1 +/− 39 mN/m, $n = 13$) than for SOPC (204.5 +/− 31 mN/m, $n = 6$) which was believed to be due to the presence of SOPS. In both cases, vesicles whose R_{ves}/R_{pip} ratio was below 2 were rejected. Radii of both set of experiments were well distributed within the 10 - 15 μm range. Compared to the previous experiments with elastin, vesicles were able to withstand higher tensions before bursting, up to 16 000 - 19 000 pN/μm.

(a) Summary SOPC GUVs (swelling)

Vesicle number	Ka (mN/m)	Rves	Rves/ Rpip	τlysis (pN/ µm)	ΔA /A max
Ves 1	255.3	26.7 µm	2.80	9650	0.165
Ves 2	355.5	14.8 µm	1.54	24319	0.086
Ves 3	203.1	12.7 µm	3.20	8079	0.075
Ves 4	193.4	13.0 µm	2.72	16192	0.128
Ves 5	188.1	12.6 µm	2.49	19038	0.240
Ves 6	220.8	15.8 µm	3.11	15113	0.103
Ves 7	163.6	15.0 µm	3.20	12465	0.153

KA mean (+/- SD): 204.1 mN/m +/- 31.3 mN/m (ves 2 discarded)

(b) Summary SOPC :SOPS 70:30 (molar ratio)

Vesicle number	Ka (mN/m)	Rves	Rves/ Rpip	τlysis (pN/ µm)	ΔA /A max
Ves 1	256.1	13.6 µm	2.76	16574	0.099
Ves 2	147.8	13.3 µm	2.96	7093	0.051
Ves 3	154.8	11.4 µm	2.94	16546	0.130
Ves 4	260.1	15.3 µm	3.17	18069	0.083
Ves 5	236.1	12.8 µm	2.50	21822	0.126
Ves 6	196.0	15.7 µm	3.06	8011	0.417
Ves 7	248.1	14.2 µm	2.84	19687	0.097
Ves 8	242.5	13.2 µm	2.63	23788	0.125
Ves 9	227.7	13.1µm	2.83	11104	0.089
Ves 10	235.1	18.3 µm	3.60	23143	0.117
Ves 11	169.7	16.5 µm	3.79	10777	0.193
Ves 12	188.9	15.4 µm	3.75	15683	0.112
Ves 13	249.6	10.8 µm	2.22	18047	0.128

KA mean (+/- SD): 216.4 mN/m +/- 39.8 mN/m (no ves discarded)

(c) Summary SOPC + Spectrin 1 mg/ml

Vesicle number	Ka (mN/m)	Rves	Rves/ Rpip	τlysis (pN/ µm)	ΔA /A max
Ves 1	259.3	22.6 µm	4.65	7721	0.053
Ves 2	200.2	16.1 µm	3.65	13058	0.092
Ves 3	197.6	16.2 µm	3.44	2981	0.081
Ves 4	233.1	20.6 µm	4.67	7015	0.073
Ves 5	306.8	14.9 µm	3.13	**13673**	0.093
Ves 6	258.1	16.9 µm	3.59	**10089**	0.108
Ves 7	213.6	24.6 µm	4.59	3768	0.103
Ves 8	637.3	16.1 µm	3.27	7439	0.050

KA mean (+/- SD): 238.4 mN/m +/- 39.3 mN/m (ves 8 discarded)

(d) Summary SOPC :SOPS + Spectrin 1mg/ml

Vesicle number	Ka (mN/m)	Rves	Rves/ Rpip	τlysis (pN/ µm)	ΔA /A max
Ves 1	147.2	20.8 µm	3.94	3188	0.086
Ves 2	252.0	19.1 µm	3.61	17190	0.087
Ves 3	249.9	14.9 µm	2.90	12154	0.143
Ves 4	131.0	14.7 µm	3.14	5170	0.118
Ves 5	182.4	16.7 µm	3.85	7893	0.070
Ves 6	189.9	13.1 µm	2.87	8033	0.134
Ves 7	191.5	13.7 µm	3.11	7466	0.101
Ves 8	162.3	18.0 µm	3.34	8377	0.118

KA mean (+/- SD): 194.5 mM/m +/- 40.4 mN/m (ves 4 discarded)

Studying the effect of Spectrin on the area expansion modulus of SOPC and SOPC:SOPS (molar ratio 70:30) GUVs.

(e) Summary SOPC:SOPS + Spectrin 0.3mg/ml

Vesicle number	Ka (mN/m)	Rves	Rves/ Rpip	τlysis (pN/ µm)	ΔA /A max
Ves 1	324.0	9.9 µm	1.82	30717	0.130
Ves 2	306.5	13.1 µm	2.58	14895	0.081
Ves 3	224.4	8.9 µm	1.77	13410	0.150
Ves 4	236.0	11.8 µm	2.48	15231	0.130
Ves 5	306.4	9.2 µm	1.95	15873	0.096
Ves 6	468.2	8.6 µm	1.83	24804	0.087
Ves 7	501.0	10.3 µm	2.19	22927	0.109

KA mean (+/- SD): 338.1 mN/m +/- 107.3 mN/m (no ves discarded)

(f) Summary SOPC:SOPS + Spectrin 0.8mg/ml

Vesicle number	Ka (mN/m)	Rves	Rves/ Rpip	τlysis (pN/ µm)	ΔA /A max
Ves 1	171.5	6.3 µm	2.31	11966	0.105
Ves 2	215.0	8.7 µm	3.05	8285	0.061
Ves 3	232.7	13.1 µm	3.24	3799	0.062
Ves 4	201.4	11.4 µm	2.71	13588	0.091
Ves 5	135.9	9.8 µm	3.05	8891	0.100
Ves 6	210.2	11.6 µm	2.92	11161	0.078

KA mean (+/- SD): 206.5 mN/m +/- 35.0 mN/m (ves 5 discarded)

Further measurements of Spectrin on the area expansion modulus.

Figure 4.11: Summary tables of MPA experiments performed on (a) SOPC GUVs (negative control), (b) SOPC:SOPS (molar ratio 70:30) GUVs (negative control), (c) SOPC GUVs incubated with spectrin (1 mg/ml); (d-f) SOPC/ SOPS GUVs incubated with spectrin at: (d) 1 mg/ml, (e) 0.3 mg/ml and (f) 0.8 mg/ml.

Studies on SOPC/SOPS GUVs with addition of spectrin (0.3 mg/ml and 0.8 mg/ml) were performed on the same day and with the same GUVs preparation as the negative SOPC/SOPS control. Further measurements with 1 mg/ml of spectrin were performed later on with new GUVs preparations from different stock lipid solutions. At the time it did not seemed necessary to repeat the negative controls as GUV from one preparation to another were thought to have the same mechanical properties.

As one can read from table d in figure 4.11, the addition of 0.8 mg/ml of spectrin did not seemed to have any effect on the area expansion modulus. The distributions of K_A with and without spectrin looked similar with an average K_A of 194.4 +/− 35 mN/m (206.2 mN/m +/− 22.5 mN/m when excluding vesicle 5) which is similar to the negative control considering the high standart deviation. When only 0.3 mg/ml of spectrin is added, spectrin effect seemed at first look, more pronounced. However in this case, most of the measurements had to be discarded as the ratio was below 2. The number of remaining GUVs was then not large enough to be able to draw conclusions.

When 1 mg/ml of pure spectrin was mixed with the vesicles, no significant changes were observed in any of the two membrane systems ($K_A = 238.4$ mN/m +/− 39.3 mN/m for SOPC and 194.5 mN/m +/− 40.4 mN/m for SOPC/SOPS); except for vesicles 5 and 8 of the SOPC set whose K_A are significantly higher which reflect the need for further measurements; these behaviours were believed to be due to the lipid systems more than due to the protein as spectrin interact preferentially with PS. The K_A values of SOPC/SOPS GUVs with spectrin were slightly lower compared to the negative control set which is also believed to be due to the lipid used [1]. There was thus a real need for getting negative controls for each set of GUVs preparations.

4.3.2 Discussion

Summary: Spectrin effect on GUVs mechanical properties

Figure 4.12-a summarises the lack of effect of spectrin on both GUVs compositions. Cholesterol effect has been added for comparison. Experimentally, it is generally quite difficult to demonstrate a lack of effect as one has to ensure that this is not a negative 'artefact'. In the present case, to conclude that the spectrin has no effect on the mechanical properties of GUVs one needs to be sure that the spectrin is ad- or absorded into the vesicle membrane studied by micropipette. To get some insights, vesicles radii for each set of experiments have been placed onto the 'fluorescence intensity as a

[1] Oxydation of unsaturated lipids with time that may influence the mechanical properties and so on.

function of the vesicles diameter graph' presented in Chapter 3 (see fig. 4.12 -b). This to try to elucidate if the studied vesicle membranes were likely to contain spectrin. As one can see, the radii of the GUVs tested when 1 mg/ml of spectrin was added (yellow line in figure 4.12 -b) are larger than the other sets of experiments[1].

To ensure the presence of spectrin in GUV membranes, it was decided to combine fluorescence and micropipette aspiration by performing micropipette aspiration on GUVs after incubation with FITC-tagged spectrin. This way, the distribution of spectrin was distinguishable - since highlighted with FITC - and the GUVs could be chosen surrounded with spectrin. For this set of experiments, vesicles were choosen smaller on purpose (their radii belonging to the 4 - 9 μm range see the red line on figure 4.12 -b). These are the same radii as when 0.3 mg/ml and 0.8 mg/ml of spectrin was added. Additionally, FITC-tagged spectrin strongly bound to smaller GUVs (see Chapter 3).

4.4 Combining fluorescence and micropipette aspiration

Material and methods

As in previous experiments, FITC-tagged spectrin and SOPC/SOPS GUVs solutions were incubated for 2 hours at 37°C, in a 1:1 volume ratio. It was then illuminated at 488 nm and fluorescence was recorded within the 510-650 nm range. For this experiment, another micropipette aspiration plate was built to fit on the confocal microscope.

4.4.1 Qualitative and quantitative studies

Qualitative study

Figure 4.13 illustrates a typical SOPC/SOPS (molar ratio 70:30) GUVs surrounded with FITC-tagged spectrin and held in a micropipette. As one can see, the pipette appears fluorescent. This is believed to be due to the presence of oil (used for oil immersion objective). Moreover, the tongues of the GUV inside the micropipette appears uniformly bright when out of focus (a, b, d) whereas only the 'characteristic outline shape' of the tongue is fluorescent when the pipette tip is in focus (c and e) proving that, in this case the giant vesicle is unilamellar.

[1] As a reminder, one of the conclusions from the graphs presented in Chapter 3, was that spectrin did adsorbed onto the lipid vesicles, but preferred the smaller vesicles (population 1)

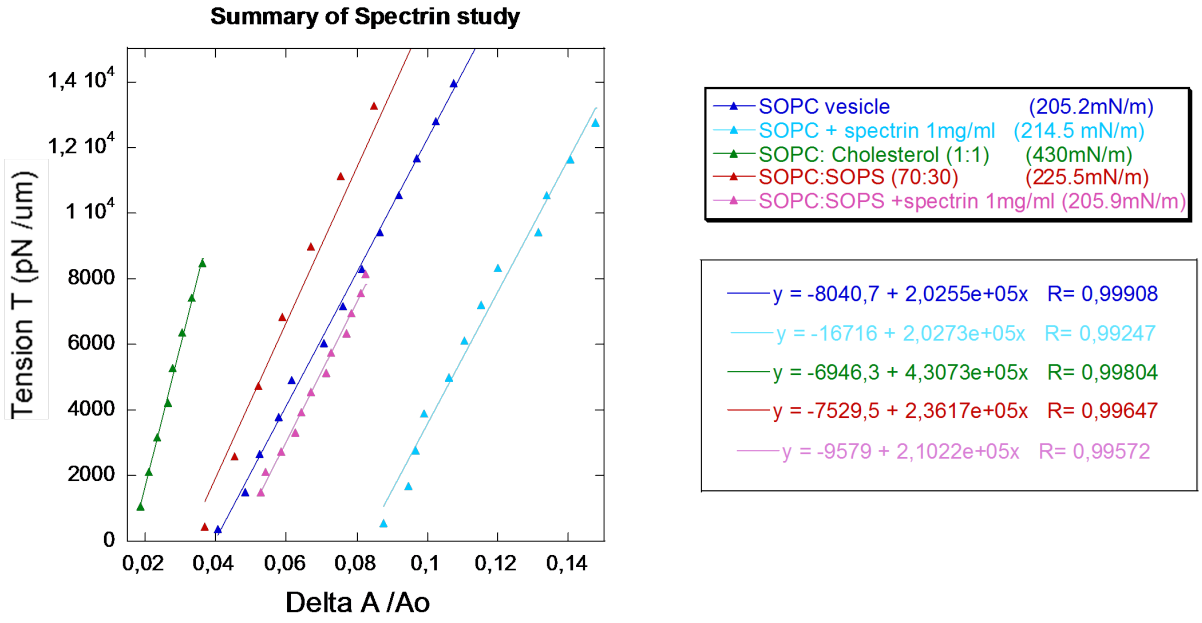

(a) Summary of experiments undertaken with the spectrin protein.

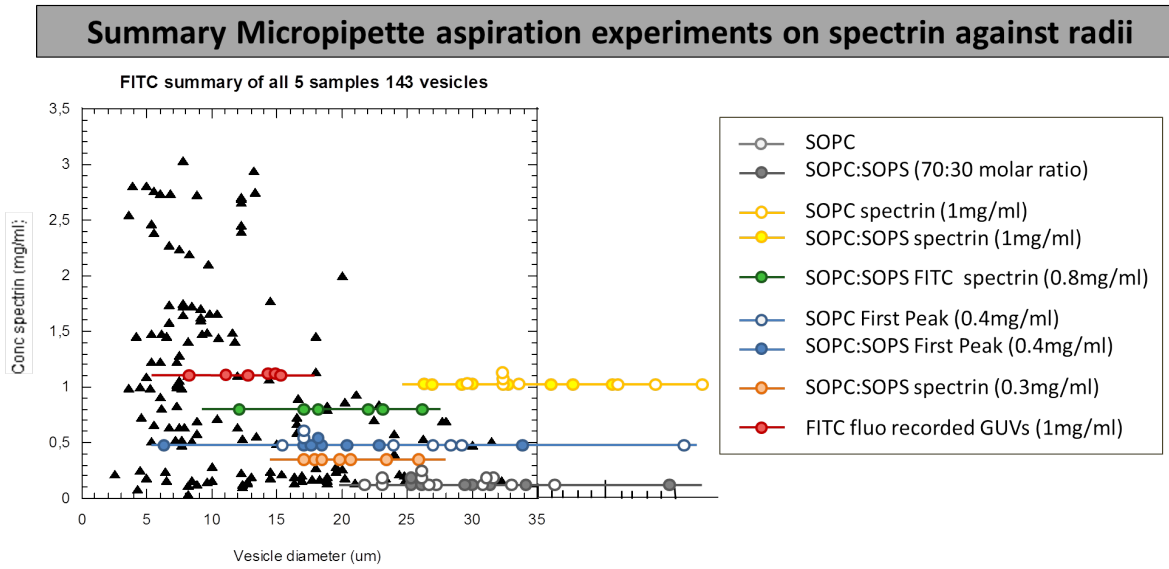

(b) Fluorescence against vesicles radii.

Figure 4.12: Spectrin effects on GUVs mechanical properties. (a) Summary graph providing the tension, τ, with respect to the relative area expansion, $\Delta A/A_0$, and giving a MPA measurement for each set of experiments (SOPC (no spectrin), SOPC spectrin (1 mg/ml), SOPC/ SOPS (no spectrin), SOPC/ SOPS spectrin (1 mg/ml)). Linear regressions are provided on the side. (b) The radii of the vesicles of each vesicle (for each set of MPA experiments) have been plotted with respect to the initial concentration of spectrin and added on the top of the graph presented in Chapter 3 (giving the relative intensity of FITC-spectrin around SOPC SOPS GUVs). The radii of the GUVs, when spectrin was added (1 mg/ml) for both sets of experiments (SOPC and SOPC:SOPS) where larger and thus less likely to be surrounding with spectrin.

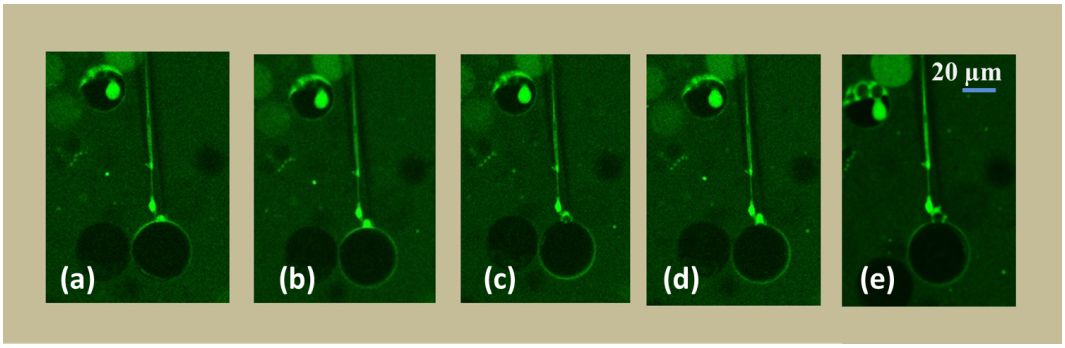

Figure 4.13: Combining fluorescence microscopy and micropipette aspiration (qualitative measurements, confocal microscope): The image is a montage of a SOPC:SOPS (70:30) GUV surrounded by FITC-tagged spectrin and hold in a micropipette. The pressure is qualitatively increased. When in focus, the characteristic shape of the tongue within the pipette is observed (images c and e). Out of focus the membrane within the pipette appears uniformly bright (a, b and d).

Quantitative study

Figure 4.14 is a montage illustrating a typical micropipette aspiration experiment while recording FITC-tagged spectrin fluorescence. The pressure applied for each measurement is given on the bottom right corner of each image; between each image the reservoir was lowered by 2 cm. As before, the membrane aspirated stabilized within seconds, and images were recorded every 30 seconds. As one can see in figure 4.14, a membrane tongue formed and elongated linearly as the negative pressure applied increased. Nevertheless in this particular case, the vesicle did not seemed unilamellar with the presence of internal structure highlighted with FITC. Moreover 2 membranes are distinguisable within the micropipette: the bright one burst right before the internal one (see the last but one and the last images respectively).

Figure 4.15-a summarises the micropipette aspiration results. As in previous experiments, the values of the area expansion modulus K_A were wide with an average value around 160 mN/m (159.2 mN/m +/− 64 mN, 176.7 when taking vesicle 3 into account). The 4th vesicle has been discarded due to it low value. Vesicles surrounded with spectrin show similar linear behaviors as in section 3. The maximum area expansion $\Delta A_{max}/A_0$ values are slighlty higher as in previous experiments which is believed to be due to the smaller size of the GUVs. From this set of experiments, the same conclusion can be drawn that spectrin is unlikely to have any large effect on vesicles mechanical properties. Figure 4.15- b gives a montage of a snapshots of the six vesicles surrounded with FITC-tagged spectrin on which micropipette aspiration has been performed. The presence of fluorescence clearly proves that the membranes had spectrin present.

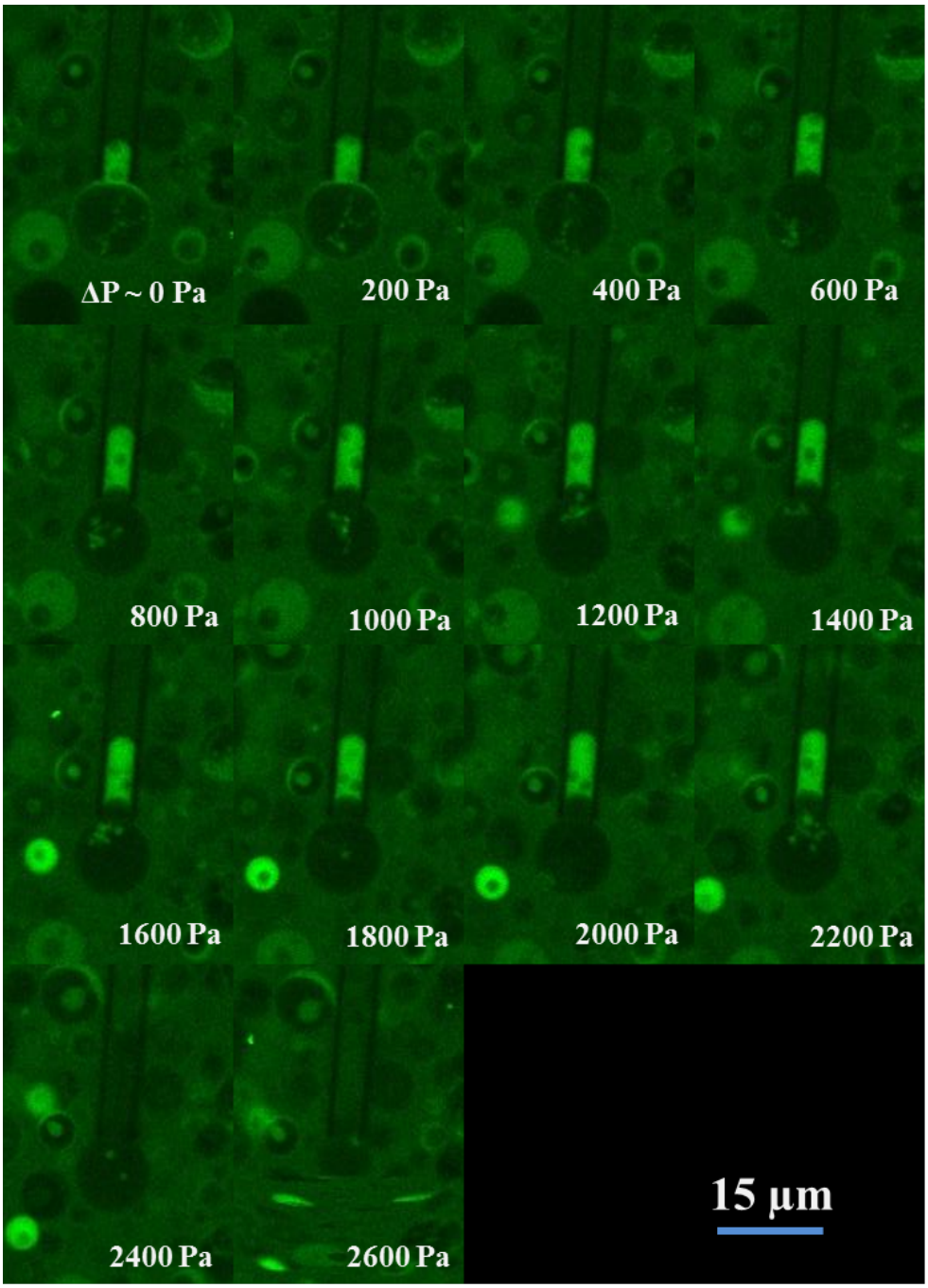

Figure 4.14: Montage of images of a SOPC:SOPS (molar ratio 70:30) vesicle surrounded with FITC-tagged spectrin (1 mg/ml) and aspired in a micropipette during a micropipette aspiration experiment (confocal microscopy). The pressure applied is provided for each image (right-bottom corner). A tongue forms and elongates linearly within the pipette while the pressure increases until the vesicle bursts when the lysis tension τ_{lysis} is reached (last image). Internal structure of the vesicle is also highlighted with fluorescence.

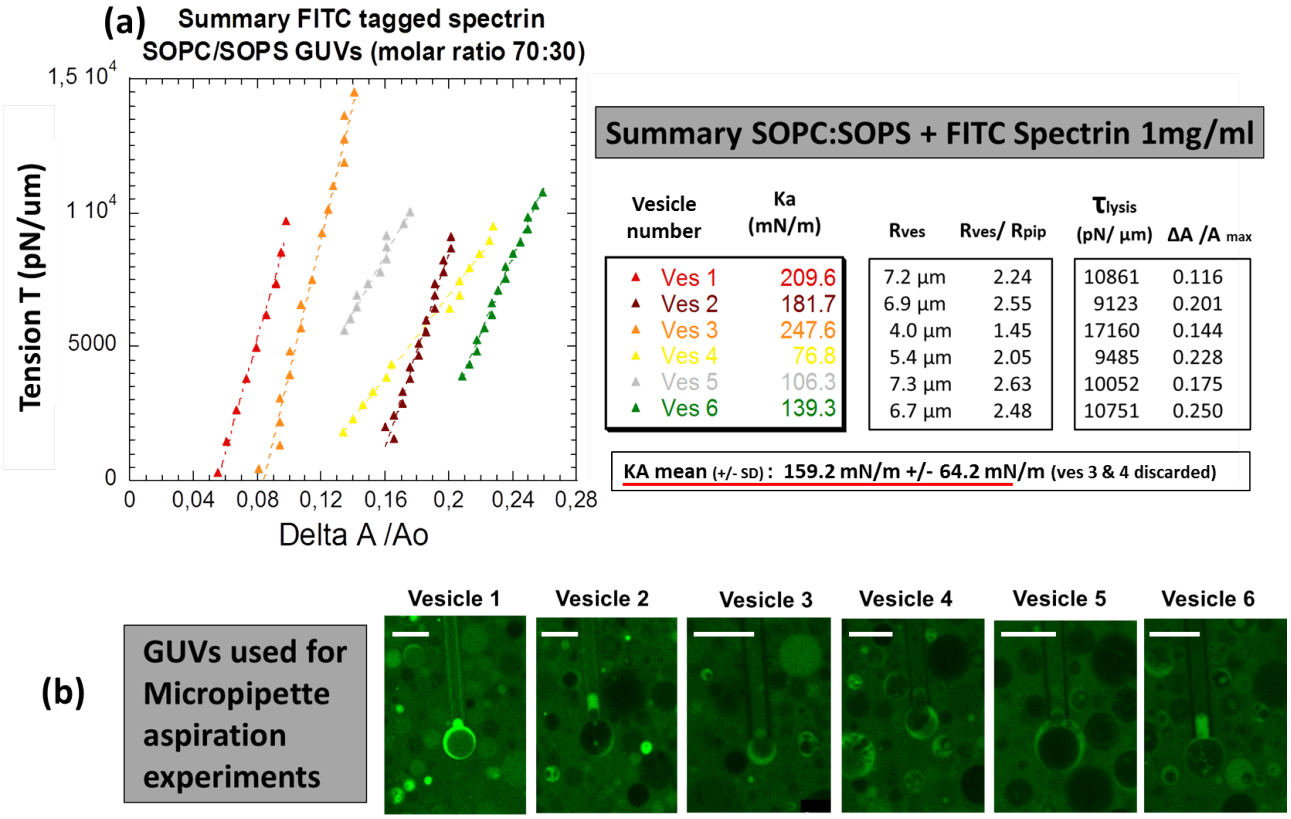

Figure 4.15: Combining one-photon fluorescence and micropipette aspiration (quantitative measurements, confocal microscope). (a) Summary graph providing the tension, τ, with respect to the relative area expansion, $\Delta A/A_0$, of MPA measurements performed on SOPC:SOPS vesicles (70:30) after incubation with FITC-tagged spectrin (1 mg/ml). The table on the side recapitulates the results. The mean value of the area expansion modulus K_A mean is similar to that of the area expansion modulus value when no spectrin is added. (b) Is a montage providing a snapshot image of each of the vesicles studied by MPA. Scale bar is 10 μm.

4.4.2 Discussion

Thermal fluctuation spectroscopy measurements on GUVs have also been performed in parallel (studies led by David Woods) to investigate spectrin-lipid interactions. Figure 4.16 gives an example of these measurements on DOPC/DOPS GUVs (molar ratio 70:30) after incubation with pure spectrin (at 37 °C, for 1 hour, at 1 mg/ml). As one can see the distributions of bending modulii (in k/k_bT) were similar with and without spectrin, in both cases: with a Legendre fit and with a statistical fit. In both fits the higher frequency is $\sim$30 k/k_bT with a second peak around 40 k/k_bT. Spectrin incubated with DOPC GUVs gave similar distributions to when no spectrin was added (data not shown).

From these experiments, spectrin did not seem to have any effect on the GUVs bending elastic modulus either. The measurements are complementray to the micropipette

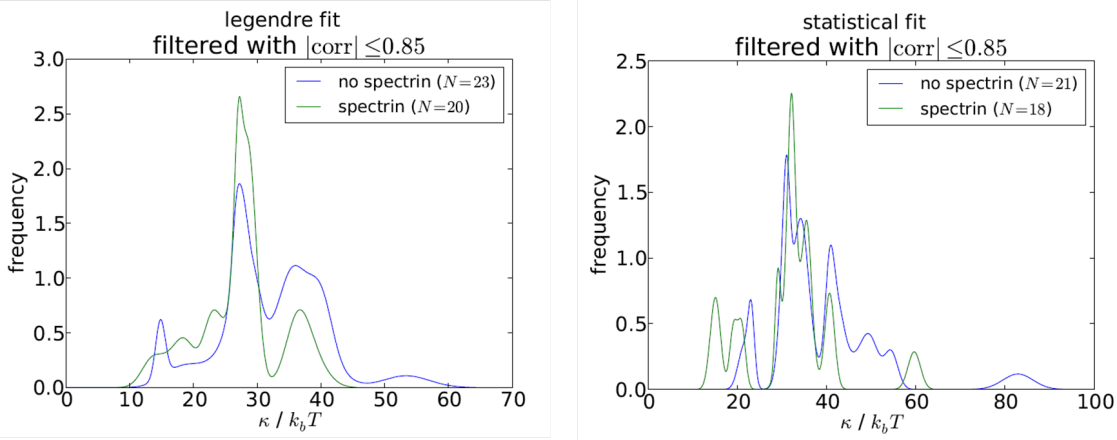

Figure 4.16: Thermal fluctuation measurements of DOPC:DOPS GUVs (molar ratio 70:30) after addition of spectrin (1 mg/ml). Spectra distributions with and without spectrin are similar. Data from David Woods.

aspiration results. They show that spectrin affect either area expansion modulus, nor membrane bending rigidity. Further experiments are necessary to investigate whether other skeleton protein components, in combination with spectrin, may affect the membrane mechanical properties.

4.4.3 Measurements on impure spectrin

A last set of experiments has been performed on SOPC and SOPC/SOPS GUVs mixed with crude spectrin (first peak from the CL-4B column). These have been performed on the same day and with the same GUVs preparations as the negative controls from section 3. Figure 4.17 summarises the results. In the case of SOPC GUVs (figure 4.17 - a) , measurements were linear (with good correlation factor). The area expansion modulii were similar to the negative control with an average K_A of $\sim$210 mN/m (213.8 mN/m, +/− 35 mN/m - vesicles 3, 5 and 7 were discarded). In the case of SOPC/SOPS vesicles, the average K_A is $\sim$ 225 mN/m (225,7 mN/m, +/− 42 mN/m - vesicles 2, 5 and 8 were discarded as their R_{ves}/R_{pip} was below 2 whereas vesicle 6 was discarded due to its low value) which is very close to the negative control. Nevertheless, as one can see in figure 4.17 - b, measurements appear less linear with lower correlation factor which might either be due to other proteins of the complex interacting with the membrane bilayer, or to 'artefacts' due to some proteins of the complex attached to PS which would stick to the micropipette. Further measurements would be necessary to draw definitive conclusions.

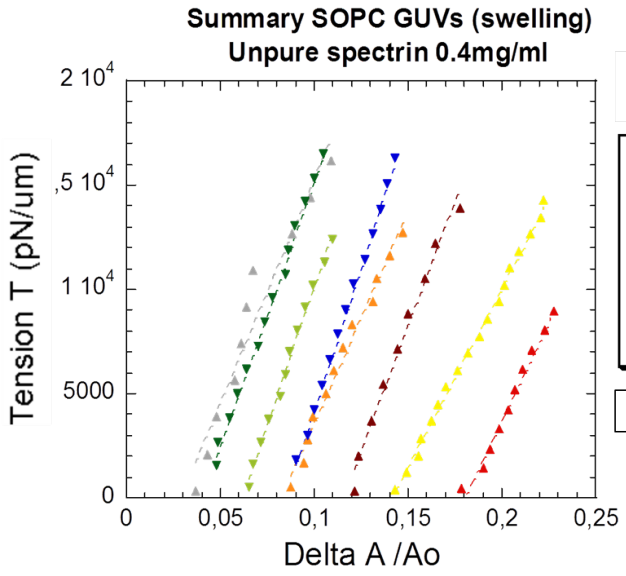

Vesicle number	Ka (mN/m)	Rves	Rves/ Rpip	τlysis (pN/ µm)	ΔA /A max
Ves 1	186.5	14.6 µm	2.54	8975	0.228
Ves 2	239.6	23.9 µm	4.53	13916	0.177
Ves 3	202.7	7.7 µm	1.69	12743	0.147
Ves 4	171.7	11.9 µm	2.46	14293	0.222
Ves 5	274.3	8.7 µm	1.72	16274	0.143
Ves 6	255.2	14.3 µm	2.87	16505	0.105
Ves 7	266.9	8.6 µm	1.80	12375	0.109
Ves 8	216.2	13.5 µm	2.92	16189	0.108

KA mean (+/- SD) : 213.8 mN/m +/- 35.0 mM/m (ves 3, 5, 7 discarded)

(a) micropipette aspiration on SOPC GUVs incubated with unpure spectrin

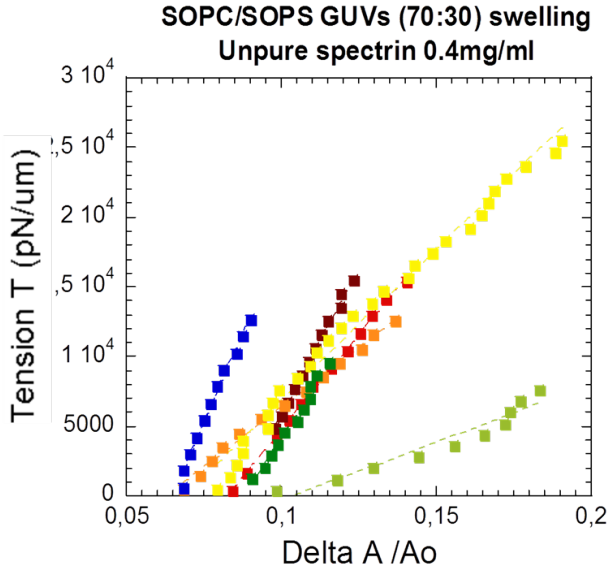

Vesicle number	Ka (mN/m)	Rves	Rves/ Rpip	τlysis (pN/ µm)	
Ves 1	271.7	17.0 µm	3.04	15798	0.140
Ves 2	423.8	8.6 µm	1.89	18357	0.136
Ves 3	171.1	10.2 µm	2.01	21632	0.132
Ves 4	217.1	9.3 µm	2.03	25494	0.190
Ves 5	522.3	8.4 µm	1.68	12686	0.089
Ves 6	82.2	10.9 µm	2.36	7621	0.182
Ves 7	243.1	8.7 µm	2.05	17849	0.173
Ves 8	116.0	9.2 µm	1.95	3847	0.450

KA mean (+/- SD) : 225.7mN/m +/- 42.7 mN/m (ves 2, 5, 6, 8 discarded)

(b) micropipette aspiration on SOPC/SOPS (molar ratio 70:30) GUVs incubated with unpure spectrin

Figure 4.17: Studying the effects of impure spectrin (first peak from the sepharose column CL-4B) on the area expansion modulus of GUVs: Summary graph of MPA measurements performed on (a) SOPC and SOPC:SOPS (70:30 molar ratio) (b) GUVs after 2 hours incubation with unpure spectrin (0.4 mg/ml). In both cases a table on the side summarises the measurements. Spectrin does not seem to have any effect on the area expansion modulus but the measurements appear less linear with the presence of PS in the vesicles (b).

4.5 Conclusions and future work

In summary, a micropipette apparatus has been built to perform micropipette aspiration measurements: it proved to be working thanks to measurements on well-known membrane systems. Measurements on GUVs when α-elastin was added demonstrated that micropipette aspiration was a suitable method to detect and study the mechanical changes caused by protein-lipid interactions as these measurements were in good agreement with other techniques (fluctuation spectroscopy).

In the case of the spectrin, no significant changes could be measured which suggests that spectrin-lipid interaction is likely to be weak. Nonetheless there were great differences from one GUV to another (high standart deviation), therefore spectrin could induce small changes in the membrane mechanical properties which were not detectable due to the high uncertainties. More sensitive methods should be used for further experiments to determinate this.

The swelling method may not have been the most suitable in this case. Therefore it might be useful to reproduce these experiments with other lipid systems which can be grown with the electroformation method, for example DOPC /DOPS /DOPE (10 % DOPE allows the system to be grown with the electroformation method in spite of the presence of PS). Once an appropriate system is found and if spectrin still does not seems to have any effects on the membrane mechanical properties, other proteins of the complex (actin, band 3) could be purified and added for further measurements.

As shown in the externalized-PS RBCs experiment in Chapter 3, pure spectrin seemed to interact with the spectrin network. It could thus be interesting to prepared inside-out (and outside-in) RBCs ghosts and perform micropipette aspiration measurements while adding pure spectrin. Those measurements could be combined with FITC-spectrin at low spectrin concentration to investigate how the free pure spectrin would interact with the spectrin-complex and deform when stress is applied.

Another idea might be to try and grow GUVs with the spectrin 'incorporated' within the bilayer [1] Micropipette could then be performed again with spectrin incorporated in different proportions with various lipid mixtures.

[1] This might nonetheless be tricky to perform for 2 reasons: first, the spectrin might not handle being in chloroform and second, the spectrin in choroform might not handle without denaturation being dryed.

In the next chapter, non-linear optic techniques are used to label-free image protein lipid interactions.

Chapter 5

Label-free imaging of protein-lipid interactions and distribution with NLO microscopy

In the beginning of this chapter the CARS/ SRS and TPF set-up used for the experiments will be described. The construction of a two-channel detector that allows simultaneous recording of deuterated and non-deuterated lipid signal will then be presented. In a second part SRS and CARS techniques will be compared for imaging GUVs. It will be demonstrated that SRS is highly efficient, especially to images domains in phase separated vesicles. In a third part, TPF will be used to highlight the distribution of an auto-fluorescent protein, the α-elastin, around vesicles of various compositions. Interaction of α-elastin with lipid membranes will then be discussed. Finally in a last section, femto/ pico-SRS and TPF will be combined in a single experiment to highlight lipid and protein simultaneously.

5.1 Material and Methods

5.1.1 Facilities

Facilities at the University of Exeter consists of a large optical bench (Thorlabs) on which ultrafast lasers, optical (flip) mirrors, polarizors, attenuator rings, filters and microscopes allows to perform TPF, SHG, CARS and/ or SRS. A schematic of the optical table set-up is given in figure 5.1. The facility provides a flexible system on which new NLO imaging techniques can be prototyped.

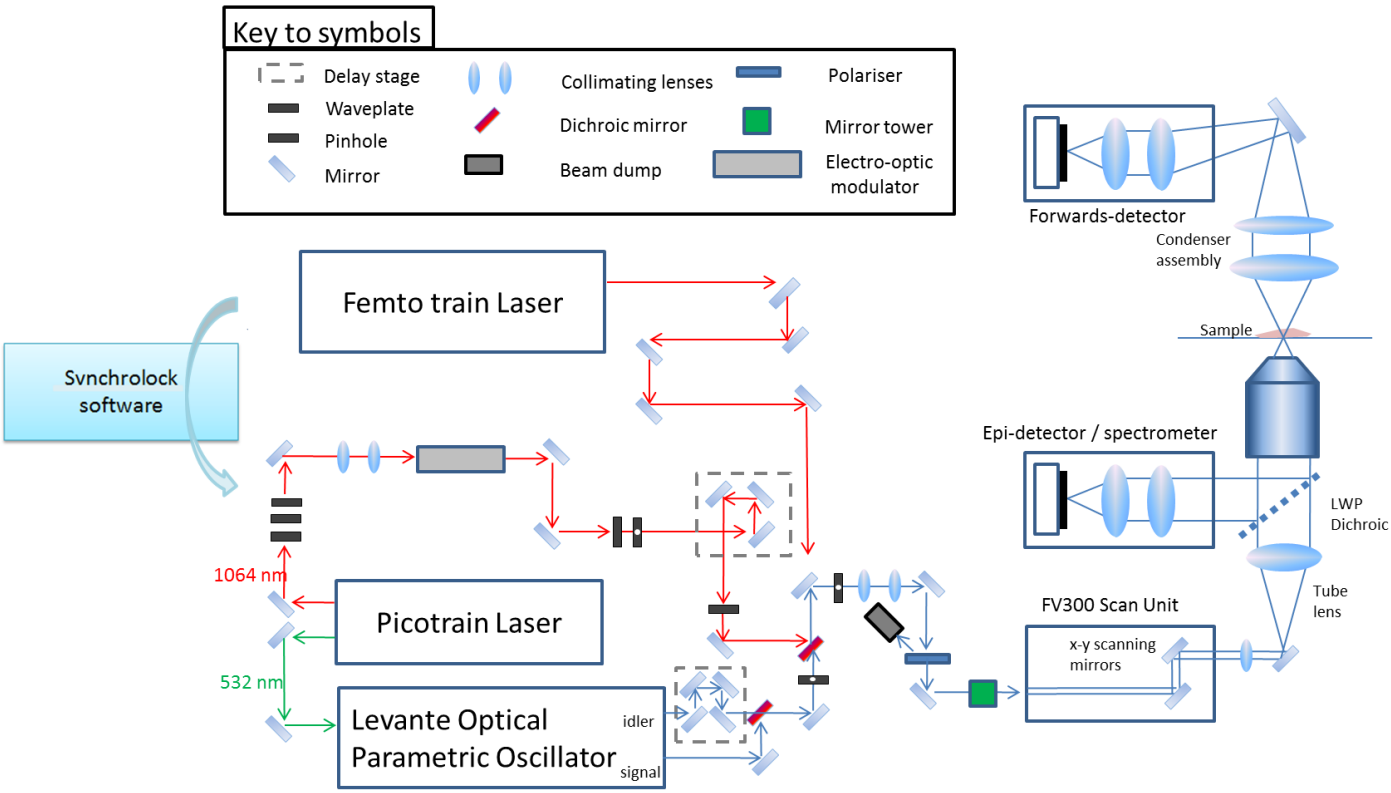

Figure 5.1: Instrumental set-up description: facilities at the University of Exeter. Reproduced with permission from a diagram by Natalie Garrett.

5.1.2 Set-up description

Pulsed excitation is provided by two ultra-fast lasers. The first one, is a Nd:Vanadium ($Nd : YVO_4$) laser (picoTRAIN, High-Q GmB) which has been split into two beams. One of the beams is kept at the fundamental frequency 1064 nm - (in red in the schematic) we will refer to this beam as the '1064 beam' - is directed via mirrors into an electro-optic modulator (as shown in figure 5.1). The second beam is frequency doubled - green beam in the schematics, 532 nm - and is directed via mirrors into an Optical Parametric Oscillator (OPO) (Levante Emerald, APE, Berlin, Germany). The $Nd : YVO_4$ laser generates a train of pulses, 6 picoseconds long, at a repetition rate of 76 MHz and generates the dual wavelength excitation required for both CARS and SRS.

As shown in figure 5.1, two beams, called **signal** and **idler** for the front and back beam respectively, emerge from the OPO box while a unique 532 nm beam was entering it. An OPO is a device which splits a monochromatic beam, the **pump beam** into two beams - an ordinary and an extraordinary beam - when passing through a non-linear

crystal. Because of the conservation of energy these two beams are of higher frequencies such that the condition $\omega_{\text{pump}} = \omega_{\text{signal}} + \omega_{\text{Idler}}$ is respected at all times. One of the great benefits of using an OPO is that the output wavelengths can be continuously tuned. In our case, the wavelengths are controlled via the temperature of the non-linear media (a birefringent LBO crystal[1]) the index of which is temperature dependent[2]. Because of the phase matching conditions, only one of the wavelengths can be chosen; in practice we use the signal beam. For our set-up the signal beam can be tuned from 690 to 980 nm whereas the idler output, is always of longer wavelengths and is emitted in the 1130 - 1450 nm range.

The second laser is a mode-locked femtosecond Ti:sapphire laser (Mira 900 D, Coherent), whose wavelength can be tuned from 680 to 920 nm and which delivers pulses approximately 100 femtoseconds long at a 76 MHz repetition rate. We will refer to this laser as the Mira laser. This laser has the ability to be configured for picosecond operation (See following 'two-channels detector' section for a quick explanation of the protocol). In practice this laser was used to generate SHG and TPF signals in the femtosecond-mode. It has been switched into the picosecond-mode and synchronized with the $Nd:YVO_4$ laser to perform CARS (see the 'Two-channel detector' section) and has been used in the femtosecond-mode to produce femto/ pico SRS (see section 5 of this chapter).

As discussed in Chapter 2, when NLO processes are involved; the light pulses of the different beams need to be both spatially and temporally overlapped. To perform temporal overlapping, delay stages (DS) are used to control the beampath lengths. Dichroic mirrors (DM) are used to combine two beams by wavelength-dependent transmission/reflection. The two pulsed trains from the OPO were combined using a 1064 DCRB (Chroma Technology) dichroic mirror. One can also find some collimating lenses and pinholes on the beams path: the collimating lenses[3] are used to collimate the laser beams so that they do not (over) expend in the x direction[4], whereas the pinholes are used for the alignement [5].

The microscope used for multi-modal imaging was a custom-built inverted Olympus microscope (IX-71, Olympus, UK) which has been combined to a confocal laser scanning - referred to as 'scan-unit'- (FV300, Olympus, UK). To minimize light losses within

[1] LBO stands for lithium triborate
[2] This also requires the inter-cavity Lyot filter to be adjusted.
[3] Sometime referred to as telescopes.
[4] Beams are expanded to 6 mm to overfill the back aperture of the objective.
[5] (To adjust both the high and parallelism with the horizontal table)

the scan-unit, the standard galvanometer scanning mirrors were replaced with silver galvanometric mirrors and the tube lens was replaced by a MgF_2-coated lens. The DM within the scan unit was replaced by a silver mirror that gave high reflectivity throughout the visible and NIR (21010, Chroma Technologies) [136]. The objective used to focus the light onto the sample was a 60 x 1.2 NA water immersion objective (UPlanS Apo, Olympus, UK). Two different condensers were used whether forward-CARS or SRS were performed. In the case of Forward-CARS or TPF it consisted of an air condenser 0.55 NA (Olympus) whereas for performing SRS a 60 x 1.0 NA dipping lens was required (Fluor x 60, Nikon, Japan) and combined to a 1.0 NA condenser lense (LUMFI, Olympus). Light was then directed toward the detectors via relay optics.

Long/short-pass and band-pass filters were necessary in front of the detectors, at the rear of the microscope, in order to be able to isolate the non-linear (NL) signal (CARS/SRS/ TPF/SHG) from the exciting wavelengths, (*i.e.* to cut off the fundamental laser). Table figure 5.2 summarizes the filters used for the techniques in both the epi and forward directions.

	Dichroic filter (to cut the fundamental λ)	**BP Filters in front of the detector**	**Detector**
Epi-TPF	670dcxr LP (Chroma technologies)	CG-BG-39 F10-400-5-QBL, CVI Laser	R38896 PMT (Hamamatsu)
Epi-SHG	670dcxr LP (Chroma technologies)	CG-BG-39 F70-500-3PFU, CVI Laser	R38896 PMT (Hamamatsu)
Epi-CARS	750 dcxr PL (Chroma technologies)	750/210 BP (Chroma technologies)	R38896 PMT (Hamamatsu)
Forward-CARS	750 dcxr PL (Chroma technologies)	660.0 IF 40-D (Ealing) X 2	R38896 PMT (Hamamatsu)
Forward-SRS	850/90 nm (Chrotecma hnologies)	850/90 nm (Chrotecma hnologies)	Photodiode FDS 1010 (Thorlabs)

Figure 5.2: Summary table of the dichroic long-pass filter and band pass filter used in front of the detector for each techniques that can be performed at the University of Exeter.

The detectors for all imaging techniques, other than SRS, consisted of red-sensitive photomultipliers (PMTs) from Hamamatsu (R3896, Hamamatsu, Japan) which required adapter pieces (E717-63 Socket Assembly, Hamamatsu) and collimating lenses.

As mentioned in Chapter 2, to generate SRS signal one needs one of the beams to be modulated. Practically this was performed using an Electro-Optic Modulator (EOM) (Crystal Technologies Inc., type S/N 3080-197) (grey square on schematic 5.1). The

EOM is placed on the 1064 nm beam path; which is thus the modulated beam. We are therefore performing stimulated Raman loss (SRL); recording intensity changes in the signal beam. The reason why we perform SRL [1] is that; in view of acquiring SRS spectra, we want to keep the freedom of tuning the signal wavelength. In SRS, since the signal intensity changes are very weak, a Lock-In Amplifier (LIA) was used to amplify the signal (SR 844, Stanford Research system). SR 844 lock-in amplifier functioning, dwell time and integration time to optimize GUVs detection will be discussed and compared to another lock-in (Zürich) in another section (see section 3.2).

Data acquisition was monitored via the Fluoview Software which also allows z-stack, time-lapse recording, and greater magnification (up to 10 times). Images were processed using the ImageJ software which is a Java-based image processing program. Experimentally, when doing NLO, alignment of the beams on the table and through the microscope needs to be checked and adjusted before each experiment.

Excitation was attenuated using $1/2\,\lambda$ plate/ polarizer to $\sim$130 mW for the 1064 nm beam and $\sim$ 220 mW for the signal beam. The Mira laser delivers a maximum of around 270 mW on the optical table. Powers of the beams were attenuated either separately or all together (to keep the same beams power ratios) thanks to gradated ND filter wheel on the table (4 in total). The scan unit attenuates the beams so that the overall power arriving on the sample is only 10%-20% of the power entering the scan unit box. Average powers at sample was $\sim$ 40 mW less than 50 mW below which no photodamage was observed.

5.2 Imaging lipids using CARS

5.2.1 Raman spectra of lipids

As explained in Chapter 2, knowing the Raman spectrum of a sample to study is usually a preliminary step before imaging it with CARS [91], [137] [138]. Therefore all the lipids used in experiments have been studied under a Raman microscope (Renishaw RM1000, plc, UK). The excitation source was a 785 nm HeNe continuous-wave laser whose power used on the sample was attenuated down to 300 mW [2].

[1] Eventhough the photodiode is more sensitive at the 1064 nm wavelength compared to the 816 nm one.

[2] Further details about data processing concerning the use of the Raman microscope will be given in Material and Method of Chapter 6

As mentioned in Chapter 2 (section 3) both the fingerprint region and the CH_2 regions provide useful information. Since signals of biological sample are usually weaker in the figerprint region, attention is given to the higher frequencies (CH_2/CH_3 region). Figure 5.3 gives an extended Raman spectrum of a dried DOPC lipid droplet. In the zoomed spectra (top right), the maximum of the peak is as presumed from the literature (ref) at the wavenumber 2845 cm^{-1}. This is the wavenumber difference required to get the maximum signal from DOPC lipid in both CARS and SRS. Practically it can be performed using either the 1064 nm beam and the signal at 816 nm, or with the idler and signal beams at 924 nm and 1254 nm, both corresponding to a frequency difference of 2845 cm^{-1}. The disadvantage of using the idler and signal is (since longer wavelengths are involved) that the resolution is lower. For SRS, the 1064 nm beam is modulated and Signal-1064 nm SRS is performed. 1064 and signal also has the advantage of allowing simulatenous acquisition of SRS and (Epi)-CARS.

Since different lipid species provide different Raman signatures in the high-frequency CH region (*i.e.* their peak shape differs since they are the sum of Raman vibrational modes present in different proportions (different chemical bonds)), many researchers try to differentiate between different lipids present in the samples by requiring SRS spectra (hyperspectral images). We will return to this topic in Chapter 6. Spectra of the lipids used during experiments will also be provided.

Deuterated lipids

Deuteration is a commonly used method that takes advantage of the region with no characteristical peaks for biological samples (1700- 2700 cm^{-1}), referred to as the **silent region** [139]. In a deuterated species, the hydrogen atoms (H) are replaced by deuterium atoms (D) which does not change the properties of molecules except that the increased mass of deuterium compared to hydrogen shifts the CH strech (2845 cm^{-1}) to CD (2105 cm^{-1}) as shown in figure 5.3.

A preferentially used GUVs system when deuterated lipid is involved was a multi-component mixture composed of DOPC, deuterated DPPC (DPPCd62) (molar ratio 1:1), mixed with cholesterol, so that the final lipid mixture contained 30% of cholesterol (molar ratio) which we will refer to as the **DOPC:DPPCd62:30%Chol** mixture. This system was chosen for its capability to segregate into macrodomains and due to the relatively low cost of deuterated DPPC compared to other lipid species[1]. Figure

[1]Deuterated compounds are usually very expensive.

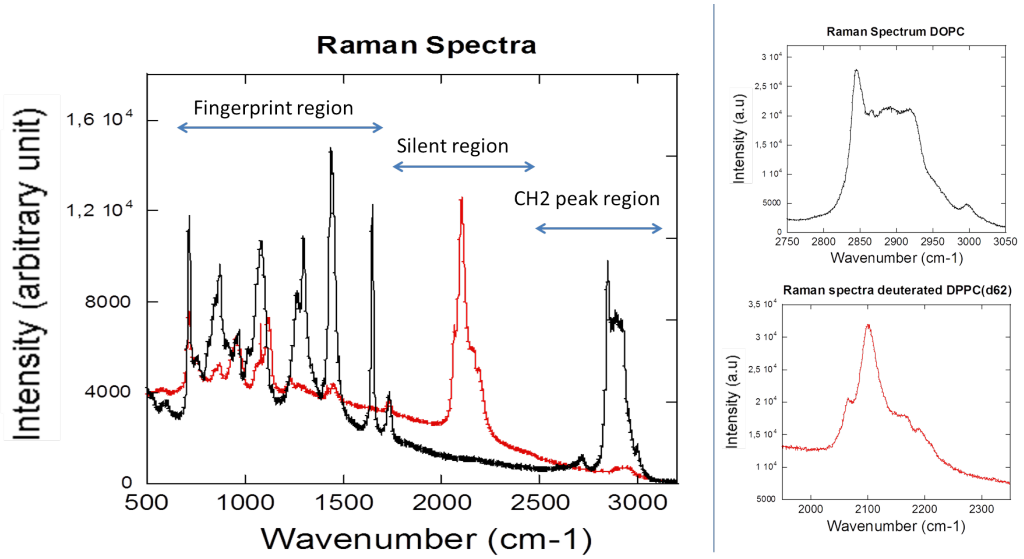

Figure 5.3: Spontaneous Raman spectra of DOPC (black) and deuterated DPPC(d62) lipids (red).

5.3 gives both an extended and a zoomed spectra (around the CD strech) of a dried deuterated DPPC(d62) lipid droplet (in red).

5.2.2 Two-channel detector

The system of interest was a solution of GUVs. Since, as described in Chapter 1, these membrane systems are floating in solution and are easily disturbed, it is difficult to study a specific GUV. If one tries to get both the deuterated lipid species distributions and the complementary non-deuterated signal, the temperature of the OPO will have to be changed, which will take minutes to stabilize; a time during which, the vesicle of interest has usually gone out of the focused window.

To overcome this problem, **a detector was built to allow the detection of both deuterated and normal lipids simultaneously in the forward direction** which could be combined with TPF/SHG detection in the Epi-direction (provided the wavelengths match). This also allows co-registering of images with high precision.

Detector principle

The schematics in figure 5.4 shows the wavelengths used to excited the sample (which need to be blocked before the detectors) and the wavelengths to detect in the different channels of the built detector. The maximum powers of the 3 beams at the entrance of the scan-unit are also indicated. Band-pass filters in front of the detector for each chan-

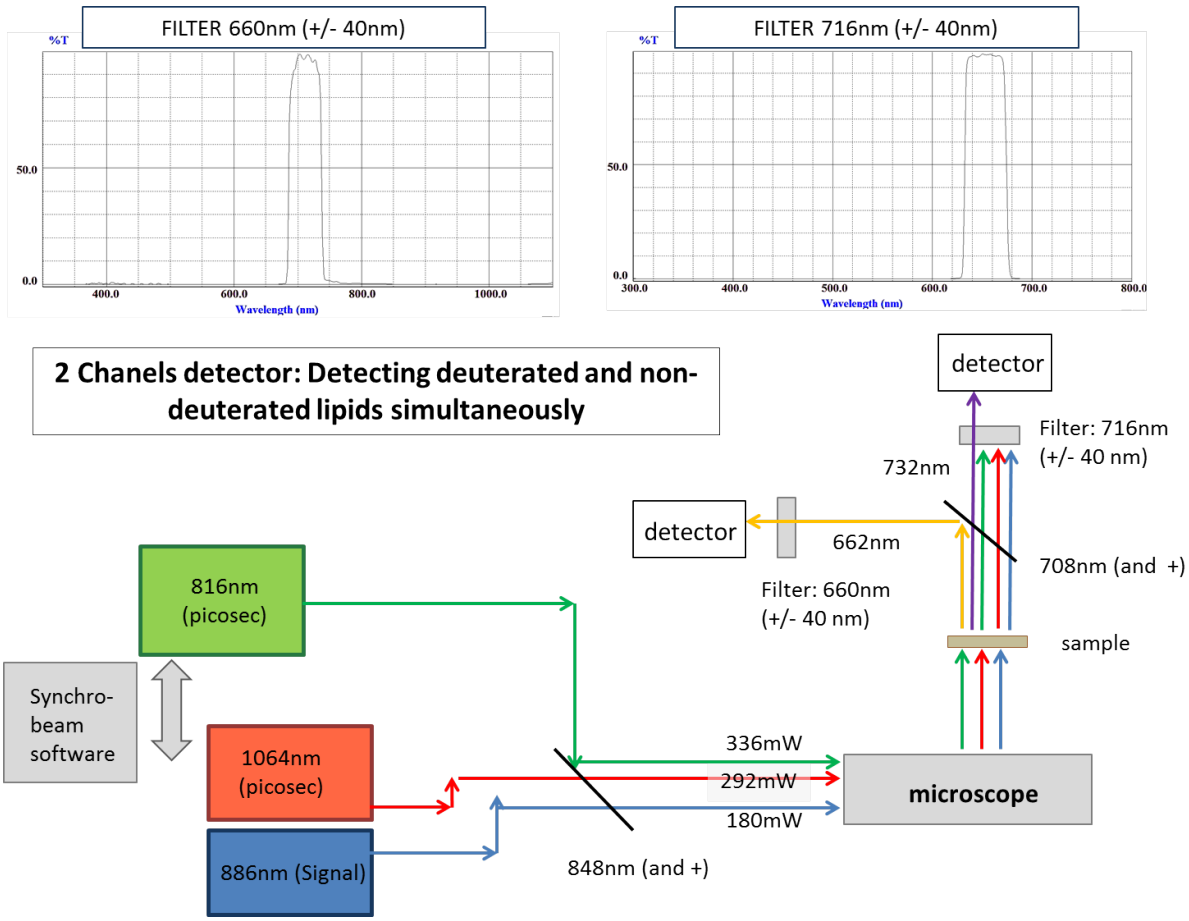

Figure 5.4: Two-channel detector schematic. The 848 nm dichroic filter allowed the 3 beams to be overlapped in space. The 816 nm beam was synchronised with the 2 other beams using the Synchrolock software. The 708 nm dichroic filter allowed the deuterated signal (at 732 nm) and the non-deuterated signal (at 662 nm) to be directed toward different detectors. OD6 band-pass filters allowed to cut off the fundamental laser wavelength.

nel were OD6 filters from Edmund (716/40 BP; NT67-039 for the deuterated channel and 655/40 BP; NT67-037 for the non-deuterated channel) whose characteristic curves are given in the top part of figure 5.4. The long-pass filter required to bring the three beams into the same light path on the table (annoted 848 nm (and+) in figure 5.4) was custom-made by Omega Optic (848 DRLP, Omega Optics,US). Figure 5.4 provides its' characteristic curve to the reader. The dichroic used to separate the deuterated and non-deuterated signals was a long-pass filter (XF 2083 708 RLP, Omega Optical, US) mounted on a rotative cage, compatible with the usual dichroic filter mount from Thorlabs (FFM1, Thorlabs, UK). This dichroic was placed after the condenser in the light path also to direct the beams into the appropriate detector channels.

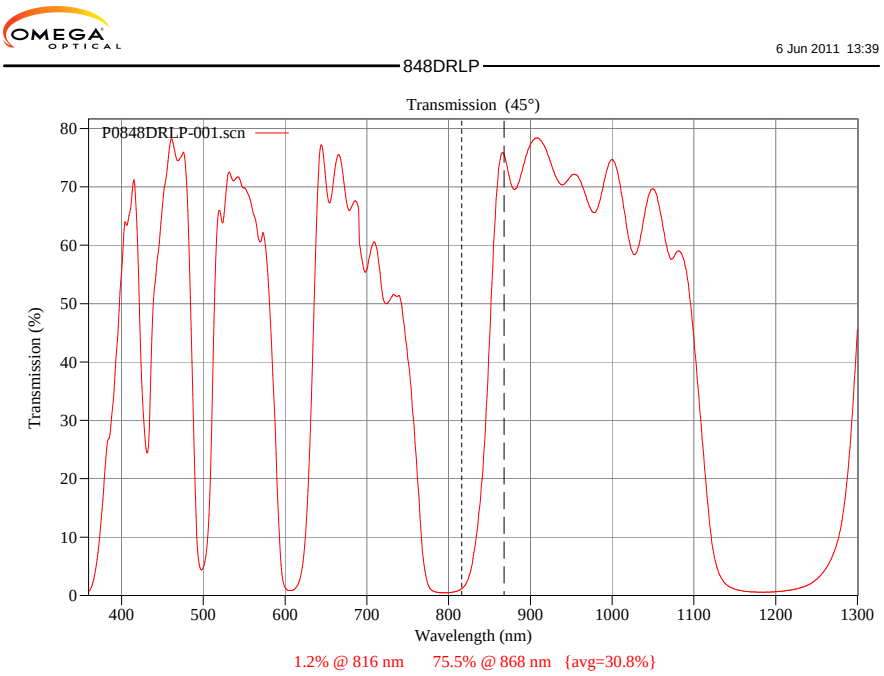

Figure 5.5: Long pass dichroic mirror 848 DRLP, characteristic curve giving the transmission at 45° as a function of the wavelengths.

Experimental protocol

Various steps needed to be performed each time before being able to use the detector. The preparation process could be broken down into 3 main parts. Firstly, the Mira laser needed to be configured for picosecond excitation. Secondly the 848 nm long-pass filter needed to be added to the light path and the three beams spatially overlapped[1]. Finally, the 816 and 1064 nm beams needed to be temporally synchronized.

In order to re-configure the Mira laser from the femto-mode into the pico-mode, several steps were necessary. First a one-direction stage was used to remove a prism from the light path so that the laser beam reached the part inside the cavity designed for the pico-mode. Then, two optics (M7 and M9) needed to be changed in the light pathway and the alignment of the beam through the cavity needed to be adjusted before, between, and after the two optics so that the laser starts lasering. Then the chosen wavelength of the Mira Laser can be selected by adjusting a birefringent filter according to a characteristic curve provided by the manufactor. Eventually, the beams needed to be realigned through the optics which allowed the light to exit the laser

[1]Since the optical bench is shared among the group, the high-pass filter was usually not present on the table at the beginning of the experiment.

cavity. The cavity alignment then needed to be optimized to maximise the power and stability of the laser[1] (for further information about this process read the Mira laser manual).

Alignment of the three beams on the optical table was performed by the usual method (using pinholes as shown in figure 5.1). The third step (synchronization of the beams) is the most challenging. To synchronize the two beams, one beam has to be defined as the 'reference' beam (also called the **master beam**) whereas the other beam, referred to as the **slave beam**, will be adjusted until synchronization. In this case, the two beams to synchronized were the 816 nm and the 1064 nm beams. Since the 1064 nm was already synchronized with the 868 nm beam (signal), the 1064 beam was the master beam whereas the 816 nm played the role of the slave beam. Synchronization was performed using the **Synchrolock software (Coherent, UK)** which could monitor parameters of the slave beam frequency phase. A small portion of the beam was fed to the Synchrolock control box via a fibre optic cable and allowed the beam to be monitored.

The first step was to reduce the difference in frequency of the delivered pulses of the lasers until it reaches zero, so that the 2 beams frequencies match. To do so, the Synchrolock software sended a message to change the length of the laser cavity within the Mira laser. [2] The second step was to adjust the phase.[3] At this stage, both beams at the output of their laser cavity boxes were synchronized. Synchronization along the optical table still needed to be performed. To do so, an auto-correlator was used: both beams were aligned into a control box with a display screen, which allowed one to 'visualize the pulses' from the two beams. A phase scan was then performed using the Synchrolock software to see at which settings the 2 beams were synchronized. The beams were synchronized when the total peak (with contribution of both pulses) 'soared' on the screen of the auto-correlator. This big peak was caused by sum frequency generation which occured when the 2 beams were synchronized[4]. Fine optimization of the synchronization could then be performed on the microscope, optimizing the CARS signal on a test sample while performing an accurate phase scan using Synchrolock (for further information, read the synchrolock manual).

[1] The alignment through the cavity is of great importance, as the better the alignment through the cavity the higher the acheivable laser power and; the higher the power at the output of the laser, the stablest the laser will be.

[2] It moved a mirror in the cavity on a motorised stage to adjust the cavity length.

[3] Stage 1 did coarse adjustements of the frequency and stage 2 adjusted the phase of the slave beam.

[4] Inside the auto-correlator the beams were aligned into a non-linear crystal and this is where the sum frequency generation took place.

Validation of the detector, discussion, and future work

Many tests were run to try and get a good contrast (*i.e.* good signal-to-noise ratio (SNR)) of complementary images of the two channels of the detector. Compromises were necessary between the quality of the background reduction and the quantity of the lipid signal cut: since the aim was to image vesicles which only produce a weak signal. Up to 3 OD6 band-pass filters were necessary in front of each PMT to efficiently block the excitation beams in the detector channels. Figure 5.6 shows the results of the detector on a test sample composed of a dried lipid droplet of a mixture of DOPC and deuterated DPPC(d62). In (c) it clearly appears that the DOPC (in red) and the deuterated DPPCd62 (in green) could be totally separated without any labelling. Moreover the signals from the two channels were complementary without any overlap (Overlapping with these artificial colours would appear in yellow).

The main drawback of this experiment was that the Mira laser appeared to be unstable when in the picosecond-mode[1] which resulted into desynchronization of the 816 nm beam with the 1064 nm and loss of the CARS signal. This mostly happened when acquiring images at low frequency (longer acquisition time: 52 seconds for a 512 x 512 image (*i.e.* dwell time $\sim$ 200 μs). Other experiments were then tested: femtosecond/ picosecond CARS for the 'normal' CH_2 lipid band (2845 cm^{-1}) in the forward direction and picosecond/ picosecond CARS in the epi-direction for the deuterated CD_2 band (2105 cm^{-1}). In this latter experiment the beams were stable and the data recorded showed similar matching features (*i.e.* images from the 2 channels were perfectly complementary) (data not shown). Images were nevertheless noisier, femtosecond / picosecond CARS being known to be noisier than normal CARS imaging [140], [141].

Unfortunately experiments on vesicles samples did not give good results (see the presence of 'stripping' due to laser instability in fig 5.7 (B)). Discovery that another imaging technique (SRS), gave much better signal than CARS - this will be discussed in the following section - led us to abandon the work on the detector. As explained in Chapter 2, SRS is known to have the advantage over CARS to be background-free and all the NLO work of the second part of the PhD was performed using SRS instead of CARS to image vesicles. The detector was nonetheless fully working on tissues and would still be really useful for example, to image and follow deuterated nanoparticles distribution/trajectory over time in biological tissue such as the skin[2].

[1] These laser are known to be less stable in the picosecond mode compared to the femtosecond one (Coherent).

[2] Using the epi-channel for the deuterated signal and the forward channel for the lipid would be the best set-up since, as explained in Chapter 2, Epi-CARS provides better signal for small elements.

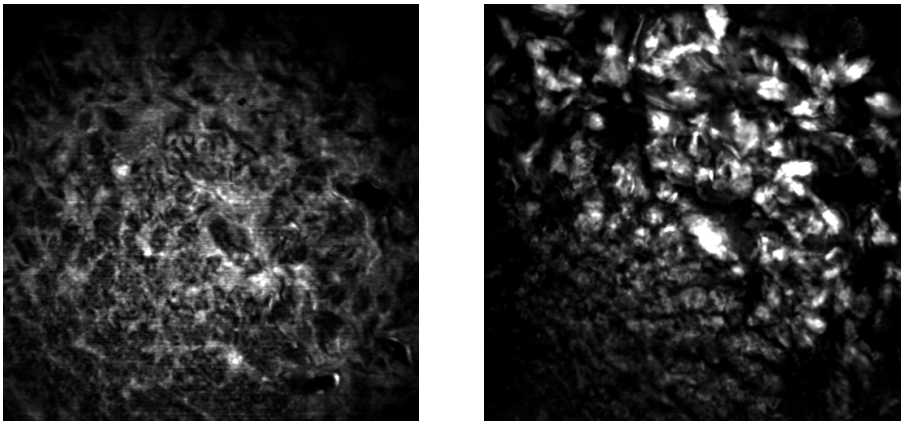

(a) CH_2 **bonds**

(b) CD_2 **bonds**

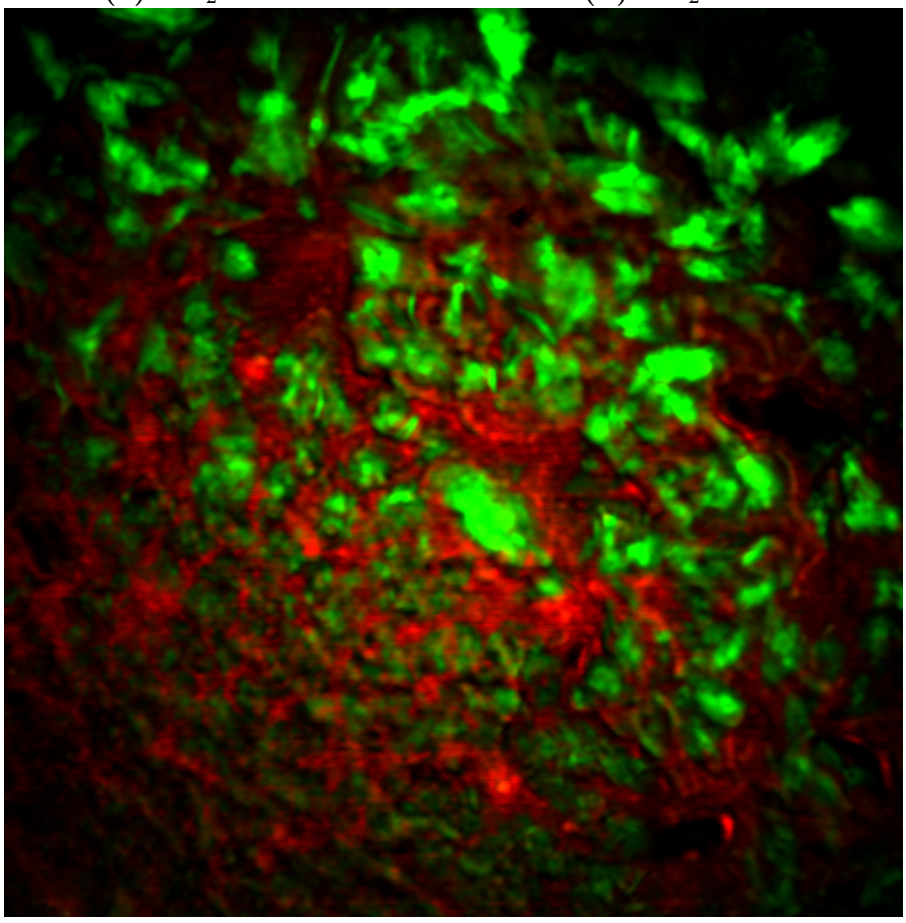

(c) Composite picture: CH_2 **signal in red;** CD_2 **signal in green.**

Figure 5.6: Mixture of DOPC, DPPCd62 lipids imaged using the two channels detector (a) DOPC lipid distribution is highlighted in the Epi direction, whereas (b) deuterated DPPCd62 is highlighted simultaneously in the forward direction; (c) is a composite image using (a) and (b) showing the perfect matching between the two lipid species.

On the same principle it would be possible to build a two-channel detector to detect the SRS signal of deuterated and non-deuterated lipids, provided one has access to two photodiodes, the appropriate filters and to two lock-in amplifiers.

5.2.3 Imaging vesicles with CARS

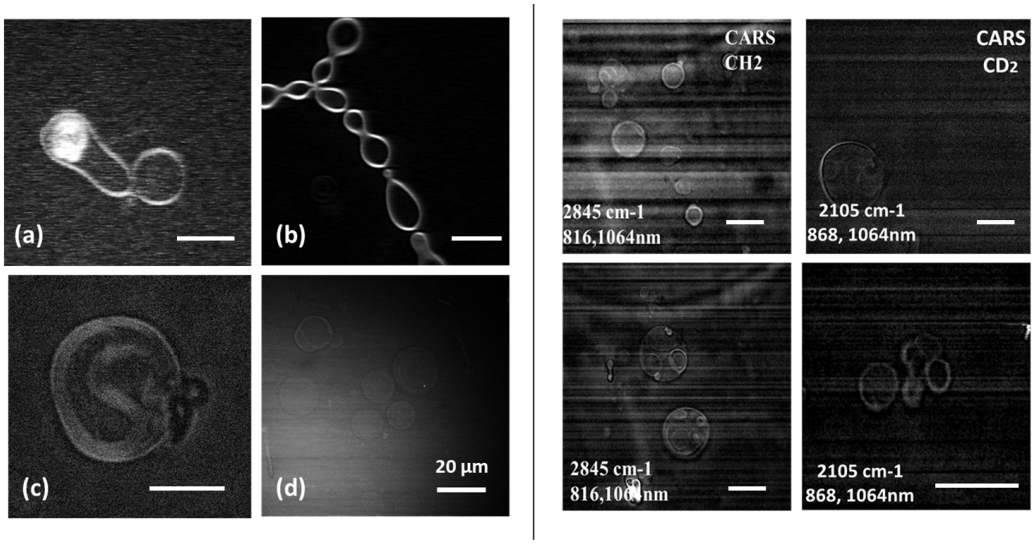

Figure 5.7: Imaging MLVs and GUVs in CARS and with the new detector. Left: (a) multimellar vesicle (MLV) in Epi-CARS, (b) MLV in forward-CARS, (c and d) solution of GUVs imaged in CARS. Right: Images of GUVs with the new two-channel detector. In both channels ($2105\,\mathrm{cm}^{-1}$ and$2845\,\mathrm{cm}^{-1}$) there is the presence of stripping in the image (instability of the Mira laser). Bar scale = $20\,\mu$m.

Figure 5.7 (left) is a collection of images of DOPC vesicles imaged with CARS. As one can see, CARS is efficient to image MLVs, Epi-CARS (fig. a) being a bit noisier than Forward-CARS (b). Nevertheless, the presence of the non-linear background was usually too important to be able to get good contrast between the bulk solution and the single bilayer membranes (see c and d). On (d) no data processing to remove the background has been performed. This low constrast of GUVs images is usual in CARS consistent with the literature [142], [143], [144], [145] . Figure 5.7 (right) is a collection of images of DOPC:DPPC(d62):30%Chol GUVs, recorded using the new detector. As one can see, both channels allow one to distinguish GUVs, nevertheless the non-linear background, and the 'stripping' (due to either interferences, or the instability of the Mira laser) reduced the quality of the images. In the next section the reason why SRS is a more suitable techique to image GUVs will be explained.

5.3 SRS versus CARS to image vesicles

5.3.1 Power beam dependence: comparison

Material and method

The dependence of the intensity of SRS and CARS signal on the pump and Stokes beams power has been introduced in Chapter 2. It was semi-quantitatively verified on three different samples: sample 1 made-up of dried starch, sample 2 consisting of a dried droplet of SOPC and sample 3 made-up of SOPC GUVs in sucrose/glucose solution. For each experiment, the contrast was optimized before the acquisition with all beams at maximum power so that the highest intensities would not saturate the detectors. The power of the studied beam(s) was then decreased step by step. To account for possible motion artefacts, the measurements were only semi-quantitative (*i.e.* since the experiment lasted 20 min, the focus slightly changed over time due to water evaporation and was likely to induce errors in quantitative measurements of the signal intensity). Since we were only interested in the profile dependence of the SNR for both SRS and CARS techniques with respect to the beam power, the Y axis is in arbitrary units on purpose.

Rich-CH_2 bond samples

As one can see in figure 5.8 both starch and SOPC lipid droplet samples have similar behaviours in the three cases studied: (A) Dependence on the total beam (signal + idler), (B) dependence on the signal beam and (C) dependence on the idler beam. When the idler beam was decreased, both CARS and SRS signal decreased in the same proportions: they both showed a linear dependence. On the other hand, when the signal beam was decreased the SRS signal could be linearly fitted whereas the CARS signals demonstrated a quadratic dependence which is predicted from the literature (see Chapter 1 section 4.2). Unsurprisingly, the CARS signal was stronger than the SRS one when both beams were attenuated, which can be understood knowing that the (signal beam) CARS process is quadratically dependent with the concentration of CH_2 bonds whereas SRS is not (SRS is only linearly dependent). In figure 5.8 C, in spite of the precautions taken during the acquisition, the system seemed to have reached some saturation above $P_{\text{Signal}} = 150\,\text{mW}$ (see the vertical gray dashed line). The higher points have thus been discarded from the fittings (which is justified since such powers are not tolerated by biological samples).

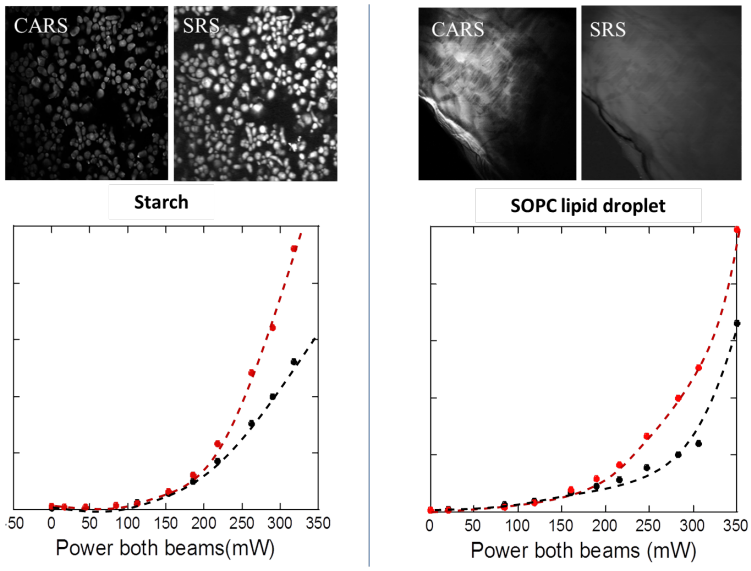

(A) Both beams dependence for statch and SOPC lipid droplet.

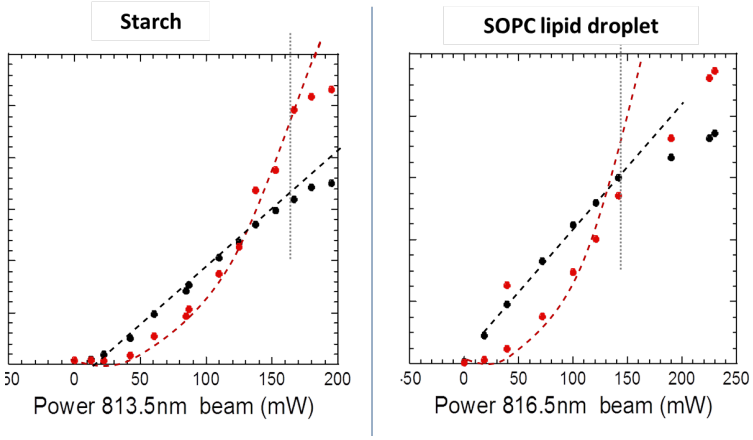

(B) Signal beam dependence for statch and SOPC lipid droplet.

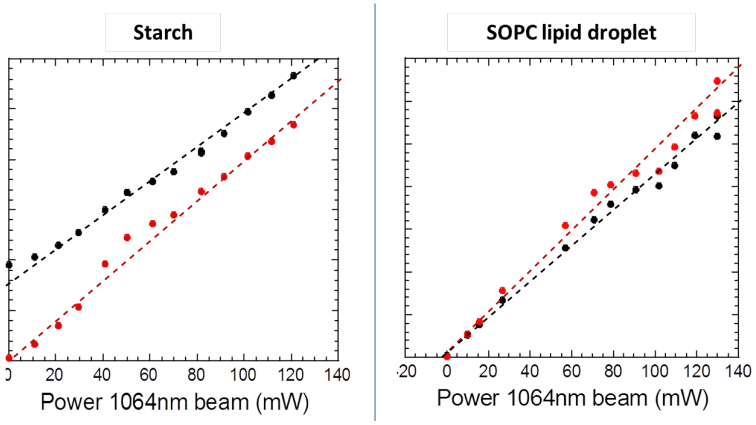

(C) Idler beam dependence for statch and SOPC lipid droplet.

Figure 5.8: Intensity dependence to the beams powers in CARS and SRS. CARS is in Red; SRS in black. (See text)

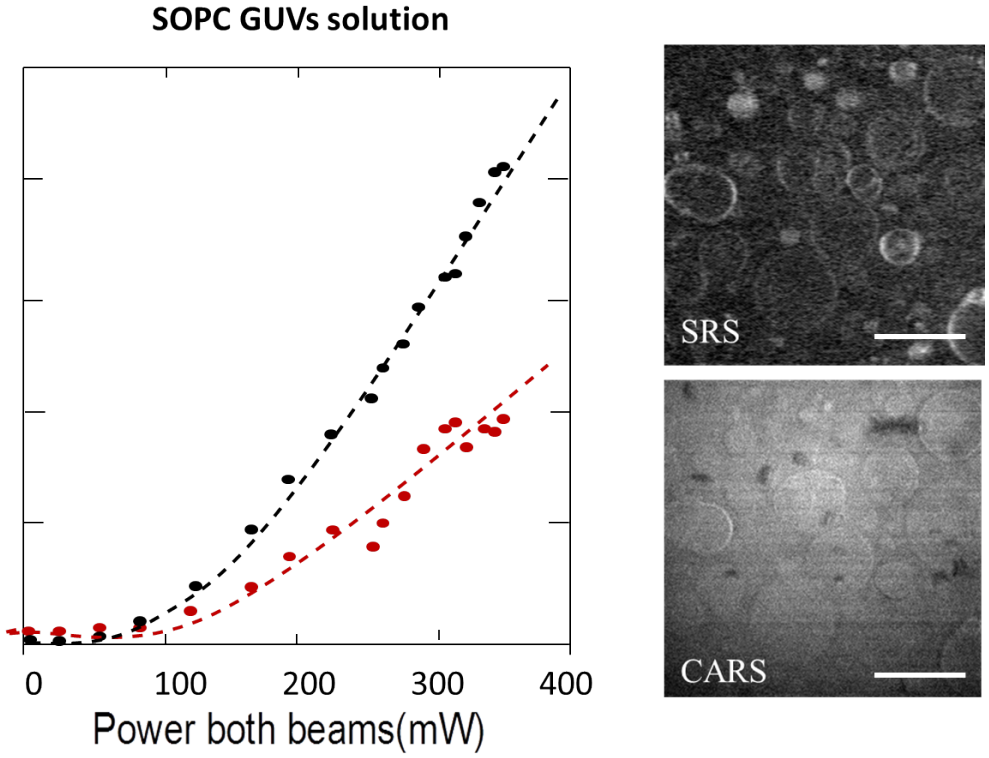

Figure 5.9: SRS versus CARS power dependence for imaging giant unilamellar vesicles (GUVs). Both beams are attenuated keeping the same signal/idler ratio. The SRS channel (in black) demonstrates a higher SNR compared to the CARS channel (in red). Bar scale = 25 μm.

Giant Unilamellar Vesicles

On the other hand, in the case of the solution of SOPC GUVs , the tendency was reversed when both beams were attenuated (see figure 5.9). The signal (SNR) from the SRS channel was higher than the signal from the CARS channel which is illustrated by the SRS and CARS pictures on the side. This effect, in agreement with the literature, also derives from the quadratic versus linear dependence discussed above. Since GUVs are unilamellar bilayer of lipids, the concentration of CH_2 bonds is low compared to that of startch and lipid droplets. It can thus be expected that the linearly dependent SRS exhibit a higher signal compared to the quadratically dependent CARS for such systems (which is taken advantage of here). Optimization of the images of GUVs recorded using SRS imaging is discussed in the next section.

5.3.2 Imaging GUVs using SRS

Improving contrast and resolution

GUVs were barely visible in SRS using the air condenser (data not shown). To be able to image the unilamellar bilayers, a dipping lens combined to a high NA condenser (1.0 NA) was required. The condenser height needed to be perfectly adjusted each time. Figure 5.10 (a) shows the effect of a non-perfectly-aligned condenser on GUVs imaging. Because of the dipping lense condenser confocal distance, a cover slip (1/10 mm thick) was used (instead of a microscopic slide) to make the vesicle chamber. Samples were usually closed with wax to minimize GUVs motions and prevent sample solution evaporation.

Different parameters needed to be adjusted to get both a good spatial resolution and a good signal-tot-noise ratio (SNR). The graph in figure 5.10 shows the theoretical profiles of noise and SNR with respect to the LIA acquisition time. Unsurprisingly, the longer the acquisition time the better the SNR. Besides, as expected, the 512x512 p setting provided higher spatial resolution images than 256x256 p images when the acquisition time was adapted for each. The reader can also notice the presence of a plateau in figure 5.10. Indeed, experimentally it was found that after a certain time (around 60 sec) the SNR was no longer significantly improved when increasing the acquisition time (no great difference in the resolution between (c) and (e)). Surprinsingly, GUVs could withstand full laser beam power (33 mW at sample), which did not seem to be the case when using CARS imaging.

To be able to acquire pictures with an acquisition time longer than 52 seconds (*i.e.* frequency rate lower than 5000 Hz) the experimenter had to switch to the 'external-clocking modulation mode' which prevented from acquiring data at a high frequency easily (short acq. t). Acquiring 512x512 p images in 52 sec was found to be a good acq. t/ SNR compromise, since, as shown in figure 5.10 (e), it gave a reasonably good contrast. Using 256x256 p images was nevertheless a necessary preliminary step, each time, to be able to find the GUVs plane and choose the vesicles of interest.

The purchase of another lock-in amplifier (Zurich) allowed to compare it to the SR 844 one for GUVs imaging. For both lock-in the integration time had been optimized before data acquisition. For 256x256 p images the SNR was much higher with the new lock-in than with the other one (for short acquistion times (4 sec)); whereas the resolution appeared around the same at longer times. There was hardly any SNR or

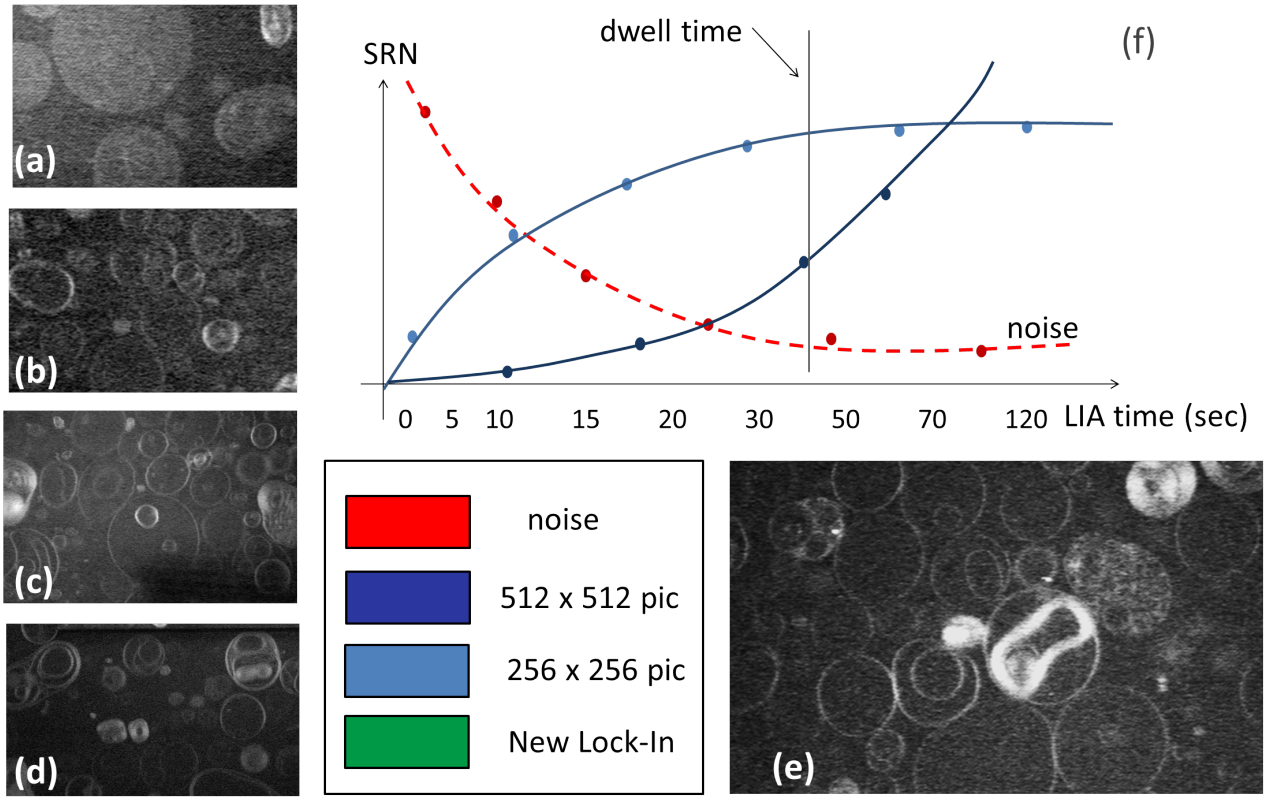

Figure 5.10: Improving GUVs signal using SRS imaging. Graph (e) is a schematic illustrating the theoretical dependence of the signal-to-noise as the funcion of the integration time. The noise (red) decreases with longer acquisition time while the images SNR logically increase. Images on the left have been acquired with different settings: (a) shows the effect of a condenser slightly misaligned on GUVs imaging; (b) 256x256 p, acq. time 13 s ; (c) 512x512 p, acq. time 69 s (external clocking); (d) 256x256 p, acq. time 4 s, lock-in Zurich, (e) 512x512 p, acq. time 52 s. (e) was found to be the best compromise (see text).

spatial resolution improvements between short and long acquistion times in the imaged acquired with the new lock-in. The same phenomena was recorded for 512x512 p images too. There are two parameters to take into account while acquiring images in SRS: **the dwell time of the scan-unit** and **the integration time of the lock-in amplifier**. The dwell time is the time spent on each pixel while acquiring an image whereas the integration time quantifies how fast the lock-in answers (*i.e.* it is the time window over which the LIA averages the signal). For an optimum spatial resolution both dwell time and integration time should match. In the case of our SR 844 LIA, the integration time is the limiting factor (maximum integration time $\sim 100\,\mu$s) hence when the dwell time is shorter than the acquisition time, information from different pixels are 'mixed' and blur the resulting picture (low spatial resolution) whereas in the opposite situation the image is not degraded. The new-lock integration is much faster (electronic integration) hence there is no difference between the 2 images (long and short acq. t).

Figure 5.10 (d) illustrates the capability of the new lock-in amplifier. As one can see both resolution and contrast are almost as good as in (c). However (d) has been acquired in a few seconds (compared to (c) - 69 sec). This latest lock-in was thus more efficient and it has been used to acquire hyperspectral images of cells (see Chapter 6).

SRS is really efficient to differentiate MLVs from GUVs

As shown in figure 5.11 when parameters had been optimized (microscope dwell time 200 μs for 512x512 p images) all the GUVs present in a sample could be detected (fig 5.11 (b)). Filled vesicles (*i.e.* lipid bulk) appeared in yellow (artificial color) due to the huge amount of CH_2 bonds. The presence of such vesicles was noticed to be more abundant when the stock lipid solution used for preparation was over 4 months old.

Finally, using SRS, clear distinction could be made between MLVs (or GUVs full of smaller GUVs) and properly unilamellar GUVs (see the montage in figure 5.11 (a) - the z-position is indicated in the right bottom corner of each picture of the stack).

5.3.3 Imaging domains in GUVs using SRS

Deuteration was also used to try and image domain distribution in lipid membrane systems. As one can see in figure 5.12, SRS was efficient to discriminate the L_β phase mainly composed of deuterated DPPC from DOPC and choleterol when illuminated with lasers at the deuterated Raman band (*i.e.* at 2105 cm^{-1}). They showed similar distributions than when GUVs were imaged with the Laurdan probe using fluorescence microscopy (which targetted the same phase, see fig 5.12 a). As one can see in the montage in (b) the other phase, L_o is just about distinguishable[1]. This short comparative study demonstrates the potential of the SRS imaging technique to study lateral segregation (*i.e.* domain formation/ distribution) in GUVs without any label.

Since we are interested in studying spectrin-lipid interactions and since spectrin preferentially interacted with PS (annexin and FITC-spectrin were competing for the same sites; see Chapter 3, section 4), it would have been interesting to be able to discriminate the PS lipid from the other lipid species, without using fluorescent probes. This could have been performed using deuterated PS in multi-component membrane systems. Unfortunately, in our case, deuterated DOPS although commercially available was prohibitively expensive. Other preliminary tests have been performed to try and grow GUVs with various lipid mixtures similar to the 4-component mixture used in Chapter

[1]Small amount of deuterated DPPC lipids is present in the L_α phase (see Chapter 1 for theoretical explanations)

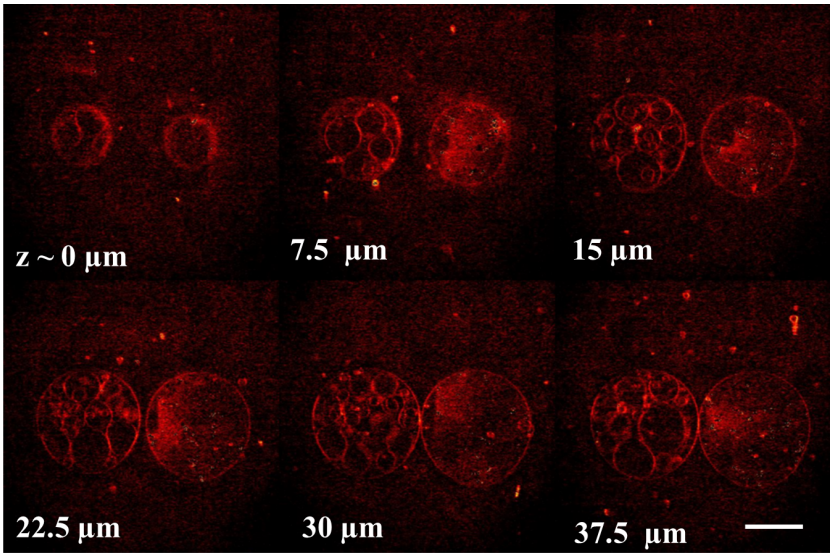

(a) Z stack Montage: Comparing GUV full of little vesicles and GUV.

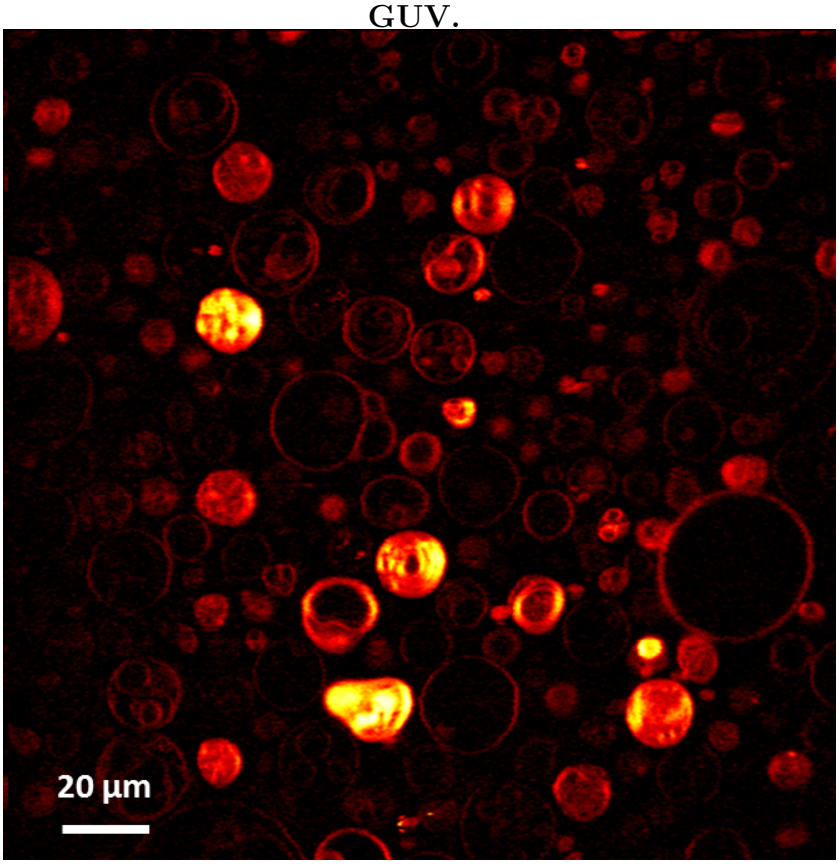

(b) Improving the contrast (dwell time and acquisition time optimization)

Figure 5.11: Solid lipids blocks and unilamellar vesicles with Stimulated Raman Scattering at 2845 cm^{-1}. Artifical color.

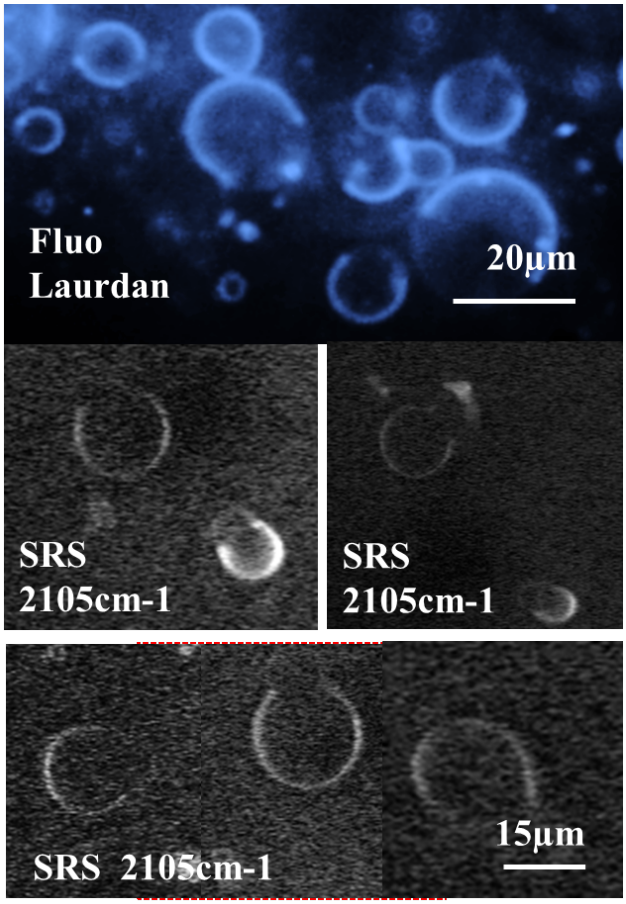

Figure 5.12: Imaging domains using deuterated lipids in domains separated vesicles. (a) Laurdan dye highlighting the L_β phase (artificial color, DIC microscope); (b) montage of DOPC:DPPC(d62):30%Chol picture, $2105\,\mathrm{cm}^{-1}$.

3. It was found that POPC/POPS/SM/Chol (25% each (molar ratio)) could also be grown with the electroformation method. The GUVs in suspension were nonetheless far less numerous than with the DOPC/DOPS/SM/Chol mixture. Both deuterated POPC(d31) and POPS(d31) were affordable as well as deuterated cholesterol (d7) and deuterated SM. Both POPC(d31)/POPS/SM/Chol and POPC/POPS(d31)/ SM/Chol were imaged in SRS at both 2105 and $2845\,\mathrm{cm}^{-1}$ (data not shown). A 'box' encapsulating the microscope area was built in order to control the temperature the experiment would be performed at. Due to a lack of time these studies could not be finished. Nevertheless, this seem a promising direction to take for label-free studies of domains formation/evolution under different temperatures/pressure/stress conditions.

Some work in another direction has also been carried in parallel, to try and study protein-lipid interactions, using label-free imaging technique in view of studying spectrin-

lipid interactions without the need for fluorescent probes (since as seen in Chapter 3 they proved to be compete for the same sites). Results are presented and discussed in the following section.

5.4 Imaging protein distribution around GUVs using TPF

5.4.1 Elastin: an autofluorescent protein

Elastin has been introduced in Chapter 4. It is an elastic protein of the extracellular matrix which is present in many types of tissue, such as the skin, the lung or the blood vessel walls and which endows them with the mechanical properties that are essential to their biological functions [146], [147]. The elastin is produced within the cell in a precursor form called **tropoelastin**. It is then transferred in the outside media and will form fibrils during tissue formations, and form an elastic crosslinked network which will not be regenerated over time [148]. Figure 5.13 gives a schematic of the elastin network present in the skin.

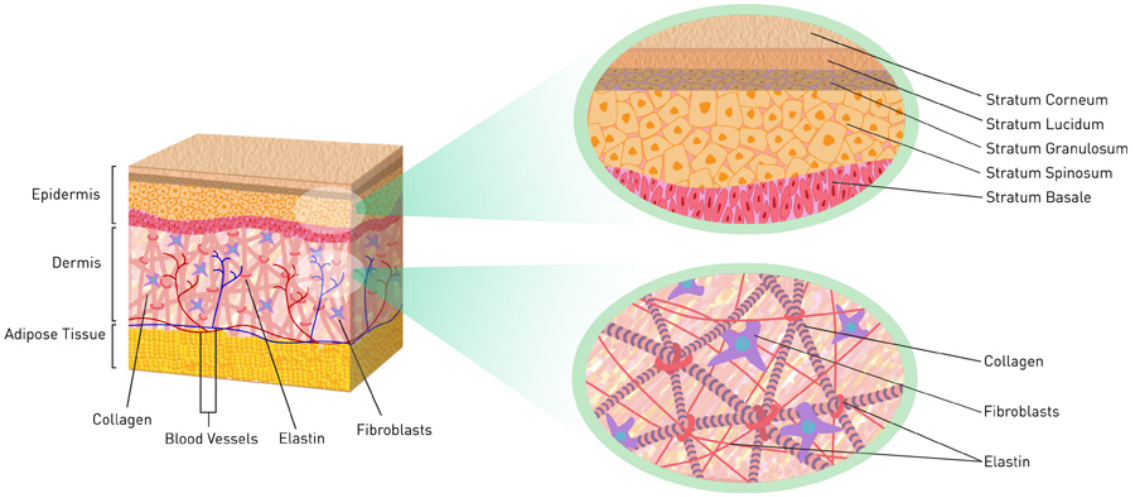

Figure 5.13: Elastin structure: an important protein for skin elasticity. From http://www.gold-collagen.com/en/skincare-science-and-research/

Elastin is an unusual protein in the fact that it possesses a lot of hydrophobic sites (they represent 60% of the protein) [149], [150]. There is some literature on binding of lipids (fatty acids and cholesterol) to fibrous elastin. It is a complex process[1]: protein and more hydrophobic lipids interact with, and change structure of, hydrophobic domains. Other will interact with hydrophilic domains, complicated to analyze because

[1]One of the elastin-lipid studies, investigated the protein-lipid sensitivity of ions. The fact that elastin is sensitive to calcium but not sodium ions was interesting and suggested that elastin-lipid interaction were more complicated than an simple electrostatic interactions (Winlove).

charge sites are not well characterized. Here we look at a different problem, the interaction of elastin monomers with a formed lipid bilayer. This is relevent to understand the interaction of cells with tropoelastin and degradation products.

There are different forms of elastin[1](α, β, κ). The elastin we studied was α-elastin. α-elastin is the preferentially studied elastin as a model since it has the closest form of mature elastin in tissue (macroscopic scale) at the microscopic scale: it still has the capability of building network-like structures. Indeed, α-elastin possesses the same properties as mature elastin within tissues (*i.e.* α-elastin most closely ressembles tropoelastin [151]): when heated at the right temperature and at the right proportions (30°C, 10 mg/ml), α-elastin can aggregate in solution [152], [151], this is called **coacervation** process. It also has the advantage to be used in a solid powder form.

Since α-elastin demonstrated the capability to interact with monolayers [146]and since it is known to be strongly auto-fluorescent [80], this protein was studied to **implement a method of label-free imaging of protein-lipid interactions**. In the next paragraphs, the results are presented and discussed.

5.4.2 Elastin-lipid interactions

In all the following experiments, two photon fluorescence (TPF) was used to image elastin. To perform TPF, the Mira laser, kept in the femto-second mode, was used at 800 nm. Appropriate filter centered at 500 nm was used (see the table in figure 5.2) which is ideal for imaging elastin as its fluorescent signal is known to be the highest at 495 nm [153]. The DOPC or DOPC:DPPCd62:30%Chol GUVs solution (200 mM sucrose/glucose)) was mixed with an elastin solution (sucrose 200 mM, Elastin 5mg/ml) and incubated at 37°C for 1 hour before imaging. The vesicle chamber was either the same as the one used for fluorescence experiments with the confocal microscope (see Chapter 3) or made of 2 cover slips[2], due to focal distance constraints in SRS. In a first set of experiments, the behaviour of the sample under laser was studied and demonstrated than the femto laser power had to be attenuated to 80 mW at the entrance of the scan-unit, to prevent sample damage (*i.e.* vesicle bursting, elastin burning).

When mixed with DOPC GUVs, α-elastin showed three main features which are summarized in figure 5.14. As one can see in (a) and (d), the elastin seems to attach uniformly around the vesicles and in some cases, more concentrated domains could be

[1] products of hydrolysis of elastin fibres.
[2] (instead of one microscope slide and a cover slip)

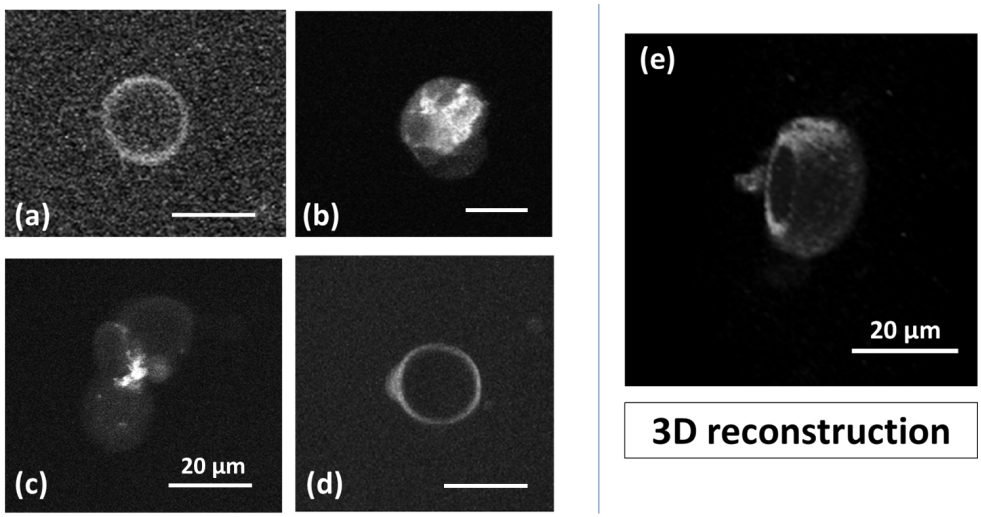

Figure 5.14: Interaction between elastin and DOPC lipid bilayers. Elastin is highlighted using two-photon fluorescence. (a, d) Elastin is uniformly adsorbed on the vesicle membrane (acq. times for (a) and (d) were 12 sec and 52 sec respectively); (b) a more concentrated elastin domain is present; (c) the protein makes vesicles cluster (see text). (e) 3D reconstruction of a stack (d) belongs to, demonstrating that the protein covers the membrane uniformly. Bar scale = 20 μm.

observed (b). Whether these concentrated elastin domain reflected the elastin preference for elastin already attached to a vesicle, or the aggregation of elastin occured within the bulk solution which would then interact with a vesicle, remains unclear[1]. Elastin also seemed to have the capability to make vesicle cluster (fig 5.14 c).

Changing the focal plane allowed to record z-stacks and build 3D reconstructed pictures using ImageJ plugins, such as in figure 5.14-e[2]. As one can see the vesicle seems uniformly covered with the protein.

Experiments performed on multi-component GUVs consisting of DOPC: DPPC: 30% Chol demonstrated similar interactions: the protein still uniformly binds to vesicles (figure 5.15 c,d). More concentrated elastin domains were also present around some GUVs (fig 5.15 a,b). These similarities demonstrate that elastin seems to interact with the lipid bilayer independently of its composition. Another effect highlighted in figure 5.15 (c) is the presence of small concentrated elastin domains within the GUV - showing the internal structure of the multilamellar giant vesicle - which might reveal the capability of the elastin to cross the membrane bilayer, perhaps due to the presence of cholesterol which increase the bilayer fluidity (as explained in Chapter 1). However further experiments need to be done to verify this hypothesis.

[1] Experiment at lower elastin concentration should be able to determine it.
[2] fig 5.14-(c) is a picture from the stack used for this reconstruction.

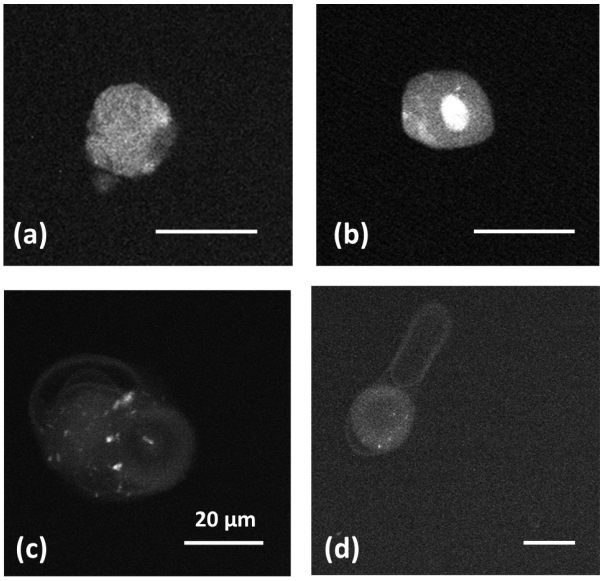

Figure 5.15: Two-photon fluorescence signal from the elastin showing the interaction between the elastin and some DOPC:DPPC:30%Chol lipid GUVs. (a, b) The vesicles are covered with elastin with the presence of more concentrated elastin domains. (c, d) The protein binds uniformely to the multilamellar vesicles, with the presence of some domains concentrated in elastin which highlight the internal structure of the membrane systems (see text). Bar scale = 20 μm.

5.4.3 Imaging lipids (CARS) and protein (TPF) of the same lipid systems

Since the aim was to be able to distinguish and image the protein distribution around the lipid bilayers, experiments combining TPF and CARS have been performed. A flip-mirror on the table allowed to easily switch from CARS to TPF (see figure 5.1, blue dashed line). Images of the same set of vesicles could be acquired a few seconds apart. The results are summarized in figure 5.16 (DOPC GUVs mixed with elastin). Once again, the CARS signal highlighting the lipid bilayer was less noisy in the forward direction compared to the epi-direction ((b) and (a) respectively). The protein distribution (TPF channel) looked very similar to that of the lipid (e-f) with slight differences which verified the conclusions drawn previously (*i.e.* uniform coverage). In addition, as one can see in (c), the group of little vesicles are clustered - they seem linked by elastin fibers - and a more concentrated elastin domain is also present at the bottom of the largest GUV. 3D reconstruction has also been implemented and demonstrated that the neckless-GUV imaged in (c-e) was uniformly decorated with elastin (fig. 5.16-g,h).

5.4.4 Imaging Elastin (TPF) and lipids (SRS) simultaneously

Since SRS had proven more efficient than CARS to highlight the lipid unilamellar bilayers (see section 3) a last set of experiments has been performed to highlight protein

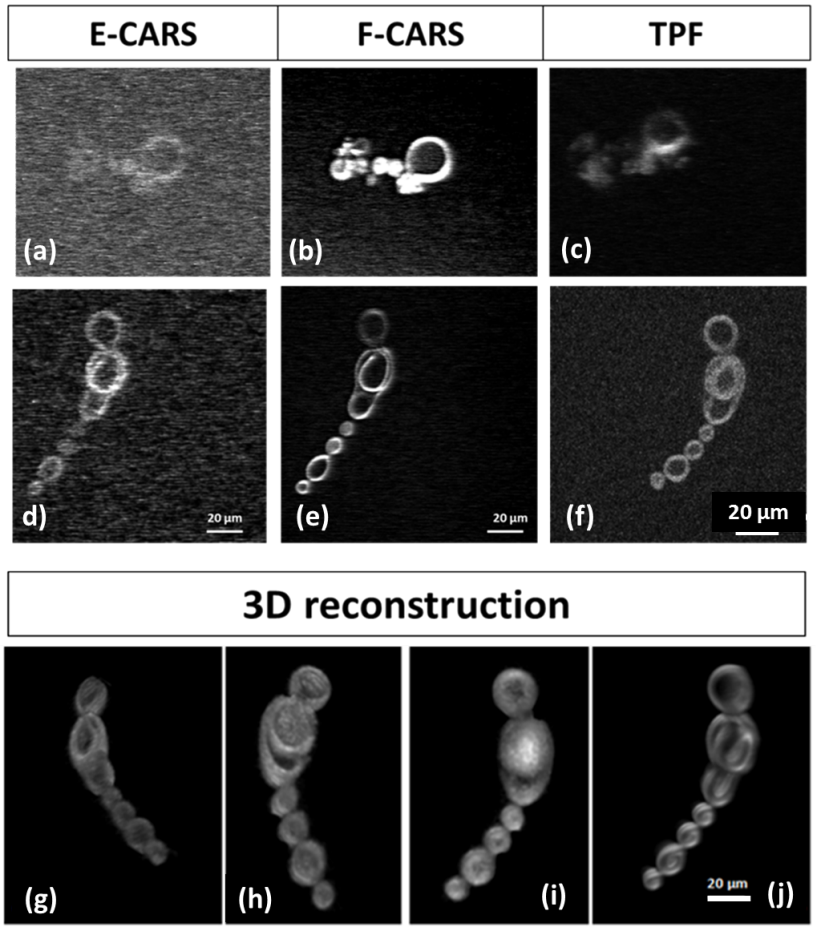

Figure 5.16: Imaging Elastin (using TPF) and lipid membrane in DOPC MLVs (using CARS) quasi-simultaneously. (a, d) Epi-CARS, (b, e) Forward-CARS, (c, f) Two Photon Fluorescence. (g-j) 3D reconstruction, (g, j) CARS, (h, i) TPF in different views. The same characteristerics as described previously could be identified (see text).

and lipid signal **simultaneously**. This derived from previous work: the idea was to record SRS and TPF signals simultaneously which could be implemented swaping the flip-miror with the 848 DRPL dichroic miror designed for section 2 ('two-channel detector').

Similar filters/method than previously detailed were used (see 'two-channel detector' section). The Mira laser was kept in the femtosecond-mode and was used at 816 nm to excite both TPF and SRS (*i.e.* femto/pico SRS was performed instead of the 'usual' pico/pico excitation). To be able to obtain SRS, the Mira Laser was synchronized with the 1064 nm using the Synchro-lock software and following the procedure detailed in section 2. TPF was recorded in the epi-direction in the exact same time as SRS was recorded in the forward direction. For this set of experiments SOPC GUVs were mixed

with the elastin solution (5 mg/ml) and incubated for an hour at 37°C as in previous experiments. Figure 5.17 summarises the results.

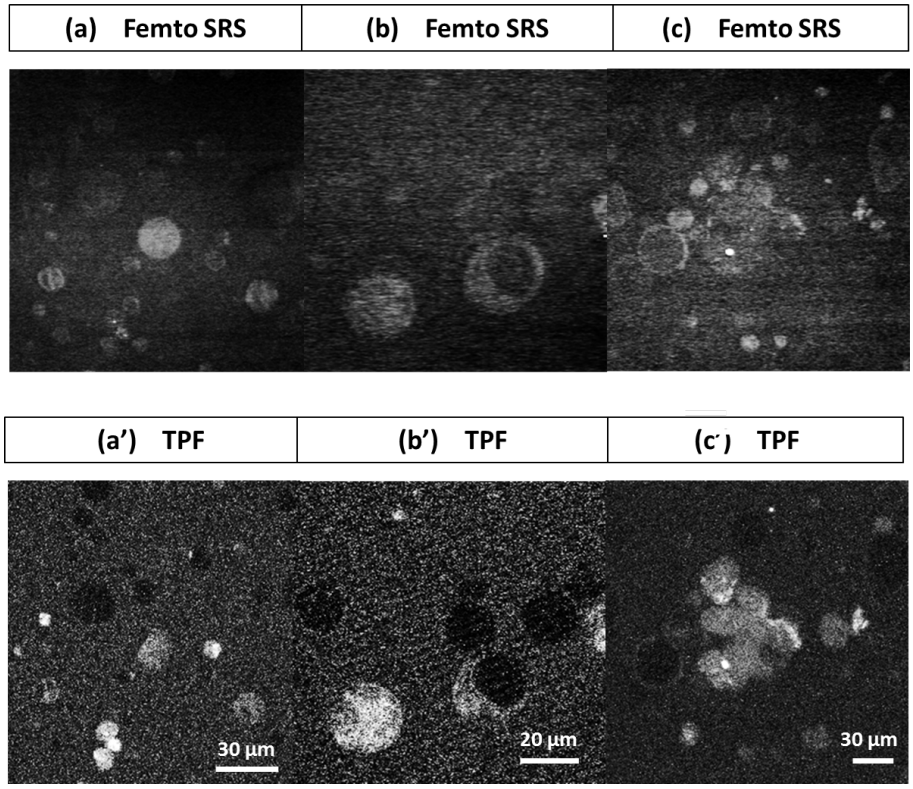

Figure 5.17: Femto/pico SRS combined with TPF. (a-c) SRS channel in the forward direction, highlighting the 2845 cm^{-1} Raman band; (a'-c') TPF channel in the Epi-direction. Elastin binds uniformly to some of the (SOPC) GUVs (c, c'). Vesicle aggregates were also present in (a,a' ;c,c') On (a,a';b,b') more concentrated elastin domains around some GUVs are distinguishable.

Results and discussion

As one can see in figure 5.17, the SRS signal was not as good as in pico/pico SRS but necessary with our set-up to be able to record both protein and lipid signals simultaneously. The weakness of the signal can also be explained by the power used: to power for the 816 nm beam had to be decreased down to 80 mW at the entrance of the scan-unit to prevent photodamages. Morever, 100 fs pulse width represents less than 2 % that of the 6 ps which reduces greatly the interaction process. Nevertheless the main features of elastin behaviour around GUVs described above could also be identified with SOPC vesicles. This corroborated the hypothesis that elastin interacts with the lipid bilayer independently of its composition. In figure 5.17 (a, b and c) are images highlighting the lipid membrane (femto/pico SRS signal) whereas (a', b' and c') are TPF signal from the elastin. As before, elastin attached uniformly on some vesicles (a, a') , with still

the presence of more concentrated elastin domains (b, b') and the protein seemed to make vesicles aggregate again (c, c'). This experiment both corroborated that elastin strongly interacts with the lipid membrane and demonstrated a new tool to acquire auto-fluorescent protein and lipid signals simultaneoulsy.

This technique could be improved by using another more appropriate longpass dichroic mirror (instead of the 848 nm DRPL) letting both 816 nm and 1064 nm beams go through and reflecting some of the 800 nm beam (since we attenuate the beam down to 80 mW, while its maximum power can reach 270 mW, we can afford to have a dichroic mirror reflecting only 30% of the beam)[1].

5.5 Discussion, conclusions and future work

NLO microscopy based on vibrational Raman signatures have proven to be very useful tools to label-free image lipids and proteins. Here we demonstrated the capability of a two-channel detector requiring 3 beams and allowing to record simultaneously the vibrational signatures of 'normal' lipid (at 2845 cm^{-1}) and of deuterated lipid (at 2105 cm^{-1}) in CARS.

Since SRS proved to be more efficient to image vesicles (and especially GUVs), this technique was used to investigate lipid distribution in bilayer membrane systems. This tool was especially interesting for imaging domains - in multi-component GUVs that are known for demonstrating lateral segregation- using deuterated lipids. For future work, further experiments involving more complex systems, *e.g.* POPC(d31):POPS:SM:Chol (25% each (molar ratio), could be investigated with and without perturbator element (protein, toxin etc). It could also be combined with the micropipette aspiration technique (combining SRS and micropipette aspiration will be demonstrated in Chapter 6) to see how the microdomain distribution reorganises itself when submitted to stress.

In all the experiments performed with TPF, (TPF alone, TPF combined with CARS, TPF combined with femto/pico SRS) elastin demonstrated high affinity with the lipid bilayer, independently of the lipid system (DOPC, SOPC, DOPC:DPPC(d62):30%Chol). This could have been expected due to its large number of hydrophobic sites. This corroborates the work performed on monolayers [146]. Moreover in presence of cholesterol, elastin seemed to have the capability to cross the bilayer membrane. It would be interesting to perform further experiments to verify this.

[1] It is usually difficult to find very sharp transition and 16 nm difference is a 'small wavelenght difference'.

Elastin-lipid interactions are actually a topic of interest, especially in the study of blood vessels since at the very early stage of artherosclosis the fat attaches and aggregates preferentially to elastin in blood vessel walls (until it spreads to the whole wall, thickens and blocks the artery). Furthermore it would also be interesting to study the distribution of elastin around GUVs for elastin of various ages (*i.e.* study new elastin, mature elastin, old elastin) and follow the evolution of its elasticity over time as it undergoes slight changes in composition due to aging (micropipette aspiration).

In the next Chapter another approach has been used to try and label-free discriminate the protein distribution from the lipid, without relying on protein auto-fluorescence but instead using hyperspectral images.

Chapter 6

Combining Micropipette aspiration and NLO

In this chapter, another approach to differentiate lipid species and to distinguish between lipids and proteins within model membrane systems is presented. Hyperspectral images of dried lipid droplets, GUV systems and cells were studied to discriminate between lipid species and/ or between lipids and proteins. A new technique combining micropipette aspiration and SRS was developed and applied to both membrane systems and cells of different types. Both qualitative and quantitative measurements will be presented. The potential of this new tool will be discussed.

6.1 Material and methods

6.1.1 Set-up description

The capability of the existing multi-modal microscope was extended to incorporate micropipette aspiration. A schematic of the apparatus is presented in figure 6.1, and pictures of the set-up are included in Appendix C.

The source used was the same as described in the previous chapter for studies using SRS. A plate, similar to that described in chapter 4, was constructed to replace the standard microscope stage. Since to move the sample, one had to move the whole microscope stage, a microscope slide-holder allowing displacements of the microscope slide only, in the $x - y$ directions was added as shown in the insert image in figure 6.1. This way the plate could be fixed to the microscope like in the micropipette post of the DIC microscope. Due to the smaller space available around the multi-modal microscope, the plate was smaller than the one of Chapter 4 but thicker to

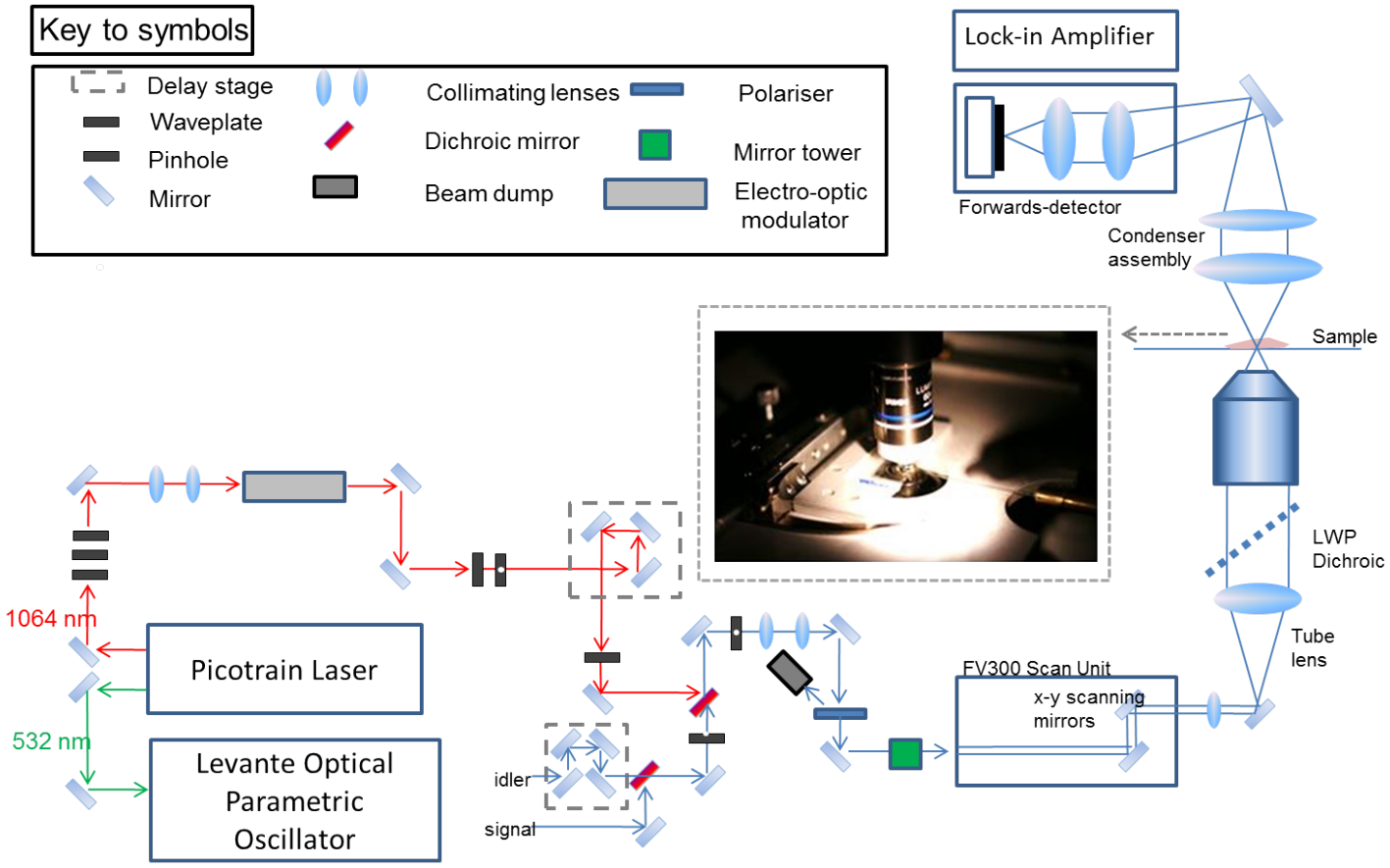

Figure 6.1: Set-up description: facilities at the University of Exeter combining micropipette aspiration and SRS. Adapted with permission from a diagram by Natalie Garrett.

provide higher stability. A smaller micromanipulator (SM3/1, from Thorlabs) was used to fit within the 'cage' present around the microscope. This new micromanipulator allowed 1.2 cm displacement in the three xyz directions, which was enough to bring the micropipette to the desired position. A replica of the micropipette holder was made and like previously, a cut-out on the plate allowed the micropipette holder to reach the sample level. The same water tubing, the graduated column and water reservoir were borrowed from the DIC micropipette apparatus.

6.1.2 Recording spectra

Raman spectra were recorded using the Raman microscope introduced in Chapter 5 (RM1000 Renishaw plc, UK). The laser was a continuous HeNe emission at 785 nm with a maximum power of 300 mW at the sample which was attenuated to 30 mW. A spectral gratting with 1200 lines/mm was used, which gives a spectral resolution of 1 cm^{-1}. The objective used was a 40x 0.55 NA from Leica (Leica, Germany). The

spectra were acquired by averaging 5 spectra using the WIRE 2.0 software (Renishaw plc,UK). Data processing was performed using Kaleidagraph.

SRS spectra were recorded either manually, changing the wavelength of the signal beam, or later on, using a home-made software writen in Labview (Labview virtual Instrument) by a summer student (Reuben, Hill) which optimized the process and allowed spectra to be recorded within a few minutes[1]. A reference diode sampling the excitation power by reflection from glass slide was used to normalize the signal. A home-made piece was used to hold the microscope slide on the normal microscope stage in place and allowed to maintain tighly the sample so that no drift in height (z direction) due to eventual water droplet evaporation occured. This allowed long acquistion times as necessary and to record accurate spectra without artefacts. They were usually acquired over the whole CH_2/CH_3 region, from 2800 cm^{-1} to 2960-3000 cm^{-1}, every 5 or 10 cm^{-1}.

Sample for pure lipids or lipid mixtures, consisted in lipid droplets from stock solutions (kept in chloroform) from Avanti, which had been dried on either a microscope cover slip for SRS imaging, or on some aluminium foil for Raman spectra[2].

6.1.3 GFP-actin tagged fibroblasts

GFP-actin tagged fibroblast were provided by Helen Dawe from Bioscience. Fibroblast cells were human neonatal fibroblast. They were tagged with green fluorescent protein using the usual protocol (LifeAct, UK)[3]. GFP-tagged cells were left to develop for 3 days after transfection. These were detached from the substrate they were grown in using trypsin. Once detached, cells were rinsed and diluted into a feeding media which deactivated the trypsin, and imaged within a couple of hours, after which time most of the cells would die [4].

[1] In this program, one could choose the spacing between 2 consecutive wavenumbers and would get a table giving the wavenumber difference and the power of the OPO for each wavenumber, out of the program. This way one could easily link the wavenumbers to the stack of the recorded images.

[2] Proteins were on the other hand dried into the incubator in the respective media they were kept in (PBS, sucrose).

[3] The cells were transfected via nucleofector (Lonza, Switzerland).

[4] To be able to perform experiments for longer time without killing the cells, one need to monitor both the CO_2 level and the temperature, which requires a specific set-up around the microscope, we didn't had access to in our lab.

6.2 Hyperspectral imaging using SRS

6.2.1 Hyperspectral images of lipid droplets: Comparing Raman and SRS spectra

Raman spectra

Figure 6.2-(a) shows the normalized **Raman spectra** around the CH_2 region of the lipid species used for experiments during the PhD. As one can see DOPC and DOPS spectra look quasi-identical exhibiting a high signal at $2840\,cm^{-1}$. On the other hand one can find 2 characteristic peaks in the DPPC spectum at 2845 and $2880\,cm^{-1}$. The cholesterol peak width is broader with characteristical high values at $2855\,cm^{-1}$ and $2920\,cm^{-1}$; the first peak appearing exactly between the two peaks of the DPPC which can be taken advantage of.

Figure 6.2-(b) gives on a same graph the Raman profiles around the CH_2 region of both another lipid species (SOPC) and the α-elastin protein. As expected from the literature (ref, ref) the spectrum of the protein is dominated by higher wavenumbers with a maximum around $2930\,cm^{-1}$ which corresponds to the CH_3 vibrational signature; present in abundance in proteins in comparison to lipids. This CH_2/CH_3 (*i.e.* $2845/2930\,cm^{-1}$) is more and more used to discriminate proteins from lipids in tissues [154]; [155].

SRS spectra

Figure 6.3 summarises the SRS spectra of lipid species recorded during the PhD. Some spectra of lipid/lipid mixtures and lipid/proteins mixtures have also been taken. The hyperspectral image used for plotting the spectra are provided for each lipid/lipid mixtures on the side. The lipid/mixture is provided on the bottom left corner of each hyperspectral image. A 'rainbow' look-up table (LUT) has been applied to all of them except starch[1]. The LUT assignates a colour to each Raman shift Ω.

We have seen, in Chapter 2 (see section 2.5) that SRS spectra do not suffer from the spectral distorsion seen in CARS spectra; and for a given sample, the SRS spectrum should perfectly match the Raman one. As one can see in figure 6.3, SRS spectra are not as accurate as Raman ones due to the much lower number of acquisition points. Nonetheless, characteristics of pure lipid species can still be identified: DOPC only exhibits very high signal at $2840/45\,cm^{-1}$, whereas, DPPC has another characteristic

[1] Starch is given for comparison in the top left corner

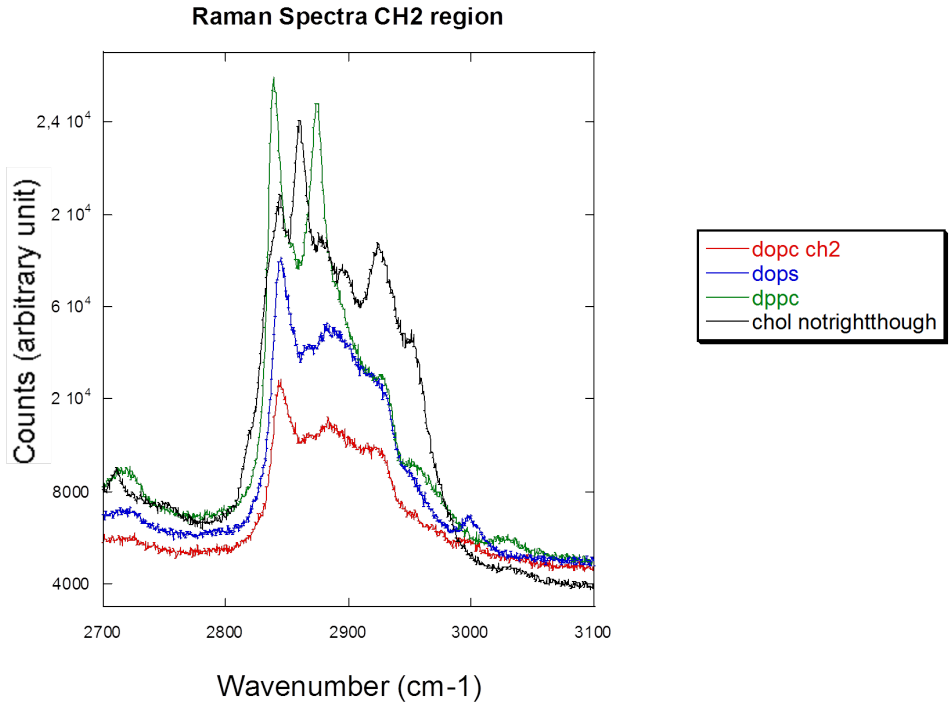

(a) Raman spectra of DOPC, DOPS, SM and Cholesterol CH_2 region

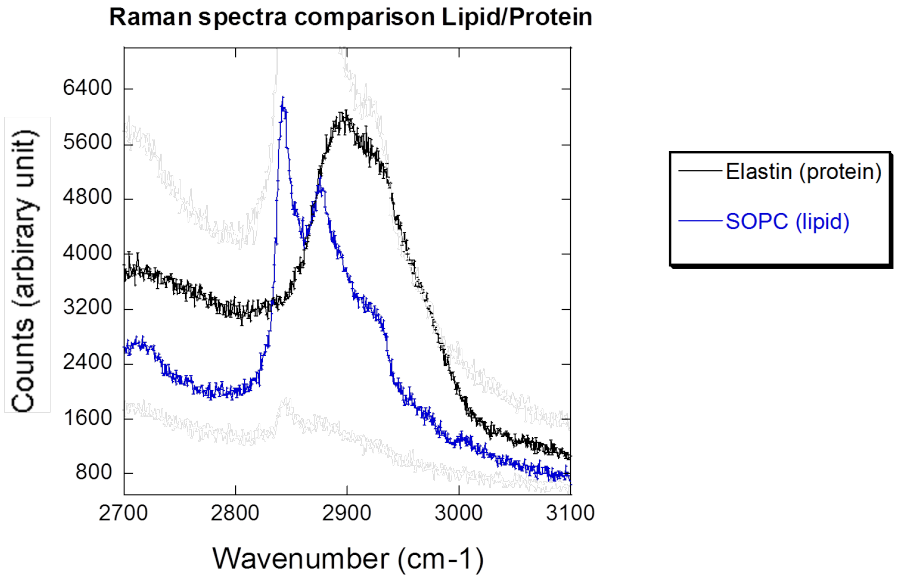

(b) Raman spectra of SOPC and elastin to compare protein/lipid peaks.

Figure 6.2: Raman spectra of lipid species and protein used during the PhD

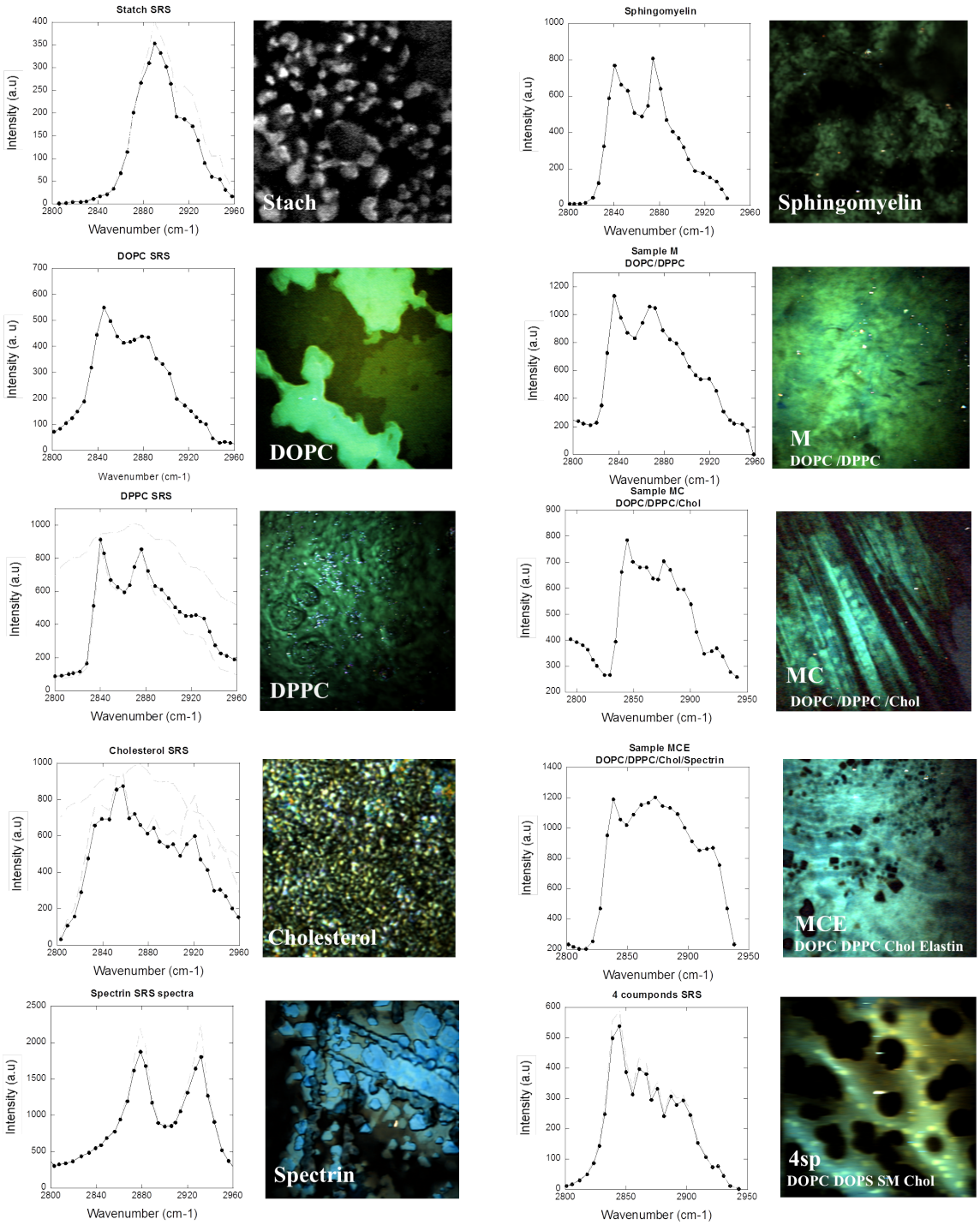

Figure 6.3: Hyperspectral images of lipids and lipid mixtures used during the PhD. (256x256 p images, gain 1, acquisition time per stack image was 12 seconds. Top left graph: Stach = Starch.

peak at 2880 cm^{-1}. Cholesterol vibrational features are also recognizable with higher signal 2860 and 2920 cm^{-1}. Finally, the spectrin protein provides among others a high signal at 2930 cm^{-1} typical of the presence of many CH_3 bonds as said previously.

Nevertheless, for lipid mixture samples: if for sample M (DOPC:DPPC, molar ratio 1:1) it is believable that its spectrum is a combination of spectra of pure DOPC and pure DPPC, for samples MC (DOPC: DPPC: Cholesterol), MCE (DOPC: DPPC: Cholesterol, Spectrin) and 4sp (DOPC: DOPS: SM: Chol) the spectra appear as a smooth broad peak, probably due to the presence of Cholesterol whose vibrational peak width is very large[1]. Several methods have been considered to try and extract informations from these hyperspectral image mixtures. Some of the techniques people use in the NLO field are briefly explained in the next paragraphs.

Methods to extract informations from hyperspectral images and limitations

Three main processing techniques commonly used to extract biochemical information from hyperspectral images were tried: decomposition of the spectrum into single vibrational bonds (Gaussian peak fitting), application of look-up table(s) and use of the principal components analysis (PCA) method. These three techniques have been thought to be implemented on the lipid mixture samples (M, MC, MCE and 4sp) and given up to the benefit of the implementation of a new technique (combining micropipette aspiration and NLO).

Figure 6.4 gives an example of decomposition of the CH_2 Raman signature of DOPC into its vibrational modes. This has been performed using Origin; the number of Lorentzian and/or Gaussian can be choosen; their highest value fixed and their width (FWHM) monitored. Tables are available to look for Raman modes susceptible to be present in the CH_2 region of samples [157], [156]. As one can see this seems already quite challenging for detailed Raman spectra of a pure lipids. SRS spectra being less accurate, a great number of attempts would be necessary, to restitute a plausible decomposition of lipid mixtures into pure lipid components. In the case of phospholipid mixtures, since phospholipids have the same main structures (they just differ from the length carbon chain and head group, see Chapter 1), they have many single vibrational bonds in common: this method therefore seemed non-accurate since one SRS spectra is likely to get several solutions for a same set of data.

[1]For all the samples, spectra have been plotted taking into account the intensity (normalized with the OPO power) of the whole image (mean intensity), averaging the intensity of all the pixels present in the image.

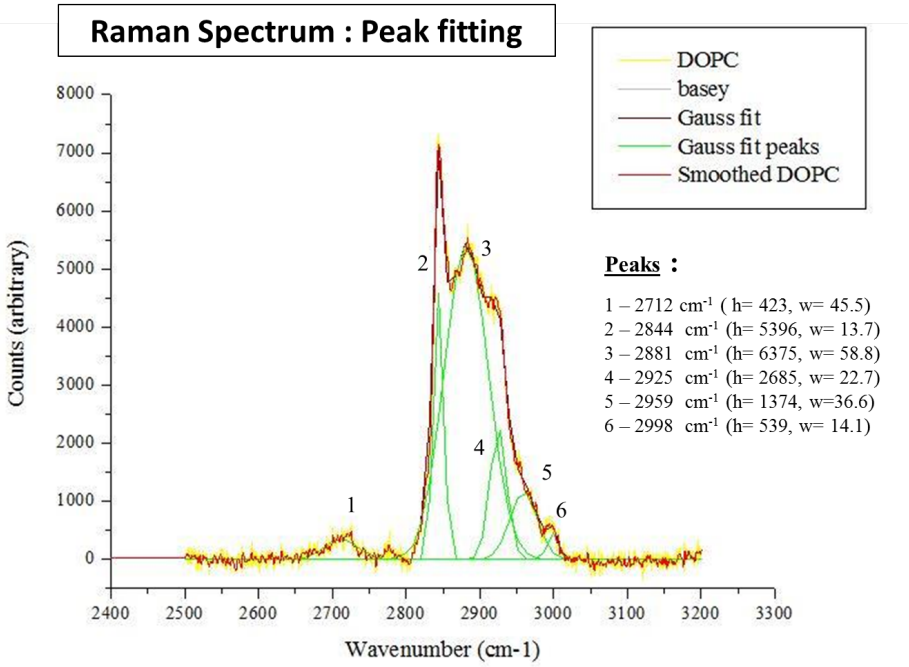

Figure 6.4: Decomposition of the Raman shift peak of DOPC (droplet lipid) in the CH_2 region into single vibrational modes. Some mode are recognizable: CH_2 symmetric (2840 cm^{-1}), CH_2 asymmetric (2870 cm^{-1}), CH_3 symmetric (2930 cm^{-1}), CH_3 asymmetric 2970 cm^{-1})[156].

Use of look up tables was also tried (see hyperspectral pictures on the side in fig. 6.3) based on what is done in other groups [158]. This method was shown to be an elegant and simple way to distinguish between chemical elements. Although very efficient in the case of minerals (whose component get narrow, well-separated spectra), distinction between lipids could not be easily performed (see fig. 6.3). All the pure lipids had similar colours due to the broad width of their CH_2 peak. One might still be able to detect slight blue/geen variations in the MC sample. Spectrin appeared in light blue while all the lipid appeared in different greens; the protein did nonetheless not seem distinguishable from lipids in the MCE sample.

Principal component analysis is a more and more used technique [159]. Easier to implement on lipid beads of distinct compositions whose spectra are clearly separated. A program was writen and tested on the M, MC, MCE samples. The program registered a spectra for each pixel of the picture into a big matrix. 3 references spectra corresponding to three distinct elements (components) were given and by iteration the program tried and found a combination of these three spectra to match the spectra for each pixel of the image. The program gave out, 3 images with the amount (in %) of each of the three reference spectra (components) for each pixel. Although preliminary results of David Woods and I program were promising, this direction was abandoned.

6.2.2 New approach: Using a micropipette to hold the GUV of interest in place

Since the systems of interest are giant **unilamellar** membrane systems, then a single layer of lipids is present. Hence one lipid species should be predominantly present inside a pixel[1]. In the case of macro-domain organisation (laterale segregation), the distinction between lipid species should be easier to implement using hyperspectral images. Hence using the relative intensity signals at 2845, 2850, 2880 and 2920/30 cm^{-1} for each pixel of the lipid membrane; one should theoretically be able to distinguish between different lipids and between lipid and proteins in multi-component GUVs.

As seen in Chapter 5, one of the drawbacks of this sample is that GUVs are easily disturbed which makes them challenging to study. One could think of using tracking methods to study a specific GUV in spite of its displacement[2]. Another idea could be to use a substrate the vesicles would stick to. In our case the final aim is to be able to image and study lipid-protein interactions (and their effect on the lipid membrane mechanical properties). To use a substrate GUVs will attach too, might interfere within the protein-lipid interaction and induce artefacts (attract the protein, make to membrane stiffer etc), they have thus been avoided.

Since micropipette aspiration technique has been used previously, the idea came to use a micropipette to hold the GUV of interest. This way the system would be immobilized and therefore it would not escape from the window and, provided the 'pipette + vesicle' system is stable, accurate hyperspectral images of GUVs could be taken. In multi-component GUVs, peaks in spectra at 2845, 2860, 2880 and 2920/30 cm^{-1} would give some insight of the vesicle composition, the protein distribution around the GUVs and its effect on the domain organisation.

Hyperspectral images of (multi-component) GUVs.

As one can see in figure 6.5, holding the vesicle of interest with a micropipette allows the acquisition of sets of images of a unique vesicle. Figure 6.5-a gives a montage of a Z-stack (the height is specified at the bottom of each picture) whereas figure 6.5-b gives a montage of a stack of images recorded to get the spectrum of the same vesicle (the wavenumber is specified at the bottom of each picture). And provided the

[1] provided there micro-domain domain organisation has domains whose size is bigger than the diffraction/image resolution

[2] But this will only works until the GUVs get out of the windows and would let to many 'power' to 'luck'.

pressure applied was not too high, a unique vesicle could be imaged for hours. Using this technique, stacks of images of different set of GUVs (DOPC, SOPC, SOPC:Chol, SOPC+α-elastin, DOPC:DPPC:Chol) have been taken for spectra reconstruction.

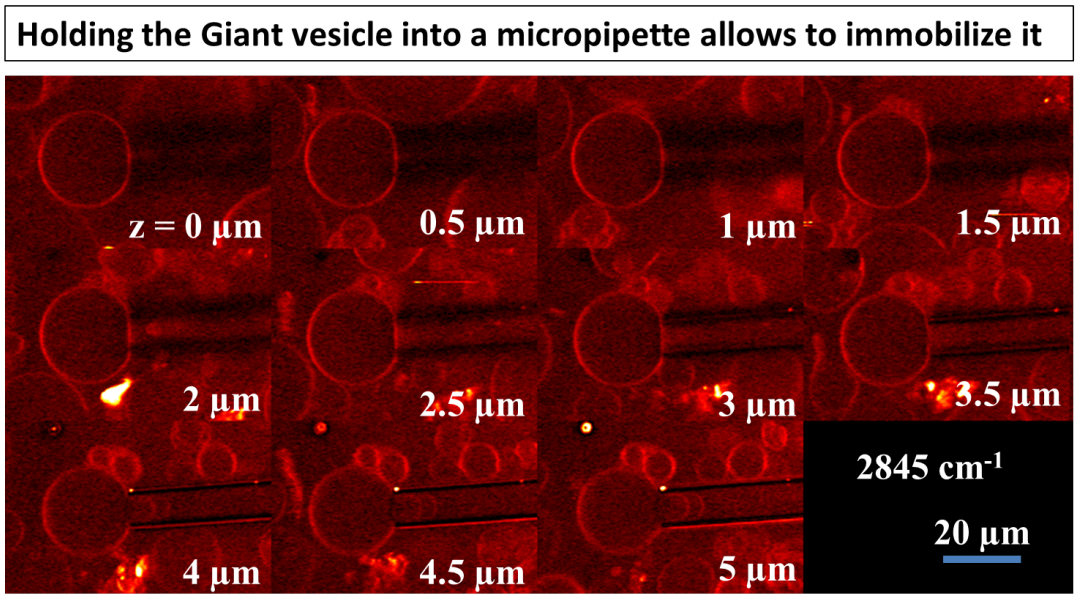

(a) Z stack of a GUV hold in a micropipette

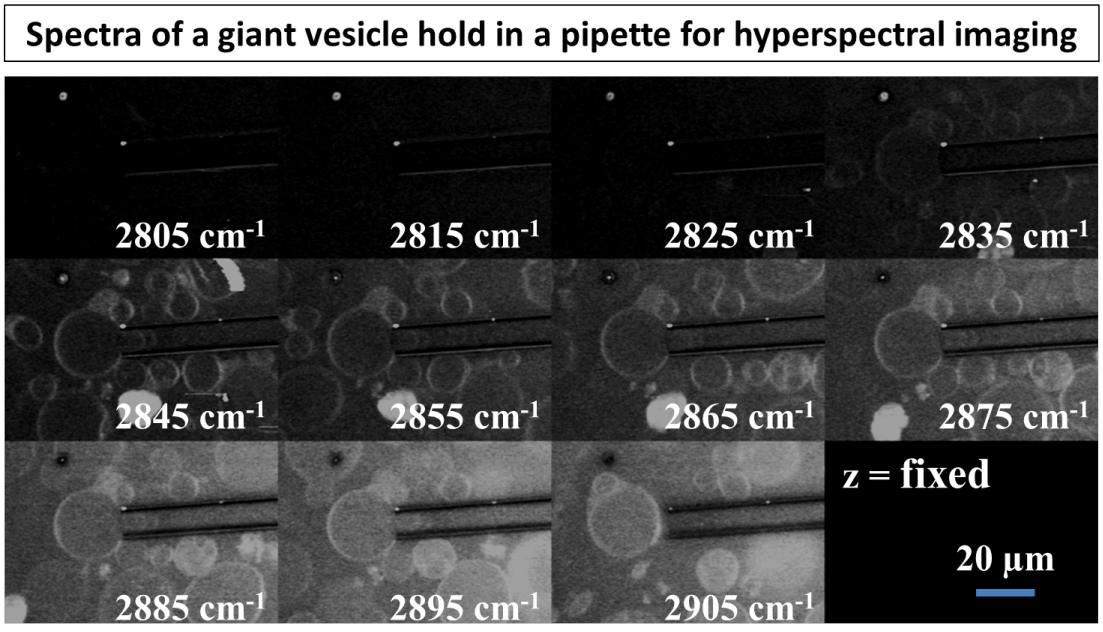

(b) Hyperspectral image of a GUV hold in a micropipette

Figure 6.5: Holding the GUV in a glass micropipette makes z stack and spectra acquisition possible.

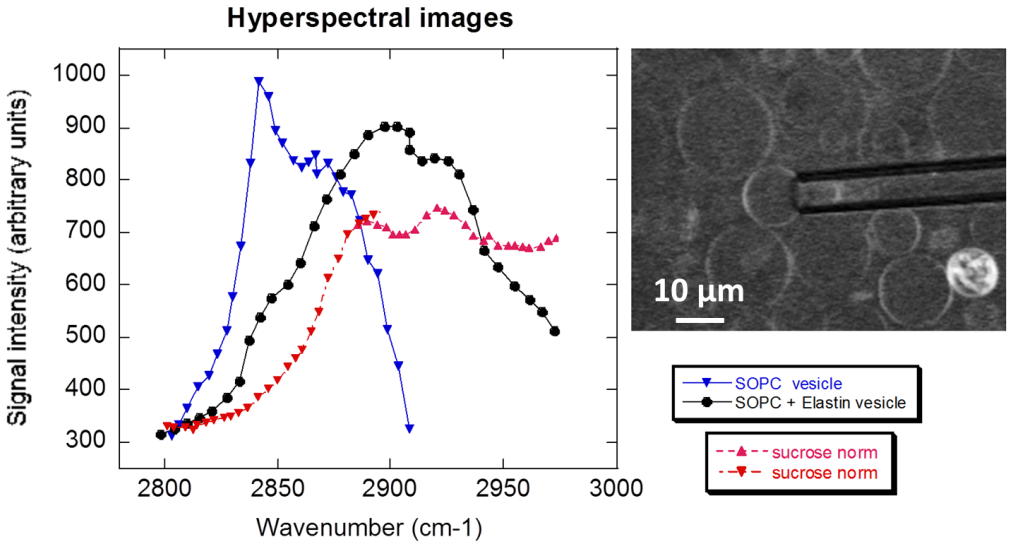

Figure 6.6: Combining micropipette aspiration and NLO for recording GUVs spectra: The SOPC vesicle (in blue on the graph) exhibits a higher signal around 2845 cm^{-1} whereas the SOPC vesicle surrounded with elastin (in black on the graph) exhibits a higher signal around 2930 cm^{-1} (protein signature). Hence recording spectra allows to distinguish between the vesicles surrounded with protein from the protein-free vesicles. As one can see, the sucrose medium (in red on the graph) exhibits a higher signal at higer wavenumbers.

Figure 6.6 summarizes some of the results. As one can see, in the case of a multi-lamellar SOPC vesicle (in blue in figure 6.6), the SRS spectrum looks similar to the Raman one of a lipid droplet (fig -6.2). When, the α-elastin protein was added (in black in figure 6.6), a peak at 2930 cm^{-1} was present allowing distinction between the two spectra which was an encouraging sign. However, in the case of mixtures (SOPC: Chol), the spectrum did not look as good as what could be expected (data not shown). The poor definition of the CH_2 peak comes from the added noise due to the bulk solution. This was due to the presence of CH_2/CH_3 bonds in both sucrose and glucose. Spectra of those have been recorded and demonstrated a 'broad peak' around 2890 cm^{-1} (in red in figure 6.6). In some pictures the signal from the bulk solution in the higher wavenumbers overhelmed the signal of lipids.

Several media were tested (glycerol, ethanol, deuterated water, lower concentration of sucrose glucose (100, 50, 20 mM)) to try and get rid of the solution background, unsucessfully. Due to a lack of time, efforts have been put toward demonstrating the potential advantages of using a micropipette together with NLO facilities using other samples, easier to manipulate (*e.g.* endothelial and fibroblast cells)(See the following sections).

Discussion

These measurements on GUVs, although preliminary, constitute promising results. After-experiments thoughts, revealed that the direction to take is probably to use deuterated sucrose/glucose [1] which would drift the bulk solution signal down to the 2105 cm^{-1} region. If unsucessful, the use of different deuterated lipid might be another answer to drift all the lipid signals away from the bulk solution signal; in the lipid silent region (provided the lipids to use can be found at affordable prices).These background issues have thus only been theoretically resolved and could not be verified due to a lack of time/funding. It is nonetheless believable that this method should allow the record of good GUV spectra. Limitations of the technique will be discussed in the last section of this Chapter (conclusions).

Finally, a program (plugin on ImageJ), was used to try and get spectral decomposition of hyperspectral stacks of image. The program was very sensitive to motion artefacts. One can find a preliminary result on which glucose and sucrose can be distinguished from lipid and the glass pipette in Appendix part F. With futher measurements, one should be able to distinguishing between lipid species (*e.g.* DOPC, DPPC and Cholesterol) as well.

6.2.3 Hyperspectral images of cells

Epithelial and fibroblast cells were used as a sample model to validate the potential of combining micropipette aspiration and NLO. As one can see in figure 6.7, epithelial cells (IMCD3s), provided a much better signal in SRS (a) than in Epi-CARS (b) and features could be distinguished at 2845 cm^{-1}, (see the montage of the Z-stack provided in (c). In the last 4 pictures the micropipette is close to one of the cells).

Spectra of epithelial cells

Since cells contain much more lipids (*i.e.* CH_2 and CH_3 bonds) than GUVs, and since they are kept in PBS (or other biological media without load of glucose/sucrose), cells signal (SNR) was much higher and extended spectra could be acquired as shown in figure 6.8. Spectra of different regions of the cells demonstrated different CH_2 spectra: area 1 (blue) exhibited a higher signal than area 2 (red) and 3 (green), at 2845 cm^{-1}. On the other hand, area 2 and 3 exhibited higher signals at 2930 cm^{-1} reflecting the presence of CH_3 bonds in these regions. Eventually the spectra of area 3 appeared

[1] or PBS buffer, but GUVs will be invisible under the microscope eye pieces and would not be easily caught

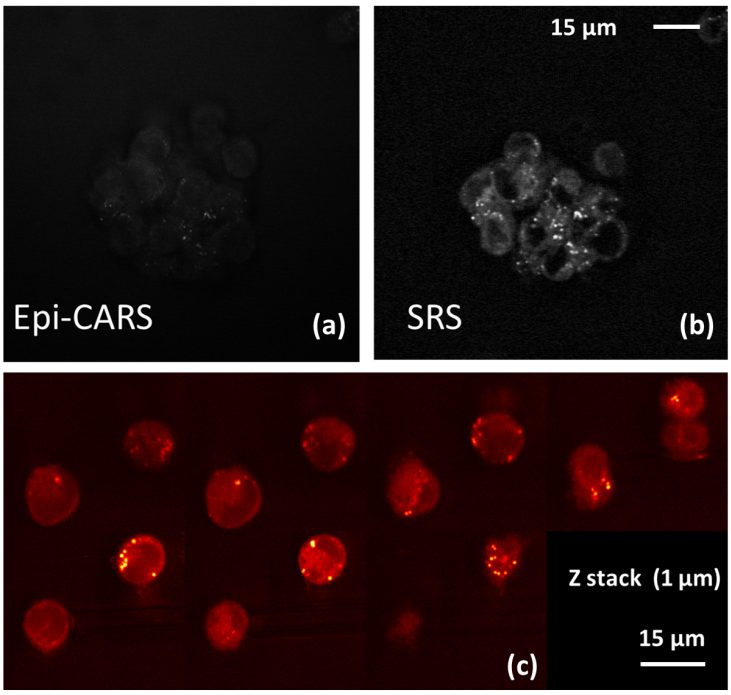

Figure 6.7: (a) Epi-CARS image of endothelial cells, (b) SRS image of endothelial cells. Endothelial cells signal recorded was better in SRS than in CARS ((a) and (b) were recorded simultaneously). (c) z stack of some endothelial cells. One of the endothelial cells is held in a micropipette (see at the bottom). Height between two consecutive slices was 1 μm.

narrower than area 1 and 2. Hyperspectral images thus provided different peak profiles allowing to distinguish between lipid droplets (area 1), protein tissue (area 2) and the nucleus (area 3) without any labelling[1]. This is of importance as labelling can be toxic for cells and might also alter the processes to be studied. The pipette present on the right side has been highlighted with a white dashed line.

6.3 Combining micropipette aspiration and SRS

To establish the potential of combining the micropipette aspiration technique together with the NLO imaging techniques and to validate the method, both qualitative and quantitative measurements have been performed. Quantitative measurements were performed on GUVs (as we know which values to expect thanks to measurements performed in Chapter 4) whereas qualitative measurements were performed on fibroblast cells and compared to fluorescent measurements performed on fibroblast whose cytoskeleton had been tagged with green fluorescent protein beforehand (GFP-actin tagged fibroblast cells).

[1]To study the ratio of peaks is another way to try and distinguish between cell components

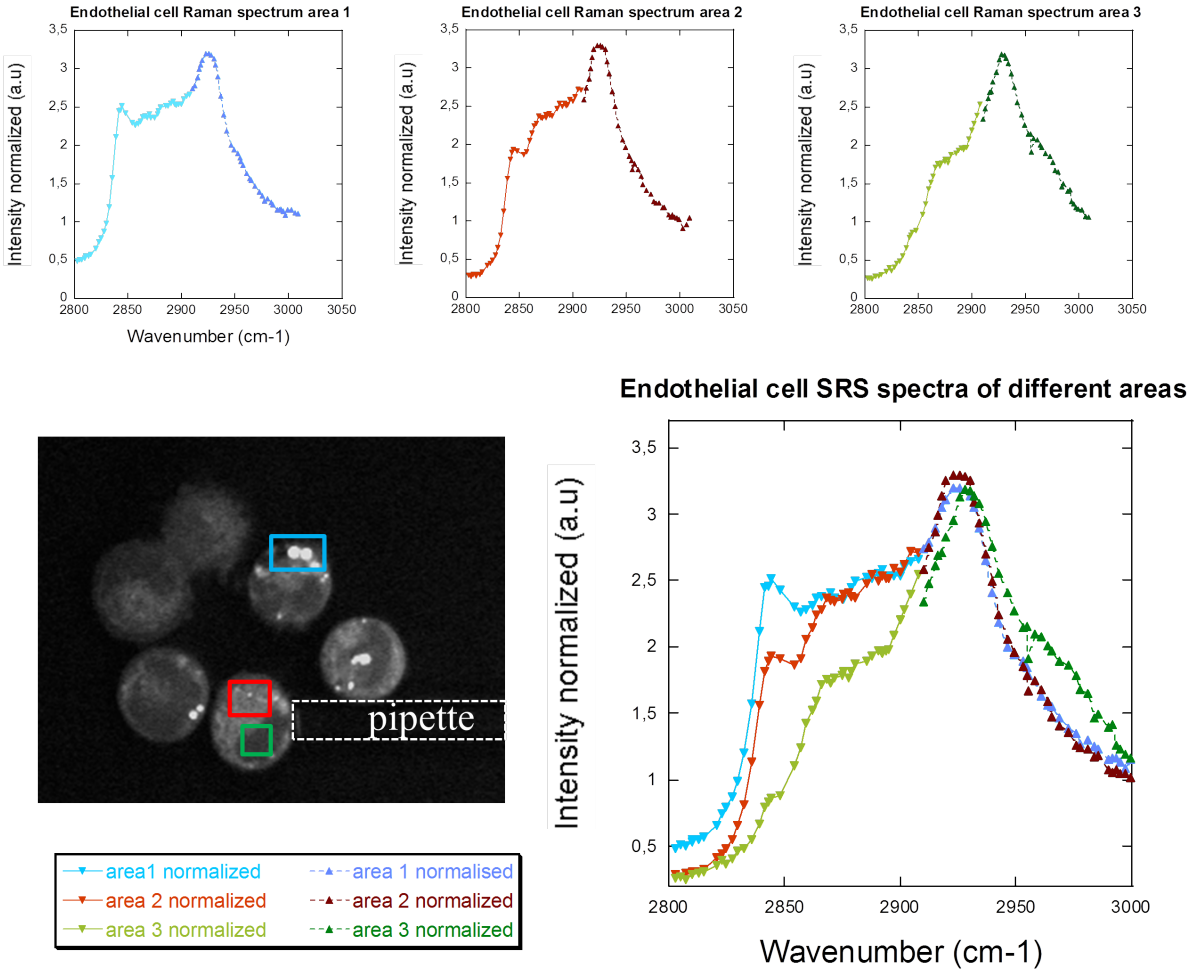

Figure 6.8: Top graphs: Spectra of different parts of the cell in the 2800-3050 cm^{-1} region. The graphs have been superimposed to highlight the differences of the peaks (*i.e.* peak ratio) at 2845 cm^{-1} and 2930 cm^{-1} respectively (bottom graph). The image in the insert shows the regions used to plot the graphs. This demonstrates that the record of hyperspectral images allows to distinguish between different areas within a cell (say nucleus (green), cytoplasm and cytoskeleton (red) and lipid droplets (blue)).

6.3.1 Quantitative measurements on SOPC vesicles

SOPC GUVs solution and chamber were prepared as described in Chapter 4 (electroformation method). Data were recorded acquiring *xyt* stacks, the acquisition time being lower enough for the membrane to stabilize within the pipette between 2 consecutive pictures, like in Chapter 4. Pressure was increased by either steps of 500 Pa or 200 Pa. Figure 6.9 is a montage of a micropipette aspiration experiment acquired using SRS. One can see a tongue formed and elongated inside the pipette until the GUV burst when the lysis tension was reached. The pressure applied to the GUV, is indicated at the bottom right corner of each image.

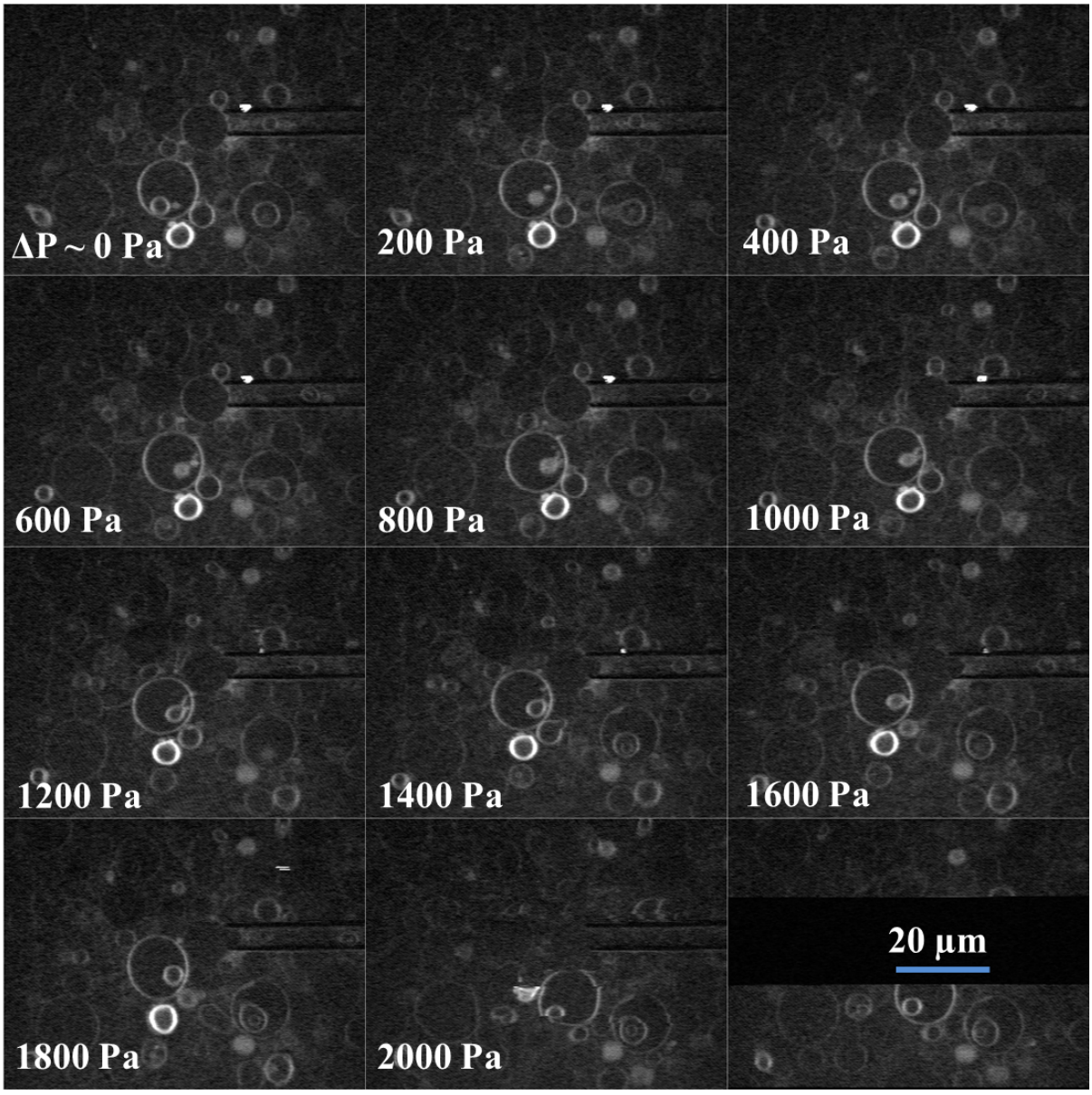

Figure 6.9: Montage of images of a SOPC GUV aspired in a micropipette during a micropipette aspiration (MPA) experiment imaged with SRS (at 2845 cm^{-1}). The pressure applied is provided for each image (right-bottom corner). A tongue forms and elongates linearly within the pipette while the pressure increases like in DIC demonstrating that SRS is a suitable technique to image MPA experiments.

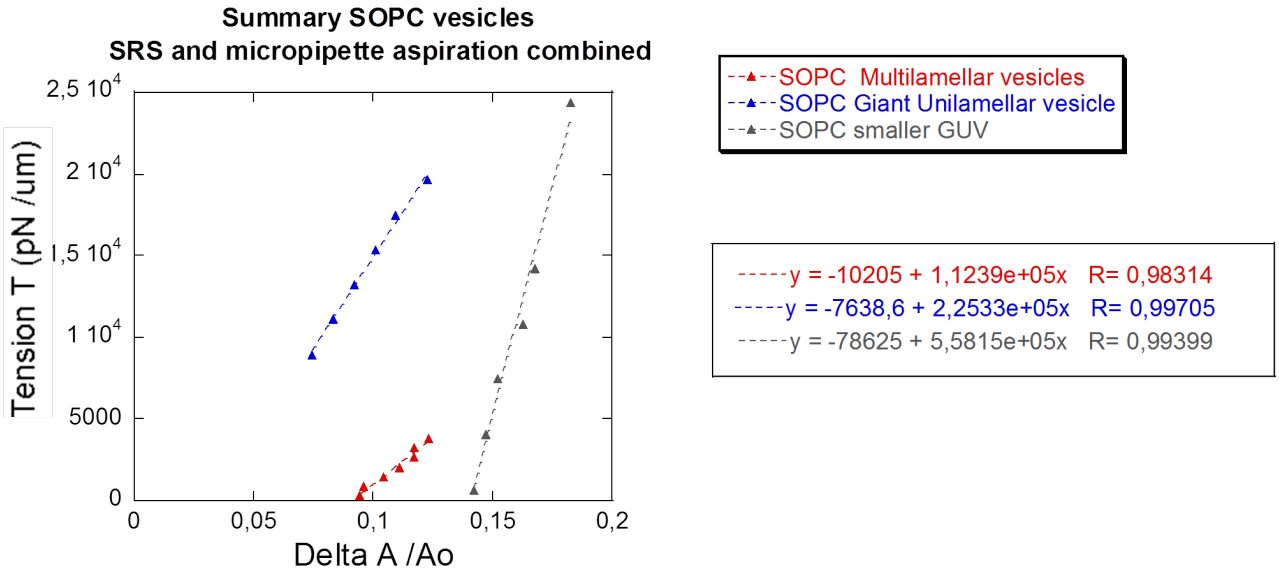

Figure 6.10: Micropipette aspiration performed on SOPC GUVs and imaged with SRS. Summary graph providing the tension, τ, with respect to the relative area expansion, $\Delta A/A_0$, givig a MPA measurement for each class of vesicles: MLVs (red), large GUVs (blue) and small GUVs (grey). Linear regressions are provided on the side. MLVs are softer than large GUVs (*i.e.* smaller area expansion modulus κ_A) and small GUVs are stiffer than large GUVs (*i.e.* higher area expansion modulus κ_A) (see text).

Comparison with DIC measurements

Micropipette aspiration was performed on a set of 15 vesicles out of which three classes could be distinguished and related to measurements acquired in DIC. One can find all the measurements, the pictures of the vesicles and the table recapitulating the results in the Appendices. Figure 6.10 summarises the results by giving an example of measurement for each of the three classes. Class 1 (vesicles 1, 2, 6 and 13) was constituted of multilamellar vesicles which had a low area expansion modulus K_A, with an average value of 152 mN/m (152,3 mN/m +/− 88 mN/m) and was down to 50,6 mN/m. Class 2 (vesicles 3, 4, 5, 7 and 15) were giant unilamellar vesicles, whose R_{ves}/R_{pip} belonged to the right range; their K_A was around 220 mN/m (219.9 mN/m +/− 55 mN/m) which is in good agreement with measurements of SOPC GUVs made by electroformation of Chapter 4 (negative control). On opposite, class 3 (vesicles 8, 9, 11, 14 and 16) was composed of smaller GUVs (hence the R_{ves}/R_{pip} ratio was below 2.5) whose K_A was much higher: 570 mN/m (569.6 mN/m +/− 206 mN/m).

Discussion and future work

Measurements performed on SOPC vesicles using SRS imaging, were in good agreement with measurements performed using actual imaging technique for micropipette

aspiration experiments (*e.g.* pH2, DIC). MLVs demonstrated a low area expansion modulus compared to GUVs; K_A of unilamellar vesicles being roughly 200 mN/m. In the same way as under DIC, GUVs measurements for which the R_{ves}/R_{pip} was too small showed a very high K_A. In practice (see measurements in Chapter 4), results from classes 1 and 3 were discarded to draw meaningful conclusions. Althought these measurements did not add anything to the field, were an essential step to ensure that pulsed lasers did not add unwanted effects on the lipid bilayer mechanical properties. This technique would be an excellent tool to both label-free image the distribution of protein / toxin around GUVs while studying its effects on the membrane mechanical properties. For example, performing micropipette aspiration using both SRS and TPF imaging facilities on GUVs after incubation with α-elastin would allow to combine results obtained in Chapters 4 and 5 in a single experiment. This would also allow to visualise the deformations the protein undergoes when pressure is applied and/or how it reorganises around the GUV.

6.3.2 Qualitative measurement on fibroblast cells: a comparative study with labelled cells

A final set of experiments was performed on fibroblast cells to demonstrate the potential of combining NLO together with the micropipette aspiration method. It was mentioned in the litterature that cells may have the capacity to separate from the cell cytoskeleton when under pressure [128], [160], [161], [162]. It will thus be interesting to image the cell membrane deformations using vibrational signature capability of SRS in combination with the micropipette aspiration to verify it. Fibroblasts thus appeared to be the perfect sample to validate this new method[1].

Fibroblast cells

Fibroblast cells, are amongst the most interesting cells since they are very chaotic. They are of great importance since all cells are fibroblasts before differentiating into specific cells. Fibroblast cells have indeed the capacity of differentiating into any kind of cells which makes it a biological sample with great potential. When unused, some cells (*e.g* muscle cells) go back to being fibroblasts; their resting state. Fibroblasts thus constitute an amazing cell base to study a wide range of diseases from mutations to injuries. Their differentiation capability would make it a very handy substrat to study for example, the effect of proteins/ toxins/ mutations onto the mechanical properties of the cell membrane.

[1] Endothelial cells, which was the first cell sample, seemed too stiff to be caught by the pipette within the pressure range available.

Performing micropipette aspiration on GFP-actin-tagged cells

For the purpose, of demonstrating the capability of SRS to label-free highlight the cytoskeleton of (fibroblast) cells; a control sample was required to make comparisons. Micropipette aspiration was thus also performed on fibroblast cells whose cytoskeleton was tagged with green fluorescent protein (GFP-actin tagged fybroblast cells)[1]. Figure 6.11 illustrates the results. The pressure applied was only qualitatively increased. Experiments on around 10 fibroblat cells were performed. All of them demonstrated a large elasticity, the answer to pressure being much slower than in the case of membrane systems. Usually when performing micropipette aspiration experiment on fibroblast cells, one needs to apply staircase-like pressure profiles, for the membrane to reach equilibrium which takes minutes [160]. This was not been performed since we were interested in recording qualitative measurements only (*i.e.* reaching 'equilibrium' is not of high importance here).

As one can see, in the bright field channel, the membrane could go a long way inside the micropipette compared to GUVs (see confocal channel in figures 6.11 (red arrows) and 6.14). Moreover, as shown in figure 6.14(confocal channel) in some cases the membrane within the micropipette thinnered while elongating (yellow circle) . Whether the phenomena was the cell answering to the stress applied, whether this was due to a leakage at the beginning of the pipette remained unclear. Futher measurements will be necessary to infirm or confirm this observation. If real, this effect would be of great interest, since it would relate to the characteristical way fibroblast move [163], [164] and the way lipid microdomain structure reorganises [165].

Fluorescence signal from the cytoskeleton was uniformly present around resting cells (see cell next to the one inside the pipette in figure 6.11 and green arrows in figure 6.14). As one can see the actin network was not uniformly distributed around the membrane present inside the micropipette (see the fluorescence channel in figure 6.11). It seemed that membrane devoid of cytoskeleton was aspired inside the pipette first which would confirm that the cell membrane separated to answer to stress. The nucleus appeared as a black body in the middle - this was checked tagging other cells with hoestch (data not shown) - and seemed to both be able to deform inside the micropipette, and might participate in giving resistence to the applied pressure (orange arrows in picture 6.14 and fluorescence channel in figure 6.11). We will come back to these features while comparing data with untagged cells pictures acquired in SRS.

[1] As seen in Chapter 2, GFP is a less toxic fluorophores)

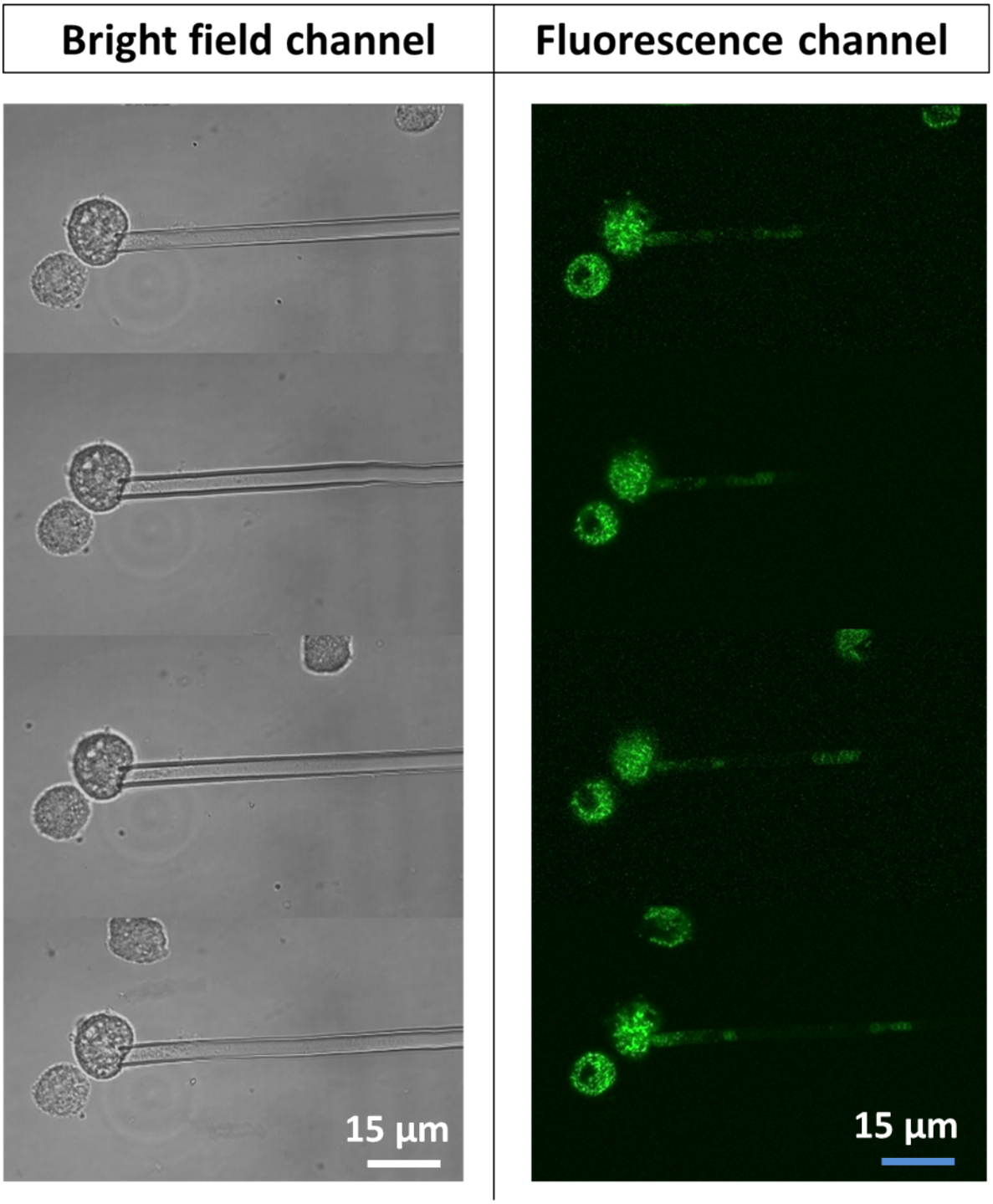

Figure 6.11: Montage of a micropipette aspiration experiment performed on an actin-tagged fibroblast cell and imaged with the confocal microscope. The channel in bright field (left) shows little about the fibroblast structure and deformation whereas the fluorescent channel (right) highlights the cytoskeleton. As the pressure is qualitatively increased, little cytoskeleton structures (like vesicles) detache from the main cell (cytoskeleton) body and are aspired in the micropipette.

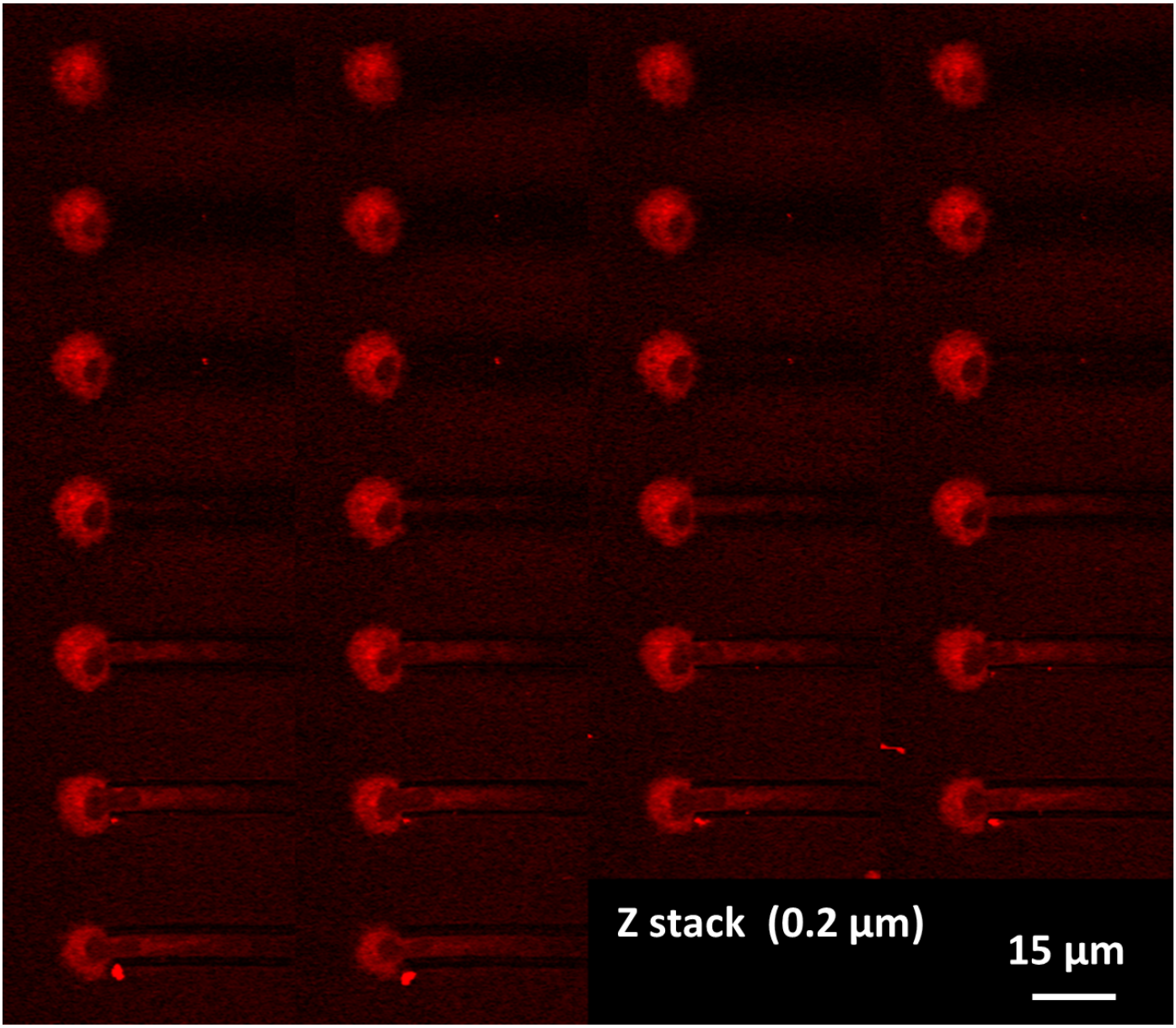

Figure 6.12: Montage of a Z stack acquired with SRS (at $2845\,\mathrm{cm}^{-1}$) of a fibroblast cell aspired in a micropipette. The montage shows the cell structure: as the pressure is applied to the cell, the nucleus (in black) surrounded with cytoskeleton (in brighter red) deforms and gets inside the pipette (bottom part of the montage image). Height between two consecutive slices was $0.2\,\mu$m.

Performing micropipette aspiration on untagged cells (SRS)

The same experiment was performed on untagged fibroblat using SRS microscopy. Once again, micropipette aspiration were performed on around 10 cells. Figure 6.12 provides a montage of an accurate Z-stack. High is provided at the bottom corner of each picture. Cell features are distinguisable: as one can see, when the pipette is out of focus, the cell is mostly uniformly bright, whereas when the pipette is in focus, the nucleus can be easily identified (black body). In the two last raws, the membrane edge is just about visible, long inside the pipette, while the nucleus deforms at te beginning of the pipette. Some part of the membrane within the pipette also appeared brighter.

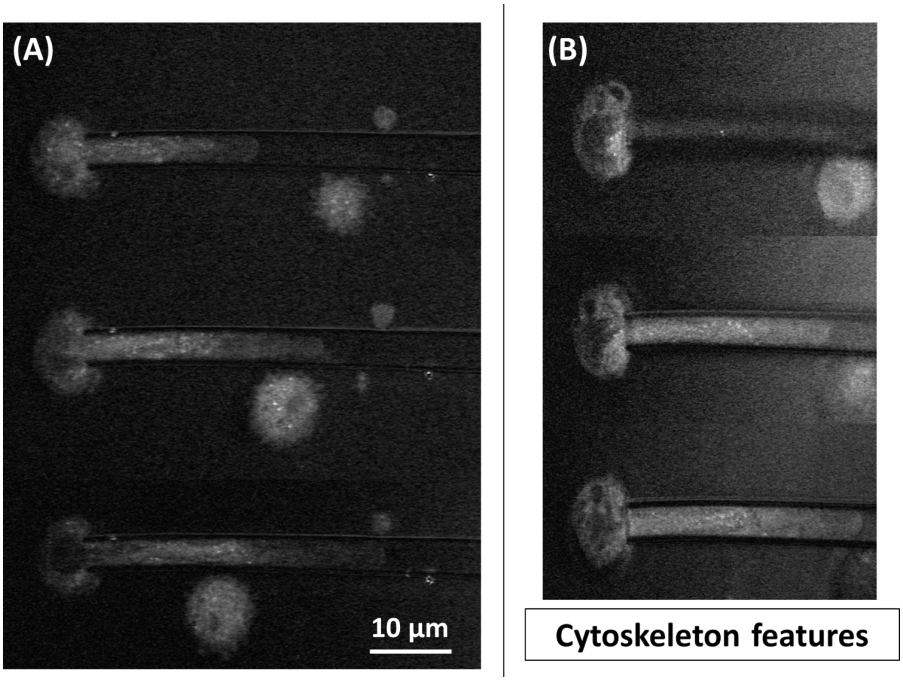

Figure 6.13: Micropipette aspiration measurement performed on fibroblast cell and imaged with SRS (at $2845\,\mathrm{cm}^{-1}$). (A) Montage demonstrating that as the pressure is increased the cytoskeleton (in bright) separates from the cell membrane (in grey) ; (B) Qualitative Z stack of the same fibroblast cell, showing the structure of the cell (see the main body outside the pipette).

The montage in figure 6.13 provides pretty clear evidence that SRS is a suitable technique to study the effect of stress on fibroblast cells. On the montage on the left, one can distinctly see the membrane edge greatly elongating inside the micropipette while some brigher tissue, believed to be the cytoskeleton, answered more slowly to the stress applied. This gives a clear visual proof that the cell membrane separates from the cytoskeleton. Moreover the structure of the cytoskeleton can be identified, the brighter structure in SRS pictures looking similar to the distribution of GFP in

actin-tagged cells (confocal experiment). One can also notice the presence of aligned small bright dots around the cell membrane within the pipette.

Discussion

Results from both experiments, GFP-tagged cells (confocal microscope) and untagged cells (SRS), have been compared, to try and identify similarities. These are summarized in figure 6.14 and as one can see all the features mentioned above were highlighted with both imaging methods. Both SRS and confocal allowed to see the membrane thinning within the pipette (yellow circles) with a very narrow middle (blue arrows). The nucleus surrounded by actin got inside the pipette and deformed (orange arrow) while the membranes devoid of cytoskeleton goes a long way inside the pipette (red arrows). The cytoskeleton usually uniformly present in the cell cytoplasm (light green arrows), answers slowly to the applied stress and separates from the membrane into cytoskeleton vesicles (light blue and light pink)

More accurate similarities between untagged fibroblast and GFP-actin tagged cells were also noticed (see fig-6.15): in both cases empty vesicles of around 2 μm in diameter could be be identified (red circles). Smaller lipid droplet-like (bright dots) distribution looked similar in both GFP-tagged and untagged cells (blue circles). From this, it can thus be asserted that the cytoskeleton provides higher SRS signal than the rest of the cell.

6.4 Discussion, Conclusions and future work

Hyperspectral imaging is a powerful technique in the field of Coherent Raman-based imaging. As it has been seen, GUVs are difficult systems to image in such a way due to their movements. The use of a micropipette holding it in place allows to record good hyperspectral images in which lipid components could theoretically be label-free distinguished. In the measurements performed, distinction between SOPC and SOPC+elastin could be made while distinction between lipid components could not; which was mainly due to the signal coming from the bulk solution.

This method has therefore a lot of potential at it will allow to distinguish any protein- not only the autofluorescent ones- using only SRS (no need for SHG or TPF). The distribution of the protein could be label-free highlighted, the way it reogarnises when under pressure could be studied. Domain segregation and reorganisation could also be

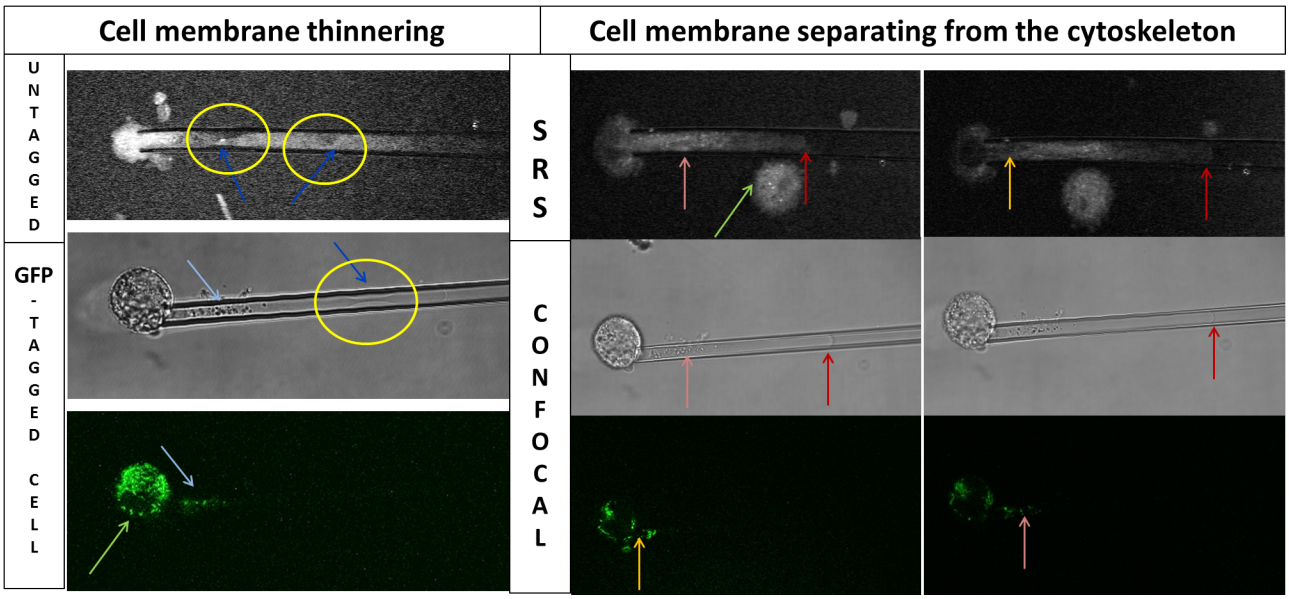

Figure 6.14: Montage table comparing one-photon fluorescence (green fluorescence), bright field (grey images) and SRS (black and white) images of fibroblast cells during MPA experiments. General features of the cell behavior could be identified between the different imaging techniques and related to one another: When pressure is applied the membrane within the pipette thinners (left column) and its separates from the cytoskeleton while the nucleus deforms at the entrance of the pipette (right column). See text for further explanations.

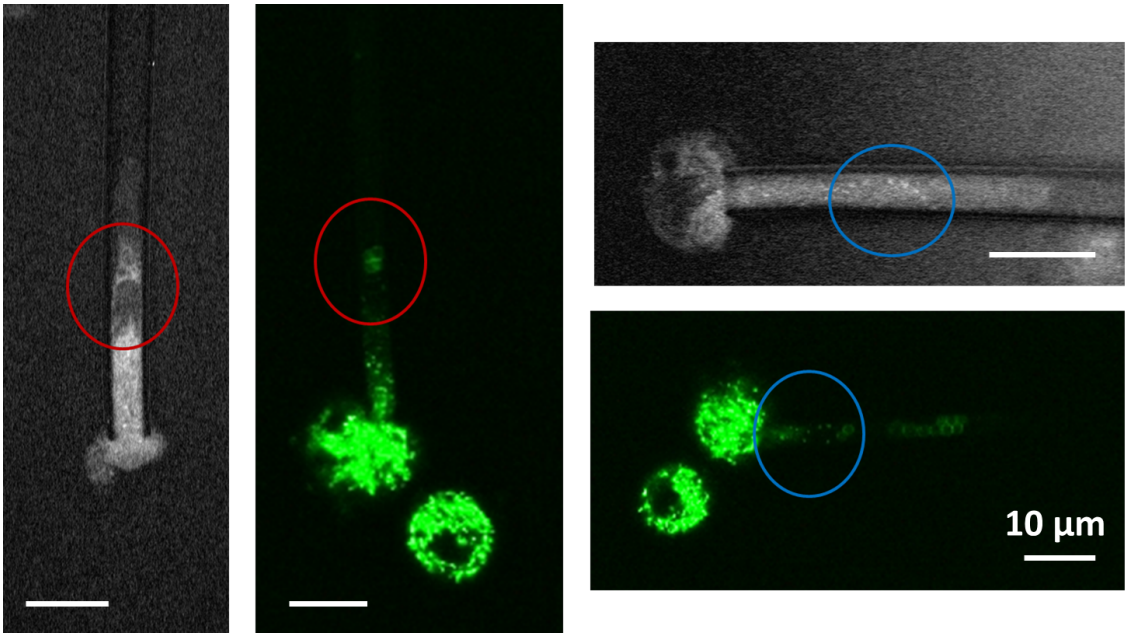

Figure 6.15: Montage of images comparing fluorescence and SRS images of tagged and untagged fibroblast cells respectively. Specific features of the cytoskeleton could be distinguished. When the cell is under stress small cytoplasm vesicles surrounded with cytoskeleton (around 1 μm in diameter) detach from the cell main body and gets inside the pipette (red circles) followed by smaller cytoskeleton (solid) vesicles (blue circles). Scale bar = 10 μm.

investigated while applying pressure to the membrane system. This is of interest since, as seen in Chapter 3, labels can interfere in the protein-lipid interaction.

Interest for domain studies in GUVs can be discussed: the lipid would nonetheless have to be in the gel state, since in the liquid state, lipid motions are likely to be quicker than the scanning rate. The acquisition time is in SRS the limiting factor to study biological processes. With our set-up the quicker time to get data that can be processed requires a few seconds per image. This means a few minutes for a single spectrum: motions or interactions could therefore not be time-lapsed studied by this technique if they happen quicker than this time: *i.e.* this methods require equilibrium (or quasi-equilibrium) of a system. Nevertheless, in other groups (Netherlands, Japan), the set-up have been optimized and allow to record spectra within one or two seconds.

This chapter presented the first application of micropipette aspiration combined with SRS. The technique was tested both qualitatively and quantitatively. Measurement on SOPC GUVs showed that the results are in agreement with other imaging techniques whereas the measurements on fibroblast cells demonstrated its capability on cells. It was handy to combine micropipette aspiration to label-free imaging technique for studying the effect of stress on the mechanical properties of the cell membrane while visualizing the deformations of its different components (nucleus, cell membrane, cytoskeleton)[1].

This method has indeed a lot of potential on fibroblast cells, since these cells require a few minutes to stabilize within the pipette. z stack could also be performed in parallel in view of making 3D reconstruction of the deformations.

This work paves the way to a large number of possible experiments since fibroblast can differentiate into a wild range of cells -and thus allows the study of a wide range of processes: effect of mutations, protein-lipid, interactions, toxins, on the cell mechanical properties. Moreover, their is hope to be able to distinguish between cytoskeleton and microtubule using SHG signal.

In the next Chapter, attention is given to the thermodynamics of the spectrin-lipid interaction.

[1] Nucleus, membrane and cytoskeleton demonstrating different signal intensities.

Chapter 7

Isothermal Titration Calorimetry to study spectrin-lipid interactions: a thermodynamics study

In this chapter we are interested in the thermodynamic aspects of spectrin-lipid interactions. To do so, a calorimetry method is used. In a first part, isothermal titration calorimetry principle will be explained along with its potential for studying protein/lipid/ligand interactions. Results of experiments performed on different LUV systems will be presented for both pure spectrin preparation and crude extract. Conformational changes due to spectrin-lipid interactions and secondary structure of the protein will then be discussed thanks to circular dichroïsm measurements. Finally, preliminary results of α-elastin mixed with various LUV systems will be presented.

7.1 Isothermal Titration Calorimetry

7.1.1 Isothermal Titration Calorimetry principle

Isothermal titration calorimetry (ITC) is a powerful method used in biology for studying biochemical processes by measuring the release or absorption of heat in a reaction/ interaction with high precision. During a single experiment, this method gives access to a wealth of information about the studied process and one is able to determine the dissociation constant, K_D, the stoichiometric number, N, and both the changes in enthalpy and entropy, ΔH and ΔS, respectively. If one performs ITC experiments at

different temperatures, this technique also gives access to the heat capacity, ΔC_p [1].

This ensues from the equations for the change in Gibbs free energy, ΔG, linking, the changes in enthalpy and entropy to the equilibrium constant K.

$$\Delta G = \Delta H - T\Delta S \tag{7.1}$$

$$\Delta G = -RT\ln(K) \tag{7.2}$$

From equation 7.1 it follows that two opposite phenomena usually compete in a reaction: On the one hand ΔH usually tries to minimize the energy of the system (by making bonds) whereas the entropy ΔS usually tries to increase (by breaking bonds) making the system more chaotic [166].

In an ITC experiment, a microcalorimeter is used to detect the variations of heat produced by a specific reaction. Figure 7.1 gives a schematic of a typical calorimeter chamber.

As one can see there are two identical cells: a reference cell and a sample cell, encapsulated within an adiabatic jacket. Water or PBS buffer is used to fill the reference cell whereas the protein of interest is placed in solution in the sample cell. Sensors[2] placed between the two cells detect temperature differences between the cells - and with the jacket - and give feedbacks to heaters placed on the side of each cell. These heaters deliver heat accordingly so that perfectly equal temperatures are maintained between the 2 cells. A syringe linked to a bladed-stirrer is used to ensure homogenization of the reaction during and after aliquot injections (injections are made from the top as shown in fig 7.1).

During an ITC experiment, aliquots of the titrant are added to the sample cell. If the ligand - in our case it will be LUVs - interacts with the protein, some heat is either absorbed or released making the sample cell warmer or cooler than the reference cell (fig. 7.2-a): **the parameter measured in an ITC experiment is the quantity of power required to maintain identical temperatures between the sample cell and the reference cell over time**, the quantity of heat measured being in direct proportion of the amount of binding [167].

[1] Since $\Delta H = \int_0^T \Delta C_p dT + \Delta H(0)$ and $\Delta S = \int_0^T (\Delta C_p/T).dT$ [166].
[2] They are sensitive thermopile/thermocouple circuits.

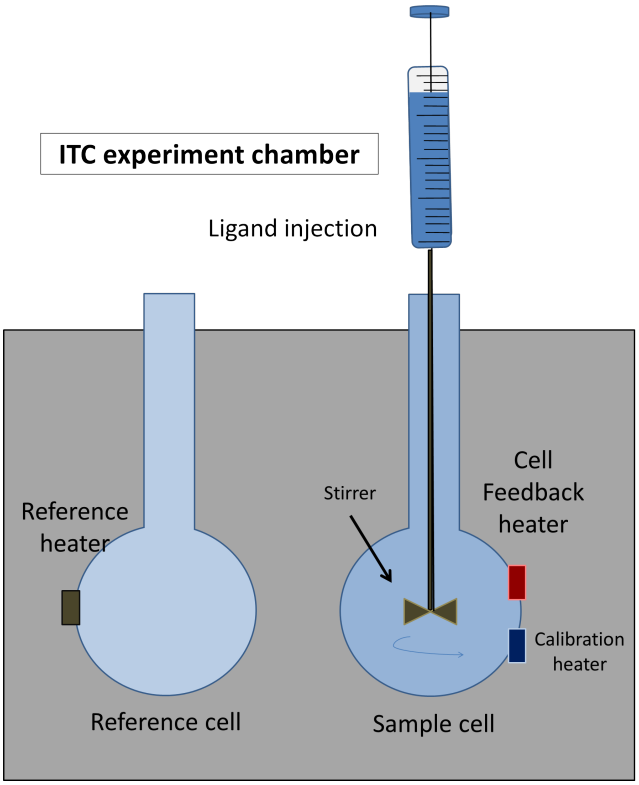

Figure 7.1: Schematic diagram of a typical ITC chamber.

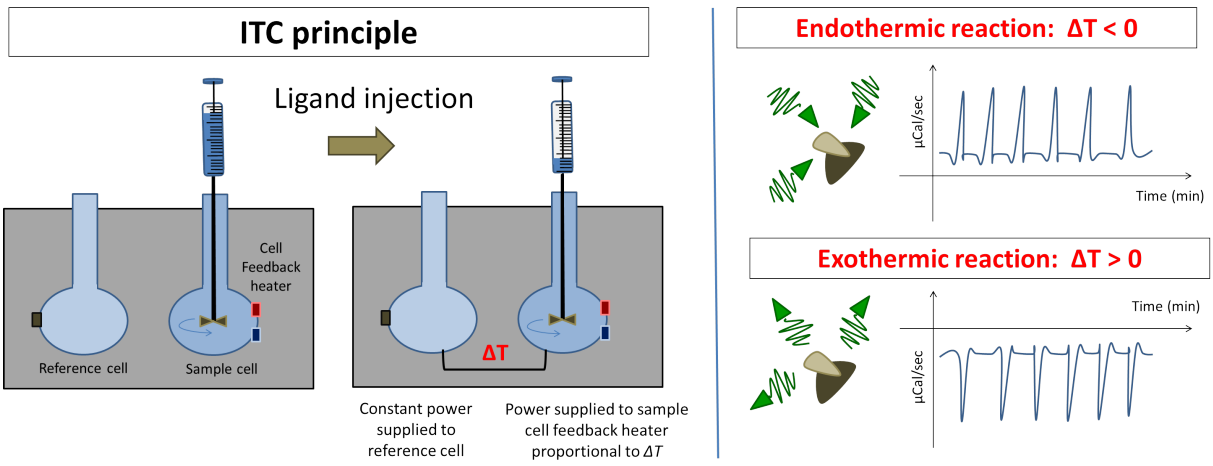

Figure 7.2: Schematic diagram showing the principle of the ITC experiment: When the ligand aliquot is injected within the sample cell, some heat is either absorbed or released inducing a difference in temperature between the cells. The difference of temperature ΔT is proportional to the amount of binding. When the reaction is endothermic, ΔT is negative. In an exothermic reaction, on the other hand, ΔT is positive.

Before the first injection, a constant power is applied to the reference cell which activates the heater from the sample cell and constitute the baseline signal. As shown in figure 7.2-b, in an **exothermic reaction**, some heat is produced and the sample cell will become warmer than the reference cell. The heater of the sample cell will hence deliver less heat until the reaction between the ligand and the protein has reached equilibrium. When stable, the heater will increase back the heating of the sample cell until it reaches its original position (*i.e.* the baseline) before the next injection. In an **endothermic reaction** the opposite occurs and more heat is given to the sample to compensate the absorbed heat due to the ligand-protein interaction. **As the aliquots are injected, 'spikes' are recorded**.

7.1.2 ITC use for studying protein/lipid/ligand interactions

ITC, is usually an efficient method to study protein-protein, protein-ligand and ligand-lipid reactions [167], [168] 2000, [169]. Figure 7.3 illustrates an ITC experiment. In our case, the sample cell is filled with spectrin and the syringe is loaded with a LUVs suspension. It is usual to place the biggest molecule within the cell and the smallest one into the loading device. At first, all the vesicles injected will interact with the protein, (first injections in fig 7.3). As the molar ratio of ligand versus protein increases, the protein becomes more and more saturated and less binding sites will be available, hence the heat produced by the binding decreases (middle injections in fig. 7.3) until the ligand becomes in large excess compared to the protein. When no other heat than the ligand diluting within the cell solution is recorded, the reaction has reached full saturation (last injections in fig. 7.3).

The methodology for processing data is widely automated in ITC experiments using routines and software sold with the microcalorimeter [170]. The way data is processed is as follows: The plot measuring the power (in μCal/sec) with respect to the time is converted into an isotherm, the area of each peak being integrated as shown in figure 7.3-b. The new plot giving the enthalpy (in kCal/mole of injectant) with respect to the ligand/protein molar ratio can be fitted to a binding model. The overall curve is usually a **sigmoïd** from which the dissociation constant, K_D, is directly deduced plotting the first derivative at the inflexion point (see fig. 7.4). The stoïchiometric parameter, N, is given by the molar ratio at the center of the isotherm (in the schematic in figure 7.4, a 1 to 1 binding model has been used). The enthalpy difference, ΔH, is also directly derived plotting the difference of the two asymptotes and constitutes the amount of heat released per mole of ligand bound.

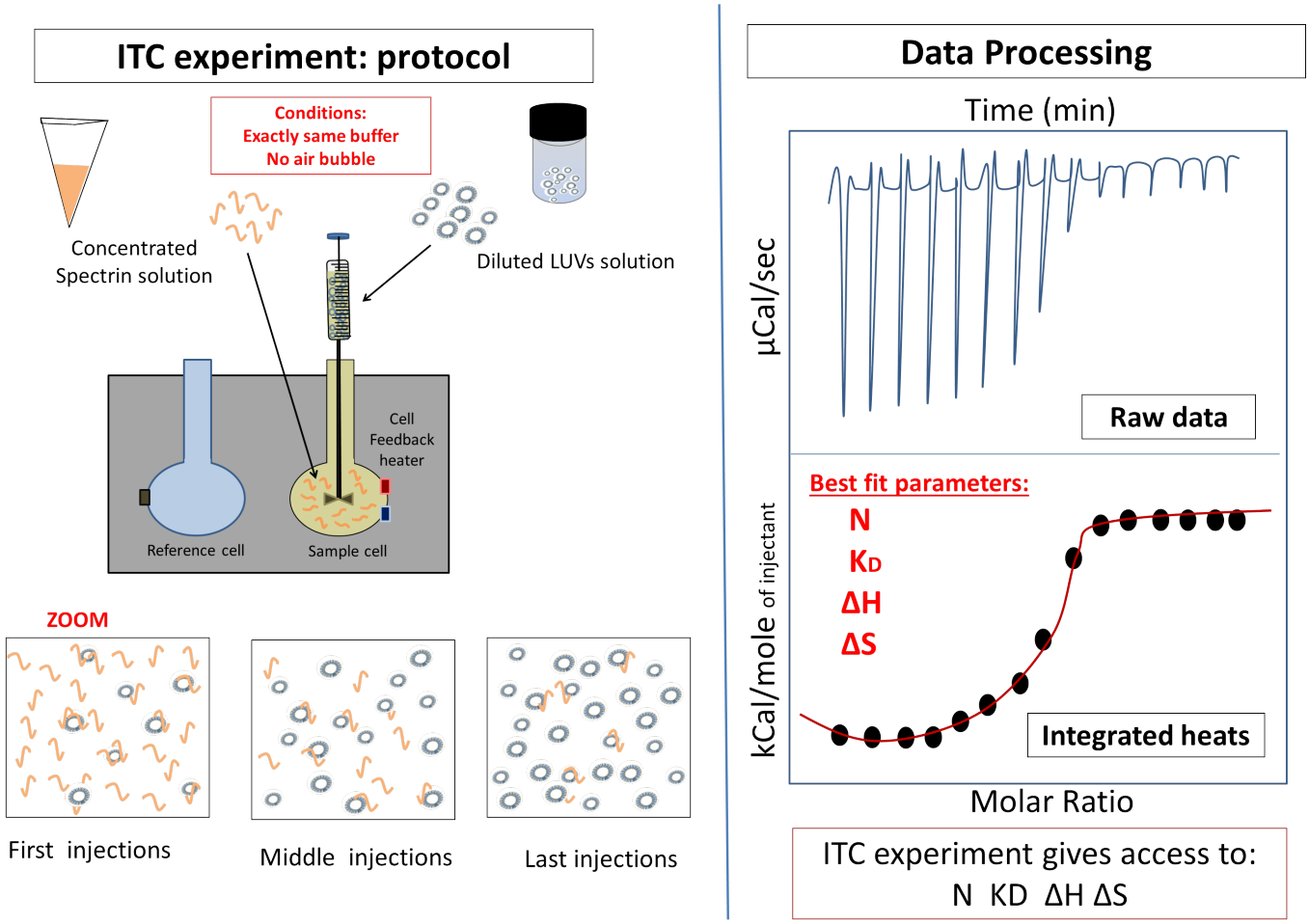

Figure 7.3: Schematic diagram illustrating a typical ITC experiment : In our experiments, the spectrin solution was placed within the sample cell while the LUVs solution was loaded into the syringe. At the beginning of the experiment (*i.e.* during the first injections) the protein is in large excess compared to the ligand. In the middle of the experiment, both ligand and protein are in similar proportions and less binding occurs (middle injections). At the end of the experiment the LUVs are in large excess compared to the protein. The system has reached saturation (last injections). As the ligand binds to the protein heat is produced, and 'spikes' are recorded. Raw titration peaks are then converted into an isotherm by integrating the heat which gives access to the thermodynamics parameter of the reaction.

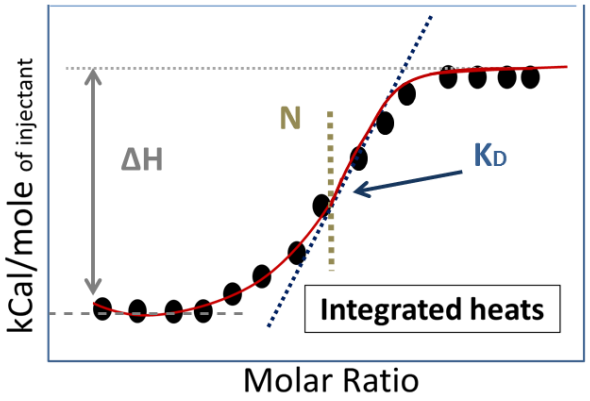

Figure 7.4: The isotherm can be fitted to a binding model from which the dissociation constant, K_D, the stochoimetric number, N and the change in enthalpy, ΔH can be extracted. K_D is given by the derivative at the inflexion. N is given by the molar ratio at the same point and ΔH is the maximum difference of heat produced. Adapted from https://www.youtube.com/watch?v=uLxvSFnuGd0 website.

Finally, knowing the temperature at which the experiment is performed, the difference of entropy, ΔS, can then be deduced from equations 7.1 and 7.2.

7.2 Material and methods

To study spectrin-lipid interactions LUVs have been used instead as GUVs which was a requirement of the ITC device.

7.2.1 LUVs preparation

LUVs were prepared using the sonication method. The protocol to prepare large unilamellar vesicles, starts similarly to the swelling method. First, glass vial bottles (8 ml from Avanti) were carefully washed 5 times first in methanol then in chloroform. A 1 ml Hamilton syringe was then washed both with methanol and ethanol. 1 ml of 10 mg/ml of stock lipid solution (Avanti, UK) was then divided into 2 glass vial bottles and the choroform was evaporated under a nitrogen flux in the same manner as in the swelling method. Bottles were then placed in the vacuum chamber for 2 hours for futher evaporation of the solvent. 5 ml of PBS (0.15 M NaCl, 20 mM sodium phosphate, pH 7.6) was then added to each vial bottle to make up a 1 mg/ml solution of lipids. Bottles were sealed using parafilm and the lipid film was rehydrated for 10 minutes at room temperature. The bottles were then placed into an **ultrasonic bath** for 20 minutes[1] before agitation. 20 minutes sonification plus shaking were repeated until the lipid was sonificated for a total of 60 minutes. At this stage the lipid suspension

[1]This step allows to accelerate multilamellar vesicles formation.

consisted of a mixture of multi-lamellar/ unilamellar vesicles of various sizes and the solution appeared milky.

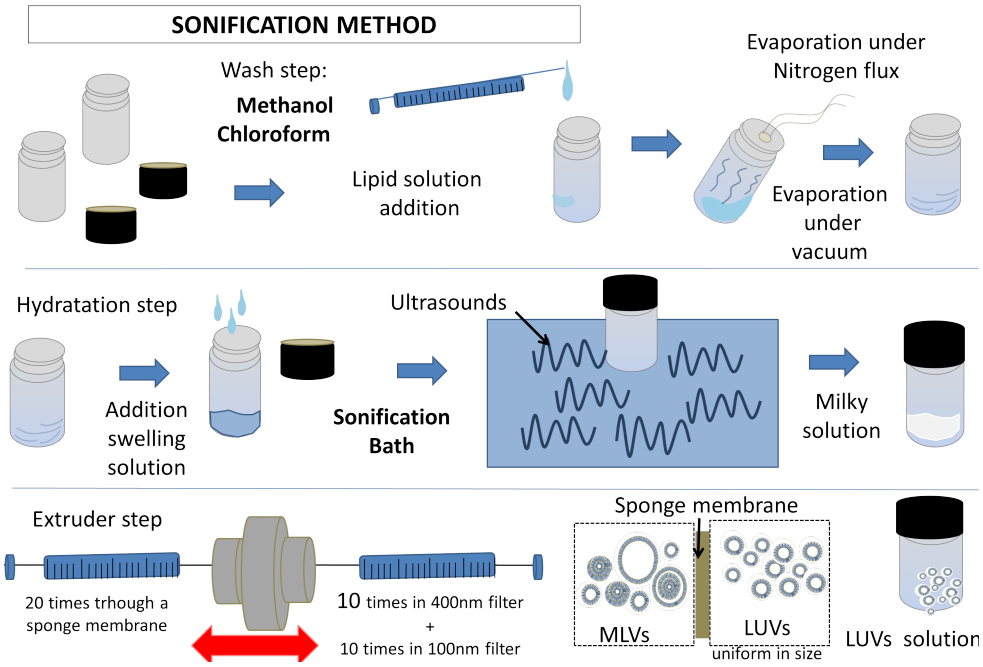

Figure 7.5: Schematic diagram illustrating the experimental protocol to make LUVs using the sonification method.

To produce LUVs from the MLVs milky solution, an **extruder** was used (see fig. 7.5). The preparation was extruded[1] through pore filters of 400 and then 100 nm. Passing 20 times through the extruder for each filter was necessary to clear the solution and obtain LUVs uniform in size as shown in figure 7.5.

7.2.2 ITC set-up at Glasgow University

All the ITC experiments were performed at the university of Glasgow together with postdoctoral researchers (Debra Shaw and David Woods) and under the supervision of Professor Alan Cooper and Dr. Sharon Kelly (University of Glasgow, Scotland). The work undertaken derives from previous work from PhD student [62].

The microcalorimeter at Glasgow University was a MicroCal VP-ITC (Microcal, MA, USA) whose cells could contain 2 ml of liquid. The VP-ITC MicroCal is one of the latest class, hence very sensitive. The loading syringe contained 400 μl of the ligand solution.

[1] To extrude is a process consisting in pushing a material through a membrane.

7.2.3 Experimental protocol and data processing

To perform ITC, it is of crucial importance that the buffers for the protein and ligand - LUVs in our case - perfectly match, otherwise heat from mixing buffers will be produced and bias the results. A large quantity of PBS buffer was made to ensure that the buffers used in all the experiments would come from the same PBS stock solution avoiding potential artefacts due to slight buffer mismatch. Spectrin was transferred from the glycerol media it was kept in, into the PBS using concentrators (100K, Millipore, Sweden). Once again compromises needed to be found for the number of washes performed as protein was lost at every wash. The protein was concentrated to $\sim 2\,\mathrm{mg/ml}$. The exact concentration of the protein was determined by absorbance at 280 nm on a spectrometer.

Since it was decided to place the protein into the 2 ml cell (as suggested in (Thompson, 2007), a large quantity of the protein was required for each experiment which could not be re-used. This way round might be counter-intuitive but is safer to record weak signals. Ideally both way round - lipid into protein and protein into lipids - should be recorded and compared to one another for agreement. Spectrin was concentrated to up to 1.5 mg/ml (0.0042 mM). Since the binding was expected to be quite weak, the lipid molar ratio had to be 20 times or higher that of the protein (Cooper) and LUVs solutions were diluted 10 times before being loaded into the syringe to obtain a molar concentration of 0.125 mM (*i.e.* to get a 30 time molar ratio)[1].

As in micropipette aspiration, in ITC experiments it is of crucial importance to avoid air bubbles since they distort the results: if some air bubble is attached to the cell wall, this can cause noise in the measurements when it detaches[2]. To prevent disturbances due to air bubbles, both protein and LUVs solutions were degassed for at least 10-15 min before being loaded into the ITC calorimeter. For further precautions, once filled, the loading syringe was purged 3 times.

The first injection consisted of 1 μl of titrant, and was performed to check both that no air bubble had been trapped into the syringe and that the injection system was properly working. The second injection occured 1 minute later and consisted of 10 μl of titrant. Aliquots of 10 μl were then injected every 3 minutes while the software recorded the evolution of heat every other second. 25 to 30 injections of titrant were performed throughout an experiment which is a usual number of injections for most reactions to

[1] Knowing the exact molar concentrations of both protein and ligand (LUVs) is of great importance if one wants to get an accurate value of the association constant K_A (where $K_A = 1/K_D$).

[2] Air bubbles are usually a reason for getting a poor baseline.

reach saturation (Cooper). Data processing was automatized and performed using a software based on Origin.

7.3 ITC on spectrin

7.3.1 Improving the experimental protocol

The first step was to try and improve the experimental protocol *i.e.* to adjust the spectrin/vesicles ratio to get the highest binding as possible. To do so, a wide range of tests/combinations have been tried (see table 7.6) in a first set of experiments in view of recording ITC data (changing the PS molar ratio in LUVs to study the thermodynamics dependence of PS in spectrin-lipid interactions). LUVs of various PC:PS molar ratio (100:0, 90:10, 80:20, 70:30, 60:40 and 50:50) of both DOPC:DOPS and SOPC:SOPS were prepared for this purpose to try to reproduce and verify the preliminary results obtained by a previous PhD students [62].

Cell	Syringe
PBS	PBS
PBS	DOPC:DOPS 70:30 1in10
Spectrin	DOPC:DOPS 70:30 1in10
Spectrin + Lipid	PBS
Spectrin + Lipid	DOPC:DOPS 70:30 conc
Spectrin	DOPC:DOPS 70:30 conc
PBS	DOPC:DOPS 70:30 conc
Diluted DOPC:DOPS 70:30 conc from above	Spectrin
PBS	SOPC:SOPS 70:30 1in10
PBS	Spectrin
DOPC:DOPS 70:30 1in10	Spectrin
Spectrin	SOPC:SOPS 70:30 1in10
Spectrin	DOPC:SOPS 50:50 1in10
PBS	DOPC:SOPS 50:50 1in10

Figure 7.6: Summary table of the ITC experiments performed to try and optimize the elastin-lipid binding. 1in10= diluted ten times, conc=concentrated, PC:PS ratios are given in mol (molar ratios).

To be cautious, ITC experiments consisting of injecting buffer into the spectrin solution and injecting LUVs into a buffer solution were performed. This was done to ensure that any of the compounds were interacting with the buffer and to take into account the heat produced by the dilution of the aliquots within the chamber, for data

processing. Spectrin in syringe, less protein-consuming, was also tried to try and reproduce previous results, but this proved unsucessful. In the first set of experiments (November 2012), pure spectrin appeared to bind weakly to DOPC: DOPS LUVs as shown in figure 7.8. This was the only experiment in the table that showed detectable interaction.

In a second set of experiments the following year (May 2013), attention was therefore given to the DOPC: DOPS LUVs sytems due to the limited amount of spectrin available (as mentioned before, each experiment required 2 ml of ~ 2 mg/ml of protein[1]). Figure 7.7 summarizes the main results of the second set of experiments which is discussed in the following section.

7.3.2 Pure versus crude spectrin preparations

As one can see in figure 7.7, when pure spectrin was tested at a concentration of 1 mg/ml no binding was recorded (the height of the peak in (a) was 0.1 μCal/sec which corresponds to the dilution of LUVs into buffer and buffer into spectrin) whereas when the protein was concentrated up to 2.5 mg/ml some heat was produced (peak down to 0.5 μCal/sec in (b)). In the case of DOPC LUVs, at the same protein concentrations no binding - other than the aliquot diluting in the chamber - could be recorded (data not shown). There is thus a critical spectrin concentration below which no interaction can be detected. These results are in agreement with the first set of experiments [2]. A gel on the side (c) attests of the purity of the protein in these experiments.

Even though no meaningful fitting could be plotted with the second set of experiments the similarities in the 'profiles of raw titration peaks' between (b) and figure 7.8 gives evidence for reproducibility. An interesting point in this set of experiments, arose from the difference of behaviour between pure spectrin protein and crude spectrin preparation (first peak of the CL-4B column) with the LUVs (see fig. 7.7).

ITC was also performed on crude spectrin preparation for both DOPC and DOPC:DOPS (molar ratio 70:30) LUVs. Figure 7.7-f provides a SDS-page gel performed on the crude spectrin preparation (*i.e.* impure spectrin) used in the experiments. As one can see comparing (d) to (e) for the same ligand and protein preparation concentrations used (0.125 mM and $\sim$ 0.0018 mM [3] respectively), DOPC:DOPS LUVs appeared to bind to

[1] Preparation of spectrin for this second set of experiments, required 2 months of full time day work of the three of us.

[2] For a concentration of 1.5 mg/ml of pure spectrin, peak down to 0.4 μCal/sec were recorded.

[3] protein preparation concentration was actually slightly higher for the experiment with DOPC LUVs compared to the experiment with DOPC:DOPS LUVs (0.0022 mM against 0.0017 mM).

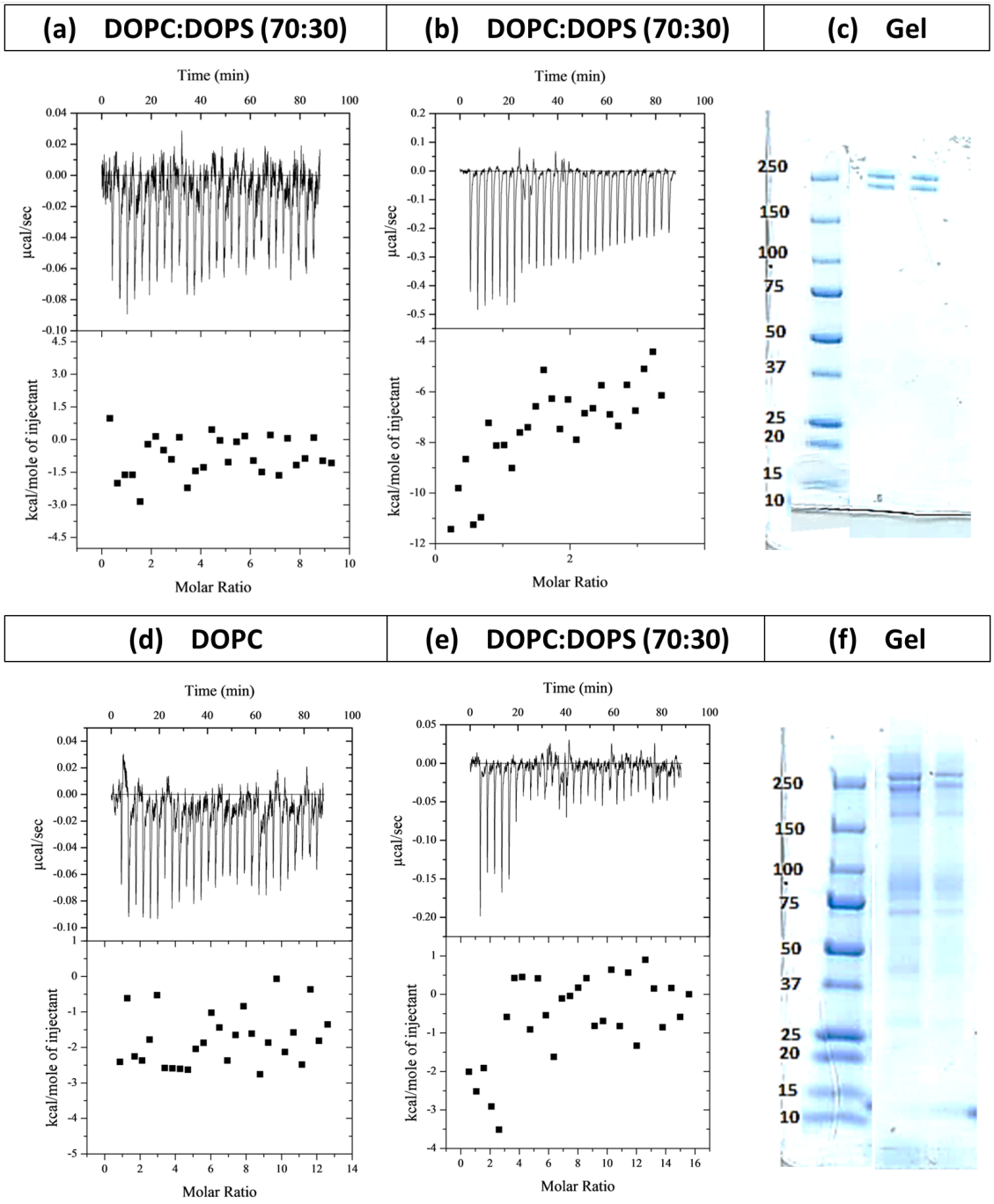

Figure 7.7: Summary of the ITC measurements on spectrin: **pure spectrin preparation (a-c)** versus **crude spectrin extract (d-f)**. ITC on DOPC:DOPS (molar ratio 70:30) LUVs into (a) diluted **pure spectrin** (1 mg/ml) and (b) concentrated **pure spectrin** (2,5 mg/ml); (c) SDS-page of the spectrin preparation. ITC on DOPC (d) and DOPC:DOPS (molar ratio 70:30) (e) LUVs into **crude spectrin extract (First Peak from CL-4B column)**(1,5 mg/ml); (f) SDS-page of the spectrin extract preparation.

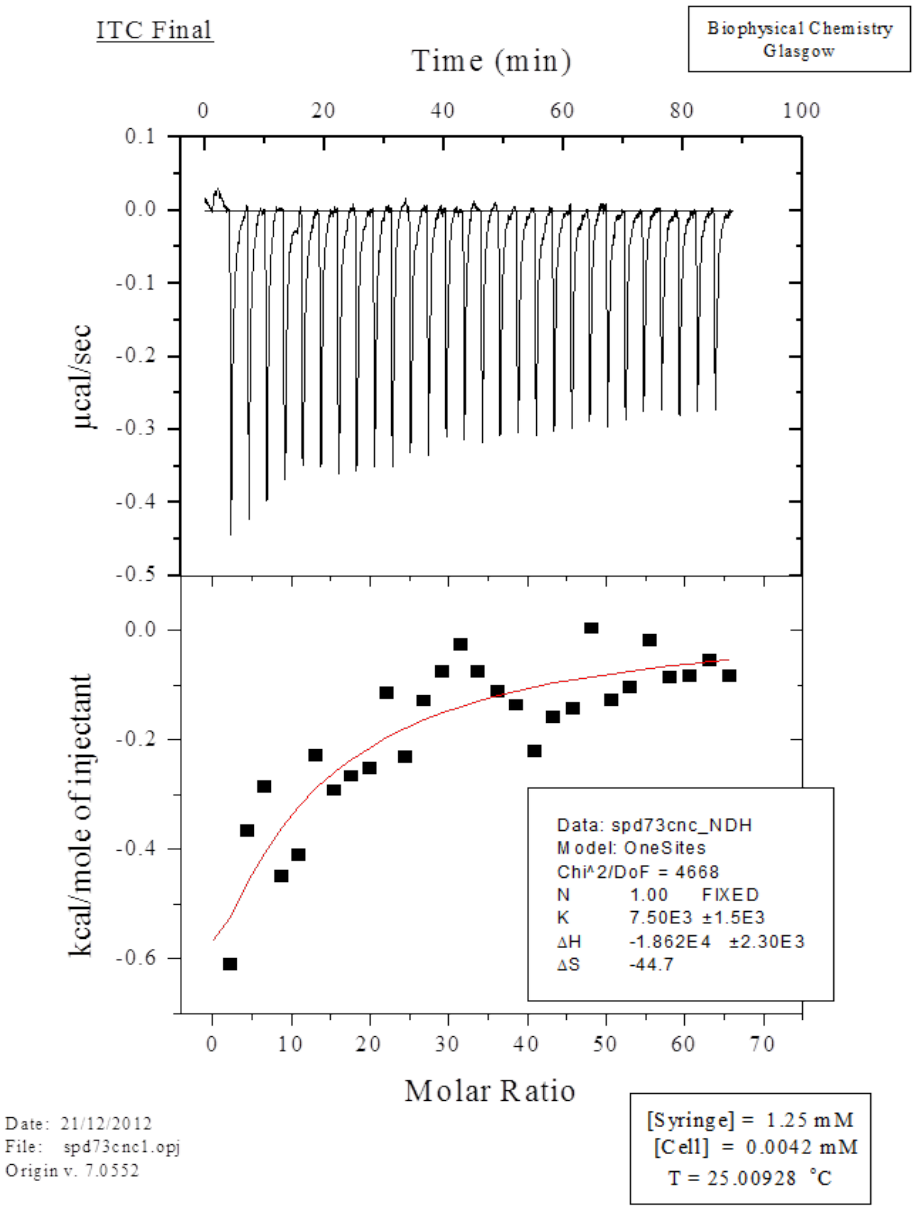

Figure 7.8: Data processing: Studying the effect of spectrin on DOPC:DOPS LUVs. Using a 1:1 binding model, the most successful experiment (*i.e.* DOPC:DOPS (70:30 molar ratio) LUVs injected into concentrated spectrin (1.5 mg/ml) (November 2012)) gave a dissociation constant, K_D, of $\sim 130\mu$M.

the impure protein giving the characteristic sigmoïd-like shape for the raw titration peaks (see (e)) whereas no binding happened in the case of DOPC LUVs (see (d)). If concentrated to the same value as the pure protein (2.5 mg/ml compared to the current 0.8 mg/ml), one could expect much higher binding to occur. Such measurements were not performed since meaningful quantitative value cannot be extracted from these kind of measurements because of the uncertainty of the proteins involved in the crude spectrin preparation (*i.e.* which protein in which proportions[1]). It is nonetheless an important qualitative result as it demonstrates the ***importance of the purity of the spectrin sample***.

Data Analysis

Figure 7.8 provides to the reader, an attempt of data analysis performed on the experiment that showed the highest binding (November 2012). This was fitted using a simple 1:1 binding model. Correction for heats of mixing was performed using the final injections (*i.e.* assuming that the binding saturates at the end of the titration). As one can see, it lacks the presence of an inflexion point which is critical to get good fits. The data nonetheless suggested a weak binding with a K_D **of 130** μ**M**. It should nevertheless be noted that this results involves the most generous assumptions since the protein did not seemed to have reach full saturation. The binding is therefore likely to be actually much weaker. It is also possible, as stated in [62], that *'the absence of the inflexion point [in ITC measurements with spectrin] might reflect the presence of a secondary interaction occuring over a longer time scale that would distort the base line'*.

7.3.3 Discussion: spectrin conformation and secondary structure

To ensure that these results were due to weak binding rather than a problem/ artefact (due to the protein degradation for example) obstructing the interaction and hence compromising the experiment, circular dichroïsm measurements were performed.

Circular Dichroïsm (DC) spectroscopy is a widely used technique in biochemistry, due to the chirality of most biological molecules [171]. When performed in the ultra-violet (UV) domains, DC provides precious information about biological sample secondary structure since α**-helix,** β**-sheets** and **random coils proportions** can be identified (they each provide different DC signals). **Denaturation** and/or **folding of**

[1] For the ITC experiments concentration of protein was measured using the absorption at 280 nm of all proteins without distinction.

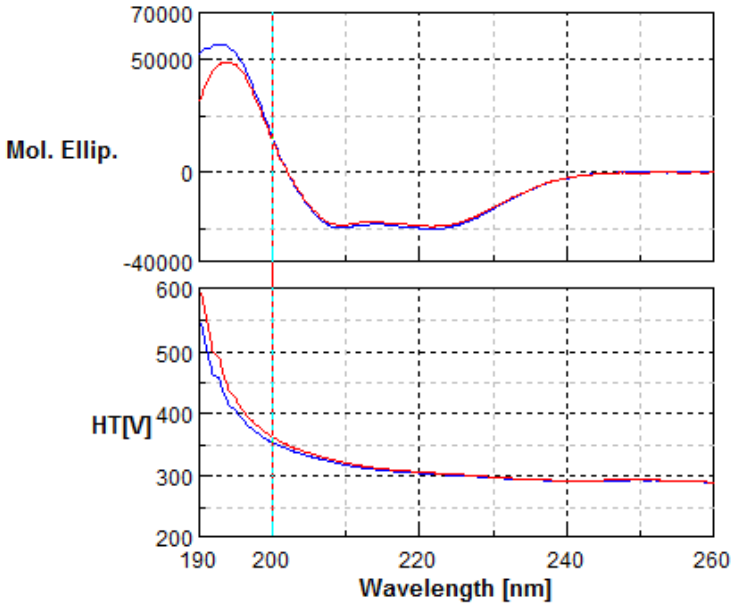

(a) Far UV CD Spectra

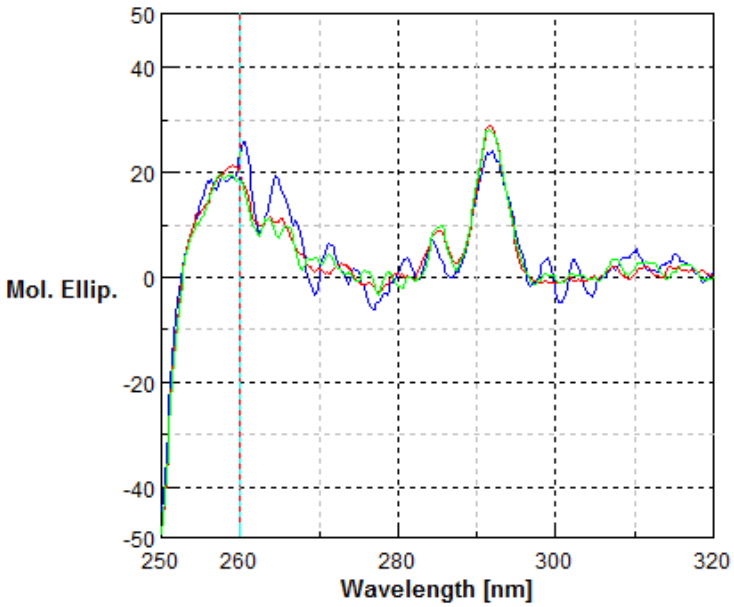

(b) Near UV CD Spectra

Figure 7.9: Studying conformational changes in the spectrin using UV Circular Dichroïsm (CD). (a) Far UV CD spectra of Spectrin in buffer (blue) and spectrin in DOPC/PS 50:50 (red). Spectra were recorded in a 0.02 cm pathlength quartz cuvette using the following parameters: bandwidth 1.0 nm; scan rate 50 nm/min; response 0.5sec; (b) Near UV CD spectra of Spectrin in buffer (blue), spectrin in DOPC/PS 50:50 (red) and Spectrin in DOPC/PS 70:30 (green). Spectra were recorded in a 0.2 or 0.5 cm pathlength quartz cuvette using the following parameters: bandwidth 1.0 nm; scan rate 10 nm/min; response 2sec.

a protein can also be studied since in the first case, the signal from α-helix and/or β-sheets decreases to the benefit of random coil signal while in the second case the α-helix ratio increases. Thermodynamics of specific biochemical interactions can therefore also be studied using the variation of these ratios. Finally, if DC measurements do not provide any insight about the location of each of the components[1]; it is a very useful tool for studying conformational changes and checking for denaturation in proteins since it is easy to implement and provides quick results.

Near versus far UV circular dichroïsm on Spectrin

As one can see in figure 7.9-a, the spectrum of spectrin in buffer in the far UV is similar to the spectrum of spectrin in DOPC/PS down to 195 nm whereas below 195 nm the intensity of the spectrum decreases in the presence of vesicles. This difference may reflect conformational changes following the association of spectrin with vesicles. It should nevertheless be noted that the vesicles themselves can cause absorption flattening due to light scattering in this region of the spectrum[2].

Small differences could also be noticed in the near UV, between spectrin in buffer (blue) and spectrin in LUVs (red and green). One should also notice that the CD spectra when there was vesicles were measured following the ITC experiment and had therefore been subject to approximately 2 hours of stirring at 25°C, which may have contributed to the small differences evidenced in figure 7.9-a and b. These experiments could be repeated by measuring CD spectra separately from the ITC experiment when the sample is not limited.

Secondary structure estimates and discussion

Following DC measurements, it is possible to evaluate the secondary structure of the protein using appropriate software. Secondary structure estimates were calculated by Sharon Kelly using the CDSSTR method on DICHROWEB website and using the fourth database reference [172], [173], [174].

One can find the measurements of the estimates in Appendix D. We found that, **the secondary structure estimates suggested that the presence of LUVs lead to small changes in the overal helical content of the protein**: helix 1 decreasing

[1] For this, one need to use more evolved techniques such as X-ray diffractometry or RMN for proteins.

[2] This can be checked by measuring vesicles alone at the same ratio as the one used in the experiments.

from 55% to 50% whereas helix 2, strands 1 and 2 remained the same (respectively 22%, and 1 or 2% twice). Both unordered and turns structures slightly increased from 6 to 8% for the first one and from 15 to 17% in the later one.

These results are also in good agreement with the literature as the spectrin is 70% composed of α-helix [175]. From these last results, denaturation of the spectrin could be discounted, and no obvious mistakes seemed to have been done. Therefore, in the conditions used for our ITC experiments spectrin-lipid interactions appeared extremely weak, or close to the sensitivity of the calorimeter.

7.4 ITC on Elastin

During the second set of experiments, preliminary ITC experiments were also performed on elastin since good results were obtained from the imaging (see section 4 of Chapter 5). Experiments were performed using both pure DOPC LUVs and ternary systems, DOPC: DPPC: Chol (1:1 DOPC/DPPC molar ratio, 30% Cholesterol) LUVs in order to be consistent with the membrane systems used in Chapter 5. The syringe was loaded with LUVs diluted 10 times (0.125 mM) in a first case then used straight at 1.25 mM whereas the cell chamber was filled with elastin solution at the same concentration (0.070 mM).

Figure 7.10 summarizes the results. As one can see mixing buffer into elastin had a small effect (in (a) the peaks go up to 0.1 μcal/sec) whereas in all other cases injecting LUVs produced peaks heat up to $\sim$0.3 μcal/sec (b-d). Contrary to spectrin, elastin-lipid interaction was endothermic. In (b) and (c) DOPC LUVs were injected into elastin whereas in (d) LUVs were DOPC:DPPC:30%Chol LUVs. Elastin seemed to interact in the same proportions with both LUVs systems indicating that the protein binds to the lipids independently of their compositions; which is in agreement with conclusions from Chapter 5.

Quantitative data could not be extracted in this case either, since the experiment did not come (even) close to saturation. The heat produced by LUVs injections remained the same independently of the concentration of LUVs in the aliquots. This suggests that either the heat produced was an artefact due to the buffer used, or the concentrations used were far away from optimum. The second possibility is more plausible since the results from micropipette aspiration and imaging experiments showed that elastin interacts with giant vesicles (see Chapters 4-6). These experiments are a good starting point. The lipid/protein ratio needs nonetheless to be optimized for obtaining

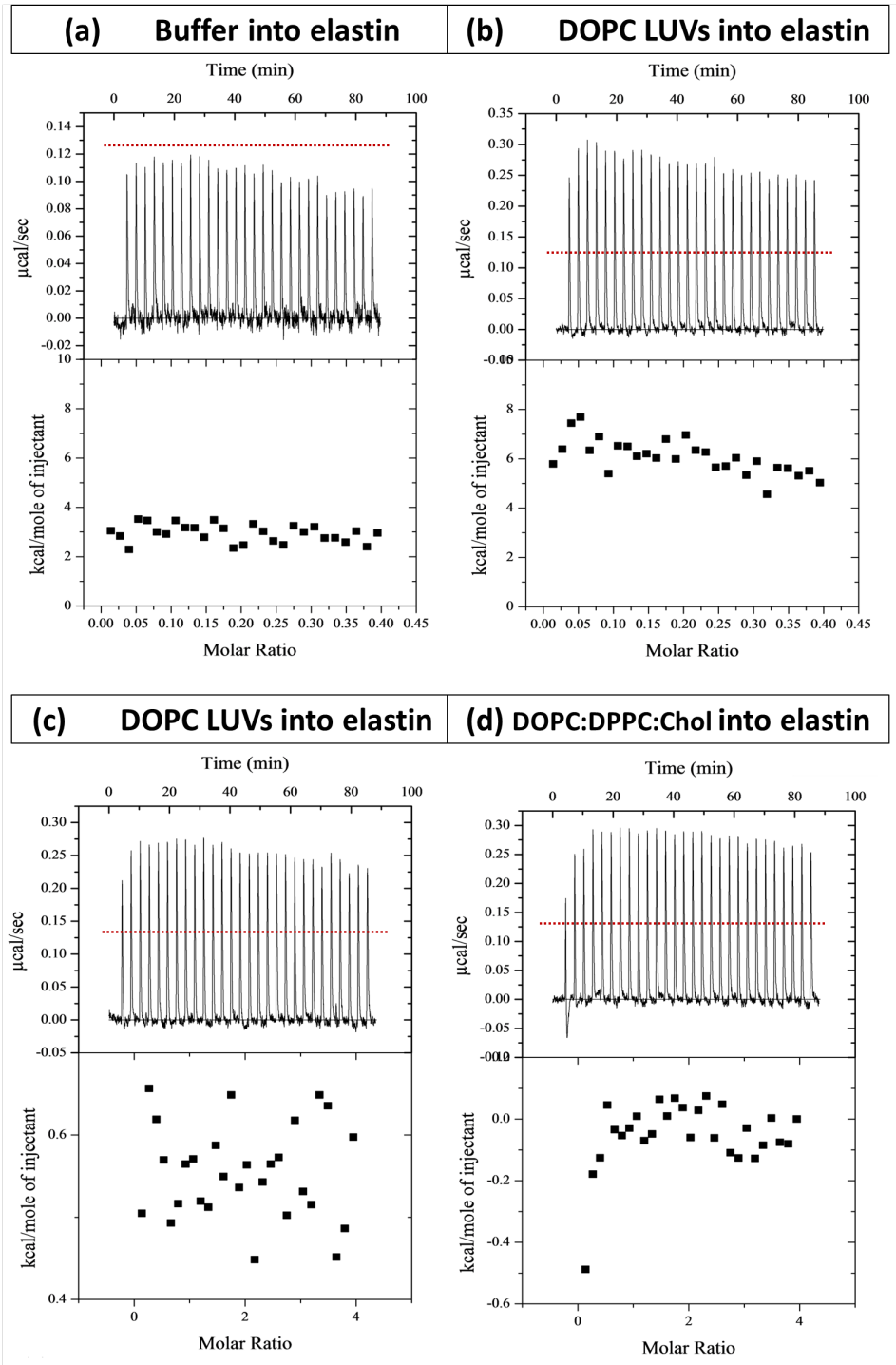

Figure 7.10: Studying the effect of Elastin on LUVs. Summary of ITC measurements with Elastin. (a) DOPC LUVs solution (0.125 mM) into buffer; (b) DOPC LUVs solution (0.125 mM) into elastin (0.070 mM); (c) Concentrated DOPC LUVs solution (1.25 mM) into elastin (0.070 mM); (d) concentrated DOPC:DOPC:Chol (1:1:30% chol) LUVs solution (1.25 mM) into elastin (0.070 mM).

quantitative values of the thermodynamics parameters of the interaction (especially K_A).

7.5 Discussion, conclusions and future work

In this chapter attention has been given to the thermodynamics aspect of the elastin and spectrin interaction with lipid systems. ITC experiments performed on spectrin demonstrated that the presence of PS was necessary for the interaction. Our estimate of K_D (130 μM) was found to be 2 to 3 orders of magnitudes higher than reported by other groups (Diakowski reported a value of 140-200 nM for PS/PC (3/2)[1] [113]; Sikorski reported a value of $\sim$50 nM for PC/PE (3/2) in its review paper [112]). This means that the interactions was in our case weaker than in the literature.

Since CD experiments demonstrated that the protein did not undergo denaturation, the differences must have come from the lipid system used (and/or the protein). In the literature most experiments were performed using lipid from either bovine tissue or eggs. Some of the experiments done by a previous student were also performed using mixed chain length lipids [62]. Its conclusions encouraged us to go in this direction and use pure lipids whose chain length were constant and well defined (DOPC and SOPC being the more sensible lipids to use). The interest was there to study the influence of head group but dependence over the PC:PS ratio could not be demonstrated due to a very weak binding. The fact that ITC did not produce measurable interaction may suggest that getting a diversity of acyl chain lengths within the lipid systems might be of greater importance than previously thought. It would thus be an idea for further measurements to revisit the egg/bovine tissues extract for PC / PS or PE lipids and mixtures.

It is also worth noticing that performing ITC on spectrin was quite challenging. One had to face several problems the biggest one being to produce a great quantity of spectrin (which was time consuming to an non-reasonable extent) without precipitation. Moreover the spectrin is a large protein which pushed the ITC machine to its limits.

The results are in good agreement with conclusions drawn in previous Chapters (see Chapter 3 (fluorescence experiments) and Chapter 4 (micropipette aspiration experiments)). All experiments together then seem to demonstrate a weak external interac-

[1] This group studied the influence of the fluidity in monolayer (*i.e.* influence of cholesterol) for spectrin-lipid interactions [112].

tion between spectrin and lipids; if the protein inserted into the the bilayer it would probably undergo noticeable conformational changes than the one detected.

ITC experiments led in parallel using α-elastin, provided interesting preliminary results. Raw titration peaks demonstrated that the spectrin-lipid interaction is exothermic whilst the α-elastin-lipid one is endothermic. Due to a lack of time (availability on the machines) the protein-lipid ratio could not be adjusted. Further measurements would therefore be necessary to obtain a value for the association constant, K_A.

Conclusions and future work

The aim of the thesis work was to study the direct interactions of spectrin (cytoskeleton of RBCs) with membrane lipid to determine its effects on the mechanical properties of the lipid bilayer. It aimed to investigate and determine how spectrin-lipid interactions influenced membrane mesoscopic morphology and biophysics in ways that could be ultimately important to cellular function. The work undertaken derived from previous PhD student work and was motivated by the lack of unanimity in the field of spectrin. Many groups state that spectrin binds preferentially to charged lipids (PS, PI) whereas others observed similar interactions between PC and mixed lipid systems (PC:PE, PC:PS). Most of the interactions have been demonstrated using indirect methods and there was a lack of direct visualization in physiological conditions of the binding. An important motivation came from the fact that spectrin was hypothesized to be able to perforate the membrane. This suggests a strong interaction which would be likely to modify the membrane mechanical properties in order to induce such effects. On the other hand, other groups hypothesized that spectrin-lipid interaction were only very weak and might have a role in stabilizing the membrane.

The work described in the different chapters in this thesis were performed for the greater part in parallel, due principally to machines availabilities and protein ressources. Work led in different directions allowed to provide a consistent understanding only at the very end.

In the first stage of **spectrin studies** (preliminary step) the spectrin extraction and purification protocol were revisited. To take into account advances in chromotograph column technology, several kinds of columns have been tested; Sepharose CL-4B appeared to provide the best results. The purified spectrin was then characterized using the techniques of SDS-PAGE electrophoresis gels and ELISA assay. Western Blots were also performed which had (curiously) not been done before. The protein proved to keep for months in its frozen medium (glycerol) without much degradation.

The protein was then tagged with fluorescein. Spectrin has been tagged with different fluorophores before, but all the experiments seemed to have been performed on LUVs or SUVs. No work with GUVs was found in the literature. Fluorescence work involving FITC-tagged spectrin demonstrated the capability of the protein to interact with both DOPC:DOPS and DOPC GUVs. No obvious correlation between the level of fluorescence and the radii of (SOPC: SOPS) vesicles could be demonstrated. Nonetheless spectrin seemed to prefer (to some extent) interacting with the smaller GUVs.

Annexin was used to highlight PS in all the GUV systems tested. Experiments performed on SOPC and SOPC: SOPS with annexin on the one hand, and FITC-spectrin on the other hand showed similiar fluorescence distributions (round microdomains and stripped microdomains) which suggested that spectrin does interfere preferentially with spectrin as stated in the literature. Work performed on 4-component GUVs corroborated this hypothesis and only very weak binding (round microdomains similar to PS microdomains) was identified. The decisive evidence came from experiments performed on externalized-PS red blood cells. Flow cytometry and confocal microscopy experiments confirmed that FITC-spectrin and annexin were competing for the same PS domains. However a limitation of this study was that fluorescence labelling interfered with the process. There was thus a real need for developing label-free imaging techniques based vibrational spectroscopic signatures.

From the fluorescence experiments it could be speculated that two different interactions, spectrin-PC, spectrin-PS, might coexist, the one with PS being stronger.

Micropipette aspiration (MPA) measurements performed on the sames GUVs systems (SOPC an SOPC: SOPS), with and without the protein, showed similar K_A which demonstrated that spectrin has no effect on the membrane mechanical properties. To demonstrate a lack of effect was challenging. To reject the possibility of negative-results due to artefacts, MPA measurements using FITC-tagged spectrin were performed, and again, spectrin, definitely present around the GUVs, showed no effect on the area expansion modulus.

Finally, isothermal titration calorimetry experiments demonstrated that the presence of PS in LUVs was necessary for spectrin-lipid interaction to be observed. The binding was nonetheless very weak (K_D of $\sim$ 130μM) compared to the literature which may have been due to the membrane lipid systems chosen.

In conclusion, all the analysis of binding were in agreement in demonstrating a weak interaction which did not modify either bending modulus, κ, or area expansion modulus, K_A. It is unlikely that spectrin inserted the membrane since, insertion will induce greater conformational changes, into the protein structure, than the one observed. Moreover, due to the elastic aspect of the protein, a single dimer (or tetramer) inserted the membrane in different sites, will surely have a strenghtening effect on the membrane or induce the vesicle burst. I would therefore be inclined to believe for a stabilizing effect of the spectrin-lipid interaction, with higher affinity for PS.

Future experiments with spectrin should involve reproducing the MPA experiments on GUVs made with egg or mix-chain lenght lipids (which can be grown with the electroformation method (addition of PE)). Other purified proteins (*e.g.* ankyrin, protein 3) should be added to the spectrin-lipid system since, preliminary experiments performed on impure spectrin demonstrated an effect in both ITC and MPA measurements. Another direction to take might be to go back to monolayer studies since microdomain formation can be more accurately monitored. Investigating protein-lipid interactions (especially at PC:PS domain boundaries) using other probes s,uch as voltage sensitive dyes, might also be informative.

The spectrin-lipid interaction work therefore allowed to implement a protocol which takes into account and evaluates all the aspects of the binding (mechanical, thermodynamic, lipid species distributions) in a complete and coherent manner. This protocol could be applied to many other proteins (or systems) and, since spectrin was found to be present in many cells, other types of spectrin (β4-spectrin, β5-spectrin) or spectrin-like molecules could be investigated. Foldrin in particular could be investigated.

Elastin was used throughout the PhD work as a comparation protein. Its autofluorescence characteristic contributed to make it an attractive model protein. In addition, elastin is similar to spectrin since both possess hydrophobic domains and entropy elasticity. TPF imaging demonstrated the capability of the α-elastin to bind to lipid membrane independently of the lipid species. In every set of experiments performed (TPF, TPF combined with CARS, TPF combined with femto-pico SRS), elastin demonstrated 3 main features: the protein uniformly bound the lipid bilayer, and sometime associated into more concentrated elastin-domains. The protein also induced small vesicles to cluster. There is a weak insight that elastin in the presence of cholesterol might be able to cross the membrane. Further measurements should be perform in this direction in order to elucidate the mechanisms of elastin secretion.

One of the most significant results came from the micropipette aspiration measurements which revealed the existence of 2 regimes in the elastin-lipid binding. On the one hand, at low concentrations, the protein stiffens the membrane while at higher concentrations, it softens it. These measurements were corroborated by measurements from other techniques (fluctuations study) from fellow researchers. They also demonstrated that MPA was a suitable technique for studying protein-lipid interactions. Finally preliminary ITC experiments showed that the binding was endothermic contrary to spectrin. No value for the association constant could be measured due to a lack of time (for optimizing the elastin/lipid ratio). Further measurements should therefore be performed in this direction.

Studying elastin is of interest and measurements of cell-elastin interaction and lipid deposition in elastic fibres may be relevant to diseases such as atherosclerosis.

Throughout the PhD, many techniques have been implemented : an apparatus for micropipette aspiration was built and tested on SOPC and SOPC:Chol GUVs and provided results in agreement with the literature. For the sake of verifying that spectrin really did not have an effect on the mechanical properties, MPA was combined to one-photon fluorescence and an apparatus was built to fit on the confocal microscope. In Non-linear microscopy, techniques have also been implemented: a two-chanel detector allowing the acquisition of deuterated lipid (at $2105\,\mathrm{cm}^{-1}$) and non-deuterated lipid (at $2845\,\mathrm{cm}^{-1}$) signals simultaneously was built and showed satisfactory functioning for lipid droplet mixtures. It would therefore be useful for studying tissues and follow the distribution of nanoparticles (or creams) in tissues in time. The deuteration technique was also used to image lateral segregation (*i.e.* micro/macro domain organisation) within mix-lipid GUVs. GUVs are system which are easily disturbed and therefore not easy to image with NLO since most techniques require long acquistion times. Up-to-now no one showed good images of unilamellar GUVs and they have (surprisingly) not been extensively studied under SRS. In the present work SRS spectra have been recorded. Hyperspectral imaging was undertaken and demonstrated the capability to distinguish between different part of the cell (lipid droplet, nucleus, tissue) as stated in the literature. Hyperspectral images of GUVs were performed using a micropipette to immobilize it. Good preliminary results were obtained and spectra from SOPC GUVs differed from spectra of SOPC GUVs surrounded with α-elastin. However the bulk solution provided a high signal at higher wavenumbers which remains an issue.

A new technique combining MPA and SRS was implemented: an apparatus was built and tested, both qualitatively and quantitatively, on cells and GUVs. Quanti-

tative measurements on SOPC GUVs were in good agreement with measurements in bright field microscopy. Preliminary results on fibroblast cells were very promising. Measurements appeared to be in good agreement with micropipette aspiration measurements performed on GFP-actin tagged fybroblasts. Characteristic features from the actin cytoskeleton could be identified. This pave the way to a wide range of potential experiments since fibroblast are excellent biological sample for studying many phenomena (mutations, diseases etc).

Combining MPA and SRS allows to study both how proteins around vesicles distributes and how it reorganizes when stress is applied.Holding the GUV in a micropipette will allow us to see domain reorganisation when stress is applied without need for label (fluorophore).

Another technique which might be employed in future investigations involves super-resolution microscopy. In micropipette studies it would allow the study of protein-lipid interactions at the molecular scale. For example, performing micropipette aspiration on inside-out ghost cells after the addition of FITC-tagged spectrin would allow to investigate very accuretely where pure free spectrin would bind on the junctional complex. It will also allow a deeper investigation to understand how the domains concentrated in elastin interact with the membrane.

The schematic diagram provided in figure 7.11 summarizes the work undertaken and highlights how the different aspects of the work are interrelated.

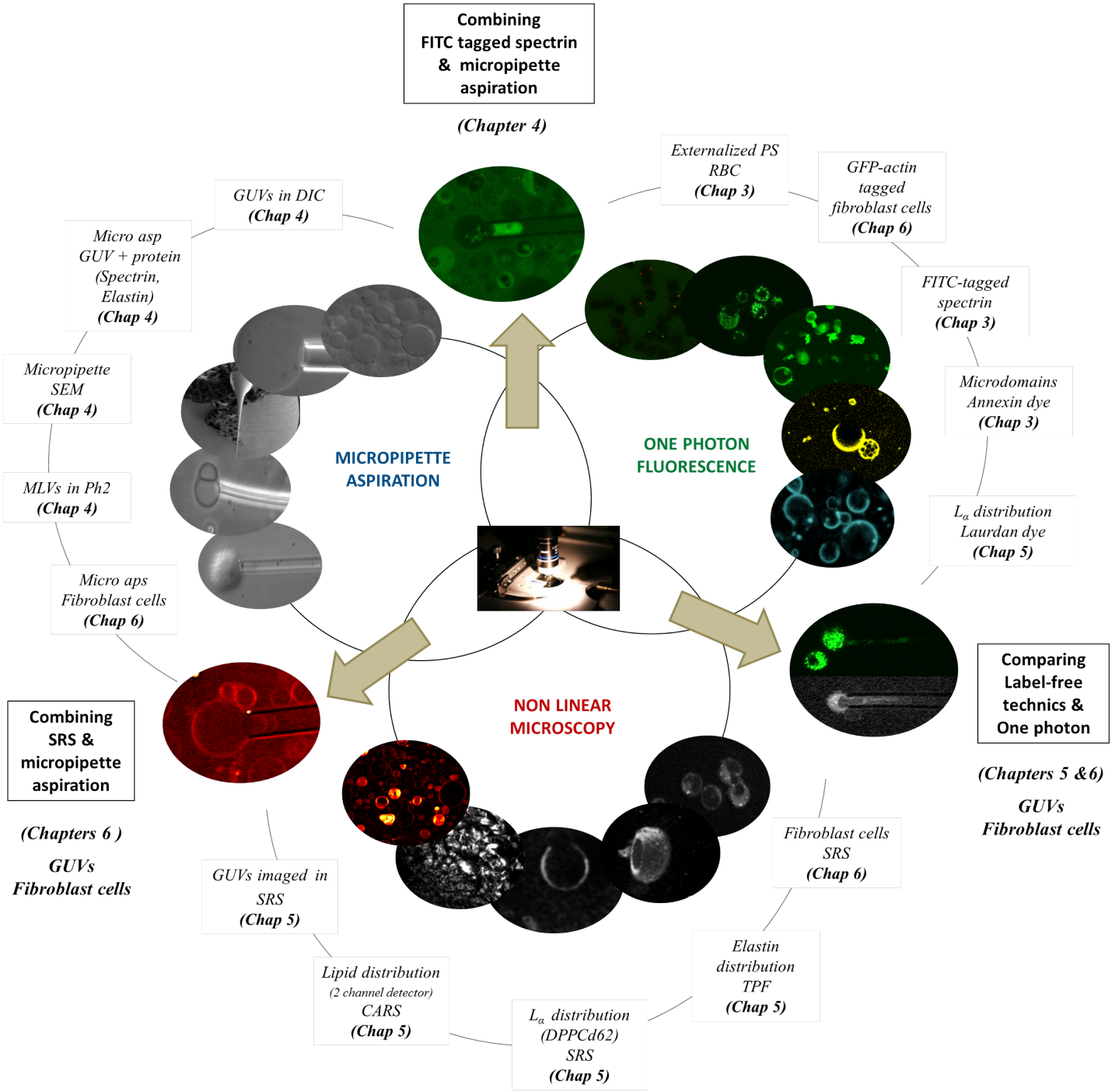

Figure 7.11: Schematic diagram summarizing the work undertaken during the PhD.

Bibliography

[1] S. J. Singer and G. L. Nicolson, "Fluid mosaic model of structure of cell-membranes," *Science*, vol. 175, no. 4023, pp. 720–&, 1972. xix, 13

[2] G. Vernier, *Protéines Amphitropiques: Diversité Conformationnelle et versatilité des Interactions Protéines-Lipides: Cas d'Etude de l'Alpha-lactalbumine et de l'apo-myoglobine*. PhD thesis, Université Joseph Fourier, Grenoble 1, 2006. 1, 2, 5

[3] C. Felton, G. C. Stevenson, and I. Godsland, "Erythrocyte-derived measures of membrane lipid composition in healthy men: associations with arachidonic acid at low to moderate but not high insulin sensitivity.," *Metabolism*, vol. 53, pp. 571–7, 2004. 2

[4] G. Van Meer and K. Simons, "Lipid polarity and sorting in epithelial cells," *Journal of Cellular Biochemistry*, vol. 36, no. 1, pp. 51–58, 1988. 3

[5] E. Sackmann, *Biological membranes architecture and function*. Elsevier Science Publishers B.V., PO Box 211, Sara Burgerhartstraat 25, 1000 AE Amsterdam, Netherlands; Elsevier Science Publishing Co., Inc., P.O. Box 882, Madison Square Station, New York, New York 10159-2101, USA, 1995. 3, 8

[6] A. G. Lee, "How lipids affect the activities of integral membrane proteins," *Biochimica Et Biophysica Acta-Biomembranes*, vol. 1666, no. 1-2, pp. 62–87, 2004. 6

[7] A. Rietveld and K. Simons, "The differential miscibility of lipids as the basis for the formation of functional membrane rafts," *Biochimica Et Biophysica Acta-Reviews on Biomembranes*, vol. 1376, no. 3, pp. 467–479, 1998. 7

[8] P. R. Cullis and B. Dekruijff, "Lipid polymorphism and the functional roles of lipids in biological-membranes," *Biochimica Et Biophysica Acta*, vol. 559, no. 4, pp. 399–420, 1979. 7

[9] J. N. Israelachvili, *Intermolecular: And Surface Forces.* New York: Academic Presse, academic p ed., 1992. 7, 8

[10] M. I. Angelova and D. S. Dimitrov, "Liposome electroformation," *Faraday Discussions*, vol. 81, pp. 303–+, 1986. 10

[11] E. Sackmann, *Physical basis of self-organization and function of membranes: Physics of vesicles.* Elsevier Science Publishers B.V., PO Box 211, Sara Burgerhartstraat 25, 1000 AE Amsterdam, Netherlands; Elsevier Science Publishing Co., Inc., P.O. Box 882, Madison Square Station, New York, New York 10159-2101, USA, 1995. 11, 12

[12] H. G. Dobereiner, J. Käs, D. Noppl, I. Sprenger, and E. Sackmann, "Budding and Fission of Vesicles," *Biophysical journal*, vol. 65, no. October, pp. 396–403, 1993. 11

[13] H.-G. Döbereiner, O. Selchow, and R. Lipowsky, "Spontaneous curvature of fluid vesicles induced by trans-bilayer sugar asymmetry," *European Biophysical Journal*, pp. 174–178, 1999. 11

[14] H. Akutsu and J. Seelig, "Interaction of metal-ions with phosphatidylcholine bilayer-membranes," *Biochemistry*, vol. 20, no. 26, pp. 7366–7373, 1981. 11

[15] E. Shechter, *Biochime et biophysique des membranes - Aspect structuraux et fonctionnels.* masson, 2 ed., 1993. 13

[16] W. H. Binder, V. Barragan, and F. M. Menger, "Domains and rafts in lipid membranes," *Angewandte Chemie-International Edition*, vol. 42, no. 47, pp. 5802–5827, 2003. 15, 24, 25

[17] P. B. Canham, "Minimum energy of bending as a possible explanation of biconcave shape of human red blood cell," *Journal of Theoretical Biology*, vol. 26, no. 1, pp. 61–&, 1970. 14, 15

[18] W. Helfrich, "Elastic properties of lipid bilayers - theory and possible experiments," *Zeitschrift Fur Naturforschung C-a Journal of Biosciences*, vol. C 28, no. 11-1, pp. 693–703, 1973. 14, 15, 16

[19] E. Evans and W. Rawicz, "Entropy-driven tension and bending elasticity in condensed-fluid membranes," *Physical Review Letters*, vol. 64, no. 17, pp. 2094–2097, 1990. 16, 111

[20] E. Sackmann, "Molecular and global structure dynamics of membranes and lipid bilayers," *Canadian Journal of Physics*, vol. 68, pp. 999–1010, 1989. 16, 17

[21] Siefert, "Configurations of fluid membranes and vesicles," *Advances in Physics*, pp. 4613–137, 1997. 17

[22] L. Miao, U. Seifert, and H. Dobereiner, "Budding transitions of fluid-bilayer vesicles: the effect of area-difference elasticity," *Physical Review E*, vol. 49, pp. 5389–5407, 1994. 17, 18

[23] H.-G. Döbereiner, *Fluctuation Vesicle Shapes, in Perspectives in Supramolecular Chemistry: Giant Vesicles, Volume 6.* Chichester, UK: John Wiley & Sons, Ltd, p.l luisj ed., 2000. 18

[24] L. Berland, *Etude physique des déformations de membranes induites par la toxine de Shiga.* PhD thesis, Université Pierre et Marie Curie Paris VI, 2009. 18, 24, 31

[25] J. B. Fournier, A. Ajdari, and L. Peliti, "Effective-area elasticity and tension of micromanipulated membranes," *Physical Review Letters*, vol. 86, no. 21, pp. 4970–4973, 2001. 20

[26] E. A. Evans, "New material concept for red-cell membrane," *Biophysical Journal*, vol. 13, no. 9, pp. 926–940, 1973. 20

[27] E. Mabrouk, D. Cuvelier, F. Brochard-Wyart, M.-H. Li, and P. Nassoy, "Les polymersomes, des vésicules robustes et stimulables pour la libération contrôlée des médicaments," *Laboratoire Physico-Chimie Curie, UMR 168, Institut Curie, CNRS, UPMC, Paris*, 2009. 21, 103

[28] D. Needham and D. Zhelev, "Use of micropipet Manipulation techniques to measure the properties of giant lipid vesicles," in *Perspectives in supramolecular chemistry: Giant vesicles, Volume 6* (P. Luisi, Luiji, Walde, ed.), ch. 9, pp. 103–147, John Wiley & Sons, Ltd, 2000. 20, 111

[29] O. G. Mouritsen, "Theoretical-models of phospholipid phase-transitions," *Chemistry and Physics of Lipids*, vol. 57, no. 2-3, pp. 179–194, 1991. 22

[30] L. Le Guyader, *Utilisation de sondes pyriniques in vivo pour caractériser l'état de phase global de la membrane plasmique des cellules eucaryotes.* PhD thesis, Université Paul Sabbatier Toulouse III, 2007. 22

[31] E. London and D. A. Brown, "Insolubility of lipids in Triton X-100: physical origin and relationship to sphingolipid/cholesterol membrane domains (rafts),"

Biochimica Et Biophysica Acta-Biomembranes, vol. 1508, no. 1-2, pp. 182–195, 2000. 22

[32] P. Meleard, C. Gerbeaud, T. Pott, L. FernandezPuente, I. Bivas, M. D. Mitov, J. Dufourcq, and P. Bothorel, "Bending elasticities of model membranes: Influences of temperature and sterol content," *Biophysical Journal*, vol. 72, no. 6, pp. 2616–2629, 1997. 23

[33] V. Coste, *Formation de domains de type 'rafts' dans des vésicules unilamellaires et mécanismes physico-chimiques de l'extraction de domaines membranaires.* PhD thesis, Université Pierre et Marie Curie Paris VI, 2006. 24, 26, 27

[34] D. Andelman, T. Kawakatsu, and K. Kawasaki, "Equilibrium shape of 2-component unilamellar membranes and vesicles," *Europhysics Letters*, vol. 19, no. 1, pp. 57–62, 1992. 25

[35] F. Julicher and R. Lipowsky, "Domain-induced budding of vesicles," *Physical Review Letters*, vol. 70, no. 19, pp. 2964–2967, 1993. 25

[36] W. Knoll, G. Schmidt, H. Rotzer, T. Henkel, W. Pfeiffer, E. Sackmann, S. Mittlerneher, and J. Spinke, "Lateral order in binary lipid alloys and its coupling to membrane functions," *Chemistry and Physics of Lipids*, vol. 57, no. 2-3, pp. 363–374, 1991. 25

[37] J. R. Silvius, D. DelGiudice, and M. Lafleur, "Cholesterol at different bilayer concentrations can promote or antagonize lateral segregation of phospholipids of differing acyl chain length," *Biochemistry*, vol. 35, no. 48, pp. 15198–15208, 1996. 25, 28

[38] J. T. Mason, "Mixing behavior of symmetric chain-length and mixed chain-length phosphatidylcholines in 2-component multilamellar bilayers - evidence for gel and liquid-crystalline phase immiscibility," *Biochemistry*, vol. 27, no. 12, pp. 4421–4429, 1988. 25

[39] J. R. Silvius, "Solid-phase and liquid-phase equilibria in phosphatidylcholine phosphatidylethanolamine mixtures - a calorimetric study," *Biochimica Et Biophysica Acta*, vol. 857, no. 2, pp. 217–228, 1986. 25, 27

[40] J. M. Boggs, "Lipid intermolecular hydrogen-bonding - influence on structural organization and membrane-function," *Biochimica Et Biophysica Acta*, vol. 906, no. 3, pp. 353–404, 1987. 25

[41] Y. Lange, M. H. Swaisgood, B. V. Ramos, and T. L. Steck, "Plasma-membranes contain half the phospholipid and 90-percent of the cholesterol and sphingomyelin in cultured human-fibroblasts," *Journal of Biological Chemistry*, vol. 264, no. 7, pp. 3786–3793, 1989. 26

[42] P. L. Yeagle, "Cholesterol and the cell-membrane," *Biochimica Et Biophysica Acta*, vol. 822, no. 3-4, pp. 267–287, 1985. 26

[43] E. Sparr, L. Hallin, N. Markova, and H. Wennerstrom, "Phospholipid-cholesterol bilayers under osmotic stress," *Biophysical Journal*, vol. 83, no. 4, pp. 2015–2025, 2002. 26

[44] S. L. Veatch and S. L. Keller, "Organization in lipid membranes containing cholesterol," *Physical Review Letters*, vol. 89, no. 26, 2002. 27

[45] P. F. Devaux and R. Morris, "Transmembrane asymmetry and lateral domains in biological membranes," *Traffic*, vol. 5, no. 4, pp. 241–246, 2004. 27

[46] P. F. F. Almeida, W. L. C. Vaz, and T. E. Thompson, "Lateral diffusion in the liquid-phases of dimyristoylphosphatidylcholine cholesterol lipid bilayers - a free-volume analysis," *Biochemistry*, vol. 31, no. 29, pp. 6739–6747, 1992. 28, 43

[47] P. E. Milhiet, C. Domec, M. C. Giocondi, N. Van Mau, F. Heitz, and C. Le Grimellec, "Domain formation in models of the renal brush border membrane outer leaflet," *Biophysical Journal*, vol. 81, no. 1, pp. 547–555, 2001. 28

[48] M. B. Sankaram and T. E. Thompson, "Cholesterol-induced fluid-phase immiscibility in membranes," *Proceedings of the National Academy of Sciences of the United States of America*, vol. 88, no. 19, pp. 8686–8690, 1991. 28

[49] J. R. Silvius, "Role of cholesterol in lipid raft formation: lessons from lipid model systems," *Biochimica Et Biophysica Acta-Biomembranes*, vol. 1610, no. 2, pp. 174–183, 2003. 28

[50] G. W. Feigenson and J. T. Buboltz, "Ternary phase diagram of dipalmitoyl-PC/dilauroyl-PC/cholesterol: Nanoscopic domain formation driven by cholesterol," *Biophysical Journal*, vol. 80, no. 6, pp. 2775–2788, 2001. 28

[51] K. Simons and E. Ikonen, "Functional rafts in cell membranes," *Nature*, vol. 387, no. 6633, pp. 569–572, 1997. 29

[52] R. G. W. Anderson and K. Jacobson, "Cell biology - A role for lipid shells in targeting proteins to caveolae, rafts, and other lipid domains," *Science*, vol. 296, no. 5574, pp. 1821–1825, 2002. 29

[53] L. J. Pike, "Lipid rafts: bringing order to chaos," *Journal of Lipid Research*, vol. 44, no. 4, pp. 655–667, 2003. 29

[54] K. Simons and W. L. C. Vaz, "Model systems, lipid rafts, and cell membranes," *Annual Review of Biophysics and Biomolecular Structure*, vol. 33, pp. 269–295, 2004. 29

[55] R. F. M. de Almeida, L. M. S. Loura, A. Fedorov, and M. Prieto, "Lipid rafts have different sizes depending on membrane composition: A time-resolved fluorescence resonance energy transfer study," *Journal of Molecular Biology*, vol. 346, no. 4, pp. 1109–1120, 2005. 29

[56] S. L. Veatch and S. L. Keller, "Miscibility phase diagrams of giant vesicles containing sphingomyelin," *Physical Review Letters*, vol. 94, no. 14, 2005. 30

[57] L. A. Bagatolli and E. Gratton, "Two Photon Fluorescence Microscopy of Coexisting Lipid Domains in Giant Unilamellar Vesicles of Binary Phospholipid Mixtures," *Biophysical Journal*, vol. 78, no. January, pp. 290–305, 2000. 29

[58] J. Pécréaux, *Mesures du spectre de fluctuations de vésicules géantes par analyse de contours; application aux membranes passives et actives.* PhD thesis, Université Pierre et Marie Curie Paris VI, 2004. 31

[59] T. J. Byers and D. Branton, "Visualization of the protein associations in the erythrocyte-membrane skeleton," *Proceedings of the National Academy of Sciences of the United States of America*, vol. 82, no. 18, pp. 6153–6157, 1985. 31, 33

[60] T. Ruetz, S. Cornick, and J. A. Guttman, "The Spectrin Cytoskeleton Is Crucial for Adherent and Invasive Bacterial Pathogenesis," *Plos One*, vol. 6, no. 5, 2011. 31

[61] V. Bennett and J. Healy, "Organizing the diseases fluid membrane bilayer: diseases linked to spectrin and ankyrin," *Trends in Molecular Medicine*, vol. 14, no. 1, pp. 28–36, 2008. 31, 67, 72, 73

[62] J. M. Thompson, *Order and Interactions in Model Biological Membranes.* PhD thesis, University of Exeter, 2007. 33, 86, 189, 191, 195, 200

[63] N. Garrett, *Nano-Biophotonics.* PhD thesis, University of Exeter, 2010. 35

[64] F. Zernike, "Phase contrast, a new method for the microscopic observation of transparent objects Part II," *Physica*, vol. 9, pp. 974–986, 1942. 36

[65] R. Yuste, "Fluorescence microscopy today," *Nature Methods*, vol. 2, no. 12, pp. 902–904, 2005. 38

[66] A. H. Coons and M. H. Kaplan, "Localization of antigen in tissue cells .2. Improvements in a method for the detection of antigen by means of fluorescent antibody," *Journal of Experimental Medicine*, vol. 91, no. 1, pp. 1–13, 1950. 38

[67] M. Chalfie, Y. Tu, G. Euskirchen, W. W. Ward, and D. C. Prasher, "Green fluorescent protein as a marker for gene-expression," *Science*, vol. 263, no. 5148, pp. 802–805, 1994. 39

[68] L. A. Bagatolli, "To see or not to see: Lateral organization of biological membranes and fluorescence microscopy," *Biochimica Et Biophysica Acta-Biomembranes*, vol. 1758, no. 10, pp. 1541–1556, 2006. 41

[69] N. Kahya and P. Schwille, "How phospholipid-cholesterol interactions modulate lipid lateral diffusion, as revealed by fluorescence correlation spectroscopy," *Journal of Fluorescence*, vol. 16, no. 5, pp. 671–678, 2006. 43

[70] J. Squier and M. Muller, "High resolution nonlinear microscopy: A review of sources and methods for achieving optimal imaging," *Review of Scientific Instruments*, vol. 72, no. 7, pp. 2855–2867, 2001. 44

[71] S. W. Hell, "Microscopy and its focal switch.," *Nature methods*, vol. 6, pp. 24–32, Jan. 2009. 45

[72] R. Carminati and C. Boccara, *ESPCI Paris Tech 2ième année, OPTIQUE: Lumière et Matière*. 2011. 46

[73] S. W. Chu, S. Y. Chen, G. W. Chern, T. H. Tsai, Y. C. Chen, B. L. Lin, and C. K. Sun, "Studies of x((2))/x((3)) tensors in submicron-scaled bio-tissues by polarization harmonics optical microscopy," *Biophysical Journal*, vol. 86, no. 6, pp. 3914–3922, 2004. 47, 49

[74] K. König, "Multiphoton microscopy in life sciences in Life Sciences," *Journal of Microscopy*, vol. 200, no. June, pp. 83–104, 2000. 48

[75] W. Denk, J. H. Strickler, and W. W. Webb, "2-photon laser scanning fluorescence microscopy," *Science*, vol. 248, no. 4951, pp. 73–76, 1990. 48

[76] P. T. C. So, "Two-photon fluorescence microscopy: A new tool for tissue imaging and spectroscopy," *Journal of Histotechnology*, vol. 23, no. 3, pp. 221–228, 2000. 48

[77] W. R. Zipfel, R. M. Williams, and W. W. Webb, "Nonlinear magic: Multiphoton microscopy in the biosciences," *Nature Biotechnology*, vol. 21, no. 11, pp. 1369–1377, 2003. 48

[78] N. Djaker-Oudjhara, *Microscopie par diffusion cohérente Raman CARS: Application à l'imagerie des milieux biologiques*. PhD thesis, Université Paul Cézanne Aix-Marseille III, 2006. 48, 59

[79] P. J. Campagnola, A. C. Millard, M. Terasaki, P. E. Hoppe, C. J. Malone, and W. A. Mohler, "Three-dimensional high-resolution second-harmonic generation imaging of endogenous structural proteins in biological tissues," *Biophysical Journal*, vol. 82, no. 1, pp. 493–508, 2002. 49

[80] J. C. Mansfield, *Multi-photon microscopy of cartilage*. PhD thesis, University of Exeter, 2008. 49, 152

[81] C. V. Raman and K. S. Krishnan, "A new type of secondary radiation," *Nature*, vol. 121, pp. 501–502, 1928. 49

[82] E. O. Potma and X. S. Xie, "Theory of Spontaneous and Coherent Raman Scattering," in *Handbook of Biological Nonlinear Optical Microscopy* (P. S. Masters and B. R., eds.), ch. 7, pp. 164–185, Oxford University Press: Peter So and Barry R. Masters, 2008. 50, 51, 58, 61

[83] G. L. Eesley, *Coherent Raman Spectroscopy*. Pergaman Press, 1981. 51

[84] P. Matousek and N. Stone, "Emerging concepts in deep Raman spectroscopy of biological tissue," *Analyst*, vol. 134, no. 6, pp. 1058–1066, 2009. 53

[85] N. Stone and P. Matousek, "Advanced transmission Raman spectroscopy: A promising tool for breast disease diagnosis," *Cancer Research*, vol. 68, no. 11, pp. 4424–4430, 2008. 53

[86] P. D. Maker and R. W. Terhune, "Study of optical effects due to an induced polarization third order in electric field strength," *Physical Review*, vol. 137, no. 3A, pp. A801–&, 1965. 54

[87] M. D. Duncan, J. Reintjes, and T. J. Manuccia, "Scanning coherent anti-stokes raman microscope," *Optics Letters*, vol. 7, no. 8, pp. 350–352, 1982. 54

[88] A. Zumbusch, G. R. Holtom, and X. S. Xie, "Three-dimensional vibrational imaging by coherent anti-Stokes Raman scattering," *Physical Review Letters*, vol. 82, no. 20, pp. 4142–4145, 1999. 55

[89] Courtois, *Cours Optic Non-Linéaire*. 2009. 55, 56

[90] Y. Shen, *The principle of Non linear Optics*. John Wiley & Sons, 1984. 57

[91] C. L. Evans and X. S. Xie, "Coherent Anti-Stokes Raman Scattering Microscopy: Chemical Imaging for Biology and Medicine," *Annual Review of Analytical Chemistry*, vol. 1, pp. 883–909, 2008. 57, 60, 134

[92] A. Volkmer, J. X. Cheng, and X. S. Xie, "Vibrational imaging with high sensitivity via epidetected coherent anti-Stokes Raman scattering microscopy," *Physical Review Letters*, vol. 87, no. 2, 2001. 58

[93] M. Jurna, *Vibrational phase contrast CARS microscopy*. PhD thesis, University of Twente, The Netherlands, 2010. 61

[94] E. O. Potma and X. S. Xie, "Coherent anti-Stokes Raman Scattering Microscopy: Instrumentation and Applications," in *Handbook of Biological Nonlinear Optical Microscopy* (P. S. Masters and B. R., eds.), pp. 412–434, Oxford University Press: Peter So and Barry R. Masters, 2008. 60

[95] E. O. Potma, C. L. Evans, and X. S. Xie, "Heterodyne coherent anti-Stokes Raman scattering (CARS) imaging," *Optics Letters*, vol. 31, no. 2, pp. 241–243, 2006. 61

[96] I. Rocha-Mendoza, P. Borri, and W. Langbein, "Quadruplex CARS microspectroscopy," *Journal of Raman Spectroscopy*, vol. 44, no. 2, pp. 255–261, 2013. 61

[97] A. Volkmer, L. D. Book, and X. S. Xie, "Time-resolved coherent anti-Stokes Raman scattering microscopy: Imaging based on Raman free induction decay," *Applied Physics Letters*, vol. 80, no. 9, pp. 1505–1507, 2002. 61

[98] J. X. Chen, A. Volkmer, L. D. Book, and X. S. Xie, "Multiplex coherent antistokes Raman scattering microspectroscopy and study of lipid vesicles," *Journal of Physical Chemistry B*, vol. 106, no. 34, pp. 8493–8498, 2002. 61

[99] H. A. Rinia, M. Bonn, and M. Muller, "Quantitative multiplex CARS spectroscopy in congested spectral regions," *Journal of Physical Chemistry B*, vol. 110, no. 9, pp. 4472–4479, 2006. 61

[100] C. W. Freudiger, W. Min, B. G. Saar, S. Lu, G. R. Holtom, C. W. He, J. C. Tsai, J. X. Kang, and X. S. Xie, "Label-Free Biomedical Imaging with High Sensitivity by Stimulated Raman Scattering Microscopy," *Science*, vol. 322, no. 5909, pp. 1857–1861, 2008. 62, 63, 64

[101] X. L. An, X. H. Guo, H. Sum, J. Morrow, W. Gratzer, and N. Mohandas, "Phosphatidylserine binding sites in erythroid spectrin: Location and implications for membrane stability," *Biochemistry*, vol. 43, no. 2, pp. 310–315, 2004. 66, 72

[102] A. M. McGough and R. Josephs, "On the structure of erythrocyte spectrin in partially expanded membrane skeletons," *Proceedings of the National Academy of Sciences of the United States of America*, vol. 87, no. 13, pp. 5208–5212, 1990. 67

[103] R. Waugh and E. A. Evans, "Thermoelasticity of red blood-cell membrane," *Biophysical Journal*, vol. 26, no. 1, pp. 115–131, 1979. 67

[104] Z. S. Zhang, S. A. Weed, P. G. Gallagher, and J. S. Morrow, "Dynamic molecular modeling pathogenic mutations spectrin self-association domain," *Blood*, vol. 98, no. 6, pp. 1645–1653, 2001. 67

[105] S. R. Goodman and K. Shiffer, "The spectrin membrane skeleton of normal and abnormal human-erythrocytes - a review," *American Journal of Physiology*, vol. 244, no. 3, pp. C121–C141, 1983. 67

[106] V. Bennett and D. Branton, "Selective association of spectrin with cytoplasmic surface of human erythrocyte plasma-membranes - quantitative-determination with purified spectrin-p-32," *Journal of Biological Chemistry*, vol. 252, no. 8, pp. 2753–2763, 1977. 68

[107] J. M. Anderson and J. M. Tyler, "State of Spectrin Phosphorylation Does Not Affect Erythrocyte Shape or Spectrin Binding to Erythrocyte Membranes," *The Journal of Biological Chemistry*, vol. 255, no. February 25, pp. 1259–1265, 1980. 68

[108] C. Mombers, J. Degier, R. A. Demel, and L. L. M. Vandeenen, "Spectrin-phospholipid interaction - a monolayer study," *Biochimica Et Biophysica Acta*, vol. 603, no. 1, pp. 52–62, 1980. 68

[109] R. Maksymiw, S. F. Sui, H. Gaub, and E. Sackmann, "Electrostatic coupling of spectrin dimers to phosphatidylserine containing lipid lamellae," *Biochemistry*, vol. 26, no. 11, pp. 2983–2990, 1987. 69, 70, 88

[110] R. I. Macdonald, "Temperature and ionic effects on the interaction of erythroid spectrin with phosphatidylserine membranes," *Biochemistry*, vol. 32, no. 27, pp. 6957–6964, 1993. 69

[111] A. F. Sikorski, K. Michalak, and M. Bobrowska, "Interaction of spectrin with phospholipids - quenching of spectrin intrinsic fluorescence by phospholipid suspensions," *Biochimica Et Biophysica Acta*, vol. 904, no. 1, pp. 55–60, 1987. 70

[112] A. F. Sikorski, B. Hanus-Lorenz, A. Jezierski, and A. R. Dluzewski, "Interaction of membrane skeletal proteins with membrane lipid domain," *Acta Biochimica Polonica*, vol. 47, no. 3, pp. 565–578, 2000. 70, 200

[113] W. Diakowski, L. Ozimek, E. Bielska, S. Bem, M. Langner, and A. F. Sikorski, "Cholesterol affects spectrin-phospholipid interactions in a manner different from changes resulting from alterations in membrane fluidity due to fatty acyl chain composition," *Biochimica Et Biophysica Acta-Biomembranes*, vol. 1758, no. 1, pp. 4–12, 2006. 70, 200

[114] M. Grzybek, A. Chorzalska, E. Bok, A. Hryniewicz-Jankowska, A. Czogalla, W. Diakowski, and A. F. Sikorski, "Spectrin-phospholipid interactions - Existence of multiple kinds of binding sites?," *Chemistry and Physics of Lipids*, vol. 141, no. 1-2, pp. 133–141, 2006. 70

[115] A. M. Cohen, S. C. Liu, L. H. Derick, and J. Palek, "Ultrastructural studies of the interaction of spectrin with phosphatidylserine liposomes," *Blood*, vol. 68, no. 4, pp. 920–926, 1986. 71

[116] M. I. Angelova, S. Soleau, P. Meleard, J. F. Faucon, and P. Bothorel, *Preparation of giant vesicles by external ac electric-fields - kinetics and applications*, vol. 89. Berlin: Dr Dietrich Steinkopff Verlag, 1992. 73

[117] P. Walde, K. Cosentino, H. Engel, and P. Stano, "Giant Vesicles: Preparations and Applications," *Chembiochem*, vol. 11, no. 7, pp. 848–865, 2010. 74

[118] W. Gratzer, "Preparation of Spectrin," *Methods in enzymology*, vol. 85, pp. 475–480, 1982. 77

[119] Tse and Lux, "Red Blood Cell membrane disorders," *British Journal of Haematology*, vol. 104, pp. 2–13, 1999. 81

[120] A. S. R. Goodman, K. E. Krebs, C. F. Whitfield, and B. M. Riederer, "Spectrin and related molecules," *Critical reviews in Biochemistry and Molecular Biology*, vol. 23, no. 2, 1988. 81

[121] P. Datta, S. B. Chakrabarty, A. Chakrabarty, and A. Chakrabarti, "Interaction of erythroid spectrin with hemoglobin variants: implications in β-thalassemia," *Blood Cells, Molecules, and Diseases*, vol. 30, pp. 248–253, May 2003. 84, 86

[122] M. Stockl, P. Fischer, E. Wanker, and A. Herrmann, "alpha-Synuclein selectively binds to anionic phospholipids embedded in liquid-disordered domains," *Journal of Molecular Biology*, vol. 375, no. 5, pp. 1394–1404, 2008. 90

[123] P. M. Henson, D. L. Bratton, and V. A. Fadok, "Apoptotic cell removal," *Current Biology*, pp. 795–805, 2001. 94

[124] V. E. Kagan, B. Gleiss, Y. Y. Tyurina, V. a. Tyurin, C. Elenstrom-Magnusson, S.-X. Liu, F. B. Serinkan, a. Arroyo, J. Chandra, S. Orrenius, and B. Fadeel, "A Role for Oxidative Stress in Apoptosis: Oxidation and Externalization of Phosphatidylserine Is Required for Macrophage Clearance of Cells Undergoing Fas-Mediated Apoptosis," *The Journal of Immunology*, vol. 169, pp. 487–499, July 2002. 94

[125] J. M. Tarr, P. J. Young, R. Morse, D. J. Shaw, R. Haigh, P. G. Petrov, S. J. Johnson, P. G. Winyard, and P. Eggleton, "A mechanism of release of calreticulin from cells during apoptosis.," *Journal of molecular biology*, vol. 401, pp. 799–812, Sept. 2010. 94

[126] V. Heinrich and W. Rawicz, "Automated , High-Resolution Micropipet Aspiration Reveals New Insight into the Physical Properties of Fluid," *Langmuir*, vol. 21, pp. 1962–1971, 2004. 103

[127] Y.-s. Kee and D. N. Robinson, "Micropipette Aspiration for Studying Cellular Mechanosensory Responses and Mechanics," in *Dictyostelium discoideum Protocols, Methods in Molecular Biology 983* (L. Eichinger and F. Rivero, eds.), vol. 983 of *Methods in Molecular Biology*, ch. 20, pp. 367–382, Totowa, NJ: Humana Press, 2013. 103

[128] R. M. Hochmuth, "Micropipette aspiration of living cells," *Journal of Biomechanics*, vol. 33, pp. 15–22, 2000. 108, 175

[129] D. V. Zhelev, D. Needham, and R. M. Hochmuth, "A novel Micropipette Method for Measuring the Bending Modulus of Vesicle Membranes," *Biophysical Journal*, vol. 67, no. August, pp. 720–727, 1994. 111

[130] W. Rawicz, K. C. Olbrich, T. McIntosh, D. Needham, and E. Evans, "Effect of chain length and unsaturation on elasticity of lipid bilayers," *Biophysical Journal*, vol. 79, no. 1, pp. 328–339, 2000. 111

[131] J. R. Henriksen and J. H. Ipsen, "Measurement of membrane elasticity by micropipette aspiration.," *The European physical journal. E, Soft matter*, vol. 14, pp. 149–67, June 2004. 111

[132] Y. Zhou and R. M. Raphael, "Effect of salicylate on the elasticity, bending stiffness, and strength of SOPC membranes.," *Biophysical journal*, vol. 89, pp. 1789–801, Sept. 2005. 111

[133] J. Song and R. E. Waugh, "Bending rigidity of SOPC membranes containing cholesterol Lt (AM)," *Biophysical Journal*, vol. 64, no. June, pp. 1967–1970, 1993. 111

[134] B. Y. S. M. Partridge and A. H. F. Davis, "The Chemistry of Connective Tissues: Composition of the Soluble proteins derived from Elastin," *Nature Methods*, vol. 6, no. 1925, pp. 21–30, 1954. 113

[135] P. Golagan, *Red Blood Cell as an Elastic Probe: Interaction with Drugs and Toxins*. PhD thesis, University of Exeter, 2013. 117

[136] J. Moger, B. D. Johnston, and C. R. Tyler, "Imaging metal oxide nanoparticles in biological structures with CARS microscopy," *Optics Express*, vol. 16, no. 5, pp. 3408–3419, 2008. 133

[137] N. Djaker, P. F. Lenne, D. Marguet, A. Colonna, C. Hadjur, and H. Rigneault, "Coherent anti-Stokes Raman scattering microscopy (CARS): Instrumentation and applications," *Nuclear Instruments & Methods in Physics Research Section a-Accelerators Spectrometers Detectors and Associated Equipment*, vol. 571, no. 1-2, pp. 177–181, 2007. 134

[138] P. Nandakumar, A. Kovalev, and A. Volkmer, "Vibrational imaging based on stimulated Raman scattering microscopy," *New Journal of Physics*, vol. 11, 2009. 134

[139] X. Nan, W. Y. Yang, and X. S. Xie, "Lights Up Lipids in Living Cells," *Biophotonics international*, no. August, 2004. 135

[140] E. Ploetz, S. Laimgruber, S. Berner, W. Zinth, and P. Gilch, "Femtosecond stimulated Raman microscopy," *Applied Physics B*, vol. 87, pp. 389–393, Apr. 2007. 140

[141] P. Kukura, D. W. McCamant, and R. a. Mathies, "Femtosecond stimulated Raman spectroscopy.," *Annual review of physical chemistry*, vol. 58, pp. 461–88, Jan. 2007. 140

[142] E. O. Potma and X. S. Xie, "Detection of single lipid bilayers with coherent anti-Stokes Raman scattering (CARS) microscopy," *Journal of Raman Spectroscopy*, vol. 34, pp. 642–650, Sept. 2003. 142

[143] E. O. Potma and X. S. Xie, "Direct visualization of lipid phase segregation in single lipid bilayers with coherent anti-Stokes Raman scattering microscopy.," *Chemphyschem : a European journal of chemical physics and physical chemistry*, vol. 6, pp. 77–9, Jan. 2005. 142

[144] L. Li, H. F. Wang, and J. X. Cheng, "Quantitative coherent anti-Stokes Raman scattering imaging of lipid distribution in coexisting domains," *Biophysical Journal*, vol. 89, no. 5, pp. 3480–3490, 2005. 142

[145] L. Li and J. X. Cheng, "Label-free coherent anti-stokes Raman scattering imaging of coexisting lipid domains in single bilayers," *Journal of Physical Chemistry B*, vol. 112, no. 6, pp. 1576–1579, 2008. 142

[146] A. Lindsay, *Behaviour of alpha-elastin in bulk and at aqueous surfaces.* PhD thesis, University of Exeter, 2011. 151, 152, 157

[147] E. Green, R. Ellis, and P. Winlove, "The molecular structure and physical properties of elastin fibers as revealed by Raman microspectroscopy.," *Biopolymers*, vol. 89, pp. 931–40, Nov. 2008. 151

[148] I. Ritz-timme, S, Laumeier and M. J. Collins, "Cutaneous Biology Aspartic acid racemization : evidence for marked longevity of elastin in human skin," *British Journal of Dermatology*, vol. 149, pp. 951–959, 2003. 151

[149] G. W. G. Chalmers, J. M. Gosline, and M. A. Lillie, "The hydrophobicity of vertebrate elastins," *The journal of Experimental Biolog*, vol. 314, pp. 301–314, 1999. 151

[150] R. P. Mecham, "Methods in Elastic Tissues Biology: Elastin Isolation and Purification," *Methods*, vol. 45, no. 1, pp. 32–41, 2008. 151

[151] B. A. Cox, B. C. Starcher, and D. W. Urry, "Coacervation of alpha-elastin results in fiber formation," *Biochimica Et Biophysica Acta*, vol. 317, pp. 209–213, 1973. 152

[152] B. Vrhovski, S. Jensen, and A. S. Weiss, "Coacervation characteristics of recombinant human tropoelastin," *European Journal of Biochemistry*, vol. 98, pp. 92–98, 1997. 152

[153] J. Mansfield, J. Yu, D. Attenburrow, J. Moger, U. Tirlapur, J. Urban, Z. F. Cui, and P. Winlove, "The elastin network: its relationship with collagen and cells in articular cartilage as visualized by multiphoton microscopy," *Journal of Anatomy*, vol. 215, no. 6, pp. 682–691, 2009. 152

[154] D. Fu, G. Holtom, C. Freudiger, X. Zhang, and X. S. Xie, "Hyperspectral Imaging with Stimulated Raman Scattering by Chirped Femtosecond Lasers," 2013. 162

[155] C. W. Freudiger, R. Pfannl, D. a. Orringer, B. G. Saar, M. Ji, Q. Zeng, L. Ottoboni, Y. Wei, W. Ying, C. Waeber, J. R. Sims, P. L. De Jager, O. Sagher, M. a. Philbert, X. Xu, S. Kesari, X. S. Xie, and G. S. Young, "Multicolored stain-free histopathology with coherent Raman imaging.," *Laboratory investigation; a journal of technical methods and pathology*, vol. 92, pp. 1492–502, Oct. 2012. 162

[156] J. C. Mansfield, G. R. Littlejohn, M. P. Seymour, R. J. Lind, S. Perfect, and J. Moger, "Label-free Chemically Specific Imaging in Planta with Stimulated Raman Scattering Microscopy," *Analytical Chemistry*, vol. 85, no. 10, pp. 5055–5063, 2013. 165, 166

[157] S. Yue, J. M. Cárdenas-Mora, L. S. Chaboub, S. a. Lelièvre, and J.-X. Cheng, "Label-free analysis of breast tissue polarity by Raman imaging of lipid phase.," *Biophysical journal*, vol. 102, pp. 1215–23, Mar. 2012. 165

[158] E. T. Garbacik, J. L. Herek, C. Otto, and H. L. Offerhaus, "Rapid identification of heterogeneous mixture components with hyperspectral coherent anti-Stokes Raman scattering imaging," *Journal of Raman Spectroscopy*, vol. 43, no. 5, pp. 651–655, 2012. 166

[159] C.-Y. Lin, J. L. Suhalim, C. L. Nien, M. D. Miljković, M. Diem, J. V. Jester, and E. O. Potma, "Picosecond spectral coherent anti-Stokes Raman scattering imaging with principal component analysis of meibomian glands.," *Journal of biomedical optics*, vol. 16, p. 021104, Feb. 2011. 166

[160] C. Lim, E. Zhou, a. Li, S. Vedula, and H. Fu, "Experimental techniques for single cell and single molecule biomechanics," *Materials Science and Engineering: C*, vol. 26, pp. 1278–1288, Sept. 2006. 175, 176

[161] A. Buxboim, I. L. Ivanovska, and D. E. Discher, "Matrix elasticity, cytoskeletal forces and physics of the nucleus: how deeply do cells 'feel' outside and in?," *Journal of cell science*, vol. 123, pp. 297–308, Feb. 2010. 175

[162] E. H. Zhou, S. T. Quek, and C. T. Lim, "Power-law rheology analysis of cells undergoing micropipette aspiration.," *Biomechanics and modeling in mechanobiology*, vol. 9, pp. 563–72, Oct. 2010. 175

[163] H.-G. Döbereiner, B. Dubin-Thaler, G. Giannone, H. Xenias, and M. Sheetz, "Dynamic Phase Transitions in Cell Spreading," *Physical Review Letters*, vol. 93, p. 108105, Sept. 2004. 176

[164] H.-G. Döbereiner, B. J. Dubin-Thaler, J. M. Hofman, H. S. Xenias, T. N. Sims, G. Giannone, M. L. Dustin, C. H. Wiggins, and M. P. Sheetz, "Lateral Membrane Waves Constitute a Universal Dynamic Pattern of Motile Cells," *Physical Review Letters*, vol. 97, p. 038102, July 2006. 176

[165] J. F. Frisz, K. Lou, H. a. Klitzing, W. P. Hanafin, V. Lizunov, R. L. Wilson, K. J. Carpenter, R. Kim, I. D. Hutcheon, J. Zimmerberg, P. K. Weber, and M. L. Kraft, "Direct chemical evidence for sphingolipid domains in the plasma membranes of fibroblasts.," *Proceedings of the National Academy of Sciences of the United States of America*, vol. 110, pp. E613–22, Feb. 2013. 176

[166] A. Cooper, "Thermodynamic analysis of biomolecular interactions," *Analytical techniques*, no. 1, pp. 557–563, 1999. 184

[167] M. M. Pierce, C. S. Raman, and B. T. Nall, "Isothermal titration calorimetry of protein-protein interactions," *Methods-a Companion to Methods in Enzymology*, vol. 19, no. 2, pp. 213–221, 1999. 184, 186

[168] E. Breukink, P. Ganz, B. D. Kruijff, and J. Seelig, "Binding of Nisin Z to Bilayer Vesicles As Determined with Isothermal Titration," *Biochemistry*, vol. 39, pp. 10247–10254, 2000. 186

[169] J. Seelig, "Thermodynamics of lipid-peptide interactions.," *Biochimica et biophysica acta*, vol. 1666, pp. 40–50, Nov. 2004. 186

[170] H. H. Heerklotz, H. Binder, and R. M. Epand, "A " Release " Protocol for Isothermal Titration Calorimetry," vol. 76, no. May, pp. 2606–2613, 1999. 186

[171] N. Greenfield and G. Fasman, "Computed Circular Dichroism Spectra for the Evaluation of Protein Conformation," *Biochemistry*, vol. 8, p. 4108, 1996. 195

[172] N. Kelly, S.M., Jess, T.J, Price, "How to study proteins by circular dichroism," *Biochimica Et Biophysica Acta*, vol. 1751, pp. 119–139, 2005. 197

[173] L. Whitmore and B. Wallace, "DICHROWEB: an online server for protein secondary structure analyses from circular dichroism spectroscopic data Nucleic Acids Research 32:W668-673," 2004. 197

[174] L. Whitmore and B. Wallace, "Protein Secondary Structure Analyses from Circular Spectroscopy: Methods and References Databases," *Biopolymers*, vol. 89, pp. 392–400, 2008. 197

[175] B. G. Vertessy and T. L. Steck, "Elasticity of the human red-cell membrane skeleton - effects of temperature and denaturants," *Biophysical Journal*, vol. 55, no. 2, pp. 255–262, 1989. 198

Appendices

Appendix A: ADE model and Lipid species

Area Difference Elasticity model

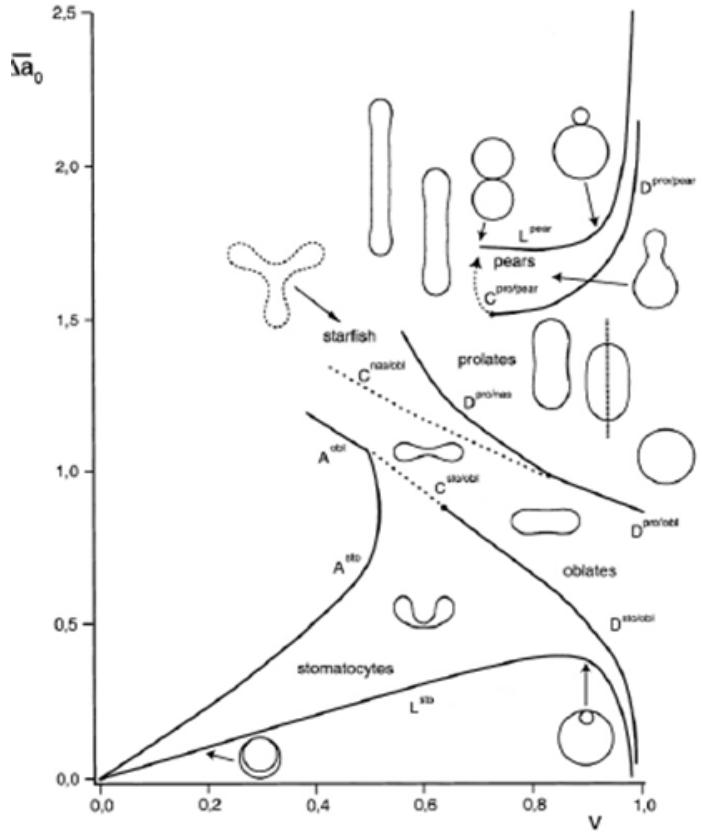

Figure 12: Vesicle Phase Diagram predicted by the Area-Difference-Elasticity (ADE) model. The shape of a vesicle that minimises its energy can be predicted using the differential area Δa_0 and the volume-to-area ratio (the reduced volulme, v). From (Döberneiner et al., 2000a)

Lipid characteristics

Lipid used during the PhD: nomenclature

Short name	synonyme	**Extended name**	**Avanti N°**
DOPC	**18:1 (Δ9-Cis) PC**	1,2-dioleoyl-*sn*-glycero-3-phosphocholine	850375
DPPC	**16:0 PC**	1,2-dipalmitoyl-*sn*-glycero-3-phosphocholine	850355
DOPS	**18:1 PS**	1,2-dioleoyl-*sn*-glycero-3-phospho-L-serine (sodium salt)	840035
Chol	**cholesterol**	cholesterol (ovine wool, >98%)	700000
SM	**18:0 SM (d18:1/18:0)**	N-stearoyl-D-*erythro*-sphingosylphosphorylcholine	860586
SOPC	**18:0-18:1 PC**	1-stearoyl-2-oleoyl-*sn*-glycero-3-phosphocholine	850467
SOPS	**18:0-18:1 PS**	1-stearoyl-2-oleoyl-*sn*-glycero-3-phospho-L-serine (sodium salt)	840039
DPPCd62	**16:0 PC-d62**	1,2-dipalmitoyl-d62-*sn*-glycero-3-phosphocholine	860355

Lipid characteristic table

	Molecular formulae	**Molecular weight**	**Percenet composition**	**Stability storage**	**T_M**
DOPC	$C_{44}H_{84}NO_8P$	786.113	C 67.23%, H 10.77%, N 1.78%, O 16.28%, P 3.94%	6 months/ -20°C	-17°C
DPPC	$C_{40}H_{80}NO_8P$	734.039	C 65.45%, H 10.98%, N 1.91%, O 17.44%, P 4.22%	2 years/ -20°C	41°C
DOPS	$C_{42}H_{77}NO_{10}PNa$	810.025	C 62.28%, H 9.58%, N 1.73%, Na 2.84%, O 19.75%, P 3.82%	6 months/ -20°C	-11°C
Chol	$C_{27}H_{46}O$	386.654	C 83.87%, H 11.99%, O 4.14%	6 months/ -20°C	---
SM	$C_{41}H_{83}N_2O_6P$	731.081	C 67.36%, H 11.44%, N 3.83%, O 13.13%, P 4.24%	1 year/ -20°C	---
SOPC	$C_{44}H_{86}NO_8P$	788.129	C 67.05%, H 11.00%, N 1.78%, O 16.24%, P 3.93%	6 months/ -20°C	6°C
SOPS	$C_{42}H_{79}NO_{10}PNa$	812.041	C 62.12%, H 9.81%, N 1.72%, Na 2.83%, O 19.70%, P 3.81%	6 months/ -20°C	---
DPPCd62	$C_{40}H_{18}NO_8PD_{62}$	796.421	C 60.32%, H 2.28%, D 15.68%, N 1.76%, O 16.07%, P 3.89%	1 year/ -20°C	

Figure 13: Characteristic of the lipid used during the PhD. Nomenclature from Avanti lipids website.

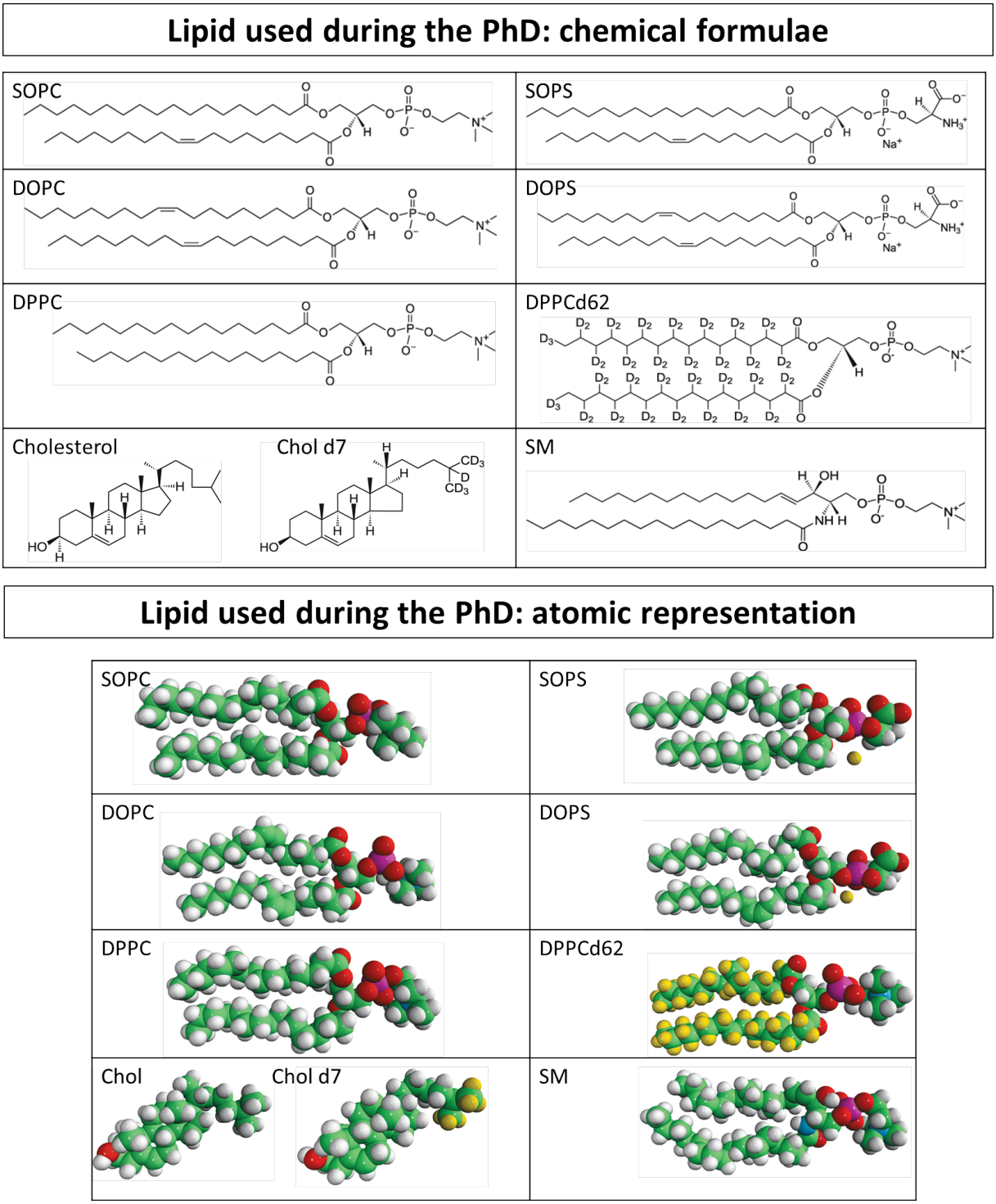

Figure 14: Chemical formulae and atomic representation of all the lipid used for experiments during the PhD. Taken from Avanti lipids website: http://avantilipids.com

Appendix B: Micropipette aspiration measurements

Micropipette aspiration graphs for elastin studies

Micropipette aspiration graphs for spectrin studies

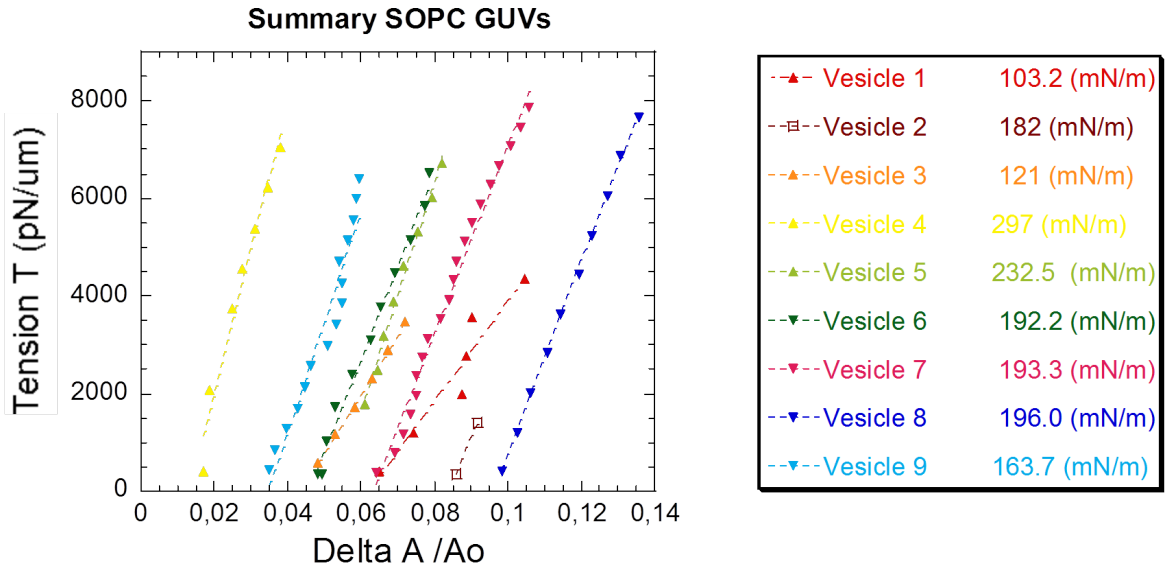

(a) SOPC vesicles electroformation

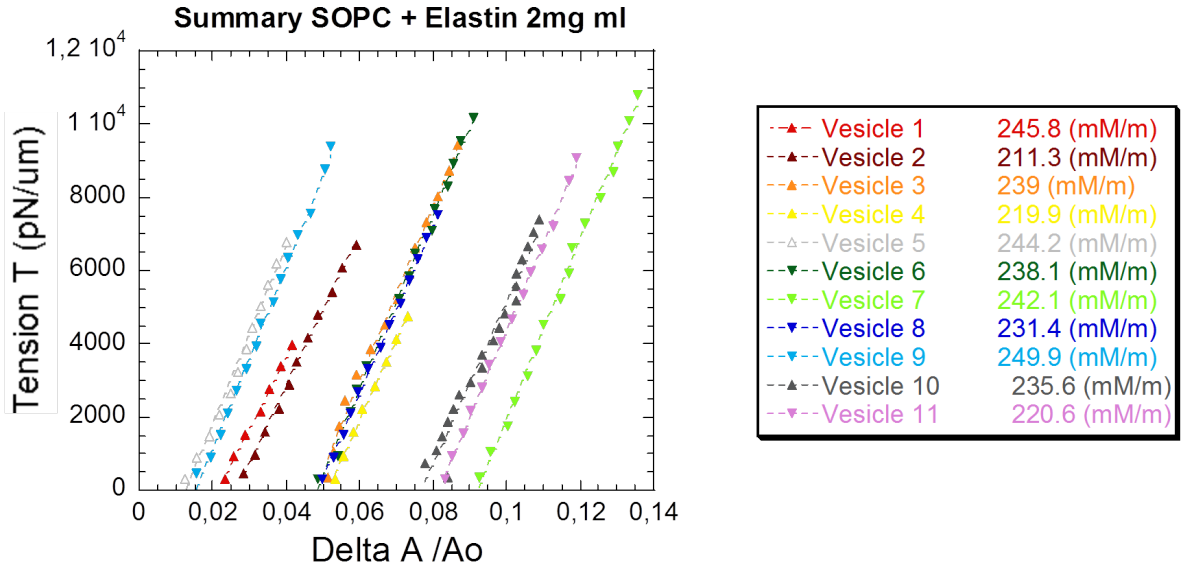

(b) SOPC vesicles plus Elastin 2mg/ml

Figure 15: Studying the effect of Elastin on the area expansion modulus of SOPC vesicles (1/2)

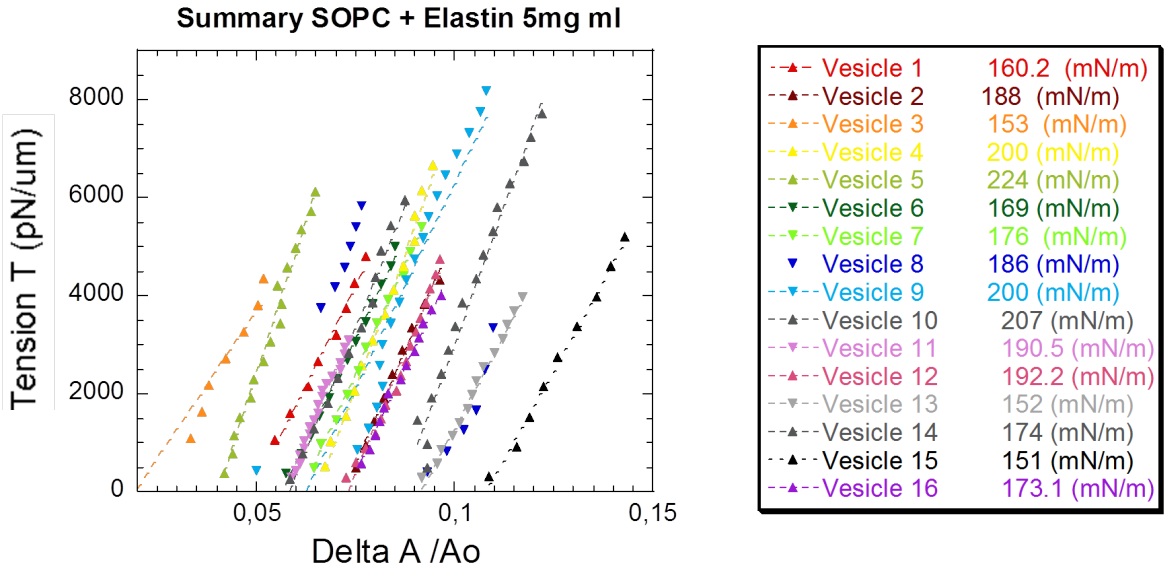

(a) SOPC vesicles plus Elastin 5mg/ml

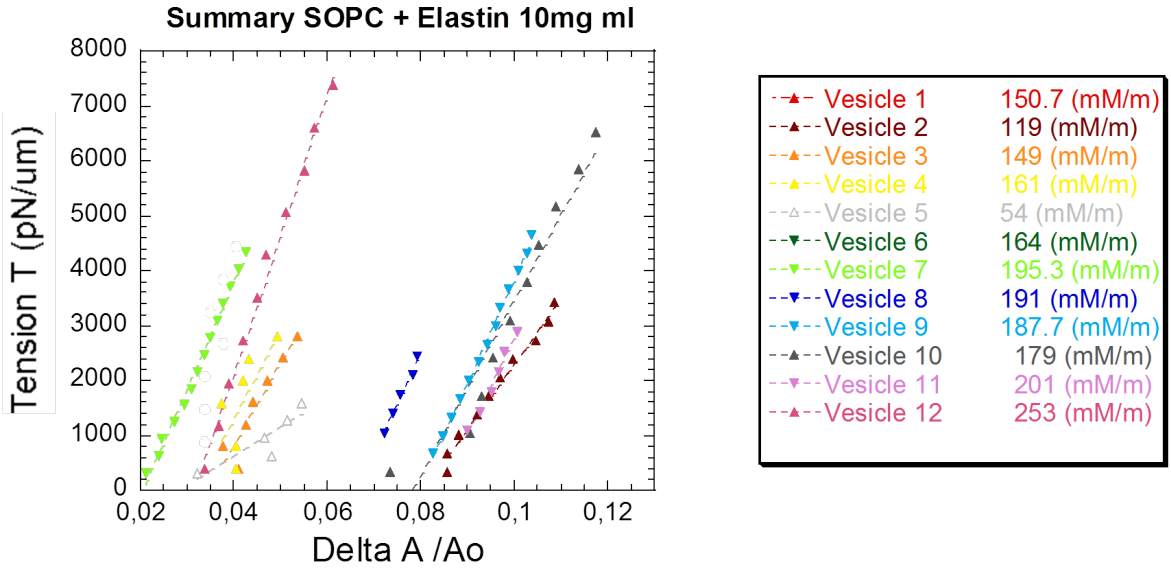

(b) SOPC vesicles plus Elastin 10mg/ml

Figure 16: Studying the effect of Elastin on the area expansion modulus of SOPC vesicles (2/2)

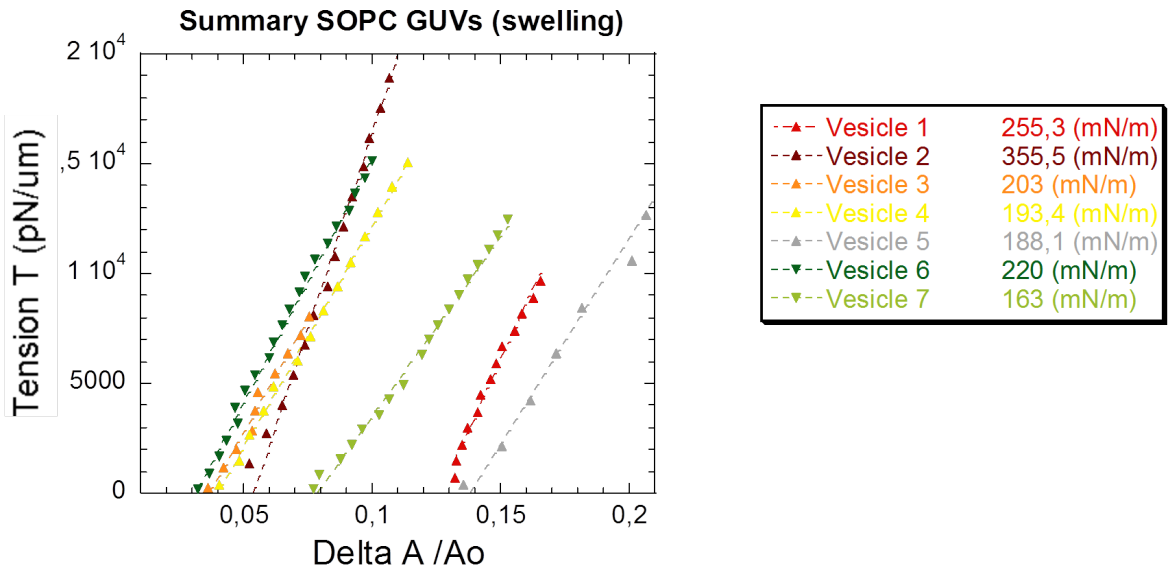

(a) SOPC GUVs swelling method

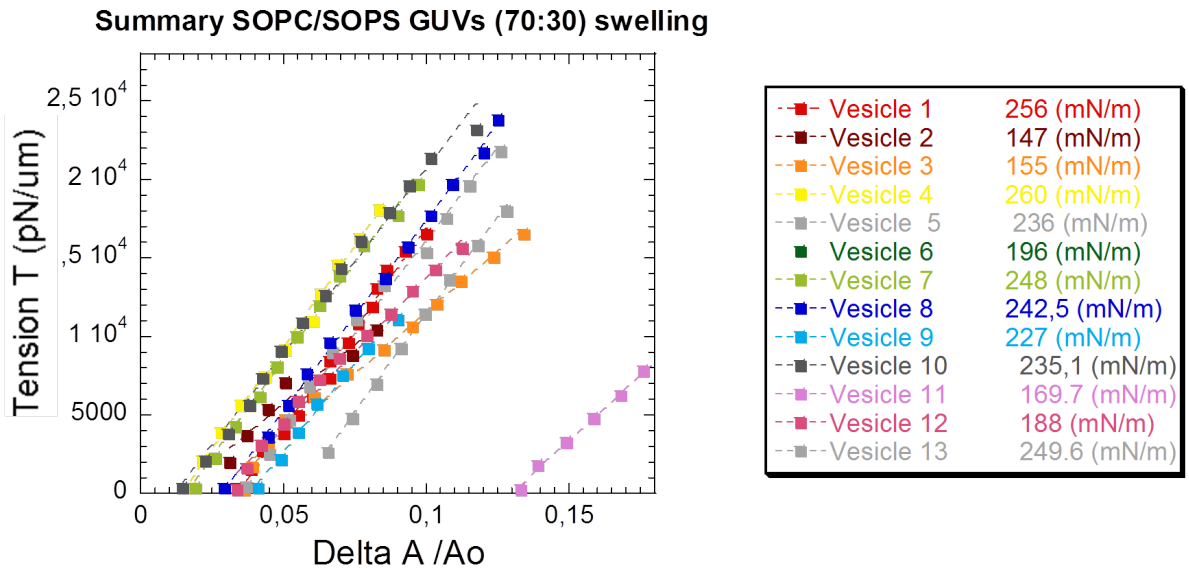

(b) SOPC/SOPS (molar ratio 70:30) GUVs swelling method

Figure 17: Studying the effect of Spectrin on the area expansion modulus of SOPC vesicles (1/3)

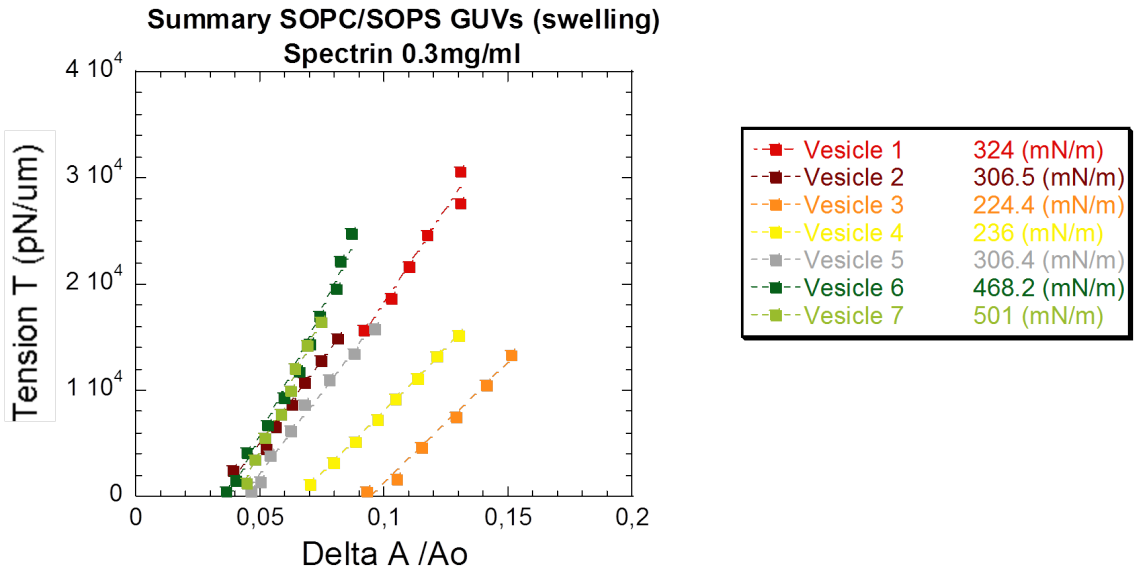

(a) SOPC/SOPS (70:30) GUVs plus spectrin diluted 0.8mg/ml

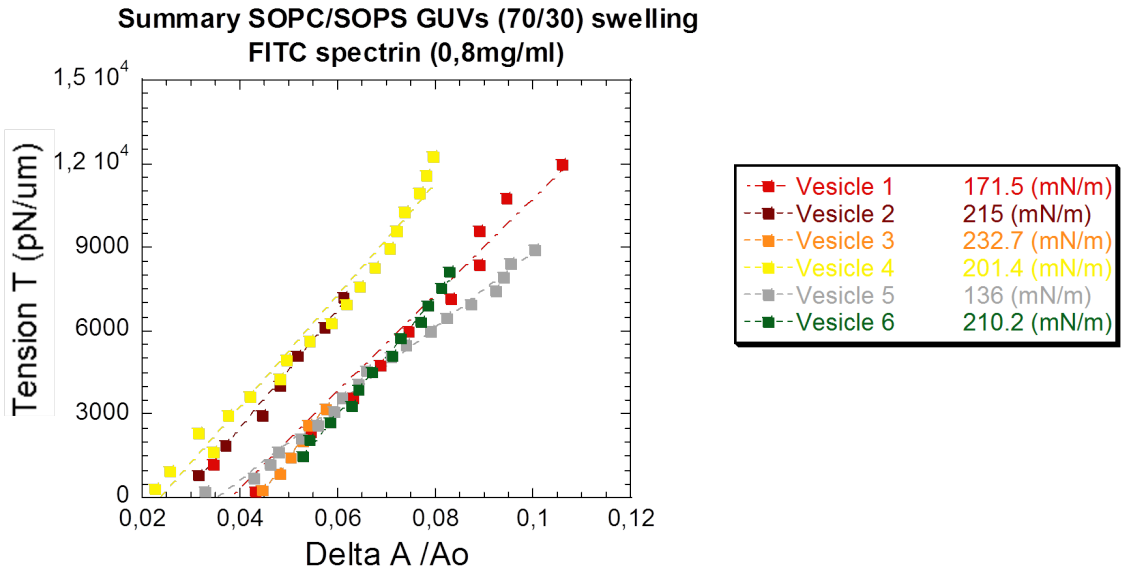

(b) SOPC/SOPS (molar ratio 70:30) GUVs plus FITC spectrin 0.8mg/ml

Figure 18: Studying the effect of Spectrin on the area expansion modulus of SOPC vesicles (2/3)

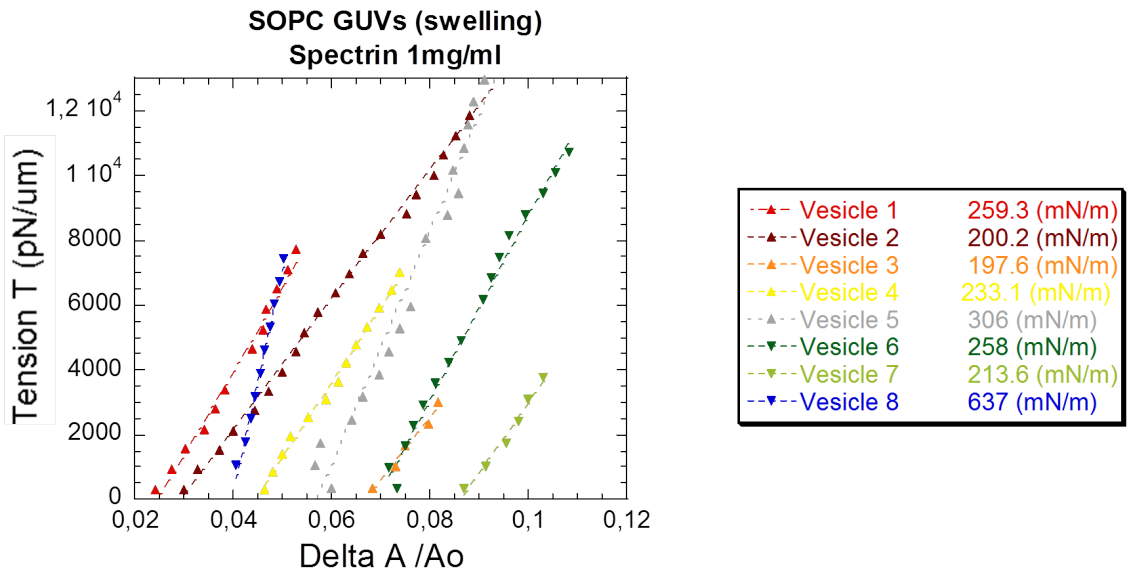

(a) SOPC GUVs plus spectrin 1mg/ml

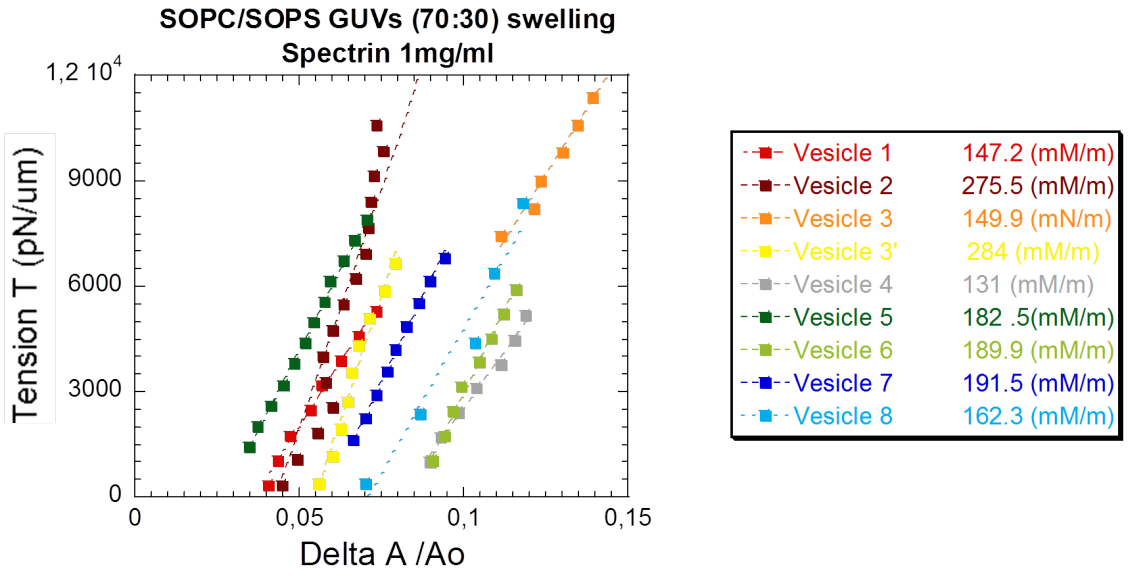

(b) SOPC/SOPS (molar ratio 70:30) GUVs plus spectrin 1mg/ml

Figure 19: Studying the effect of Spectrin on the area expansion modulus of SOPC vesicles (3/3)

Appendix C: Combining micropipette aspiration and SRS: pictures and measurements

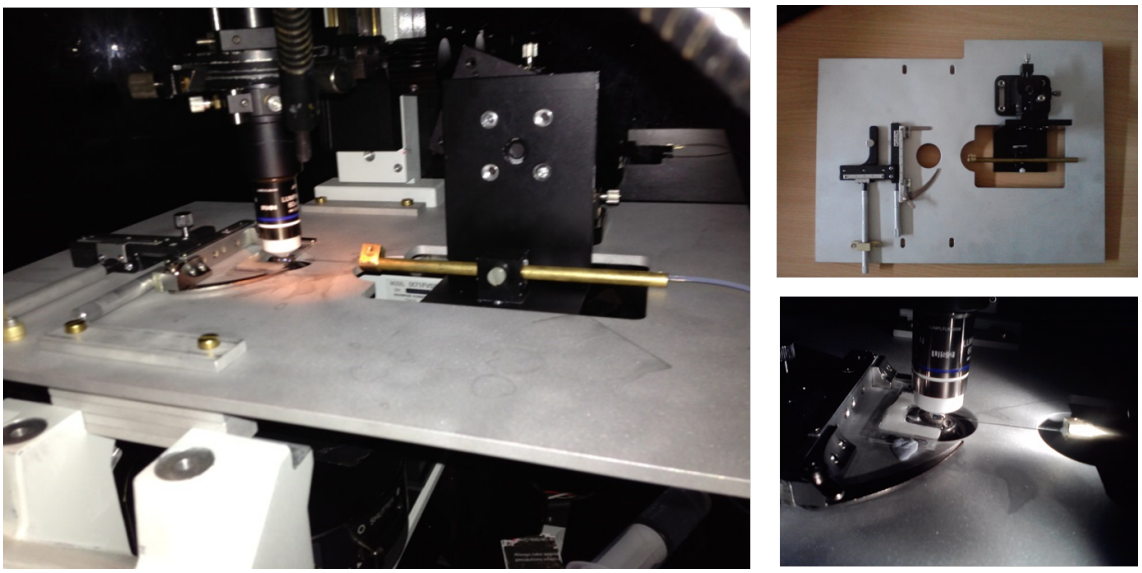

Figure 20: Combining Micropipette aspiration and SRS. Set-Up at the University of Exeter.

Pictures of the set-up

Combining micropipette aspiration and Stimulated Raman Scattering.

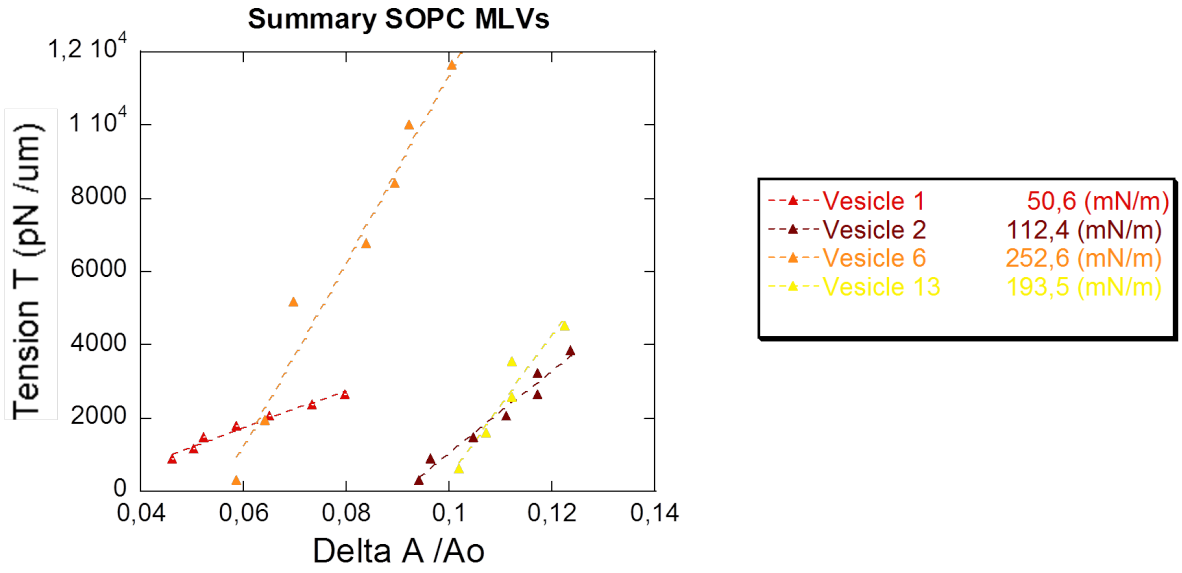

(a) Micropipette aspiration performed on SOPC MLVs.

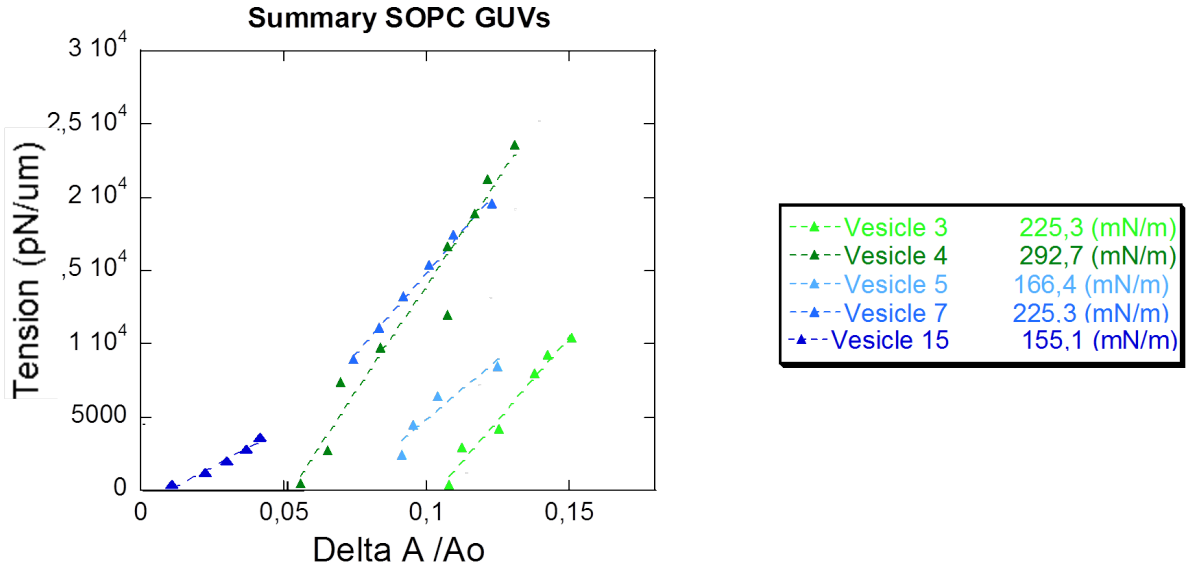

(b) Micropipette aspiration performed on SOPC GUVs.

Figure 21: Micropipette aspiration on SOPC vesicle (1/2)

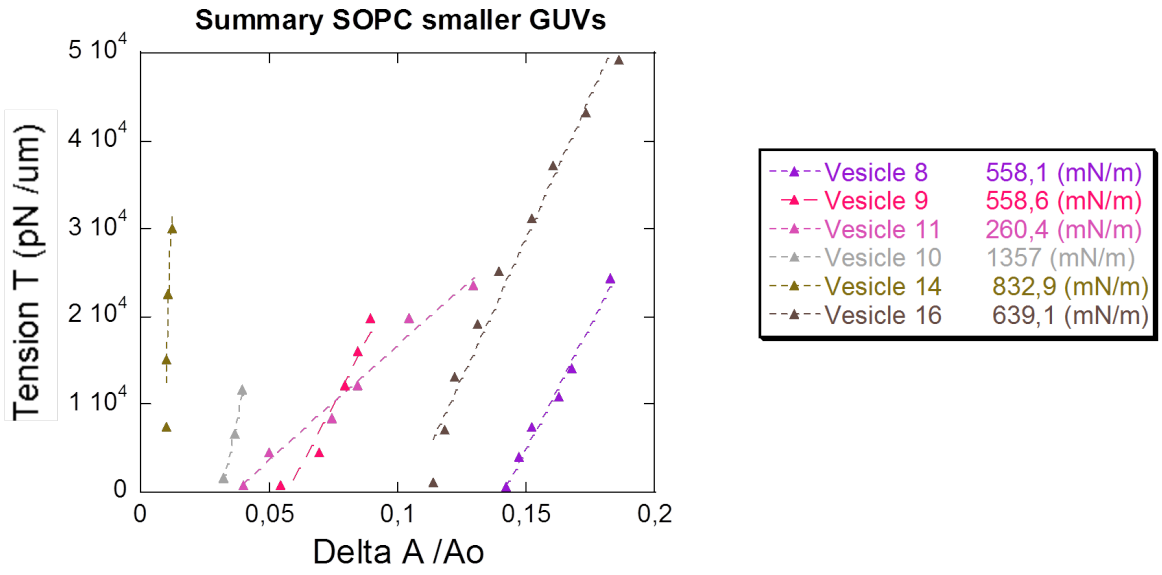

(a) Micropipette aspiration performed on SOPC GUVs (small radii).

$R_{vesicle\ 1}$	14,25 µm
$R_{vesicle\ 2}$	14,21 µm
$R_{vesicle\ 3}$	8,34 µm
$R_{vesicle\ 4}$	7,63 µm
$R_{vesicle\ 5}$	8,64 µm
$R_{vesicle\ 6}$	11,81 µm
$R_{vesicle\ 7}$	8,20 µm
$R_{vesicle\ 8}$	6,04 µm
$R_{vesicle\ 9}$	5,04 µm
$R_{vesicle\ 10}$	4,46 µm
$R_{vesicle\ 11}$	5,76 µm
$R_{vesicle\ 12}$	4,25? µm
$R_{vesicle\ 13}$	6,19 µm
$R_{vesicle\ 14}$	4,79 µm
$R_{vesicle\ 15}$	12,86 µm
$R_{vesicle\ 16}$	8,0 µm

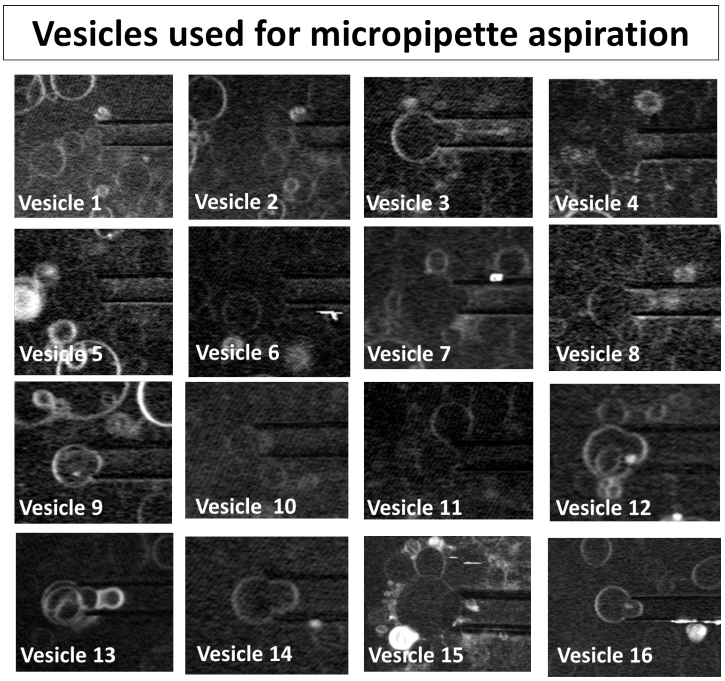

(c) Summary of micropipette aspiration SOPC vesicles imaged with SRS: table of the vesicles measured.

Figure 22: Micropipette aspiration on SOPC vesicle (2/2)

Appendix D: Secondary structure estimate

Secondary structure estimates

Secondary structure estimate Spectrin in buffer

NRMSD:0.008

Helix segments per 100 residues: 5.559
Strand segments per 100 residues: 0.378
Ave helix length per segment: 13.839
Ave strand length per segment: 4.046

Calculated Secondary Structure Fractions

Helix1	Helix2	Strand1	Strand2	Turns	Unordered	Total
0.55	0.22	0.01	0.01	0.06	0.15	1

(a) Spectrin in buffer Solutions from the CDSSTR method
Solutions using reference database: 4

Secondary structure estimate Spectrin 50:50 DOPC/DOPS

NRMSD:0.011

Helix segments per 100 residues: 5.286
Strand segments per 100 residues: 0.774
Ave helix length per segment: 13.442
Ave strand length per segment: 4.536

Calculated Secondary Structure Fractions

Helix1	Helix2	Strand1	Strand2	Turns	Unordered	Total
0.50	0.21	0.02	0.02	0.08	0.17	1

(b) Spectrin 50:50 DOPC/DOPS Solutions from the CDSSTR method
Solutions using reference database: 4

Figure 23: Secondary structure